Structure Formation as Studied by EPR Spectroscopy: From Simple Solutions to Nanoparticles

Dissertation
Zur Erlangung des Grades
„Doktor der Naturwissenschaften"
im Promotionsfach Chemie

am Fachbereich Chemie,
Pharmazie und Geowissenschaften
der Johannes Gutenberg-Universität Mainz

von

Jeannine Heller

geboren in Fulda

Mainz, den 19. Mai 2010

Die vorliegende Arbeit wurde von November 2006 bis
Mai 2010 am Max-Planck-Institut für Polymerforschung in Mainz angefertigt.

Dekan:

1. Berichterstatter:

2. Berichterstatter:

Tag der mündlichen Prüfung: 21.07.2010

Dedicated to Daniel

To every action there is always opposed an equal reaction.
~~~~
*Sir Isaac Newton*
*1687*
~~~~

Contents

List of Symbols and Abbreviations

a_{iso}	isotropic ^{14}N hyperfine coupling
a_k	length of statistical segment
b	average distance between two charged groups along the polymer chain
c_0	salt concentration
c^*	critical concentration of coil overlap
cmc	critical micelle concentration
δ	density
λ_B	Bjerrum length
λ_D	Debye-Hückel screening length
D	diffusion coefficient
DEER	double electron-electron resonance
DSA	4,4-dimethyl-oxazolidine-*N*-oxyl octadecanoic acid (DOXYL stearic acid)
ε	dielectric constant
e	elementary charge
EPR	electron paramagnetic resonance
ENDOR	electron nuclear double resonance
ESE	electron spin echo
ESEEM	electron spin echo envelope modulation
FJC	freely jointed chain
FRC	freely rotating chain
FS	Fremy's salt
HYSCORE	hyperfine sublevel correlation
I	nuclear spin
k_B	Boltzman constant
l_B	Bjerrum length
l_c	contour length
l_p	persistence length
M	molecular weight
M_n	number average molecular weight
M_w	weight average molecular weight

m_S	electron spin quantum number
m_I	nuclear spin quantum number
mw	microwave
N	degree of polymerization
N_A	Avogadro constant
μ_B	Bohr magneton
μ_N	nuclear magneton
ξ_M	Manning parameter
ρ_m	immobilized charge density of the macroion
PB	Poisson-Boltzmann
PEL	polyelectrolyte
PDADMAC	poly(diallyldimethylammonium chloride)
$\rho(r)$	charge density
$\psi(r)$	electrostatic potential
Q	quadrupole moment
R	end-to-end distance
R_g	radius of gyration
R_g^2	mean square radius of gyration
R_F	Flory radius
S	electron spin
rf	radiofrequency
t_p	pulse length
τ_{corr}	rotational correlation time
τ	interpulse delay
T	temperature
T_K	Krafft temperature
tmhd	2,2,6,6-tetramethyl-3,5-heptanedionate
X-band	microwave frequency range of ~9.1 to ~9.8 GHz
W-band	microwave frequency range of ~93 to ~94 GHz
WLC	wormlike chain
ω_{Ex}	exchange coupling frequency
ω_{dip}	dipolar coupling frequency

1 Introduction

In *ionic* systems the charges interact with each other via *electrostatic forces.* These belong to the group of electromagnetic interactions, which causes electric and magnetic effects such as repulsion between like electrical charges or the interaction of bar magnets. The electromagnetic interaction is one of the *four fundamental interactions* in particle physics and is described by quantum electrodynamics (the other three interactions are strong and weak nuclear force and gravity and not meaningful for this thesis). However, if the electrical field is strong enough, as it is the case for ions and molecules, quantum effects may be neglected and the classical electromagnetism, based on the Coulombs law (see Figure 1.1) can be used to describe the system.

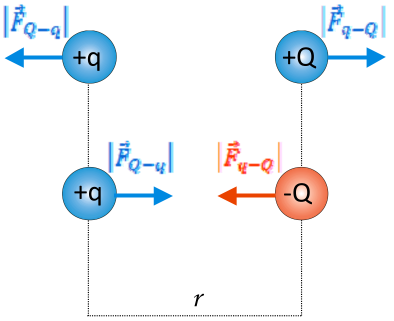

$$\vec{F}_{Q-q} = \vec{F}_{q-Q} = \frac{1}{4\pi\varepsilon_0}\frac{|q||Q|}{r^2} \qquad (1.0)$$

Figure 1.1 The electrical force acting on a point charge +q as a result of the presence of a second point charge +Q is given by the Coulomb law. Like charges (upper) repel each other, unlike charges (lower) attract each other.

In eq. (1.0) ε_0=8.854187·10^{-12} Fm^{-1} is the dielectric permittivity of free space. The law is in the form of a vector equation and includes the fact that the force acts along the line joining the point charges and describes a force of infinite range which obeys the inverse square law.

For inorganic salts like sodium chloride in aqueous solution, the Coulomb force is dominating and the spherical ions are octahedrally solvated by six water molecules [4]. The way how ions are solvated in water or solvent mixtures has a profound influence on many chemical phenomena such as solubility and rates of chemical reactions [5]. For a more complex, molecular ion that has further functional groups (e.g. amine- or hydroxyl-functionalities) hydrogen-bonding with the polar groups and water alters the water structure around the ion, depending on their size and capability to form H-bonds. Extending the ionic molecule further with an apolar alkyl chain, hydrophobic interactions between the apolar parts will dominate the structure if the alkyl chain is long enough to be repelled from the polar water phase (self-aggregation or micelle formation, see Section 5.2.1). Thus, the structure of the assembled molecules depend on the chemical composition of the molecules and other factors like temperature, pH, solvent polarity and ionic strength of the solution as well as other chemical interactions like coordinative bonding, chemical exchange or redox reactions. The energy of hydrogen-bonding is typically ~26 kJ/mol and much higher than van der Waals forces (~1 kJ/mol), that are always present between molecules on short distances (for comparison: the covalent bond energy is ~400 kJ/mol) [4].

In macromolecules with high charge density this ionic organic molecule is repeated many times. Such “polyelectrolytes” can be found in nature e.g. DNA, alginate, xanthan or actin but the synthetic ones are also equally important in industry and daily life. For polyelectrolytes the interplay between electrostatic (repulsion between the charged units) and hydrophobic interactions (attraction of the carbon-based backbone) is responsible for their properties in solution, which has stimulated extensive experimental [6] and theoretical [7-8] investigations for several decades now. Protein folding, which is currently a very active research field is also attributed to the delicate interplay between hydrophobic and electrostatic interactions [9].

The structural characterization of soft matter systems with lacking long-range order is one of the most challenging problems. Magnetic resonance methods, such as nuclear magnetic resonance (NMR) and electron paramagnetic resonance (EPR) spectroscopy are non destructive highly selective methods to probe nanoscopic structure (up to 8 nm) and dynamics (ps to μs regime) in solution [10], and are such complementary to light scattering, X-ray and neutron diffraction. The basic requirement for EPR is paramagnetism of the system, i.e. the availability of unpaired electrons, like a radical or a paramagnetic transition metal.

Since most soft matter systems are not intrinsically paramagnetic, it is necessary to introduce stable free radicals (based on nitroxides see Scheme 2.1) either covalently or by non-covalent self-assembly. In both techniques it is assumed, that the nitroxide does not interrupt the original structure [11].

In this thesis, three nitroxide based ionic systems of increasing complexity are chosen for the investigation of the structure and dynamics of their respective aqueous solutions. A variety of EPR methods is applied to elucidate the interactions between several spin probes and their environment. It is the aim of this work to deepen the insights of how non-covalent interactions govern the self assembly of ions or charged molecules in solution in particular when other comparable strong interactions are present. An overview about the systems and the used methods is given below.

The thesis is divided into seven chapters. Chapter 2 reviews the basic principles of electron paramagnetic resonance (EPR) spectroscopy, explains continuous wave (CW) EPR spectra for nitroxides at X- and W-band (9.5 and 94.5 GHz, respectively) and elucidates the extraction of the EPR parameters by means of computer simulations. Chapters 3, 4, and 5 show the experiments and results on the systems under investigation. Chapter 6 gives a summary about the experimental findings and Chapter 7 lists all laboratory work.

- *The solvation of Fremy's salt (Chapter 3)*

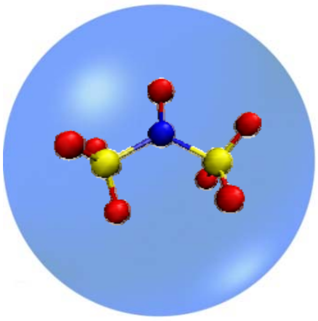

Figure 1.2 Scheme of the solvation shell of Fremy's salt $ON(SO_3^-)_2$.

The solvation of dissolved ions determines many of the properties of electrolyte solutions [5], including their redox, complexation and kinetic behavior. In Chapter 3 the solvation of Fremy's salt (FS), the paramagnetic nitrosodisulfonate anion $ON(SO_3^-)_2$, in binary solvent mixtures is investigated by means of high-field/high-frequency (W-band ~94.5 GHz) pulse (Mims- and Davies-type) electron nuclear double resonance (ENDOR) spectroscopy (Section 2.9.4) and molecular dynamics simulations (Section 3.4). Isotope-substituted solvent mixtures of either *methyl* protons from the alcohol moiety or *exchangeable* protons from the alcohol-hydroxyl group and water are used. Orientation-selective high-field/high-frequency ^1H and ^2H pulse ENDOR spectra are recorded for different solvent compositions in frozen solution that reveal the hyperfine (hf) splitting between the radical and the solvent protons. Analysis of the hf splitting yields spatial, orientation selective information about the different proton species around the ion. The elucidation of the microscopic solvation of a small probe molecule in binary solvent mixtures represents the first step for understanding the interactions in more complex biochemical systems. In particular this includes the potential perturbation of H-bond network due to presence of a spin probe or other polar molecules.

- *Polyelectrolyte conformation in divalent salt solutions (Chapter 4)*

Polyelectrolytes (PEL, see Figure 1.3) are water soluble macromolecules. They play an important role not only in fields of scientific research but also in drug delivery [12], water treatment [13], cosmetics [14] and nanotechnology [15].

Analogous to small electrolytes they can be divided into strong (complete dissociation) and weak (pH dependent dissociation) polyelectrolytes. Nonetheless, they cannot be understood as a simple superposition of electrolyte and polymer properties [16] due to the mentioned interplay of electrostatic and hydrophobic interactions. The balance between them can be shifted by adding simple inorganic salts that screen the intramolecular electrostatic repulsion and lead to more dominant hydrophobic interaction.

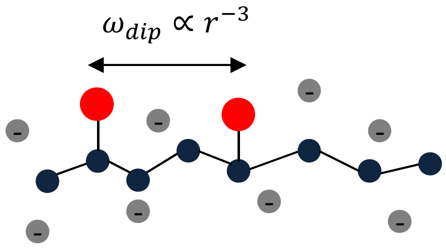

Figure 1.3 Scheme of a statistically spin-labeled polyelectrolyte with counter-ions. The charged monomers are colored in blue, the spin label in red and the counterions in grey. From the dipolar coupling ω_{dip} of the electron spins, the distance information can be extracted.

The conformation of spin-labeled poly(diallyldimethyl ammonium chloride) PDADMAC – a strong polyelectrolyte – in binary solvent mixtures is investigated by means of double electron-electron resonance (DEER) spectroscopy. DEER measures the dipolar coupling ω_{dip} between two electron spins that can be used to calculate the distance and distance distribution of the spins (see Section 2.9.3) [10, 17]. The influence of divalent salt addition on conformational changes is interpreted on the basis of the wormlike chain model [18].

- *Structure and dynamics of miniemulsions (Chapter 5)*

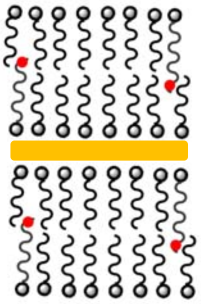

Figure 1.4 Surfactant bilayers in a miniemulsion in presence of a lanthanide complex (orange). The spin label is colored in red.

Miniemulsions are heterogeneous systems consisting of an unpolar phase dispersed in water. The exact composition and preparation method is explained in Chapter 5. In this thesis the nanostructures observed in presence of a lanthanide complex (orange line in Figure 1.4) are characterized with CW EPR spectroscopy for different surfactant systems (sodium dodecyl sulfate, -octadecyl sulfate, -laurate, -carboxylate). The CW spectra are analyzed in terms of the exchange frequency ω_{Ex} and the rotational correlation time τ_{corr} by means of computer simulations.

It is the aim of this work to deepen the insights of how non-covalent interactions govern the self assembly of ions or charged molecules in solution in particular when other equally strong interactions are present.

2 Principles of Electron Paramagnetic Resonance Spectroscopy

Electron paramagnetic resonance (EPR) spectroscopy is a technique based on the resonant absorption of electromagnetic radiation by a paramagnetic sample within a magnetic field. Paramagnetic species are atoms, ions or molecules that exhibit unpaired spins ($S \neq 0$). EPR and electron spin resonance (ESR) are synonyms but the term EPR is used in this work. Like all spectroscopic methods, EPR is based on the measurement and interpretation of the energy differences ΔE between spin (or atomic, ionic or molecular) states according to Planck's law

$$\Delta E = h\upsilon, \tag{2.0}$$

where h is Planck's constant ($h =$ 6.626068· 10^{-34} Js) and υ is the frequency of the radiation. Eq. (2.0) is the fundamental equation for all spectroscopic methods that allows studying energy levels and their respective populations. Compared to other spectroscopic methods, magnetic resonance techniques posses a remarkable difference: The splitting ΔE between the energy levels is not constant but can be varied to a large degree by variation of an external magnetic field (see Section2.2.1). Dependent on the magnetic field strength (typically at 0.1 to 3.5 T) EPR spectrometers work with GHz resonance microwave frequencies. At small magnetic fields electromagnets are used with typical field strengths of 0.3 T (X-band, 9.5 GHz). Higher fields require helium cooled superconducting magnets, most commonly working at 3.4 T (W-band, 94.5 GHz).

If the system of interest is diamagnetic, stable organic or inorganic radicals can be introduced by simple mixing or covalent attachment, the latter requires a further chemical step. Such spin probes or spin labels are usually derivatives of nitroxides and are presented in Section 2.7.

After this very short introduction, the following Section 2.1 briefly presents the spin Hamiltonian description before the concept of the electron spin and the interactions present in an external magnetic field is presented Section 2.2. It is supposed that the basic laws of (macroscopic) electromagnetism and quantum mechanics are known. The aim of this chapter is to provide the basic information about the phenomenon of electron paramagnetic resonance (EPR). The paramagnetic species studied in this work are nitroxide radicals, thus, in particular EPR spectra of nitroxides in solution at low and high magnetic field will be described together with the properties that influence the shape of the spectra and the intensity of the spectral lines (Section 2.7).

2.1 Spin Hamiltonian Formalism

For interpretation of spectroscopic data in magnetic resonance spectroscopy the spin Hamiltonian approach is a common method. Actually, this formalism is not a full physical model, but it accurately describes and parameterizes the interactions that influence NMR, EPR and ENDOR spectra [19-20].

In MR experiments one observes transitions between quantum states associated with the magnetic dipole moment under influence of an external magnetic field. The quantum energies of magnetic transitions are typically small compared to electronic or nuclear transitions energies. Thus, it is possible to treat MR experiments by perturbation theory. Using this approach simplifies the theoretical treatment tremendously since it can be confined to a Hilbert space with only spin and angular momentum components. Shortly, the true Hamiltonian of the system is replaced by an effective Hamiltonian that contains only spin operators. In many cases the effective values obtained from such analysis are not directly related to the physical properties of the system under investigation and theoretical calculations are necessary to obtain specific properties of the system. An extensive review about the spin Hamiltonian approach can be found in [20].

The Hamiltonian models the system by a power law series expansion in angular momentum operators $\mathbf{j_i}$, that are also called spin operators (even though they may have orbital momentum contributions):

$$H = \sum_{i} c_i^{(1)} \mathbf{j_i} + \sum_{i,j} c_{ij}^{(2)} \mathbf{j_i}\,\mathbf{j_j} + \sum_{i,j,k} c_{ijk}^{(3)} \mathbf{j_i}\,\mathbf{j_j}\mathbf{j_k} + \cdots, \tag{2.1}$$

where the coupling constants $c^{(n)}$ of n-th order reflect the effect of the neglected electronic states and the strength of the external magnetic field B_0. Mostly, the convergence of the series allows restricting the spin Hamiltonian to only a few low-order terms.

The complete, *time-independent* spin Hamiltonian H is given in eq. (2.2).

$$H = H_{EZ} + H_{ZFS} + H_{HF} + H_{NZ} + H_{NQ} + H_{el} \tag{2.2}$$

H_{EZ} denotes the electron Zeeman interaction, H_{ZFS} the zero-field splitting, H_{HF} the hyperfine interaction, H_{NZ} the nuclear Zeeman interaction, H_{NQ} the nuclear quadrupole interaction and H_{el} weak electron-electron interaction. In the following description of the terms the Hamiltonians are given in angular frequencies, i.e. in energies divided by $\hbar$.

2.2 Electron-Zeeman Interaction

2.2.1 The Electron Spin in a Magnetic Field

The foundation of magnetic resonance is built on the existence of the spin (in NMR the nuclear spin, in EPR the electron spin) that has no classical analogue. Experimental evidence like the hydrogen fine structure [21-22] and the Stern-Gerlach experiment [23] suggested that the electron has an intrinsic angular momentum S independent of its orbital angular momentum L. Angular momenta are vector properties that are defined by their magnitude and the direction in space. The electron spin is described by the spin operator $\boldsymbol{S}$ with the eigenvalue $S\hbar$ and a magnitude of:

$$|\mathrm{S}| = \sqrt{S(S+1)}\hbar. \tag{2.3}$$

For a single electron the spin quantum number S takes the value ½ and it follows from eq. (2.3) for the magnitude of the vector $|\mathrm{S}| = \sqrt{3/4}\hbar$. The relation between the magnitude |S| and its projection along any direction in space is commonly visualized by the vector model (see Figure 2.1).

In the Cartesian frame with an unique z-axis it is necessary to define three spin operators S_x, S_y, S_z in the three spatial dimensions. The electron spin states have definite components S_z only along the z-axis, while the components of the perpendicular axes cannot be determined. This is a consequence of the orthogonality of the three S_i operators: only *one* of them commutes with the Hamilton operator ($[S_z, H] = 0$), while the remaining components do not commute ($[S_{x,y}, H] \neq 0$). This leads to a quantization of $\boldsymbol{S}$ in z-direction.

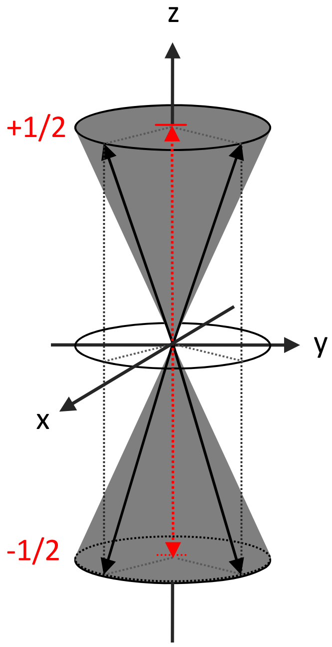

Figure 2.1 Vector model of the electron spin angular momentum $\boldsymbol{S}$ (black arrow). The length of the vector is $|\mathrm{S}| = \sqrt{3/4}\,\hbar$. In the Cartesian frame the z-axis is conventionally the unique axis and only the S_z component (projection of $\boldsymbol{S}$ onto z-axis) of the spin vector has a definite value of either $1/2$ or $-1/2$ (in $\hbar$ units). The z-component S_z is shown as a dotted red arrow, pointing in the positive (m_s=+1/2 or α spins) or negative z-direction (m_s=-1/2 or β spins). However, the components in the xy-plane are not defined, which means that the α and β spins are allowed to point in every direction on the surface of the cone. On this cone surface, the spin is precessing with the angular frequency ω_s, the Larmor frequency.

The magnetic spin quantum numbers m_s are found in the range $\{-S, -S+1, \dots, S\}$. For a single electron with $S = 1/2$, the values are $m_s = \pm 1/2$. In the vector model, the two m_s values (black arrows in Figure 2.1) describe the orientation of the spin vector $\boldsymbol{S}$ on the surface of a cone with the fixed height of the eigenvalue $m_s \hbar$ (red arrows), e.g. the α and β states differ in the orientation of the angular momentum in space but not in the magnitude. If there is no particular interaction of the electron spin with its environment, any direction of the z-axis is allowed (space isotropy) and all energy levels are degenerate, i.e. they have the same energy and no resonance phenomenon can occur in presence of an oscillating radio-frequency field.

In presence of an external magnetic field B_0, the energy levels are split (Figure 2.2 b), as the magnetic moment $\boldsymbol{\mu}$ associated with the electron spin $\boldsymbol{S}$ tends to be oriented parallel or antiparallel to the magnetic field vector (see Figure 2.2 a). Per definition the magnetic field vector is aligned along the z-axis. This splitting that is called *electron Zeeman interaction* is the most fundamental interaction in EPR. The energies E_{m_s} for the spin states in frequency units vary linearly with the magnitude of B_0:

$$E_{\mathrm{m_s}} = g_e \frac{\mu_B}{\hbar} B_0 m_s = -\gamma_e B_0 m_s \qquad (2.4)$$

$\hbar$ is Planck's constant h divided by 2π, g_e the g- value (2.0023193) and γ_e the gyromagnetic ratio ($1.761 \cdot 10^{11}$ $\mathrm{s^{-1}T^{-1}}$) of the free electron and μ_B the Bohr magneton ($927.401 \cdot 10^{-26}$ $\mathrm{JT^{-1}}$) [24]. The energy difference between the two Zeeman levels can be calculated according to:

$$\Delta E = E(m_s = 1/2) - E(m_s = -1/2) = \hbar\omega_s = g_e \mu_B B_0 \qquad (2.5)$$

If this resonance condition is fulfilled, i.e. the energy of the irradiation field matches the energy gap ΔE, transitions between the two spin states are induced by absorption or induced emission that flip the spin from one orientation to the other. In eq. (2.5) ω_s is referred to as the Larmor frequency.

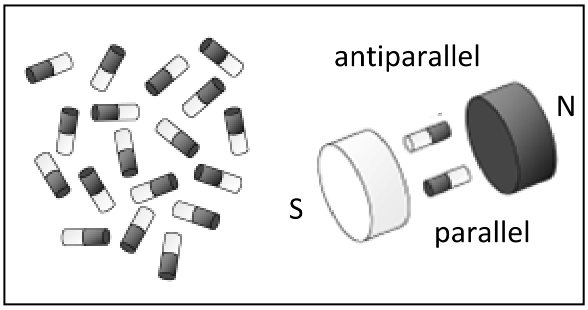

a) Molecular Magnets

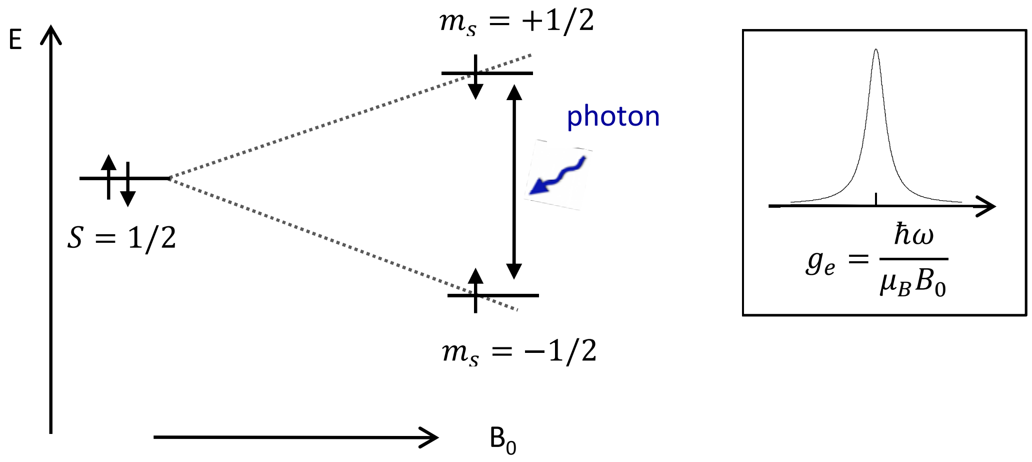

b) Electron Zeeman effect

c) EPR spectrum

Figure 2.2 The electron spin in the magnetic field ($S = 1/2$, $L = 0$). a) Alignment of the magnetic moments of unpaired electron spins in a model of molecular magnets from randomly ($B_0 = 0$) to parallel and antiparallel ($B_0 > 0$). b) Energy-level scheme for a *free electron* as a function of the applied magnetic field B_0. At zero magnetic field ($B_0 = 0$) the electron spin states are degenerate. In presence of a static magnetic field the β spin state is lowered and the α spin state is increased in energy. The energy separation ΔE is proportional to the field intensity. At a constant irradiation frequency ω a transition between the Zeeman states occurs during the field sweep when the resonance condition is fulfilled. c) The resulting EPR spectrum is a single absorption line that appears at a characteristic position $g_e$in the EPR spectrum. The spectrum is shown in the absorption mode.

During EPR transitions, quantum coherence between both m_s eigenstates is generated, that will finally lead to a change in the polarization by one unit of $\hbar$ by lowering or rising m_s by 1. This is a consequence of the selection rule

$$\Delta m_s = \pm 1. \tag{2.6}$$

2.2.2 g-Anisotropy

The g-factor (or g-value) characterizes the position of the EPR resonance line in an EPR spectrum. The g-value of the free electron (having no orbital angular momentum $L = 0$) is ~2.0023. Paramagnetic systems with highly delocalized electrons show a g-value very close to this value which always indicates a very small coupling of spin and orbital moments (spin-orbit coupling, SOC). However, g often differs from this value if the contribution of SOC is *not* negligible. In this case, interaction of excited states with the electron ground state admixes orbital angular momentum L to the ground state that couple to the electron spin S. As a result, the g-value is no longer isotropic and the splitting of the Zeeman levels depends further on the environment of the electron spin (e.g. the symmetry of the crystal field or the orientation of the system within the magnetic field). Therefore, the g-values are a 'fingerprint' of the electronic environment of the observed electron spin, analogous to the chemical shift in nuclear magnetic resonance.

The 'effective field' B_{eff} experienced by the electron spin is a superposition of the internal and external fields and the energy of this anisotropic interaction is given by:

$$H_{EZ} = g_e \frac{\mu_B}{\hbar} \boldsymbol{B}_{eff} \boldsymbol{S} = \frac{\mu_B}{\hbar} \boldsymbol{B}_0^T \, \mathbf{g} \, \boldsymbol{S}, \tag{2.7a}$$

$$= \frac{\mu_B}{\hbar} \left(B_{0,x}\; B_{0,y}\; B_{0,z}\right) \begin{pmatrix} g_{xx} & & \\ & g_{yy} & \\ & & g_{zz} \end{pmatrix} \begin{pmatrix} S_x \\ S_y \\ S_z \end{pmatrix} \tag{2.7b}$$

The orientation dependent Zeeman interaction is expressed by a (3x3) **g** interaction matrix, that can be represented in its principal axes system (PAS) by a diagonal matrix (eq. (2.7a)), where (x, y, z) is the PAS and g_{xx}, g_{yy} and g_{zz} are the principal values of the **g**-matrix, commonly denoted as the g-tensor.

For an axially symmetric **g**-matrix, the two identical elements are combined to $g_{xx} = g_{yy} = g_{\perp}$ and the remaining element is denoted as $g_{\parallel}$. Per definition $g_{\perp}$ is perpendicular and $g_{\parallel}$ is parallel to the unique axis of the **g**-matrix. In liquid solution when molecular rotation about the three axes is fast, the g-anisotropy is averaged to the isotropic g_{iso}-value that can be calculated from the **g**-tensor according to eq.(2.8). Often used definitions related to the **g**-tensor are the anisotropy Δg and the asymmetry η.

$$g_{\mathrm{iso}} = \frac{1}{3}(g_{xx} + g_{yy} + g_{zz}) \; = \frac{1}{3} trace(\mathbf{g}) \tag{2.8}$$

$$\Delta g = g_{zz} - g_{iso} \qquad \eta = \frac{g_{yy} - g_{xx}}{\Delta g}$$

On the basis of the element pattern of the **g**-matrix several cases of matrix symmetry can be distinguished, namely isotropic, axial, or rhombic. Examples for powder EPR spectra for different **g**-anisotropies are shown in Figure 2.3.

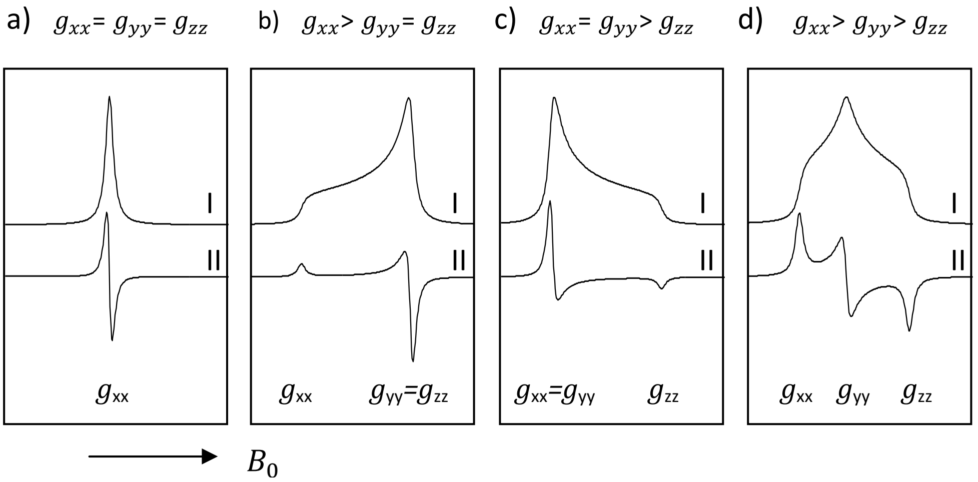

Figure 2.3 Simulated EPR spectra in absorption (I) and first derivative (II) mode for isotropic (a), axial (b,c) and rhombic (d) g-tensor.

The anisotropy of $\mathbf{g}$ can be measured by recording the EPR spectra of a *single crystal* (where the molecules are in fixed orientations) by rotating the crystal in the magnetic field with respect to three orthogonal axes in the sample and transforming the sample frame (that may be given by e.g. the crystal symmetry) into the molecular frame (the PAS of the $\mathbf{g}$-matrix), which can be further transformed into the laboratory frame (where the z-axis is collinear the direction of B_0). The EPR spectrum of a *powder* is a superposition of EPR lines of randomly oriented microcrystals. The same is true for paramagnets in *glassy matrices*. However, the $\mathbf{g}$-anisotropy can be measured even for such samples (see Section 2.9.4).

For B_0 pointing along one of the principal axes, the spin vector $\boldsymbol{S}$ is quantized along B_0 and the resonant field value can easily be calculated from the resonance (eq. (2.5). For an arbitrary direction of B_0 the $\mathbf{g}$ -matrix can be expressed as a symmetric tensor and three Euler angles α, β and γ describing their orientation relative to each other.

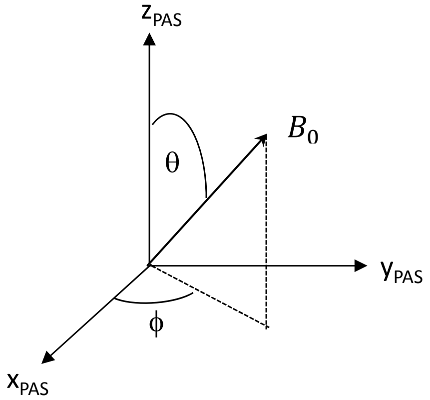

Figure 2.4 The orientation of the magnetic field vector $B_0$with respect to the $\mathbf{g}$-tensor principal axes system is defined by the polar angles θ and ϕ.

Note, that the orientation of the PAS with respect to B_0 is usually specified via the polar angles θ, ϕ or the direction cosines and the transformation of an interaction tensor into the laboratory frame $R(\theta, \phi)$ is also an Euler rotation where only *two* angles are required (in the laboratory frame no distinction is made between the x and y axes). Within this nomenclature θ denotes the Euler rotation about the y-axis, which is $R_y(\theta)$ and corresponds to $\beta = 0$.

In computation of anisotropic EPR spectra, Euler angles are required as input variables to reduce the number of free parameters and the interactions need to be represented in the laboratory frame. In principle, one has to define the rotation of the $\mathbf{g}$-tensor from its PAS into the laboratory frame. The analogous rotation of the $\mathbf{A}$-tensor is expressed via two rotations, first from its PAS into the PAS of the $\mathbf{g}$-tensor and second into the laboratory frame (the hyperfine tensor $\mathbf{A}$ is introduced in Section 2.4):

$$g_{PAS} \xrightarrow{R(\theta,\phi)} g_{lab} \qquad\qquad A_{PAS} \xrightarrow{R(\alpha,\beta,\gamma)} A_{g_{PAS}} \xrightarrow{R(\theta,\phi)} A_{lab}$$

So far the interaction of *one* electron (S=1/2, without any nuclei) in an external magnetic field was considered, that leads to a single resonance line by an on-resonant rf-field, that may be broadened due to $\mathbf{g}$-anisotropy. In the following section this approach is extended to interactions of the electron spin with other magnetic nuclei (electron or nuclei) that are close to the electron.

2.3 Zero-field Splitting

If more than one interchangeable electron is present in the system, the individual electron spins S_i are coupled to form a total spin of $S = \sum S_i$, where each electron contributes to S with the value ½. As a result, the two state system of the single electron is converted to a $(2S + 1)$ manifold even in absence of an external magnetic field. Since transitions may then occur at zero magnetic field this interaction is called zero-field splitting. The Hamiltonian of this interaction is

$$H_{\mathrm{ZFS}} = \boldsymbol{S}^T \mathbf{D} \boldsymbol{S}, \tag{2.9}$$

with $\mathbf{D}$ the symmetric and traceless zero-field interaction tensor. This 'fine-structure' term vanishes completely for cubic symmetry of the spin system.

The discussion about electron-electron interactions much weaker than zero-field splitting is presented in Section 2.5.

2.4 Interactions with Nuclear Spins

2.4.1 Nuclear Zeeman Interaction

In organic samples, the most abundant nuclei that exhibit a nuclear spin I>0 are protons (^{1}H, $I = 1/2$), nitrogen- (^{14}N, $I = 1$ and ^{15}N, $I = 1/2$) and the naturally less abundant ^{13}C-isotopes ($I = 1/2$). In analogy to the electron spin, the nuclear spin momentum $\boldsymbol{I}$ is associated with a magnetic moment, that tend to align in a magnetic field and cause quantization of $\boldsymbol{I}$ along $\boldsymbol{B}_0$. The splitting of the nuclear spin states is called *nuclear Zeeman* (NZ) interaction and the energy is given by:

$$H_{NZ} = -g_n \frac{\mu_N}{\hbar} \boldsymbol{B}_0^T \boldsymbol{I}, \tag{2.10}$$

μ_N is the nuclear magneton (5.050783·10^{-27}JT^{-1} [24]) and g_n is the nuclear g-value, that depends on the type of nucleus (e.g. $g_{1_H} = 5.5857$, $g_{2_H} = 0.8574$ [24]). Anisotropy in the nuclear spin manifold in EPR is negligible, thus g_n is given in the scalar (isotropic) form. Since the magnetic moment of the electron is roughly 660 times bigger than that of the proton, the electron Zeeman splitting is much larger (GHz) as compared to the nuclear Zeeman interaction (MHz) and its energy contribution to the energy of the electron spin states is low.

2.4.2 Hyperfine Interaction

The local magnetic field experienced by the electron spin is influenced by these nearby magnetic moments of the nuclei and the coupling between electron spin and nuclear spin is called hyperfine (hf) interaction. It is extremely useful in EPR spectroscopy, as information on the direct magnetic environment of the electron spin can be gained. The hf interaction between the electron and nuclear magnetic moments split the electron Zeeman levels into the hyperfine levels. The number of hyperfine levels depends on the nuclear spin quantum number I and is:

$$(2I + 1) \tag{2.11}$$

Each hf level is characterized by a nuclear magnetic spin quantum number m_I that can take values in the range $(I, I - 1, \dots - I)$. The energy level diagram for the case of coupling of an electron spin $S = 1/2$ with a nuclei $I = 1/2$ and $I = 1$ is shown in Figure 2.5 (a) and (b), respectively. In this picture isotropic electron Zeeman and hf interaction are assumed. According to eq. (2.11) the coupling of an $I = 1/2$ ($I = 1$) nucleus with a single electron results in the splitting of each Zeeman states into two (three) levels. Transitions between the levels follow the selection rule $\Delta m_s = \pm 1$ and $\Delta m_I = 0$.

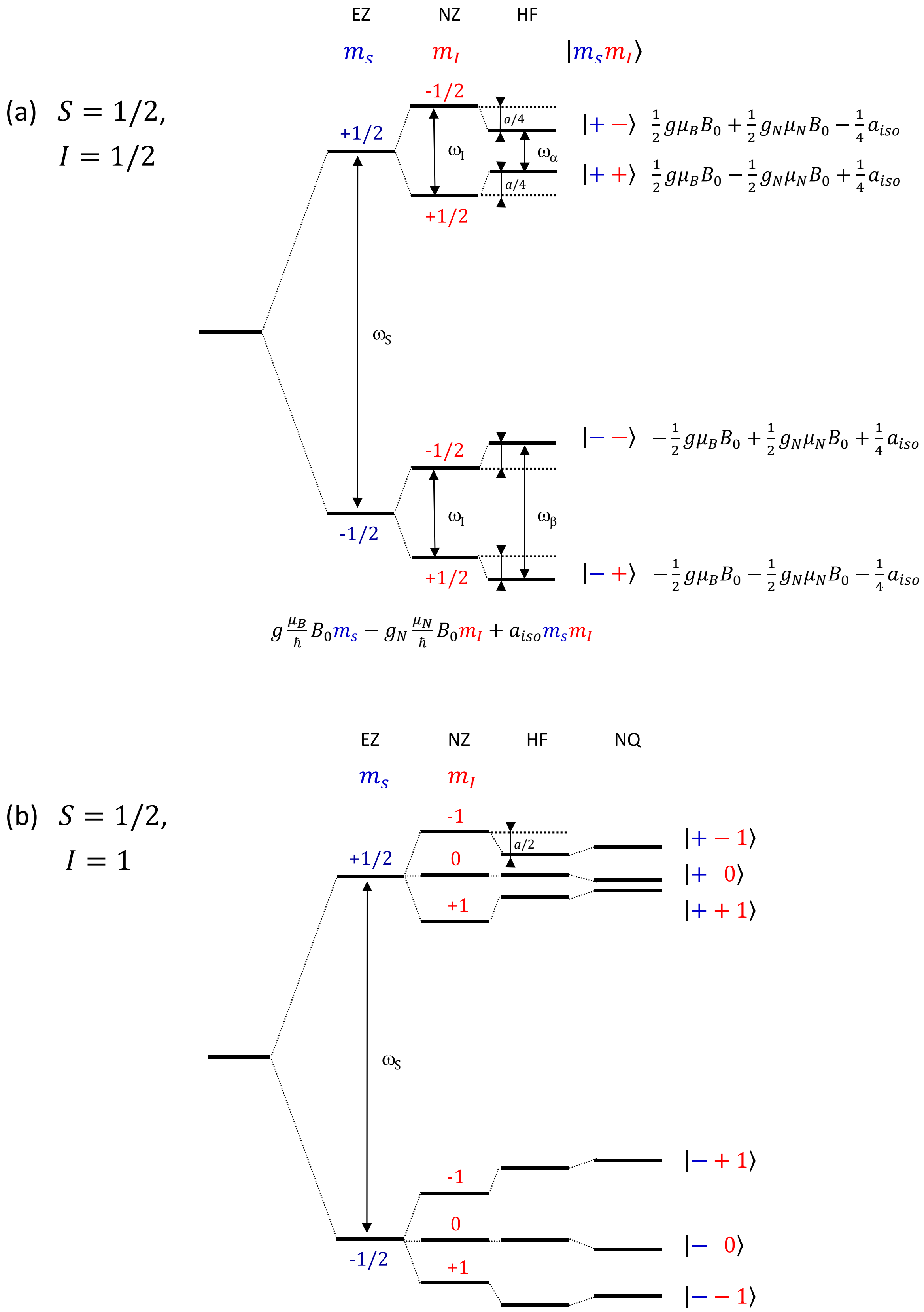

Figure 2.5 Energy level scheme for an electron spin $S = 1/2$ interacting with a nucleus with nuclear spin of (a) $I = 1/2$, e.g. ^{1}H or (b) $I = 1$, e.g. ^{2}H, ^{14}N. EZ is the electron Zeeman, NZ the nuclear Zeeman, HF the hyperfine and NQ the nuclear quadrupole interaction. Only for nuclear spins $I \geq 1$ the NQ interaction has to be taken into account. The weak coupling case is shown where $\omega_I > a_{iso}/2$ and $g_N, a_{iso} > 0$ were assumed. In (a) the energies for the four levels are given. Electron (nuclear) spin states are colored in blue (red).

The energy level schemes are shown for weak coupling ($\omega_I > a_{iso}/2$), which means that the direction of the nuclear spin quantization is given in first order by the direction of the B_0 field vector. The strong coupling case ($\omega_I < a_{iso}/2$), where the direction of quantization is given by the hf-field, is not discussed.

Two different physical effects can contribute to the hf interaction: the anisotropic *dipole-dipole* interaction (acting through space solely) and the isotropic *Fermi-contact* ('trough bond') interaction. These can be classified according to the 'effective distance' of the electron to the nuclear spin into two regions, one inside and one outside the nuclear volume. Quantum mechanics allows an electron to enter the volume occupied by nuclei, whereas outside the nuclear volume the hf field is the classical field of magnetic dipoles.

The dipole-dipole interaction between two spins can be derived from the classical physics, where the spins are treated as bar magnets, interacting in an outer magnetic field. Additionally, each bar magnet creates a magnetic field, which in turn influences the local field at the other nuclei's place. The dipolar interaction Hamiltonian is derived from the classical energy expression for two interacting dipoles μ_1 and μ_2 separated by the distance r by replacing μ_i by the corresponding electron or nuclear spin that is $\boldsymbol{\mu_e} = g\mu_B\boldsymbol{S}$ for the electron and $\boldsymbol{\mu_e} = g_N\mu_N\boldsymbol{I}$ for the nuclear spin, which leads to the expression:

$$H_{dd} = \frac{\mu_0}{4\pi\hbar} \cdot \frac{1}{r^3} g g_N \mu_B \mu_N \left[\boldsymbol{SI} - \frac{3(\boldsymbol{S}\mathbf{r})(\boldsymbol{I}\mathbf{r})}{r^2}\right] = \boldsymbol{S}^T\mathbf{T}\boldsymbol{I} \tag{2.12}$$

In eq. (2.12) μ_0 is the vacuum permeability ($4\pi\cdot10^{-7}$ NA^{-2}) and r the distance between the two spins connected by the vector $\mathbf{r}$. $\mathbf{T}$ is the traceless dipolar hyperfine coupling tensor. The dipolar interaction depends on the orientation of the connecting vector $\mathbf{r}$ with respect to the outer magnetic field and is thus anisotropic. The dipolar interaction is expected to be the main contribution to the overall hf interaction when the electron spin is located in an orbital with a nodal point at the nucleus (which includes all orbitals except s-orbitals) and a symmetry of the full spin system that is lower than cubic. The dipolar interaction is averaged out for rapidly tumbling paramagnets, as it is usual for liquid solution at ambient temperatures or above. In the solid state (e.g. frozen solution) the dipolar contribution to the hf field is important and can be used to calculate the distance between the electron and nuclear spin.

The Fermi-contact interaction is isotropic and a consequence of a finite amplitude $|\Psi(0)|^2$ of the electronic wave function at the nucleus. Hence, this mechanism works through direct contact of the unpaired electron and the nucleus and the energy of this interaction is given by:

$$H_{fc} = \frac{2\mu_0}{3\hbar} g g_N \mu_B \mu_N |\Psi(0)|^2 = a_{iso}\boldsymbol{S}^T\boldsymbol{I} \tag{2.13}$$

Thus, the overall energy of the hyperfine interaction between electron and nuclear magnetic moments is given by the sum of the isotropic and anisotropic hf interactions in the spin Hamiltonian:

$$H_{HF} = H_{fc} + H_{dd} = \boldsymbol{S}^T\mathbf{A}\boldsymbol{I} \tag{2.14}$$

A is the hyperfine interaction matrix, that is represented in the PAS:

$$\mathbf{A} = \begin{bmatrix} A_{xx} & & \\ & A_{yy} & \\ & & A_{zz} \end{bmatrix} = \mathbf{1}a_{iso} + \begin{bmatrix} T_{xx} & & \\ & T_{yy} & \\ & & T_{zz} \end{bmatrix} \tag{2.15}$$

For *axial* symmetry of the dipolar interaction tensor **T**, the principal values would be $T_{xx} = T_{yy} = -T_{\perp}$ and $T_{zz} = 2T_{\perp} = T_{\parallel}$. For electron-nuclear distances r greater than 0.25 nm, and when spin delocalization is negligible, $T_{\perp}$ can be described by the point-dipole approximation [25]:

$$T_{\perp} = \frac{\mu_0\rho}{4\pi\hbar} \cdot \frac{g\mu_B g_N \mu_N}{r^3} \tag{2.16}$$

where $\rho = |\Psi(0)|^2$ is the electron spin density. This relation in eq. (2.16) is important because it allows a straightforward interpretation of the anisotropic hf interaction in terms of distances between the electron and the hyperfine coupled nucleus. Alternatively, when the distance is known, it can provide the spin density ρ on the nucleus.

2.4.3 Nuclear Quadrupole Interaction

A nucleus with $I \geq 1$ may have a non-spherical charge distribution, and the electric quadrupole moment of the nucleus interacts strongly with the electric field gradients generated by the surrounding electron. The coupling of the charge distribution with an electric field gradient is called quadrupole interaction. If the nuclear quadrupole (NQ) interaction is smaller than the electron Zeeman and hf interactions, the energy levels are shifted according to the nuclear states m_I. The quadrupole Hamiltonian is:

$$H_{NQ} = \boldsymbol{I}^T\mathbf{Q}\boldsymbol{I}, \tag{2.17}$$

with **Q**, the quadrupole interaction tensor that is symmetric and traceless. Since the **Q**-tensor is traceless, it is usually described by two quantities, the magnitude e^2qQ/h and the asymmetry parameter $\eta = (Q_{xx} - Q_{yy})/Q_{zz}$. The further contains the product of the electric field gradient eq and the quadrupole moment Q. The NQ interaction is a second order effect and thus usually not detectable in CW EPR spectra ($\Delta m_s = \pm 1$, $\Delta m_I = 0$), as it acts on both m_s manifolds in the same way (see Figure 2.5 b). However, it is readily observed in hyperfine spectra such as HYSCORE, ENDOR or ESEEM ($\Delta m_s = 0$, $\Delta m_I = \pm 1$) and can be observed as first order splitting or may substantially broaden the line shape of hyperfine spectra [26].

2.5 Electron-Electron Interactions

Electron spins may interact weakly or strongly with each other. Strongly interacting individual spins contribute to an overall spin, which is only possible for electrons located on the same atom like transition metal ions. This case was presented in Section 2.3.

Weak electron-electron interactions maintain the individual electron spins and the interaction can be treated as a pertubation of the two electron spin states. Two types of electron-electron interactions can be distinguished, namely *spin exchange* and *dipolar coupling*. The Hamiltonian that describes the weakly coupled system of two electron spins becomes:

$$H(S_1, S_2) = H(S_1) + H(S_2) + H_{ex} + H_{dip} \tag{2.18}$$

where $H(S_1)$ and $H(S_2)$ represents the Hamiltonian of the uncoupled, individual electron spins. H_{ex} is the exchange coupling between the electron spins and is discussed in Section 2.5.1. The dipolar interaction H_{dip} allows for determination of the distance between the spin bearing units and is explained in Section 2.5.2.

2.5.1 Exchange Interaction

The exchange interaction is a true quantum mechanical phenomenon and a consequence of the Pauli principle, which states that the total wave function of a many particle-system consisting of fermions has to be antisymmetric under exchange of particles. A discussion of the terms that contribute to the exchange interaction are beyond the scope of this work but can be found in [27]. In general the spin exchange interaction is given by

$$H_{ex} = \boldsymbol{S}_1^T \mathbf{J} \boldsymbol{S}_2, \tag{2.19}$$

where **J** is the exchange coupling tensor. If one deals with individual radicals, spin exchange is the *exchange of spin states* of the paramagnetic species during collisions, in which the

SOMOs overlap. It is a result of exchange interaction of the partner, triggered by Coulomb repulsion and the spin orientation. At short distances (e.g. between atoms in molecules) the energy of exchange interaction is larger than the thermal motion and will lead to a bond formation. Therefore, exchange interactions appear in *solids* as ferro- or antiferromagnetic properties (parallel $S = 1$ and antiparallel $S = 0$, spin alignment, respectively).

In general, exchange interaction consists of an isotropic and anisotropic part. The isotropic part consists of the Heisenberg exchange interactions (as described below for radicals in solution) and a second contribution that is indirect exchange or super-exchange ([28] see Figure 2.6 b). The latter is mediated via bridging ligand orbitals located between the two interacting centers, so that the ligand forms a bond with each center. The strength of indirect exchange depends on the delocalization of the electron spin density onto the ligand and is also correlated to polarization effects on the electron density in the neighboring nuclei/molecule. Mostly, direct exchange is antiferromagnetic (S=0) because an electronic configuration with paired spins is energetically favorable. Super-exchange may be ferro-or antiferromagnetic ($S = 1$ or 0, respectively) depending on the overlap of the magnetic orbitals and hence on the particular bridging situation. In most cases, antiferromagnetic ($S = 0$) contributions are dominant.

For organic radicals, such as nitroxides in solution, the anisotropic part of the exchange coupling tensor that arises from SOC is often negligible and eq. (2.19) can be written as:

$$H_{ex} = J(r)\boldsymbol{S}_{\boldsymbol{1}}^{T}\boldsymbol{S}_{\boldsymbol{2}}, \tag{2.20}$$

where $J(r)$ is the exchange coupling constant that is given by the exchange integral

$$J(r) = \left\langle \Psi_1 \middle| \frac{e^2}{4\pi\varepsilon_0 r} \middle| \Psi_2 \right\rangle, \tag{2.21}$$

that accounts for the Coulomb interaction between the electrons.

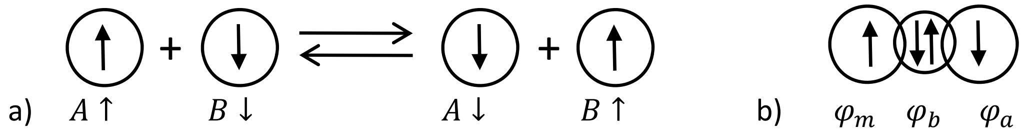

Figure 2.6 Spin exchange processes. a) Direct overlap of the electron orbitals during binary collision lead to a change in the spin state. The arrows indicate the spin orientations. b) Exchange interaction via a diamagnetic molecule without direct overlap between $\varphi_a$and φ_m orbitals. However, both orbitals overlap with φ_b of the bridging diamagnetic molecule. In this case the scope of exchange interaction depends on the extent of delocalization of unpaired spin density onto the orbitals of the atoms in contact. The exchange interaction in (a) is called (direct) Heisenberg exchange and (b) indirect exchange or super-exchange. Both are isotropic contributions to the exchange interaction.

In *solution* the spin exchange is induced by far weaker interactions that take place during binary collision of two paramagnets as illustrated in Figure 2.6a. In analogy with bimolecular chemical reactions its rate (frequency of molecular collisions) can be expressed and kinetic expressions can be derived [27].This Heisenberg spin exchange is characterized by the spin-exchange integral $J(r)$ that depends on the distance of approach between the spin carrying molecules. $J(r)$ decreases exponentially with the distance r between the interacting centers ($J(r) \propto e^{-r}$) and the main contribution to $J(r)$ is given by $\sigma-$orbitals of the atoms. When $J(r) := J$ is assumed to switch from zero to a defined value for a time interval τ_c, the exchange frequency ω_{Ex} is given by:

$$\omega_{Ex} = \tau_E^{-1} p \frac{J^2 \tau_c^2}{1 + J^2 \tau_c^2} \qquad (2.22)$$

τ_E denotes the mean time between probe collisions and p the collision efficiency, that is p_{max}=0.5 for nitroxides, but depends on the shape and charge of the molecule [27]. For *strong exchange* the condition $J^2 \tau_c^2 \gg 1$ holds, which simplifies eq. (2.22) and yields a spin exchange frequency ω_{Ex} that is half of the collision frequency:

$$\omega_{Ex} = \frac{1}{2} \tau_E^{-1} \qquad (2.23)$$

In this case, the limiting step is diffusion and the collision frequency can easily be obtained by measuring ω_{Ex}. In the other case of *weak exchange* (this means a small value of the exchange interaction energy and a short time interval of collision), the 'collision efficiency' is much smaller and the process is limited by the spin exchange itself [27]. Thus, in the diffusion-limited region every collision leads to spin-exchange, while in the kinetically controlled case repeated collisions are needed. This makes the latter more complicated to describe and in the following only strong exchange is regarded. General, for higher radical concentrations c a higher exchange frequency ω_{Ex} is predicted according to:

$$\omega_{Ex} = c K_e \qquad (2.24)$$

K_e is the spin exchange rate constant and its magnitude gives valuable insights into the spin exchange mechanism. It can be determined by studying ω_{Ex} as a function of the radical concentration. This rate of bimolecular spin exchange K_e is basically defined as the product of the rate constant of diffusion encounters, K_D, and the probability p of a spin exchange in the case that the colliding partners get into the sphere of interaction:

$$K_e = p f K_D \qquad (2.25)$$

The factor f is a steric factor and accounts for the mutual orientation of the interacting orbitals (anisotropy of exchange interaction). The spin exchange rate constant K_e is related with the viscosity η of the solvent via the Stokes-Einstein theory:

$$K_e = \frac{2bN_AkT}{3a\eta} \tag{2.26}$$

where b is the distance of bimolecular approach at which collision occurs and a is the radius of the molecule in the fluid. In the easiest case, one may approximate the distance as two times the molecule radius $b \approx 2a$:

$$K_e = \frac{4N_AkT}{3\eta} = \frac{4RT}{3000\eta} \tag{2.27}$$

With this equation it is possible to estimate the spin exchange rate constant K_e for a given ratio T/η without knowing the size of the colliding particles (this is only valid within the hydrodynamic model of diffusion collision as mentioned above).

The spin exchange frequency ω_{Ex} can be studied using CW EPR spectra by analysis of the line broadening, the line shift or the line narrowing [27]. The latter finds only less application since this requires high radical concentrations that are unfavorable for biological and most chemical systems. Usually, the line broadening is used to experimentally determine the spin exchange frequency, since it is easy to extract from the spectra from the peak-to-peak width (ΔB_i see Figure 2.13 b). Analogously, the broadening can be fitted to experimental spectra. It is known, that the line shape departs from a pure Lorentzian as ω_{Ex} is increased and simultaneously, the outer lines are shifted towards the central line [27, 29-30]. Recently a 'new' method has been proposed [29-31], that is based on the extraction of intensities and signs of the dispersion component of the CW EPR spectrum with the help of a least-squares fitting software. The line shape could be expressed as a sum of two components: an absorption and a spin exchange-induced dispersion part. This method could precisely determine the exchange frequency via the dispersion line in the outer lines within a high T/η range. Recently, this method was also used to separate exchange from dipolar broadening [31], a well-known problem [32] that is especially present for low T/η –ratios.

Figure 2.7 represents a typical example of the change of EPR spectra due to Heisenberg spin exchange (simulated spectra with identical parameters except ω_{Ex}). The broadening with increasing ω_{Ex} occurs in accordance with the uncertainty principle as a result of the shortened lifetime of the electron spin state due to spin exchange.

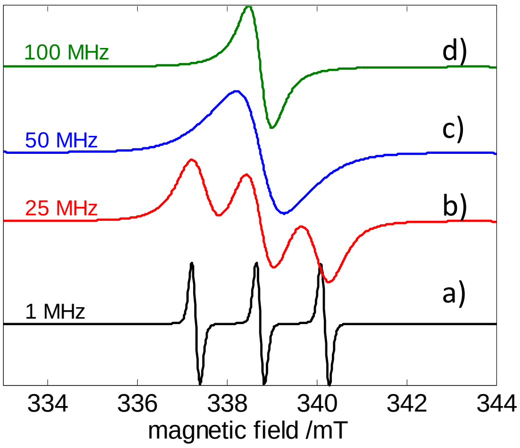

Figure 2.7 The influence of spin exchange on the CW EPR spectrum of a nitroxide in solution. The rate of spin exchange increases from the bottom to the top as a result of increased radical concentration. a) The spectrum was simulated with an exchange frequency of ω_{Ex} = 1 MHz, the EPR spectrum is not visibly influenced. b) The spectrum shows significant exchange broadening. c) Collapse of the hyperfine structure into one line, d) that is narrowing when the exchange interaction grows further (ω_{Ex}= 100 MHz).

The magnitude of the broadening can be related to the rate constant of spin exchange K_e and the concentration of the paramagnetic substance (eq. (2.24)).

In frozen solution, the spin exchange can take place through bond or through solvent and is significant up to an electron-electron distance of ~1.5 nm [10]. Above 1.5 nm dipolar interactions are dominant.

2.5.2 Dipolar Interaction

This section discusses the electron-electron dipole-dipole interaction for an isolated electron-electron two spin pair ($S_1 = S_2 = 1/2$) in the point-dipole approximation. Dipolar interaction of the magnetic moments of the electron spins can be derived from classical physics, similar to the electron-nuclear dipolar interaction as described in Section 2.4.2.

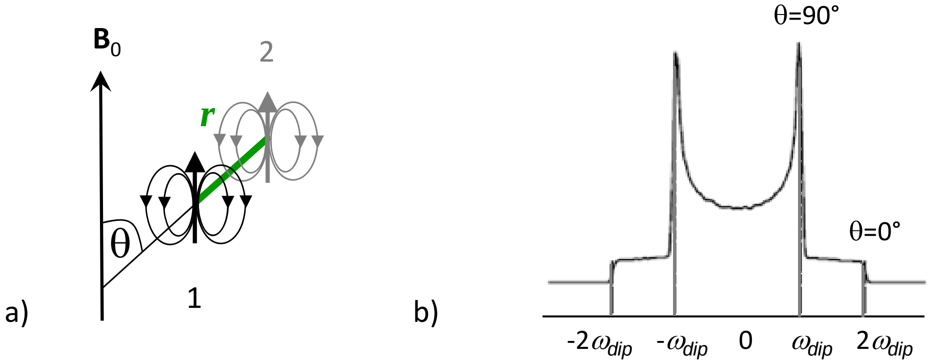

Figure 2.8 a) Dipolar coupling between two spins 1 and 2 with interspin vector r that draw an anlge θ with the outer magnetic field B_0. b) Calculated dipolar powder spectrum (Pake-pattern) for randomly oriented molecules. In the absence of exchange interaction ($J = 0$) the splitting between the two peaks is ω_{dip} ($\theta = 0°$) and between the two outer shoulders $\omega_{dip}(\theta = 0°) = 2\omega_{dip}(\theta = 90°)$. For pulsed EPR experiments like DEER (see section 2.9.3) the peaks appear at $\pm\omega_{dip}$ and $\pm 2\omega_{dip}$.

The anisotropic dipolar (through-space) interaction between two electron spins that are separated by the distance vector $\mathbf{r}$ (see Figure 2.8a) is described by:

$$H_{dip} = -\frac{\mu_0 g_1 g_2 \mu_B^2}{4\pi\hbar}\left(\frac{\boldsymbol{S_1 S_2}}{r^3} - \frac{3(\boldsymbol{S_1}\mathbf{r})(\boldsymbol{S_2}\mathbf{r})}{r^5}\right) = \boldsymbol{S_1^T}\mathbf{D}\boldsymbol{S_2} \tag{2.28}$$

Where $\mathbf{D}$ is the dipolar coupling tensor between the spins $\boldsymbol{S_1}$and $\boldsymbol{S_2}$. Expanding the scalar products in eq. (2.28) the dipolar Hamiltonian with $\mathbf{r}$ expressed in spherical coordinates r, θ, ϕ, representing the orientation of the molecule with respect to the external magnetic field (see Figure 2.8 a) is:

$$H_{dip} = \frac{\mu_0 g_1 g_2 \mu_B^2}{4\pi\hbar}\frac{1}{r^3}[A + B + C + D + E + F] \tag{2.29}$$

$$\begin{aligned}
A &= S_{1z}S_{2z}(1 - 3cos^2\theta) \\
B &= \frac{1}{4}\left[S_{1,+}S_{2,-} + S_{1,-}S_{2,+}\right](1 - 3\cos^2\theta) \\
C &= -\frac{3}{2}\left[S_{1,+}S_{2,z} + S_{1,z}S_{2,+}\right]\sin\theta\ \cos\theta\ e^{-i\phi} \\
D &= -\frac{3}{2}\left[S_{1,-}S_{2,z} + S_{1,z}S_{2,-}\right]\sin\theta\ \cos\theta\ e^{+i\phi} \\
E &= -\frac{3}{4}S_{1,+}S_{2,+}\sin^2\theta e^{-2i\phi} \\
F &= -\frac{3}{4}S_{1,-}S_{2,-}\sin^2\theta e^{+2i\phi}
\end{aligned} \tag{2.30}$$

With the raising operator $S_+ = S_x + iS_y$ and the lowering operator $S_- = S_x - iS_y$ either raising or lowering the magnetic quantum number by 1. The terms A to F are ordered in a way reflecting their influence on the magnetic quantum number $M_S = m_{S,1} + m_{S,2}$. The A and B terms correspond to zero-quantum transitions ($\Delta M_s = 0$), C and D to single-quantum transitions ($\Delta M_s = 1, -1$ respectively) and E and F to double-quantum transitions ($\Delta M_s = 2, -2$, respectively). E and F are forbidden transitions, i.e. for quantization along the magnetic field (high-field approximation) only the A and B terms are relevant, leading to:

$$H_{dip} = \frac{\mu_0 g_1 g_2 \mu_B^2}{4\pi\hbar}\frac{1}{r^3}\left[S_{1,z}S_{2,z} + \frac{1}{4}\left(S_{1,+}S_{2,-} + S_{1,-}S_{2,+}\right)\right](1 - 3\cos^2\theta) \tag{2.31}$$

$$H_{dip} = \omega_{dip}\left[S_{1,z}S_{2,z} + \frac{1}{4}\left(S_{1,+}S_{2,-} + S_{1,-}S_{2,+}\right)\right] \tag{2.32}$$

with ω_{dip} the dipolar splitting between the two spins:

$$\omega_{dip} = \frac{\mu_0 g_1 g_2 \mu_B^2}{4\pi\hbar}\frac{1}{r^3}(1 - 3cos^2\theta) \tag{2.33}$$

For randomly oriented (static) spins with respect to the field, integration of ω_{dip} over the angle θ gives a symmetric Pake pattern in which singularities ($\theta = 90°$) are separated by ω_{dip}, whereas for fast rotating molecules the dipolar interaction will average to zero.
In the weak coupling limit the coupling tensor $\mathbf{D}$ in its principal axes system (PAS) becomes:

$$\mathbf{D} = \begin{bmatrix} -\omega_{dip} & & \\ & -\omega_{dip} & \\ & & 2\omega_{dip} \end{bmatrix}, \tag{2.34}$$

Like all anisotropic interactions, the dipolar coupling is averaged out in liquid solution. However, in high viscosity liquids (and low temperatures) it cannot be neglected any more. With eq. (2.33) it is possible to calculate the spin-spin distance from the dipolar splitting, thus, EPR methods that measure the dipolar coupling are frequently used for the determination of distance distributions of nitroxide spin probes in frozen solution [33] (e.g. double electron-electron resonance, DEER).

2.6 The Complete Spin Hamiltonian

The energy terms introduced in the previous sections can be added to form the complete spin Hamiltonian, which was given in the general form in eq. (2.2):

$$H = \underbrace{\frac{\mu_B}{\hbar}\boldsymbol{B}_0^T\mathbf{g}\boldsymbol{S}}_{\text{EZI}} + \underbrace{\boldsymbol{S}^T\mathbf{D}\boldsymbol{S}}_{\text{ZFS}} + \underbrace{\boldsymbol{S}^T\mathbf{A}\boldsymbol{I}}_{\text{HFI}} - \underbrace{g_N\frac{\mu_N}{\hbar}\boldsymbol{I}^T\boldsymbol{B}_0}_{\text{NZI}} + \underbrace{\boldsymbol{I}^T\mathbf{Q}\boldsymbol{I}}_{\text{NQI}} + \underbrace{\boldsymbol{S}_1^T\mathbf{D}\boldsymbol{S}_2 + J_{12}\boldsymbol{S}_1^T\boldsymbol{S}_2}_{\text{el-el}}. \tag{2.35}$$

Depending on the electron and nuclear spin quantum numbers of the interacting particles and their relative magnitudes, some terms can be neglected (e.g. zero-field splitting for $S = 1/2$ systems, or dipolar electron-electron interactions in highly diluted liquid solutions at high T/η ratios). The most important terms are the EZ and the HF interaction with typical values given in Table 2.1. For CW EPR of electron spins centered at not too heavy elements, second-order terms can usually be neglected, e.g. the ZFS and the NQ terms.

Table 2.1 Orders of magnitude of the energy for the Hamiltonian components.

Interaction	E /Hz
EZ	10^9
ZFS	10^7–10^{12}
HF	10^6-10^8
NZ	10^6-10^7
NQ	10^5–10^7

Knowledge of the complete spin Hamiltonian including the relative orientations of the PAS of the interaction matrices allows for calculation of the CW and pulse EPR spectra. This is illustrated in the next section for a nitroxide radical.

2.7 EPR of Nitroxide Radicals

In this section, the structure and stability of nitroxides is discussed and factors are presented that influence CW EPR spectra at X- and W-band (9.5 and 94.5 GHz, respectively) of nitroxides in liquid and frozen solution. In particular, the effects of molecular dynamics on CW ER spectra will be discussed.

2.7.1 Structure and Stability of Nitroxides

Nitroxides are compounds containing the $>\overset{\bullet}{N}-O$ group which has an unpaired electron. The unpaired electron is located in a $2p_\pi$ (π^*) orbital of the nitrogen and the oxygen atom. Since there is also an N-O σ-bond and two electrons that fill a π-bonding orbital between these atoms, the effective N-O bond order is 1.5 (two center- three electron- bonding, 2c-3e). The structure of this group can be considered as a superposition of two mesomeric structures [34]

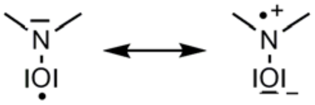

Scheme 2.1 Mesomeric formula of the nitroxide group.

The contributions of both structures to the ground state may be different, depending on the polarity of the medium and conjugation within the molecule. In apolar solvents both structures have the same weight while polar solvents will favor the charged mesomeric structure, leading to a higher charge density on the nitrogen (which can be observed as increased nitrogen hyperfine splitting in EPR spectra). The electronic structure is influenced in a similar way by π-complex formation with aromatic rings. Depending on the structure, the spin density on oxygen is ρ_O=0.58-0.72 and on nitrogen it is ρ_N=0.42-0.28 [35].The dipole moment of the N-O bond is 2.7 D and the distance is 1.26-1.29 A. The 2c-3e N-O bond has an energy of 419 kJ/mol, midway between the energy of an N-O single bond (230 kJ/mol) and N=O double bond (600 kJ/mol) [36]. As a result of the electron delocalization, nitroxides are relatively stable molecules. The energy gain from delocalization has been calculated as 126 kJ/mol [37].

The stability of nitroxides may be attributed to three factors: electron delocalization within the molecule, steric shielding of the paramagnetic center and stability towards disproportionation. If H–atoms in α-position to the NO moiety are available, disproportionation reactions will be favored, leading to diamagnetic substances. Thus, the majority of stable nitroxides are secondary amine N–oxides without α–hydrogen atoms. Bulky substituents on the α–carbon atoms do not only prevent disproportionation but also the tendency towards dimerization, particularly in the solid state. Thus steric hindrance is mainly responsible for kinetic stability. The more pronounced effect for stability is the electronic configuration of the N-O group. General structures for stable nitroxides are shown in Figure 2.9 with the simplest representative di-*tert*-butylnitroxide DTBN (a). The most common derivates stem from six-membered piperidine rings (b) and five-membered pyrrolidine (c), oxazolidine (d) pyrroline (e) rings. Since chemical structures of nitroxides are relatively complex, trivial names formed by abbreviations are usually employed.

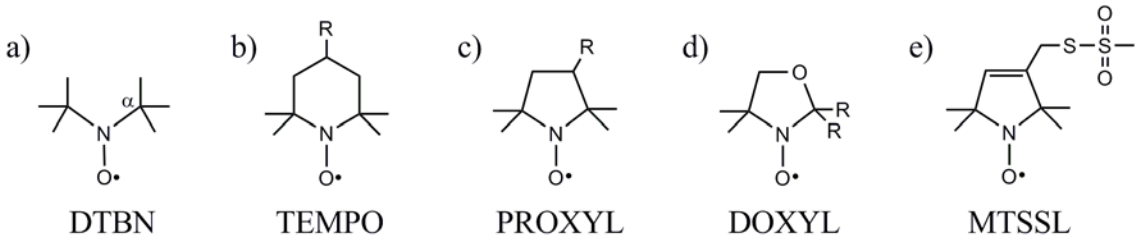

Figure 2.9 The main types of stable nitroxides contain no hydrogen atom at the α-carbon and are cyclic analogs of a) di-*tert*-butyl nitroxide, derivates of b) piperidine, c) pyrrolidine d) oxazolidine and e) pyrroline. Labeling reaction is possible with suitable functional group R. DTBN: di-*tert*-butyl nitroxide, TEMPO: 2,2,6,6-tetramethylpiperidine-*N*-oxyl, PROXYL: 2,2,4,4-tetramethylpyrrolidine-*N*-oxyl, DOXYL: 4,4-dimethyloxazolidine-*N*-oxyl, MTSSL: (*N*-oxyl-2,2,5,5 tetramethylpyrroline-3-methyl)methane thiolsulfonate.

2.7.2 EPR of Nitroxides

Generally, four basic quantities can be derived from CW EPR spectra: (1) the g-factor or **g**-tensor, (2) the hyperfine splitting parameter a_{iso} or the full $\mathbf{A}$ -tensor, (3) the line shape and line width and (4) the signal intensity as a measure of the number of spins. Yet, the EPR spectrum is determined by the resonator Q-factor, the field modulation amplitude, the magnetic field inhomogenity and spin-spin interactions in the sample. An analysis of the quantities (1)-(3) reveals information about the environment (polar, unpolar, H-bonding), the nearest neighbours, the distribution of unpaired spin density over the neighbours and the number of paramagentic centers per unit volume. In particular, nitroxides are very sensitive towards their environment, that is the micropolarity (observed by the magnitude of a_{iso}) and microviscosity (observed by the spectral shape and line width). For analysis of the spectra numerical simulation are used as described in Section 2.8.

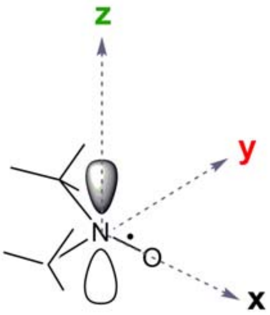

Figure 2.10 Molecular coordinate axis system of a nitroxide with the x-axis along the NO bond and z-axis along the $2p_{\pi}$ orbital. The **g**-tensor principal axes system and the molecular frame are identical. [1].

For a nitroxide it is custom in literature [1] to choose a right-handed Cartesian molecular coordinate system (x, y, z) in such a way, that the x-axis coincides with the direction of te NO-bond and the z-axis is directed along the $2p_{\pi}$ orbital as shown in Figure 2.10.

In this molecular coordinate system, the axes coincide with the axes of the **g**-matrix and the $\mathbf{A}$-tensor because of the symmetry of the $2p_{\pi}$ orbital. Higher-order effects cause small tilt between the principal axis of the **g**- and $\mathbf{A}$-tensor, that can usually be neglected (and with this all off-diagonal elements). Note, that Euler rotations can be used to transform one frame into the another (see Section 2.2.2). When not stated otherwise explicitly, in the following the hyperfine tensor $\mathbf{A}$ is assumed to be collinear with the **g**-tensor.

For a nitroxide at low concentration (in absence of spin-spin interactions) the electron Zeeman and the hyperfine interaction with ^{14}N ($I = 1$) reflect the most important contributions to the spin Hamiltonian (the nuclear Zeeman term can also be neglected unless the experiments are carried out at very high frequencies of >250 GHz [1]):

$$H = \frac{\mu_B}{\hbar}\boldsymbol{B}^T\mathbf{g}\boldsymbol{S} + \boldsymbol{S}^T\mathbf{A}\boldsymbol{I}. \tag{2.36}$$

The two terms have different symmetry and different field dependences: The hyperfine tensor $\mathbf{A}$ is almost axial with $A_{zz} > A_{yy} \approx A_{xx}$, while the **g**-matrix has a rhombic character

$g_{xx} > g_{yy} > g_{zz}$. Under the high-field approximation (quantization along B$_0$) eq. (2.36) simplifies to:

$$H = g_{zz}\frac{\mu_B}{\hbar}B_0S_z + A_{zz}I_zS_z \tag{2.37}$$

Solving the time-independent Schrödinger equation with this Hamiltonian under the high field condition $\mu_B g_{zz} B/\hbar \gg A_{zz}$ yield the energy eigenvalues in zero approximation (in frequency units):

$$\omega(m_{s,}m_I) = g_{zz}\frac{\mu_B}{\hbar}B_0m_s + A_{zz}m_sm_I \tag{2.38}$$

with $m_s = \pm 1/2$ and $m_I = 0, \pm 1.$ Thus, the anisotropic EPR spectrum consists of three equal lines that are split by A_{zz} (measured in Hz) with the middle line positioned at $B_0 = \hbar\omega/\mu_B g_{zz}$. The same results are obtained for the y- and the x-orientations of the B-field in the molecular coordinate system. Before considering this anisotropic case, we have a closer look at the (much simpler) isotropic case.

In liquid solution the principal values in eq.(2.38) can be replaced by their isotropic analogues and from the resonance condition (eq. (2.5)) it follows for the frequency of transition:

$$\omega(m_I) = g_{iso}\frac{\mu_B}{\hbar}B_0 + a_{iso}m_I \tag{2.39}$$

Together with the selection rules for EPR ($\Delta m_s = \pm 1$, $\Delta m_I = 0$), eq.(2.39) explains the three line pattern of a nitroxide CW EPR spectrum.

For technical reasons the frequency is not varied until the resonance condition is fulfilled, but the magnetic field B_0. The allowed transitions and the observed absorption and derivative CW EPR spectra for a nitroxide are shown in Figure 2.11. It consist of three lines centered at g_{iso} that are split by a_{iso}. CW EPR spectra are recorded in the first derivative mode due to the field-modulation technique. In the following, the recorded CW EPR spectra are always shown in the derivative mode.

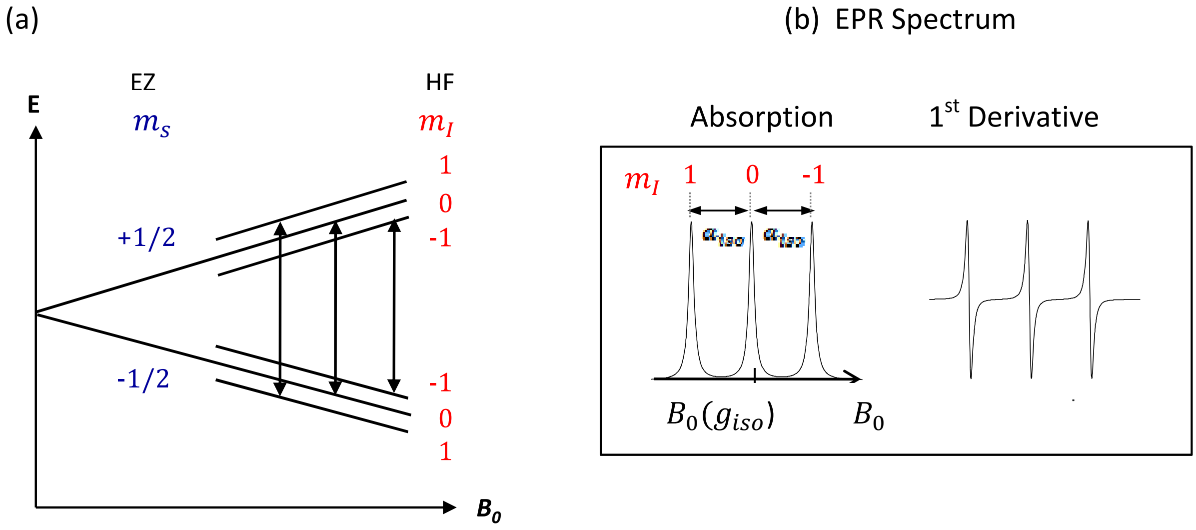

Figure 2.11 Energy level diagram (a) and EPR spectrum (b) for a spin system consisting of one electron $S = 1/2$ and a nuclear spin $I = 1$ (e.g. ^{14}N) with isotropic electron Zeeman (g_{iso}) and hyperfine (a_{iso}) interaction. b) The left EPR spectrum is shown in the absorption, the right in the first derivative mode. The center of the spectrum is determined by the g_{iso} -value, the splitting between the lines is given by the isotropic hf coupling constant a_{iso}. As a second order effect, the NZ interaction has no influence on the CW EPR spectrum. The spectrum is representative for nitroxide radicals in liquid solution, where fast tumbling leads to an averaging of $\mathbf{g}$- and $\mathbf{A}$- anisotropies. Note, that in Figure 2.5 (b) the order of the upper m_I-levels is inverse since it was specified by the combination EZ and NZ interaction, whereas in the present figure it is the EZ and HF interaction.

From the magnitude of the hf splitting constant a_{iso} one gets direct information about the spin label's environment, with more polar surroundings leading to higher a_{iso}-values. This can be explained by stabilization of the charged mesomeric resonance formula of the nitroxide group, where more spin density is located at the nitrogen nucleus (see Scheme 2.1).

In frozen solution (polycrystalline) or glassy matrices, each paramagnetic center exhibits its own resonance position depending on its orientation. Thus, the powder spectrum is a weighted distribution of all possible resonance fields and as a result the spectrum becomes broad and splits into distinct regions arising from anisotropies in the $\mathbf{g}$- and hf-tensor.
Single-cystal EPR spectra are obtained for measuring the EPR spectra along the molecular coordinate axis of a nitroxide as described in Section 2.2.2. Such theoretical spectra are illustrated in the middle of Figure 2.12. The spectra were calculated for 9.4 GHz (a) and 94.4 GHz (b) with $\mathbf{g}$=[2.0093, 2.0063, 2.0023], i.e. orthorhombic symmetry and $\mathbf{A}$=[0.42, 0.47, 3.26] mT, i.e. nearly axial hyperfine symmetry. At 9.4 GHz, the small differences between g_{xx} , g_{yy} and g_{zz} cause only a very small shift between the center lines of the single-crystal EPR spectra at the three principal axes orientations x (in black), y (in red) and

z (in green). Thus, the spectra overlap, specifically making the x-and y-orientations indistinguishable.

The advantages of going to high magnetic fields can be seen from eq. (2.38): The EZ-term is field-dependent, while the HF-term is field-independent. Thus, at tenfold higher field (W-band), the field positions are shifted proportionally to B_0. This leads to a complete separation of the $\mathbf{g}$-tensor elements (Figure 2.12 b).
The total width of a typical X-band spectrum is 8.5 mT, while it is 20 mT at W-band.

Now, the isotropic solution EPR spectrum (Figure 2.11 b) and the frozen, rigid-limit EPR spectrum (Figure 2.12 a) were shown. Between these two cases, the whole dynamic range of the nitroxide can be probed by CW EPR spectroscopy.

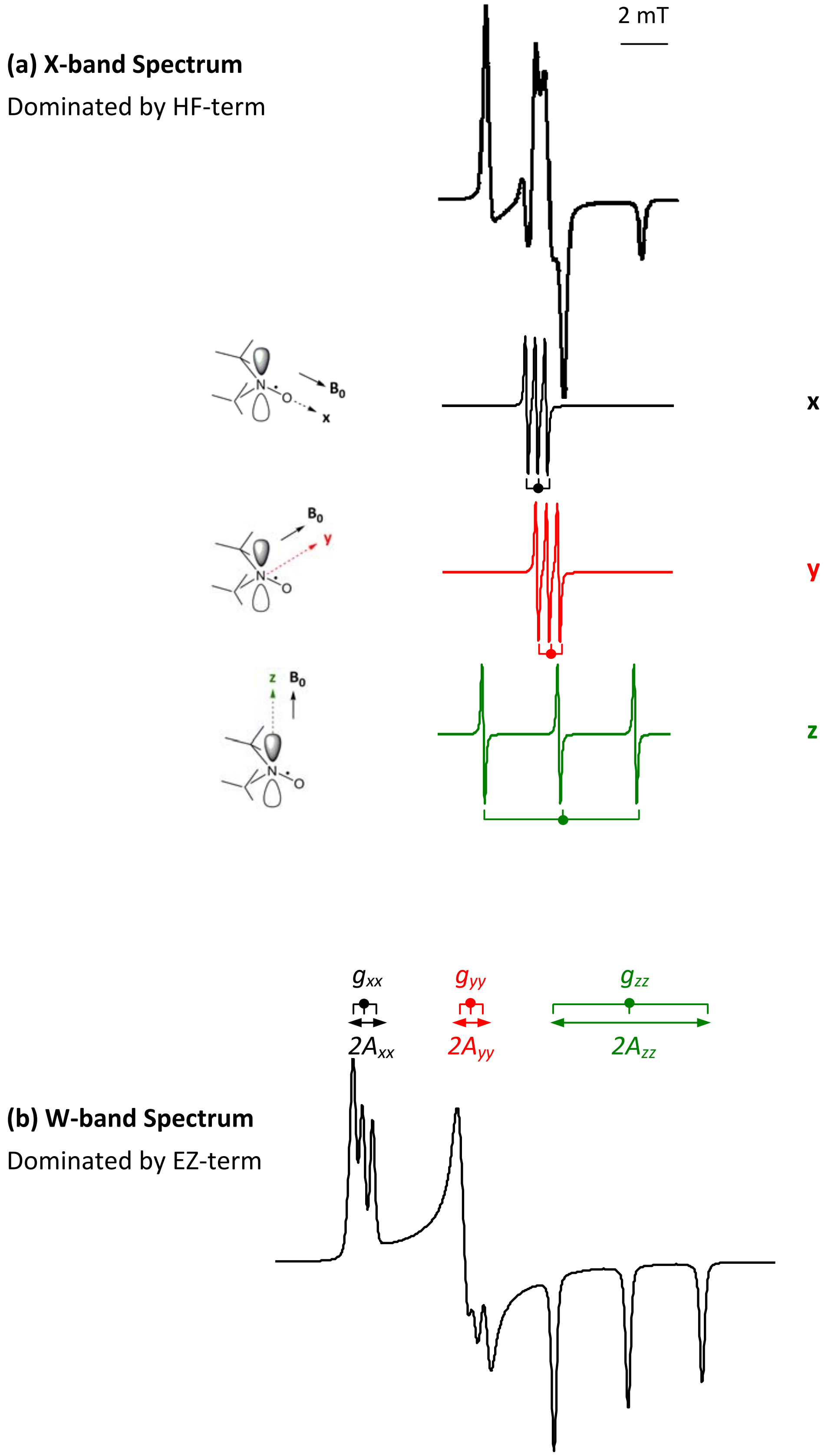

Figure 2.12 CW-EPR powder spectra (first derivative mode) of a nitroxide at X-band, 9.4 GHz (a) and W-band, 94.4 GHz (b). The middle section of the figure shows theoretical single-crystal EPR spectra with the magnetic field directed along the nitroxide principal axes x, y and z, as depicted schematically on the left side. The approximate positions of the principal axis orientation of the -tensor are indicated by filled circles and those of the ^{14}N hyperfine $\mathbf{A}$-tensor by bars. The magnitudes of the A_{ii} - components are given by arrows. Since the hf coupling is field independent, the single-crystal spectra are identical for X- and W-band and are only shown once. For the simulation parameters see text.

2.7.3 Linewidths

EPR resonance lines can be broadenend due to homogeneous or inhomogeneous mechanisms. The type of line broadening determines the response of the spin system to an external pertubation (e.g. pulses) [25].
Homogeneous broadening is due to the uncerteinty principle and usually neglibible in solid-state EPR. If the excited state has a decay constant T_2 the width of the associated resonance line is $1/2\pi T_2$. T_2 is the spin-spin (or transversal) relaxation time and is a measure of the amplitude of stochastic variations of local magnetic fields for individual spins, for example due to electron or nuclear spin flips. Its magnitude is in the order of 4 ms and shorter [25]. The measured EPR spectrum is the sum of a number of spectra, all having the same shift and linewidth.
Inhomogeneous broadening occurs since the total number of spins in a sample are (chemically and/or magnetically) not identical, i.e. there are random static variations of the molecular structure around the electron spin. These slightly different environments are often found in frozen solutions induce distributions of the principal values of the interaction tensors, so called strains (g- and A-strain). An inhomogeneous external magnetic field also accounts for variable local magnetic fields actoss the sample. This spatial variation in Zeeman frequencies is relevant for radicals in solution. Further, unresolved hyperfine splittings inhomogeneously broaden the EPR line exponentially with the number of coupled nuclei. All these effects cause individual Gaussian resonances (that have slightly different shifts) to overlap to one broad signal (that is usually Gaussian, too). Per definition such individual spin packets can be excited independently of each other [25]. Thus, if a *homogeneous* broadened line is irradiated at any position within the line, the overall intensity of the line will be reduced, while for an *inhomogeneous* broadened line a transient spectral hole will be burnt into the EPR line.

In polycrystalline materials, the most important contribution to the linewidth is due to the statistical distribution of orientations of the paramagnets, an effect that is usually more pronounced than broadening due to unresolved hyperfine splittings [25].

The Gaussian and Lorentzian line shape functions are given by [38]:

$$\text{Gaussian} \qquad f(\nu) = \sqrt{\frac{2}{\pi}}\frac{1}{\sigma} e^{-2(\nu-\nu_0)^2/\sigma^2} \tag{2.40}$$

$$\text{Lorentzian} \qquad f(\nu) = \frac{2}{\pi\sqrt{3}}\frac{1}{\sigma}\cdot\frac{1}{1+\frac{4}{3}\left(\frac{\nu-\nu_0}{\sigma}\right)^2}$$

Where σ is the distance between the inflection points and ν_0 is the center of the line. Such line shape functions are shown in Figure 2.13 a.

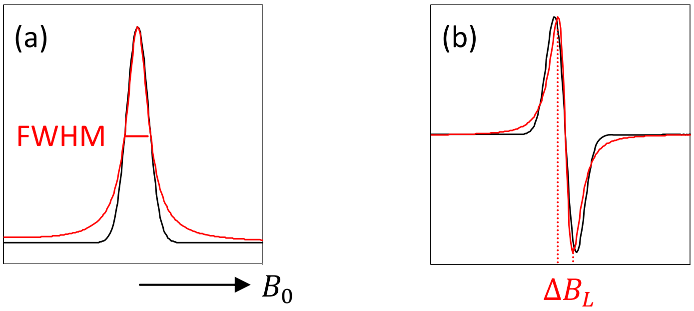

Figure 2.13 EPR line shapes in absorption (a) and first derivative mode (b), normalized by their maximum. Gaussian lines are shown in black and Lorentzian lines in red. In (a) the full width at half height (FWHM) is shown, in (b) the peak-to-peak linewidth of the Lorentzian line is shown, that is correlated to the FWHM by (2.41).

The lw parameter ΔB_i, that can be read out from the experimental CW EPR spectra, describes the full width at half heigth (maximum slope, FWHM) of the shape function and is related to the Gaussian and Lorentzian absorption line by:

$$\begin{aligned} &\text{Gaussian} \qquad \Delta B_G = \frac{\mathrm{FWHM}}{\sqrt{2\ln 2}} \\ &\text{Lorentzian} \qquad \Delta B_L = \frac{\mathrm{FWHM}}{\sqrt{3}} \end{aligned} \tag{2.41}$$

The Voigtian line shape is a convolution of a Lorentzian and a Gaussian line shape and cannot be expressed analytically. Its shape lies in between Gaussian and Lorentzian. In practice, lineshape analysis is used to gain insights into dynamic processes (flexibility, rotational barriers, counterion migration) as described in Section 2.8.1.

For inhomogeneously broadened EPR spectra caused by unresolved hf structure, ENDOR spectroscopy yields a resolution enhancement.

2.7.4 Rapid Anisotropic Motion about a Molecular Axis

The motional characteristics of a nitroxide spin label in solution predominantly influences the shape of the CW EPR spectra. For small spin probes in homogeneous solution the rotational motion can be easily described in terms of Brownian diffusion and discussed in connection with the calculation (simulation) of CW EPR spectra in Section 2.8. However, for most spin-label studies on biological systems, isotropic reorientation of the label about the three molecular axes is not possible due to the sample geometry or microscopic ordered domains within the sample. The DOXYL spin label (Figure 2.14 a), that is used in this work for the study of miniemulsions, is a prominent example to explain anisotropic motional effects on the CW EPR spectrum.

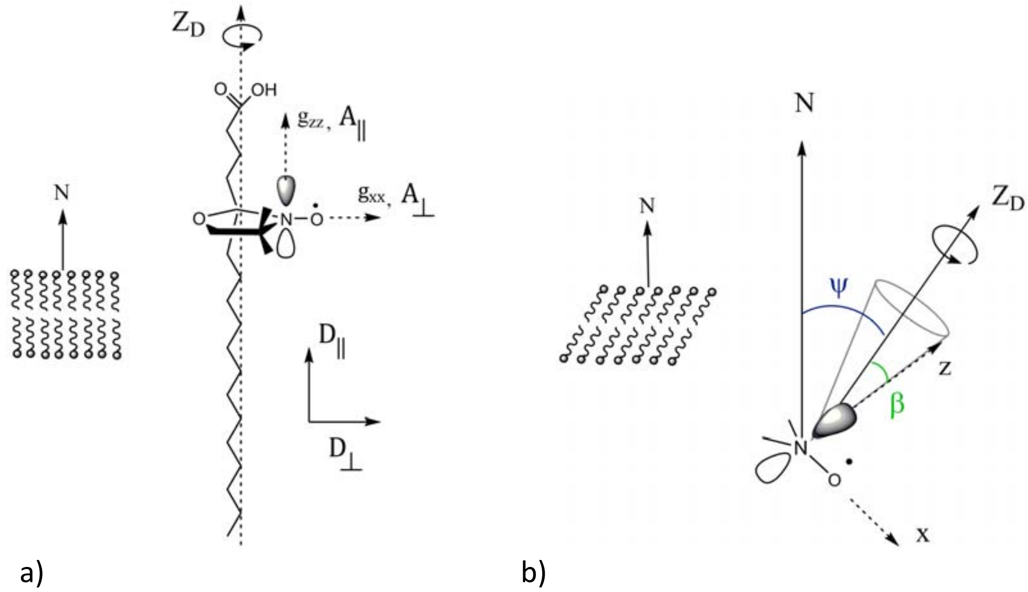

Figure 2.14 a) Axial symmetry of DOXYL stearic acid spin probes and their orientation in a bilayer (N is the normal to the bilayers interface). The molecular z-axis along the $2p_z$-orbital is identical with the direction of the extended alkyl chain, the x-axis is along the NO bond (y-axis not shown). The elongated shape of this molecule gives rise to anisotropic motion: The motion around the alkyl chain, denoted as Z_D, is much faster (~one order of magnitude) than the motion around the perpendicular axes x and y. These motions are characterized by the rotational diffusion rates $D_{\parallel}$ and $D_{\perp}$. b) Precessing label model with tilt angle ψ in an *oriented* bilayer. The nitroxide precesses within a cone around the director axis Z_D (symmetry axis of the anisotropic rotation). The angle β is the half cone angle. A high value for β is equivalent to less ordered chains due to increased mobility. For the limiting case that no motion in present, β=0 and the director axis Z_D coincides with the molecular z-axis This in return is the case illustrated in (a) where further the normal axis N is parallel to the director axis Z_D. The tilt angle ψ can only be observed in oriented samples (e.g. on a glass substrate), otherwise this angle is averaged out.

For DSA in oriented samples (e.g. lipid bilayers, liquid crystals) two different motions for the nitroxide group can be distinguished: The flexing mobility of each carbon-carbon segment (rotational isomerization) and the rapid rotation along the molecular long axis [39]. The alkyl chain flexibility is known to be high in saturated hydrocarbons. Alkyl chains near the polar interface are well-ordered (rigid-like), but motion becomes increasingly more random towards the center of the bilayer. Such flexibility gradients have been found in phospholipid bilayers [40], biological membranes and liquid crystals [41] with the help of spin labeled fatty acids that are known to diffuse into the bilayer and orient themselves with their long axes preferentially perpendicular to the interface [40, 42]. The rapid rotational motion is likely to occur for elongated spin label in an anisotropic sample. In this type of molecular motion the alkyl chain precesses rapidly on a cone about the normal to the interface. The $2p_z$ orbital of the nitroxide moiety is at an angle β with the normal and this angle denotes the angle from normal. This is the axis of motional averaging and is called director axis Z_D. The rapid anisotropic motion about the long chain axis gives rise to axial symmetry and this leads to two modes of interaction between the electron spin and the outer magnetic field. The observed shape of the spectrum is characteristic for axial symmetry, where the parallel $A_{\parallel}$ and axial $A_{\perp}$components of the hf tensor $\mathbf{A}$ are resolved (the corresponding **g**-matrix lacks axial symmetry for DSA, but the approximation of axial symmetry is adequate to interpret 9.5 GHz EPR spectra [43]). Such a simulated spectrum is shown in Figure 2.15. The quantity $A_{\parallel} - A_{\perp} = \Delta A$ is an indirect measure of the order of the system. The order parameter S, which depicts the average position of the molecule with respect to the director axis Z_D is given by [44]:

$$S = \frac{A_{\parallel} - A_{\perp}}{A_{zz} - 1/2(A_{xx} + A_{yy})} \qquad (2.42)$$

Where A_{xx} A_{yy} and A_{zz} are the principal values of the hyperfine tensor **A** of the spin probe. For purely axial systems $A_{xx} = A_{yy}$ and the term ½$(A_{xx} + A_{yy})$ can be reduced to A_{xx}. The hyperfine tensor elements have to be determined from (x-,y- and z-) oriented samples, e.g. in host crystals [45] or from high-field EPR. The value A_{zz} can also be obtained from EPR measurements in absence of motion (at cryogenic temperatures) (see Figure 2.12b). For some frequently used spin probes the values can be found in literature [46]. The values of $A_{\perp}$ and $A_{\parallel}$ can simply be read out from the experimental spectrum as the apparent splittings (see Figure 2.15). The order parameter S is related to the angle of deviation β by the expression:

$$S = 1/2(3cos^2\beta - 1) \qquad (2.43)$$

Generally, order parameters represent time averages over molecular motion. The longer the time involved in averaging, the lower the order parameter. The time that is involved in the averaging depends on the magnitude of all anisotropies present in the spin Hamiltonian. In this case, the hyperfine anisotropy is the dominant contribution. A decrease in the order parameter S denotes an increase in deviation of the rotational axis from the normal. An increased angle β is an indication of enhanced mobility of the chains. If the amplitude of motion of the spin label is increased, coupled with a decrease in the rate of rotation, the anisotropy disappears and the usual isotropic three line pattern is obtained.

Up to now it was assumed, that the director axis Z_D is parallel to the layer normal, but there may also be a tilt angle ψ between the layer normal and the director axis Z_D of the nitroxide (see Figure 2.14 b).The tilt angle ψ can only be observed in oriented samples (e.g. planar or cylindrical) but is averaged out in random distribution.

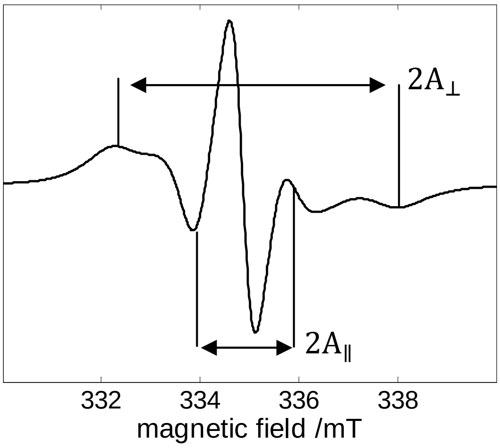

Figure 2.15 EPR spectrum for rapid anisotropic motion of an elongated spin probe (model: 5-DSA). The spectrum was calculated with axial symmetry of the $\mathbf{A}$- tensor. The rotation around the z-axis $(1/D_{\|} \sim 0.2\,\mathrm{ns})$ was assumed to be 20 times higher than around the perpendicular axes x and y $(1/D_{\perp} \sim 4\,\mathrm{ns})$.

Such nitroxide spectra were first observed in sonicated phospholipid dispersions and oriented erythrocytes [42] and the method has become very famous in membrane research (lipid bilayers), since a variety of information can be obtained. This includes the flexibility gradient of the alkyl chain at different positions [40-41], local viscosity measurements, rates of lateral diffusion and rates of transmembrane motion. For a review see ref. [47]. For a theoretical treatment of rapid anisotropic motion see ref. [46], where general equations for the tensor elements are given for different models of motion. Besides (uni)-axial rotational diffusion, these models include rotation about an arbitrary axis that is present in other elongated spin labels like cholestane.

2.8 Numerical Simulation of EPR and ENDOR Spectra

For detailed interpretation of EPR and ENDOR measurements, computer simulations are necessary. In order to calculate the exact eigenvalues of the general spin Hamiltonian, a numerical solution of the secular equations has to be derived. As mentioned, the appearance of the spectrum does not only depend on static interactions but also on dynamic processes on the timescale of the respective EPR experiment. Thus, for many spectra simulations are necessary for their reproduction and recovering of underlying structural and dynamic parameters. These tasks are taken into account by the software package *EasySpin* [48]. Full details about the sofware can be found in [49-51]. Here, the concept is presented in the depth necessary for interpretation of the spectra obtained in this work.

2.8.1 Dynamic Regimes in CW EPR

In CW-EPR the EPR timescale is determined by the spectral anisotropy $\Delta\omega$, which is the maximum difference between the line positions, when the orientation of the paramagnet is varied. Typically, for nitroxides $\Delta\omega/2\pi\sim$ 130 MHz at X-band [51]. All dynamic processes that are not frozen on this timescale have an influence on the lineshape. The most important dynamic process is molecular tumbling, that is a random rotational motion that modulates the resonance frequencies and gives rise to fluctuating local magnetic fields, which induce transitions. This diffusional process is characterized by the rotational correlation time τ_{corr}, the characteristic time after which molecules with initially identical orientations loose their alignment. Comparing $\Delta\omega$ with the rotational diffusion τ_{corr}^{-1} four dynamic regimes can be distinguished (illustrated in Table 2.2): (1) isotropic limit, (2) fast motion, (3) slow motion and (4) rigid limit. Note, that the boarders between the regimes are not sharp and that the terms ‘slow’ and ‘fast’ do not refer to the absolut velocity of reorientation but are understood relative to the spectral broadening. For each regime, line positions (resonance fields), intensities and widths are computed with a different algorithm.

- *Isotropic limit* ($\tau_{corr}^{-1}/\Delta\omega > 1000$, $\tau_{corr} <\sim 1$ ps)

In the isotropic limit the paramagnetic molecules are tumbling fast which averages out anisotropic interactions. The observed parameters are the isotropic g-value, g_{iso} and the isotropic hf coupling constant, a_{iso} and the spectrum consists of symmetric (Gaussian) lines with equal width. Such spectra are obtained for organic radicals in low-viscosity solutions at room temperature. Spectra with one electron coupled to one nucleus can be computed by analytical diagonalization of the isotropic spin Hamiltonian with the EasySpin function ‘garlic’. The resulting energy levels as a function of the magnetic field are given by the Breit-Rabi formulae [52] and the resonance field is calculated numerically. The transition probabilities are assumed to be equal.

Input parameters for the simulation are the g_{iso} and a_{iso}-values, the nuclear isotope (^{14}N) and the lineshape and -width, which can be Gaussian, Lorentzian or Voigtian. The mw frequency and sweep width are needed as experimental parameters.

- *Fast motion regime* ($1000 < \tau_{\mathrm{corr}}^{-1}/\Delta\omega > 1$, $\tau_{\mathrm{corr}} \sim 0.1$ ns)

In this regime the rotational motion is fast and the spectrum appears like in the isotropic case, but the line width now varies with m_I. For simulation of fast-motion spectra also the EasySpin function 'garlic' is used, but the linewidth for each line is calculated separately. Based on the Redfield-theory, the apparent line width of the m_Ith line is given by the Kivelson formula [53]:

$$T_2^{-1}(m_I) = A_0 + A + Bm_I + Cm_I^2 \qquad (2.44)$$

The terms with coefficients A, B and C describe the broadening contribution from rotational motion and A_0 from all other broadening effect. With known $\mathbf{g}$- and $\mathbf{A}$-tensors (principal values), the isotropic rotational correlation time τ_{corr} can be calculated exactly. The A and B terms depend on both tensors ($\mathbf{g}$ and $\mathbf{A}$) and are thus field-dependent, e.g. at higher magnetic field an increased broadening is found.

As input for the simulation ('garlic') the $\mathbf{g}$ -and $\mathbf{A}$ -tensor (in their PAS) and additionally the isotropic rotational correlation time τ_{corr} are needed. Each tensor may have an arbitrary orientation with respect to the molecular frame, specified by three Euler angles (see Appendix).

- *Slow motion regime* ($1 < \tau_{\mathrm{corr}}^{-1}/\Delta\omega > 0.001$, $\tau_{\mathrm{corr}} \sim 1$ ns)

The rotational motion of the nitroxide is slower and the spectrum looses the similarity to the isotropic case. The lines are substantially broadened, become asymmetric and distorted. The theory for slow-motional CW EPR spectra was developed by Schneider and Freed [54] and is based on the stochastic Liouville equation (SLE):

$$\frac{\partial}{\partial t}\chi(\mathbf{\Omega},t) = -i\big[H\big(\mathbf{\Omega}(t)\big),\sigma(\mathbf{\Omega},t)\big] - \Gamma_\Omega[\sigma(\mathbf{\Omega},t) - \sigma_0(\mathbf{\Omega})] \qquad (2.45)$$

The SLE describes the time dependence of the density matrix σ in terms of the spin Hamiltonian H and the diffusion superoperator Γ_Ω. σ_0 is the density matrix in thermal equilibrium and all quantities depend on the orientation $\mathbf{\Omega}$. With an out-of-equilibrium density $\chi = \sigma - \sigma_0$ equ.(2.45) can be rewritten:

$$\frac{\partial}{\partial t}\sigma(\mathbf{\Omega},t) = -\big[iH^{\times}\big(\mathbf{\Omega}(t)\big) + \Gamma_\Omega\big]\,\chi(\mathbf{\Omega},t) = -L(\mathbf{\Omega},t)\chi(\mathbf{\Omega},t) \qquad (2.46)$$

Where $H^{\times}$ is the Hamiltonian commutation superoperator and L the sochastic Liouville superoperator ($L = \big[iH^{\times}\big(\mathbf{\Omega}(t)\big) + \Gamma_\Omega\big]$).

Table 2.2 Timescale of rotational dynamics accessible by continuous wave (CW) EPR spectroscopy and representative spectra at 9.4 GHz (X-band). The spectra were simulated using the *EasySpin* functions as denoted in the right arrow. τ_{corr}: rotational correlation time, $\Delta\omega$: spectral anisotropy (for nitroxides at X-band $\Delta\omega/2\pi \sim 130$ MHz) [51].

Dynamic Regime	**X-band CW EPR spectra**	**Theoretical basis**	**EasySpin function**
Isotropic limit	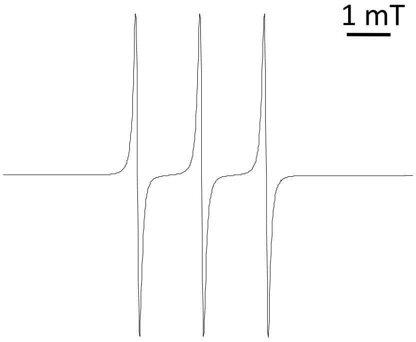	Breit-Rabi formula	garlic
Fast-motion regime	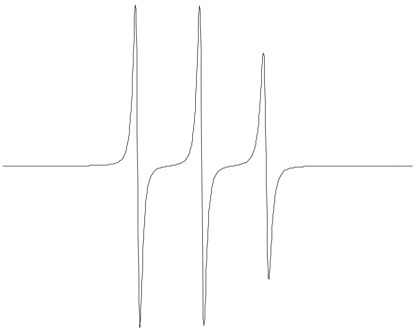	Redfield theory	garlic
Slow-motion regime	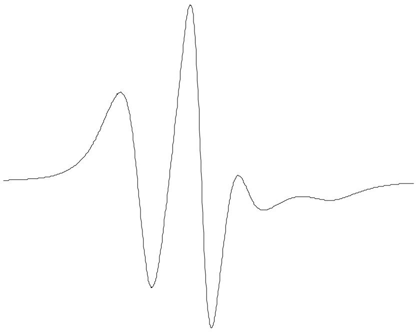	Stochastic Liouville equation	chili
Rigid limit	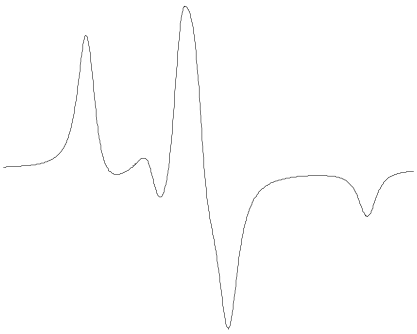	Energy level modelling	pepper

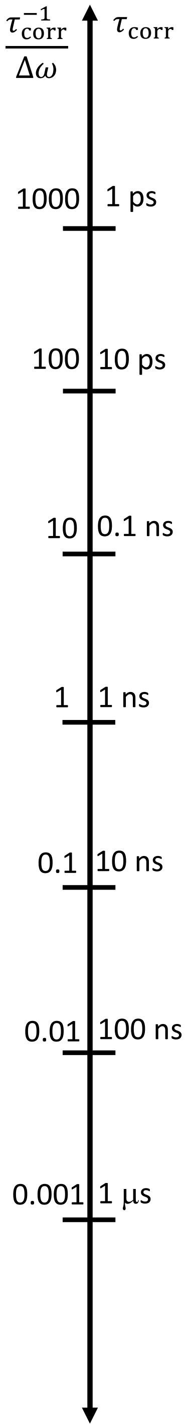

The absorption signal that can be measured by CW EPR is:

$$I(\Delta\omega) \propto Re(\boldsymbol{v}^{\dagger}\boldsymbol{u}) \tag{2.47}$$

$$(L + \mathrm{i}\Delta\omega)\boldsymbol{u} = \boldsymbol{v} \tag{2.48}$$

$\boldsymbol{v}$ is the supervector that describes the x magnetization and $\Delta\omega$ is the frequency offset from the center of the spectrum. In numerical simulations, superoperators are represented by matrices and supervectors by column vectors.

The diffusion matrix Γ_{Ω} depends on the model for the roational motion. Most commonly this is Brownian diffusion. Other models are jump diffusion and free diffusion. In the former, the resting molecule jumps instantaneously into another orientation, while in the latter it rotates directly and unimpeded to another orientation. For isotropic Brownian motion, the motional operator Γ_{Ω} is given by:

$$\Gamma_{\Omega} = -D_r \nabla^2_{\Omega,} \tag{2.49}$$

where D_r is the Stokes-Einstein coefficient of rotational diffusion and $\nabla^2_{\Omega,}$ is the angular Laplacian operator. The rotational correlation time τ_{corr} is related to the rotational diffusion D_r by:

$$\tau_{\mathrm{corr}} = \frac{1}{6D_r}. \tag{2.50}$$

Within the Stokes-Einstein hydrodynamic framework, τ_{corr} can be correlated to the solvent viscosity η and tmeperature T (only valid for spherical molecules):

$$\tau_{\mathrm{corr}} = \frac{4\pi\eta r^3}{3kT}. \tag{2.51}$$

In contrast to the isotropic and fast-motion regime, the quantities $\boldsymbol{v}$**,** Γ_{Ω} and $H^{\times}$ are orientation dependent. Thus, three Euler angles might be used to desribe the rotation as explained in Section 2.2.2. However, Wigner rotation functions $D^L_{KM}(\boldsymbol{\Omega})$ (with $L \geq 0$ and $-L \leq K,\ M \leq L$) are more convenient, since they are eigenfunctions of the rotational diffusion operator. Each of this functions $D^L_{KM}(\boldsymbol{\Omega})$ describe a continous orientational distribution and by performing linear combinations any distribution can be modeled. The higher the values for the parameters L, K, M, the stronger the oscillation of the function as illustrated in Figure 2.16.

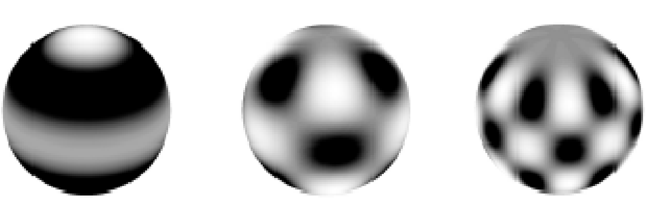

$D^{4}_{0,0}(\mathbf{\Omega})$ $D^{5}_{3,0}(\mathbf{\Omega})$ $D^{8}_{6,0}(\mathbf{\Omega})$

Figure 2.16 Rotational basis functions $D^{L}_{KM}(\Omega)$, all with $M = 0$. Black and white corresponds to negative and positive values. Since $M = 0$, the functions depend only on two Euler angles that describe the orientation. The figures are taken from [51].

The orientational distribution is represented by a linear combination of infinite rotational basis functions $D^{L}_{KM}(\mathbf{\Omega})$. For practical reasons the basis size is truncated to a number N by specifying maximum values for L, K, M so that the error produced is minimum. If too few orientational basis functions are used, the spectrum will show oscillating noise. For each $D^{L}_{KM}(\mathbf{\Omega})$, the number P of EPR transitions and dynamic processes are included in the computation. Thus, the total number of basis functions for the representation of the Hamiltonian and the diffusion operators is PN. Then, the simulation of the spectra involves three steps: (1) construction of the matrices $H^{\times}, \Gamma_{\Omega}$ and vector $\boldsymbol{\nu}$ in the basis, (2) tri-diagonalization of $L = iH^{\times} + \Gamma_{\Omega}$, (3) use of L for computation of the spectrum.

The function 'chili' is used for computing slow-motion spectra. For microscopically oriented samples, like lipid bilayers or liquid crystals, an ordering potential can be included. As input for dynamic simulation parameters an isotropic or axial diffusion tensor can be defined. Further, Heisenberg spin exchange can be included for computation, which is specified by the exchange frequency ω_{Ex}.

- *Rigid limit* ($\tau_{\mathrm{corr}}^{-1}/\Delta\omega < 0.001$, $\tau_{\mathrm{corr}} > 1$ μs)

In the rigid limit the paramagnetic molecules are immobilized and show no translational or rotational motion. The spectrum reveals full anisotropy of all interactions. Such spectra are obtained for powders, frozen solutions and glasses at low temperatures (depending on the solvent this temperature may be reached between -10°C to -80°C). Powder spectra can be calculated with the function 'pepper'. It calls the function 'resfields' to calculate spectra over a triangular orientation grid. The grid is chosen to coincide with the symmetry of the Hamiltonian. The spectra are then calculated for every point of the grid and are interpolated with cubic polynomials- splines, in order to get data for a much finer grid. This procedure quickly yields many more resonant position, intensity and linewidth data than a calculation for every single orientation [51]. Such subspectra are computed with the assumption that within the given triangle the resonance positions vary linearly. The line intensities are calculated proportional to the population difference of the two levels involved in the transition. The anisotropic line width is assumed to be Gaussian due to inhomogeneous broadening by unresolved hf-splittings (see Section 2.7.3) or random variations of the molecular structure around the unpaired electron spin, which leads to small distributions of the principal values of the $\mathbf{g}$- and $\mathbf{A}$-interaction tensors (so called strain). Both types of broadening give orientation-dependent line widths and frequency units, and as a consequence of the A-strain the high-field EPR line exhibit m_I- dependent broadening, but unlike in the fast-motion regime, this asymmetric broadening is due to static distributions and not dynamic processes.

The EPR spectrum is then constructed from the positions, intensities and widths of all transitions and summed over all contributing orientations (the number orientations is automatically chosen from ‘pepper’). The resulting computed spectrum eventually can be fitted to the experimental spectrum.

The simulation of oriented phases such as liquid crystals can be included by a weighting factor during the summation of the subspectra.

- *Simulation of ENDOR spectra*

The function ‘salt‘ is used for the simualtion of ENDOR spectra, the algorithm is similar to the used in ‘pepper’, both provide an identical powder averaging, but the computation of line positions, intensities and widths is different in ‘salt’. The computation of line positions is dependent on the Larmor frequency of the nucleus in the paramagnetic molecule coupled to the electron spin. The presence of further (strongly) coupled nuclei result in second-order line shifts. For nuclei with $I \geq 1$ the nuclear quadrupole interaction affects the line position. The function salt accounts all of these effects and is based on numerical computation of the energy levels by diagonalizing the spin Hamiltonian. The involved energy levels only need to be computed once for each orientation, since the magnetic field position is kept constant during an ENDOR experiment.

The line intensity for each ENDOR transition is a product of three terms: (i) the ENDOR transition rate (includes hf enhancement), (ii)a polarization term and (iii) a selectivity factor (accounting for those ENDOR transitions whose one level is also involved in the EPR transition that is saturated).

2.9 Pulsed EPR Spectroscopy

Pulsed EPR is an approach to measure the response of the electron spins that are excited (usually tens of nanoseconds) with microwave pulses. CW EPR spectroscoy is usally the most *efficient* way to record an EPR spectrum. However, this method observes the complete spin Hamiltonian and provides spectra that contain a lot of information that cannot be separated into the different contributions. The power of pulsed EPR is the targeted manipulation of the spin system by pulses to produce a signal that contains only the desired information, like hf or electron dipolar interaction.

Most EPR pulse sequences are based on the free induction decay (FID) and Hahn echo (see Section 2.9.1). Typically, a pulse sequence can be divided into time periods: (1) the preparation, (2) free evolution, (3) mixing and (4) the detection period.

The preparation period (1) consists of a series of of pulses and delays that remains constant for the measurement. Its function is to convert the initial equilibrium magnetization $\mathbf{M}$ into into some nonequilibrium magnetization at the start of the evolution period. During the evolution time (2) different processes make the system to evolve, then modifying its non-equilibrium state. In some experiments a mixing period (3) can be present at this stage. The detection period (4) starts with one or more mw pulses during which the spectrometer collects the FID of the excited spins. The detection process involves sampling (digitising) the oscillating FID at regular time intervals dictated by the Nyquist condition for an appropiate aqucisition period. The collected data is Fourier transformed to produce the required frequency domain spectrum.

The quantum mechanical description of the spin evolution under the influence of the applied pulses is quite complex and beyond the scope of this introduction. It can be found in textbooks [55]. In the follwing only a short summary of the used experiments is given.

2.9.1 Primary Electron Spin Echo (ESE) Experiment

In the primary (two-pulse) echo experiment the sequence is $\pi/2$-τ-π-τ-echo (see Figure 2.17 a) and the echo amplitude is recorded as a function of the field position B_0. It is the pulsed analogue to a CW EPR experiment.

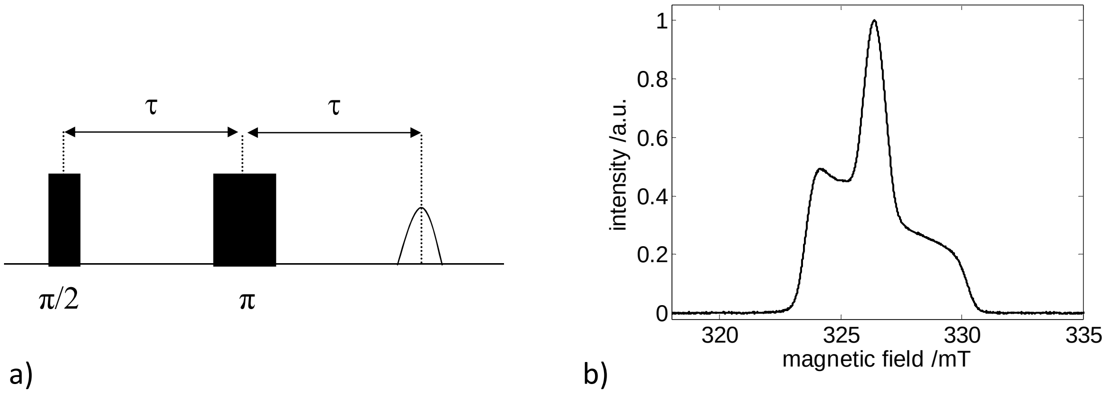

Figure 2.17 Electron spin echo experiment (a) pulse sequence, (b) recorded nitroxide signal.

The first pulse excites spin transitions and cause the appearance of a free induction decay (FID) signal, i.e. an oscillating macroscopic transverse magnetization. Here, the flip of the magnetization vector from the z-orientation is achieved by applying a pulse that causes a 90° flip ($\pi/2$) into the -y-direction. The signal decay is caused by a scattering of precession frequencies of spin packets due to field inhomogeneities or spin-spin interactions. Due to technical reasons, the observation of the FID is hard to achieve (spectrometer dead-time of ~ 100 ns after the first pulse). If a second π-pulse after a time delay τ is applied, the phase of spin precesion in the xy-plane is changed (which coresponds in the vector model a 180° flip in the xy-plane) and the precessing spin packets will refocus after the time τ in +y-direction. This is the spin echo.

The phase memory time T_m governs the decay of transverse magnetization created by the first $\pi/2$-pulse, while the spin-lattice relaxation time T_1 (that is of the order of 10^{-6} s) governs the decay of the longitudinal magnetization created by the π-pulse. Thus, the dependence of the echo signal amplitude on the time delay τ is a factor of (1) the relaxation processes T_m and T_1 and (2) hf interactions with nearby magnetic nuclei causing oscillations in the echo signal decay or "electron spin echo envelope modulation". Since processes (1) and (2) are mutually independent , it is possible to obtain information about the nuclear environment around the unpaired electron. However, the hf interaction can be obtained more precisely from hyperfine spectra, as will be discussed in Section 2.9.4.

2.9.2 Relaxation Measurements

There are several methods to measure longitudinal T_1 and transversal T_2 relaxation times. Here the inversion recovery experiment is described for T_1 and the 2-pulse ESEEM experiment for T_2 measurement. For the processes that contribute to relaxation as well as for basic relaxation theory the reader is referred to standard textbooks [25, 33], this section is focused on the pulse experiments and the data processing.

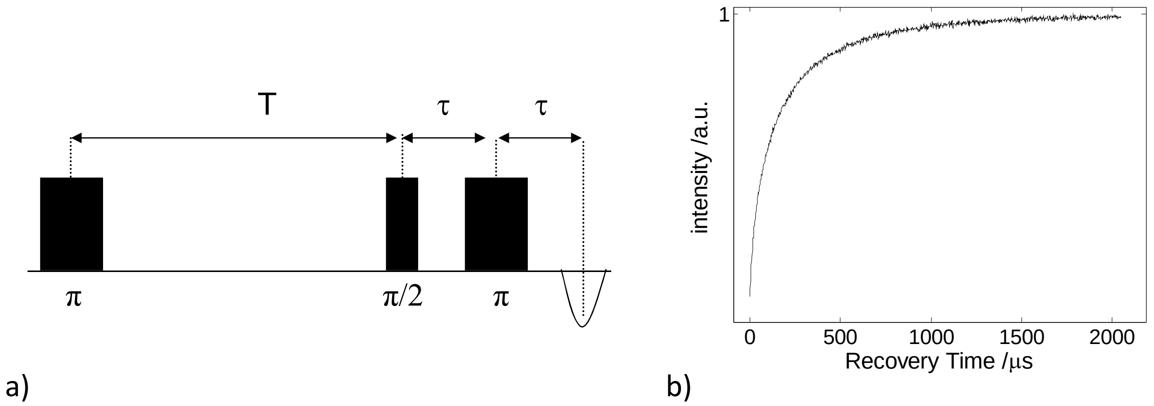

Figure 2.18 Inversion recovery pulse sequence (a) for the measurement of the longitudinal relaxation time T_1 and obtained experimental signal (b).

The experiment is based on the inversion of the magnetization with a π pulse in $-z$ followed by signal detection via the Hahn echo. The time T between the inversion pulse and the detection sequence is incremented, thus, it is possible to observe the recovery of the spin system. To minimize contribution from spectral diffusion to the signal the first pulse is hard, whereas the detection sequence uses soft pulses. Nevertheless, spectral diffusion cannot be neglected.

The obtained signal can be fitted by:

$$I(\mathrm{T}) = I_0\left[a - 2\exp\left(\frac{\mathrm{T}}{T_1}\right)\right], \tag{2.52}$$

with I_0, the echo intensity extrapolated to zero time. In the ideal case (inversion of all spins by the initial π pulse) $a = 1$, however, due to the limited excitation bandwidth and spectrometer dead-times a is usually much smaller than 1.

For the measurement of the transverse relaxtion time T_2 the Hahn echo sequence as depicted in Figure 2.19 (a) can be used, where the echo intensity is recorded as a function of the time τ. The echo is observed at the the time 2τ after the first pulse. Incrementation of the time τ yields the echo envelope modulation due to the coupling to nearby nuclear spins. This ESEEM modulation on the echo decay can be seen in Figure 2.19 b.

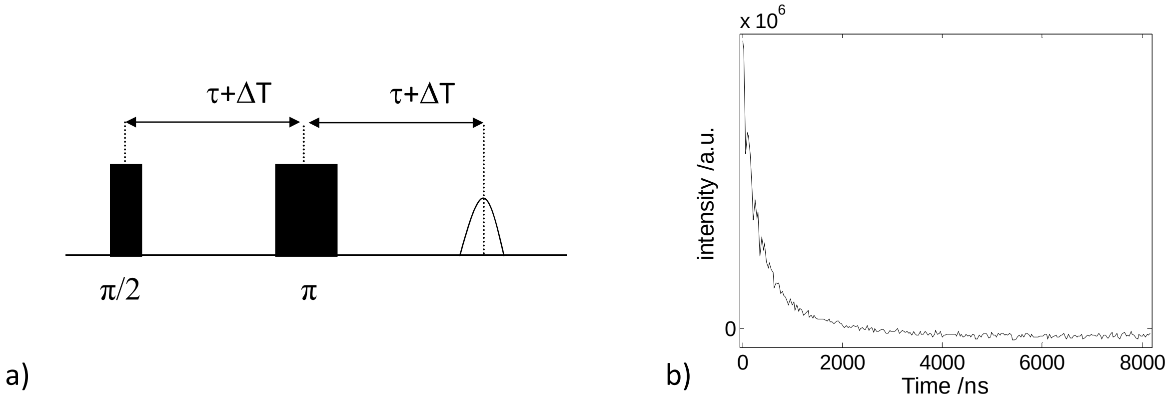

Figure 2.19 2-pulse ESEEM sequence (a) for the measurement of the transversal relaxation time T_2 and obtained experimental signal (b). The difference to the standard Hahn echo experiment is that the position of the refocusing π pulse is increased in steps of ΔT, i.e. the echo position is increased by 2ΔT.

Again, in ideal case the signal can be fitted by a single exponential decay with characteristic time constant T_2, which is rather rarely obtained since the transverse relaxation time is a product of different independent processes (spectral diffusion, instantaneous diffusion, dipolar relaxation, cross relaxation). In this case the decay can be analyzed as a biexponential or a stretched exponential decay.

In the present work, a home-written program was employed that assumes that transverse relaxation time can be described by a stretched exponential decay [56]. Thus, the time-domain signal $I(T)$ is given by:

$$I(\mathrm{T}) = I_0 \exp\left[-\left(\frac{2\mathrm{T}}{T_2}\right)^x\right], \tag{2.53}$$

where the parameters x (stretch factor) and T_2 describe the shape of the echo decay. ESE data are fitted to eq. (2.53) using a Levenberg-Marquardt algorithm. The interpretation of realxation data based on stretched exponentials is less straight forward as with single exponentials, nontheless valueable insights into the radical’s environment, that strongly effects ESE decay can be obtained.

2.9.3 Double Electron-Electron Resonance (DEER) Spectroscopy

Double electron-electron resonance (DEER) is a pulse EPR method to determine interspin distances between electron spins in the range of 1.5-8 nm [10]. It is the analog of spin echo double resonance (SEDOR) techniques in solid state NMR. The physical basis for distance measurements is the dipolar interaction between the electron spins is a function of the distance between them and their mutual orientation as developed in Section 2.5.2. Thus the *distance* can be calculated without calibration.

The original DEER pulse sequence is based on a primary echo and was developed by Milov (3-pulse DEER) [57-58] and further improved to the dead-time free 4-pulse DEER [17], that made it possible to obtain the *distance distribution* and, since it is a constant-time experiment, it keeps relaxation contributions (T_m, T_2) to the echo amplitude constant. Besides the distance and distance distribution the modulation depth of the dipolar spectrum can be used to calculate the number of coupled spins [58-59]. These advantages allow to gain valuable structural information from samples in which other techniques like X-ray crystallography or solution NMR prove difficult.

The pulse sequence (Figure 2.20 a) involves two microwave frequencies that excite separately different spin packets. The sensitivity of the DEER measurement depends on the total amplitude of the observed echo and on the fraction of pumped spins that determines the modulation depth, thus the pump pulse at the frequency ν_{pump} is applied at the maximum of the EPR spectrum (see Figure 2.20 b) and with a maximum excitation bandwidth of the observer pulses. For nitroxides at X-band the global and local maximum are separated by roughly 65 MHz, thus, a pump pulse of 12 ns and observer pulses with 32 ns can be applied without causing overlap.

On an observer spin packet in the powder spectrum with resonance frequency ω_{obs} (black arrow in Figure 2.20 b) a refocused echo is performed. The evolution period of fixed length $\tau_1 + \tau_2$ starts at the end of the second preparation pulse and ends with the π pulse in the observer channel that initiates the detection period. During the evolution the spin packets diphase, undergo a phase conjunction at the π pulse and rephase to form a refocused echo at the time $2(\tau_1 + \tau_2)$ that is detected.

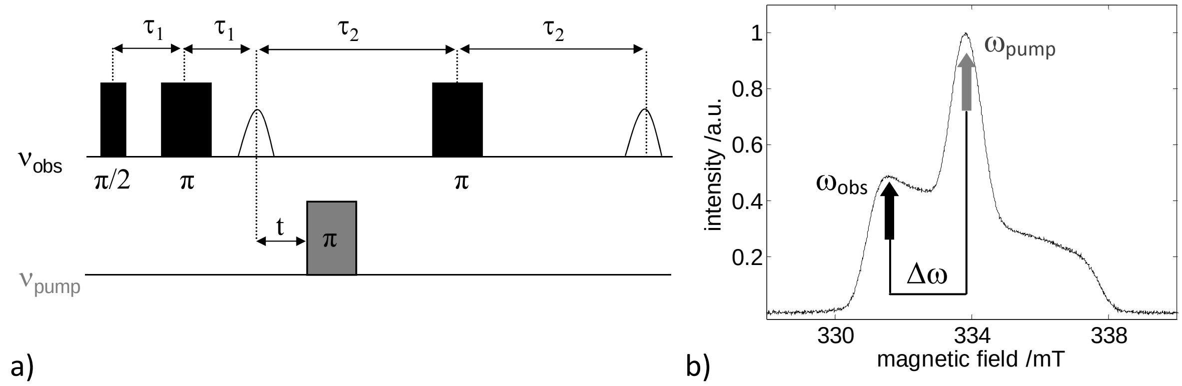

Figure 2.20 a) The 4-pulse DEER sequence and b) positions of the observer (ω_{obs}, black arrow) and pump (ω_{pump}, grey arrow) frequency in the nitroxide EPR spectrum. For nitroxides at X-Band the frequency difference is $\Delta\omega \sim 65$ MHz.

During the evolution period a pump pulse at the frequency ω_{pump} (grey arrow in Figure 2.20b) is irradiated that will only cause electron spin flips in the spectrum near ω_{pump}. If one of those spins is dipolar coupled to an observed electron spin, the observed one undergoes a frequency shift equal to the dipolar coupling ω_{dip}. The dipolar interaction causes an oscillation in the echo intensity with a period that is characteristic of the interspin distance.

Using the point-dipole approximation the DEER echo amplitude $I_{intra}(t)$ is given in the high-field limit by:

$$I_{intra}(t) = \cos\left(\omega_{ee} t\right) \tag{2.54}$$

$$\omega_{ee} = \omega_{dip} + J = \frac{\mu_0 g_1 g_2 \mu_B^2}{4\pi\hbar} \frac{1}{r^3} (3cos^2\theta - 1) + J \tag{2.55}$$

In eq. (2.55) ω_{ee} is the electron-electron coupling frequency, and J the exchange coupling constant, that can be neglected for interspin distances >1.5 nm for non-conjugated systems.

For randomly distributed spin pairs and in absence of orientation selection the Fourier transform of $I_{intra}(t)$ yields after the performance of a proper background correction the Pake pattern (see Figure 2.8 b). The background correction separates homogeneous intra- from intermolecular dipolar interactions. The homogenous contribution is dependent on the volume spin concentration c and the fraction of pumped spins:

$$I_{inter}(t) = \exp(-\kappa c F_{pump} t) \tag{2.56}$$

Whit the constant parameter κ:

$$\kappa = \frac{2\pi\mu_0\mu_B^2 g_1 g_2}{9\sqrt{3}\hbar} \tag{2.57}$$

One difficult aspect of DEER measurements is the extraction of the distance distribution function from the experimental data. This is an ill-posed mathematical problem in which the calculation of the DEER time domain spectrum from a distance distribution is easy, but the recovery of the distance distribution from a DEER spectrum is not possible since many distance distributions can reproduce the experimental data within a given noise level. The common approach is to assume a particular distribution function, e.g. Gaussian distribution and fit a small number of parameters, like the mean distance and standard deviation until the best fit of the DEER signal is obtained. Different distribution models are included in the software *DeerAnalysis2008* [60].

2.9.4 ENDOR Spectroscopy

Electron-nuclear double resonance (ENDOR) spectroscopy detects NMR transitions as induced by an incident radio-frequency (rf) fields that are applied in conjunction with a mw field. The NMR transitions are not detected directly, but through the change in the EPR signal intensity. Thus, it is often called “EPR-detected NMR”. It is used to determine the geometric and electronic structure of paramagnetic entities from hyperfine interactions that are too small to be resolved in the EPR spectrum and measures the NMR frequencies of those nuclei that are hf coupled to the unpaired electron spin. Thus, it is possible to identify the coupled nuclei and gain structural information regarding the close environment.

The ENDOR experiment can be carried out in CW or pulsed modes. CW ENDOR is only used for liquids and provides the isotropic hf coupling constant, while in solids both, isotropic and anisotropic hf interactions are observed. In EPR spectroscopy, the number of transitions increases *multiplicatively* (Π) with the number N of non-equivalent coupling nuclei:

$$\mathrm{N_{EPR}} = \prod_{k=1}^{N} (2I_k + 1), \tag{2.58}$$

but in ENDOR only *additive* (Σ) behavior is obtained:

$$\mathrm{N_{ENDOR}} = 4 \sum_{k=1}^{N} I_k, \tag{2.59}$$

which leads to a strongly reduced number of lines compared to CW EPR spectra in particular for complicated spin systems.

Pulsed methods have become very popular in recent years, since a variety of pulse sequences are available [61-63], which yield undistorted line shapes. Finally, The ENDOR intensity does not depend on the delicate balances between electron and nuclear spin relaxation rates and the power applied This simplifies signal analysis even further.

- *Orientation selection*

EPR spectra of nitroxides in frozen solutions result from the superposition of EPR signals from all molecular orientations with respect to the outer magnetic field. Depending on the magnitude of the magnetic field B_0, the g-anisotropy and the inhomogeneous line width due to unresolved hf couplings, each field position in the EPR spectrum represents a specific manifold of relative molecular orientations from the entire orientation distribution. Going from conventional X- (~9.4 GHz) to W-band (94.5 GHz) frequencies, the increase of the Zeeman energy will lead to a higher spectral resolution in the EPR spectrum (see eq.(2.36)). Especially for nitroxides, which have only small g-anisotropies (in the range of 10^{-3} to 10^{-4}), the respective increase of B_0 to 3.4 T is necessary to resolve the **g**-tensor principal values [1]. This is not yet possible at X-band and only partially achieved at intermediate frequencies (e.g. Q-band, 35 GHz). If the g-anisotropy is larger than the hyperfine interaction (as it is the case for nitroxides at W-band), specific turning points in the spectrum can be used to select molecules with specific orientations to the magnetic field. From these magnetic field positions (see Figure 2.21) “single-crystal-like” ENDOR spectra can be obtained equivalent to those from oriented single crystals, and hf tensors can be elucidated with respect to the **g**-tensor principal axes system. This is commonly known as “orientation-selection” or “angle-selection” [64] and was first introduced 1970 by Rist and Hyde [65].

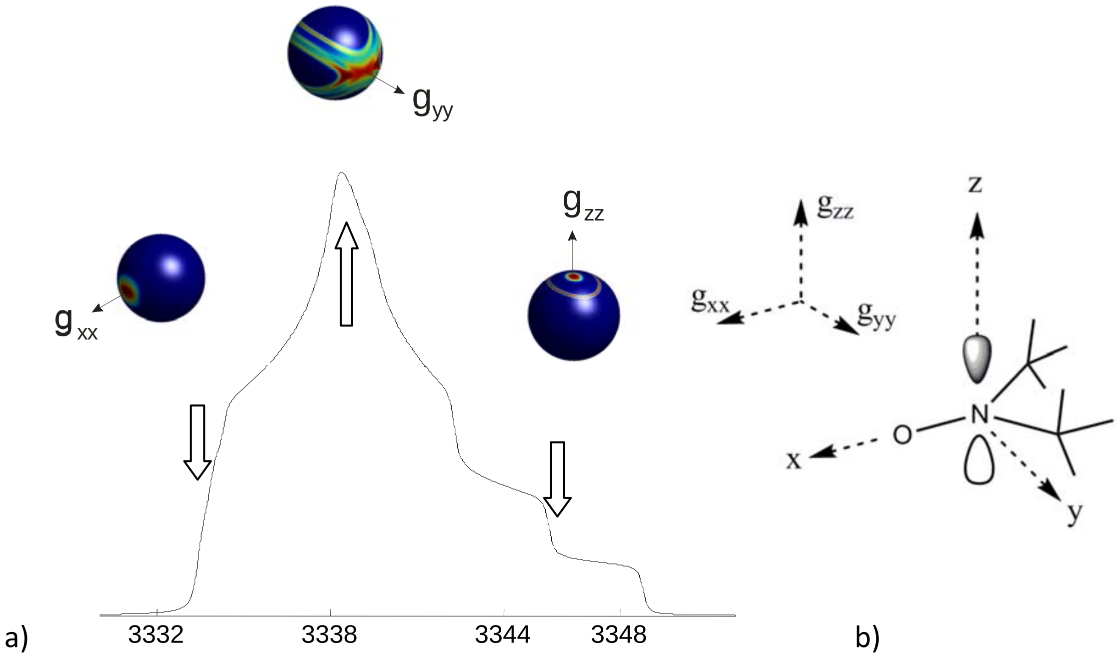

Figure 2.21 a) ESE-detected EPR spectrum of a nitroxide at 94.14 GHz. The field positions that correspond to the canonical values of the **g**-tensor g_{xx}, g_{yy}, and g_{zz} are marked with an arrow. The unit spheres show the representation of orientation selections for the field positions as determined from the simulation, and that were used for simulation of ENDOR spectra. b) Nitroxide molecular frame.

- *ENDOR of a system S=1/2, I=1/2*

The resonance condition for an ENDOR transition is calculated using the spin Hamiltonian given in eq. (2.36), with the EZ and HF terms. At high field, the ENDOR frequencies for an axial system can be described in first order approximation:

$$\nu_{\alpha,\beta} = \left|\nu_I \pm \frac{A}{2}\right| \qquad (2.60)$$

Where A is the hf coupling, that contains both, isotropic and anisotropic contributions as given in (2.16). This yields a doublet of symmetrically situated lines about the nuclear Larmor frequency ν_I(see Figure 2.22 b,c). For weak coupling, $|\nu_I| > |A/2|$ (see Figure 2.22b), e.g. for protons (^{1}H) at 94.5 GHz the first order approximation is valid because of the large ν_{1H}, ~140 MHz at this frequency.

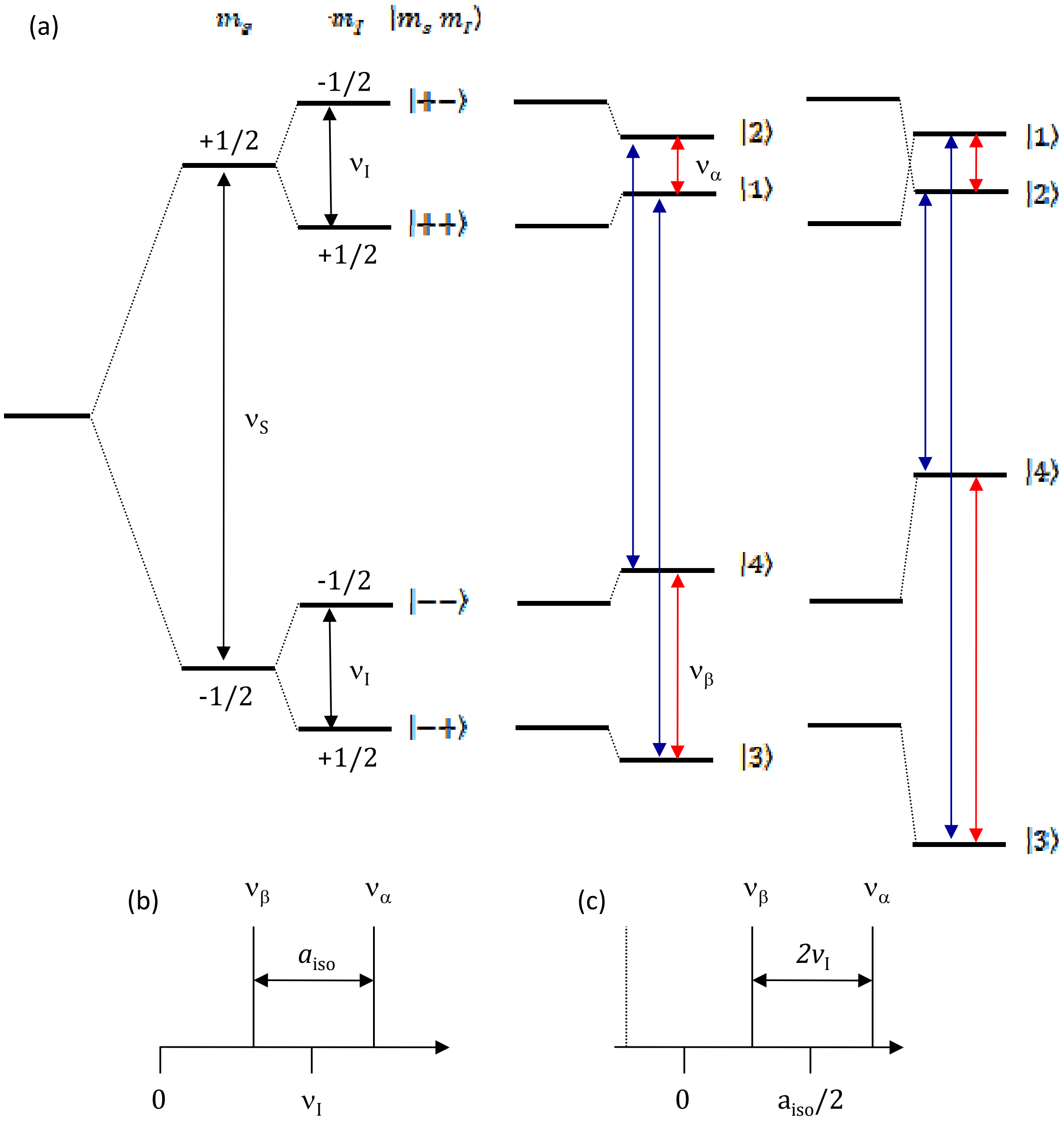

Figure 2.22 Energy level diagrams (a) and line spectra (b,c) of ENDOR transitions for a spin system $S = 1/2$, $I = 1/2$ with isotropic g-factor. For $a_{iso} > 0$ the resulting ENDOR frequencies are shown for weak (b) and strong (c) coupling. The EPR transitions are colored in blue and the ENDOR transitions in red. During an ENDOR experiment, an EPR transition (2→4) is driven at resonance and partially saturated. If the varying radiofrequency is resonant with a nuclear transition, the respective NMR transition (2→1) is induced. The selection rules for ENDOR are $\Delta m_s = 0$ and $\Delta m_I = \pm 1$.

For $I > 1/2$ (e.g. deuterons, ^{2}H) the nuclear quadrupole interaction also becomes simpler at high field and can be treated in frist order [25].

- *ENDOR pulse sequences*

The Davies [62] and Mims [61] ENDOR sequence are illustrated in Figure 2.23 (a) and (b), respectively. The ENDOR spectrum is obtained by recording the echo intensity as a function of the radiofrequnecy.

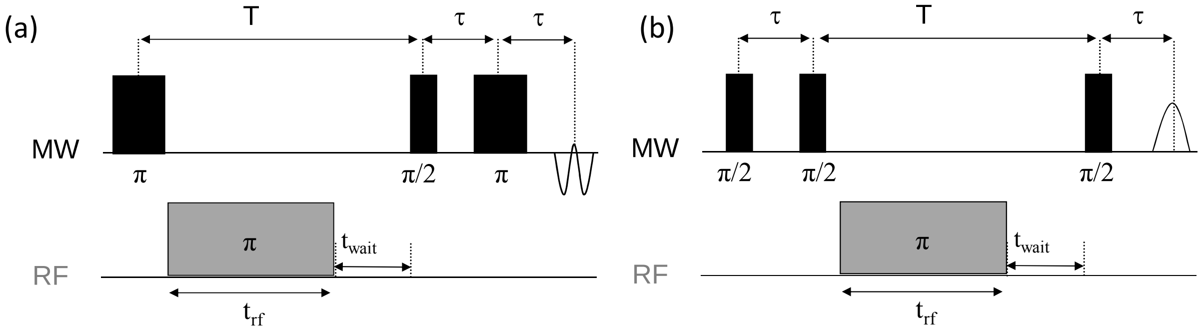

Figure 2.23 Pulse sequence for the Davies- (a) and Mims- ENDOR (b) experiment.

The Davies-ENDOR sequence is based on a selective excitation of one of the EPR transitions, thus, this sequence is suitable for systems with medium to large hf couplings ($A > 2$ MHz). For the second method, Mims-ENDOR, the pulse length is chosen very short in order to excite the whole bandwidth of the electron polarization. After the first two pulses, the spins are not inverted over the entire inhomogeneous EPR line since a spin packet with a dephasing frequency of $\mathrm{n}\pi/\tau$ (with n=1,3,5…) in the rotating frame wil be turned back into positive polarization by the second $\pi/2$ pulse. Rather a sinusoidal magnetization pattern (Figure 2.24) is created by the preparation pulse sequence with the encoding frequency $\omega = 2\pi/\tau$ [66-67]. This function is shown for different τ/t_p ratios, where the mw field strength is chosen in such a way that the flip angle for spins with $\Delta\omega = 0$ fulfills the condition $2\pi\omega t_p = \pi/2$. For $\tau = 0$ (a) the function of a π-pulse is obtained. The other two ones are calculated with $\tau = 4t_p$ (b) and $\tau = 8t_p$ (c) and show in principal the periodic pattern with a mean periode of $\tau + t_p$, where small distortions at small τ-values are indicated. This relative simple pattern in the frequency domain corresponds to a very complicated population pattern in the level scheme, and therefore impedes the discussion of the ENDOR effect in the level scheme.

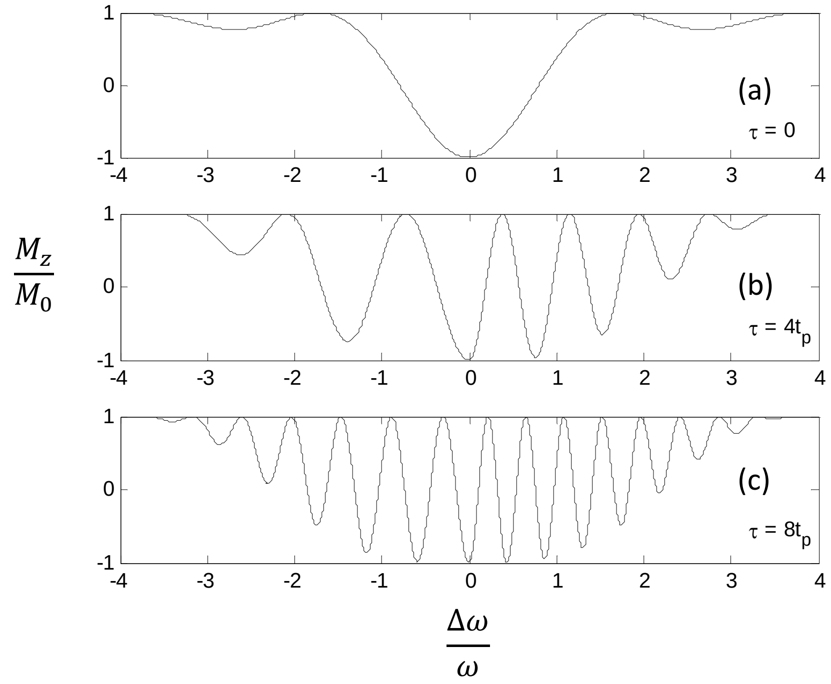

Figure 2.24 Calculated EPR spectrum after the preparation period (after the second $\pi/2$ pulse) in a Mims-ENDOR experiment (with $\Delta\omega$ the offset frequency in the rotating frame). For different interpulse delays τ the magnetization pattern M_z/M_0 gets finer. t_p is the length of the mw pulse. The spacing is given by the hyperfine coupling A by 2π/τ.

The following rf pulse is capable of moving spin packets within the polarization pattern by driving nuclear spin transitions. The drawback of the Mims sequence is the existence of blind spots, where no magnetization is transferred from one maximum (minimum) to another maximum (minimum) in the polarization pattern. Thus, hyperfine couplings of the strength $A = \mathrm{n}/\tau$ (with n=1, 2, 3…) cannot be detected. In Figure 2.24 the polarization pattern for different interpulse spacings τ is shown.

Mims-ENDOR is particular suitable for detecting weakly coupled nuclei, whose hf coupling constants are small as compared with $1/\tau$.

The intensity of the ENDOR response depends on the strength of the hf coupling according to [25]:

$$I \sim 1 - \cos(2\pi A\tau) \tag{2.61}$$

In pulse ENDOR, two common artifacts are present in the spectra: baseline distortion and asymmetric ENDOR intensities [68]. Baseline distortions are due to heating of sample and resonator by the RF pulses which changes the resonator coupling and matching. Asymmetric intensities are a phenomenon arising from the interplay of numerous relaxation processes in the system. These two artifacts can be eliminated via the stochastic excitation mode. Therefore in each scan, a random excitation, not a continuous sweep, of RF frequencies is applied resulting in truly stochastic excitation of the sample. The heating profile of each scan is different and baseline problems are eliminated through averaging. This leads to sensitivity enhancement for slowly relaxing species, for which a very long repetition time had to be used in order to avoid saturation of the NMR transitions.

For the pulsed ENDOR experiments in this work the couplings detected are smaller than 6 MHz for ^1H and smaller 4 MHz for ^2H. Thus, for ^2H only Mims-ENDOR was applied. For ^1H nuclei both methods were used and their information were combined (see Chapter 3.3.2).

3 The Solvation of Fremy's Salt Studied with High-Field Pulse ENDOR Spectroscopy

In this chapter the experimental work on the solvation of a small probe molecule in binary solvent mixtures is summarized and interpretation of the experimental results is given. The chapter starts with the motivation of using Fremy's salt as spin probe to investigate the solvation around this ion and presents the investigated samples. In the next section, performed experiments are described, followed by explanation of the accompanying molecular dynamics simulations. In the last section the solvation characteristics of the molecule in methanol/water mixtures is discussed.

3.1 Introduction

3.1.1 Motivation

Solvation in aqueous solutions has been a most intensive studied problem in chemical physics. The understanding of ion solvation in multicomponent systems is crucial for nearly every chemical reaction [69], for electrochemistry [70] and is fundamental for understanding the role of ions in biological systems. Ions in solutions interact with one another and with solvent molecules. In mixed solvents the solute may interact much more with one solvent species, thus, changing the composition of solvation shell from that of the bulk. This phenomenon of "preferential solvation" [5] makes the solute-solvent and solvent-solvent interactions more complex in mixed solvents than in pure ones. If the preference proceeds to the extremity that one solvent is practically excluded from the vicinity of the solute, it is called "selective solvation" [5]. The comprehension of these phenomena may help the elucidation of kinetic [71-72], spectroscopic [73-74] and equilibrium [75-76] data in binary mixtures. Thus, preferential solvation has been studied extensively during the last years by applying experimental [73, 77-85] and theroretical [86-94] methods.

The study of solvation of paramagnetic ions with methods of electron paramagnetic resonance (EPR) spectroscopy was established more than 20 years ago, in particular for transition metal ions [95-100]. The solvation of shell of the VO^{2+} ion was one of the first examined with continous wave (CW) electron nuclear double resonance (ENDOR) spectroscopy [96, 98], a method that was already introduced in 1956 [101]. These measurements were restricted to paramagnetic ions that exhibit large g-anisotropy even at low magnetic field. Today, modern spectrometers operating at higher magnetic field offer the possibility to study systems with very small g-anisotropies like nitroxides.

EPR spectra are very sensitive to environmental changes like polarity of the solvents, and especially the A_{zz} principal value of the nitrogen hyperfine tensor and the g_{xx} principal value of the $\mathbf{g}$-tensor were found to depend on the local dielectric medium and hydrogen bonding to the N-O group. This allows their use in biochemical research of diamagnetic proteins in combination with site-directed spin labeling [102-104]. Although in such EPR measurements binary solvent mixtures are usually employed because of the need for an cryoprotectant (pulsed measurements are usually performed at cryogenic temperatures) the effect of the nitroxide solvation is only rarely discussed. In this study, we chose Fremy’s salt as a simple model ion to investigate its solvation in binary water-organic solvent mixtures.

In magnetic resonance spectroscopy Fremy’s salt is used as an EPR standard for g-value determination and radical quantitation [105]. The CW EPR spectrum of Fremy’s salt in solution [106-110], single crystal [111-112], trapped crystal matrix [113-116] and frozen solution [117] is well known and was one of the first investigated. Like all nitroxides, Fremy’s salt exhibits a characteristic three line pattern with a spacing between adjacent lines of 13 G [106]. The unavailability of intermolecular protons that usually cause line broadening due to unresolved hyperfine splitting leads to very narrow lines and line shapes that are almost purely Lorentzian-like [109]. It was proposed as internal thermometer in solution EPR due to the sensitivity of its ^{14}N hyperfine splitting towards temperature [118]. The radical is widely used as model for reactive oxygen species (ROS) [119] (e.g. peroxyl or superoxyl $O_2^{\cdot-}$, both important oxidizing agents in cells): it reacts with antioxidants (e.g. ascorbic acid) similarly to ROS [120-122], allowing the investigation of the induced reduction of Fremy’s salt by different natural compounds. Combined with stopped-flow EPR spectroscopy, insights into kinetics and mechanisms were obtained for aqueous solution [122] and micellar systems, which mimic living cells [120]. Recently, the narrow lineshape of FS - resulting from the lack of unresolved ^{1}H hyperfine splittings - has been utilized in new applications. It could e.g. be used to study the distribution of counterions in polyelectrolyte systems in solution [123-125] and for NMR signal enhancement by dynamic nuclear polarization (DNP)[126].

Thus, from the magnetic resonance point of view the nitrosodisulfonate ion is a versatile spin probe. However, ENDOR measurements on Fremy’s salt are rarely found in the literature [127].

Further, there is an active research field devoted to mechanistic studies of Fremy’s salt oxidation reactions in organic and inorganic chemistry [121-122, 128-130]. As one of the simplest odd electron species, its reactions with metal-centered reducing agents in

aqueous media have also been investigated [129, 131-132]. Particularly, these redox reactions give insights into electron-transfer mechanisms in solution.
Beside electronic effects the solvation plays a crucial role for reactivity and regioselectivity of nearly every agens in chemical reactions. Thus, different regioselectivities can usually be observed in different solvents [69]. The understanding of solvation is a prerequisite for understanding the effects of solvents and their mixtures on reaction rates and equilibria.

Methanol-water mixtures were chosen as binary solvent systems for Fremy’s salt due to their widespread use e.g. as custom reaction media in organic synthesis [69]. It was found that a higher methanol content is responsible for enhanced kinetics in some oxidation reactions [133]. The size of polymer particles synthesized by dispersion polymerization in methanol-water mixtures also depends on the methanol content [134]. Even the shape of polymer-silica nanoparticles can be adjusted by the amount of methanol [135]. In microemulsion systems primary alcohols are used as cosurfactants to reduce surface tension of the interface [136]. In analytical chemistry methanol-water mixtures are most frequently used to tune retention in reversed-phase liquid chromatography (RPLC) [137-138]. Eluation characteristics of some solutes do not vary linearly with the total amount of methanol and water, and it was first proposed by Katz in 1989 that the methanol-water system is at least a ternary system with free water (water-clusters), free methanol (methanol-clusters) and methanol-water clusters [139]. This has stimulated a lot of research to investigate the properties of water-methanol mixtures over the whole composition range by experimental and theoretical methods. Among others, this includes density/refractive index measurements [139], heat capacity [140], IR [141], NIR [142], Rayleigh scattering [143], X-Ray emission [144], neutron diffraction [145-146] experiments, as well as MD simulations [147-148].

3.1.2 The Solvents Water, Methanol and their Mixtures

Pure water and methanol are rather small molecules that are in the liquid phase at room temperature due to strong intermolecular hydrogen bonds. Their permanent dipole moments are 1.85 D and 1.70 D [36], respectively, thus, water is only marginally more polar than methanol. Water has two H-bond acceptor and two H-bond donor sites, leading to a highly ordered, tetrahedrally structured network. This is a highly simplified view, though, as research on the structure of bulk water has evolved different models, e.g. the clustering model [149], the clathrate cage model [150], the broken down ice lattice model and the significant structure theory [151]. A purely theoretical treatment of water structure and properties is given in the books of Eisenberg/Kautzmann [152] and Ben-Naim [153] and will not be discussed in this work.

Among the alcohols, methanol is the closest analogue to water and therefore one of the simplest organic solvents. Like water it is also a highly structured, associated liquid but due to its single hydroxyl H-atom, methanol is only a single H-bond donor while the methyl group does not participate in H-bonds. The H-bonds dominate the structural and dynamic behavior of the liquid. Pure methanol forms clusters $(CH_3OH)_n$ of two (n=2) and more molecules in *cyclic* or *linear* chains as visualized in Scheme 3.1. Winding chains with more than three (n>3) methanol molecules are preferred. However, the results obtained by experiment and simulation differ significantly depending on the method that was used. X-ray and neutron diffraction data yield cyclic hexamers (n=6) [154] or chains up to ten molecules with an average of three molecules [155]; from thermodynamic measurements cyclic tetramers (n=4) [156] and penta -or hexamers [157] were concluded. MD simulations predict mainly open chains from 2-6 molecules [158-159]. The scientific discussion in literature about the structure of these two pure liquids has been an active field of research for decades and computer simulations now show new insights on a molecular scale that so far cannot be provided experimentally by measuring macroscopic properties. Especially density functional theory (DFT) calculations combined with the recently developed quantum cluster equilibrium (QCE) model [160] seem to be promising for the simulation of liquid structures.

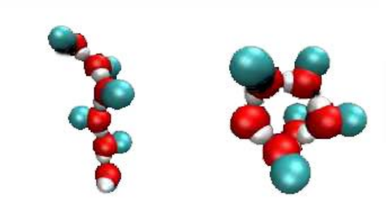

Scheme 3.1 Molecular structures in pure liquid methanol are hydrogen-bonded chains and rings. The hexamers with n=6 molecules of methanol were chosen. The bulky methyl groups are ordered in such a way to adopt most possible space, leading to winded structures. In these structures each methanol molecule acts as an one H-bond donor and one H-bond acceptor. The pictures are adapted from Ref. [2].

Water and methanol are miscible over the whole composition range without phase separation. There is an associated decrease in volume upon mixing indicating strong interactions between the molecules. The mixing entropy increases less strongly than expected for an ideal solution [161-163], in which all molecules are distributed randomly and dielectric properties of the mixtures vary not linearly upon composition [164]. The anomalous thermodynamic behavior of methanol-water (or generally alcohol-water) systems is well-known and was traditionally explained by the "iceberg" model of hydrophobic hydration. This model describes the hydration of non-polar molecules or sites of molecules as enhancement of the water structure in the vicinity of the solute [163] (ordering of water molecules around the hydrophobic part). This more than 50 year old theory has been shown to be wrong. In 2002 new neutron diffraction data showed, that incomplete mixing on the molecular level is the key for explaining the negative excess entropy upon mixing [145] rather than restructuring of water (the number of H-bond in mixtures was found to be not significantly different from that in pure liquids). This was also confirmed by X-Ray emission [165].

In this work isotope substituted methanol-water mixtures were used, where the chemically different protons were marked (methyl protons from –CH_3 groups or exchangeable protons from the hydroxyl-group –OH and water). An exchange of H_2O by D_2O will alter the properties of water slightly. In D_2O, the bond length is slighty longer (D_2O: 95.75 pm, vs. H_2O: 95.718 pm) and the bond angle is slightly smaller (D_2O: 104.474°, H_2O: 104.523°), thus, equilibrium length and angles of the isotopic molecules are nearly equal [152]. Classical mechanics predict the structures of liquids to be independent of isotope substitution, but newer studies based on computer simulation and diffraction experiments show that there actually is an isotope effect. D_2O seems to be more ordered than H_2O [166] and for isotopically substituted methanol a maximum deviation of 10% from the structure of non-substituted methanol was observed [167]. No data is available for isotopically modified water-methanol mixtures but based on the known studies for the pure liquids it should also show slight deviations. However, for the studied systems the perturbation by the dissolved ion obviously the solvent structure to a much larger extent than isotope modification, as will be seen in Chapter 3.3. Furthermore, with EPR we get only exact information about the immediate surroundings, the first salvation shells of the ensemble of paramagnetic centers. Structural information about the bulk solvent regions in the system is not available with our methods and hence beyond the scope of this study.

The CH_3 group of methanol is quite bulky, which not only prevents strong electrostatic interaction of the methyl group with other species, but also makes the methanol molecule considerably more bulky as a whole. This, combined with methanol's slightly lower dipole moment, should result in water being the preferred solvent for charged solutes, like Fremy's salt.

Mims [61] and Davies [62] pulse ENDOR experiments are applied to study the solvation of Fremy's salt in methanol-water mixtures at 94.5 GHz. The main tool to achieve selectivity concerning the solvation of the small probe molecule is the selective isotope modification of either *methyl* protons (-CH_3) of methanol or *exchangeable* protons from the alcohol-hydroxyl (-OH) group and water (H_2O).

3.2 Studied Systems

This section describes the main features of sample preparation (details are given in Section 7.1) with notice about Fremy's salt decomposition and presents the investigated methanol/water samples (Table 3.1).

Fremy’s salt is soluble in water in large quantities. In aqueous solution, the orange diamagnetic dimer dissociates into nitrosodisulfonate radical ions that appears as violet-blue solution [168] according to Scheme 3.2. In this work the term ‘Fremy’s salt’ is used for both forms, although strictly speaking Fremy’s salt (peroxylamine disulfonate) is the solid form and the nitrosodisulfonate anion the monomeric form. The radical ion bears two charges that favor the solubility in solvents with high dielectric constant, whereas it is insoluble in dry organic (especially unpolar) solvents.

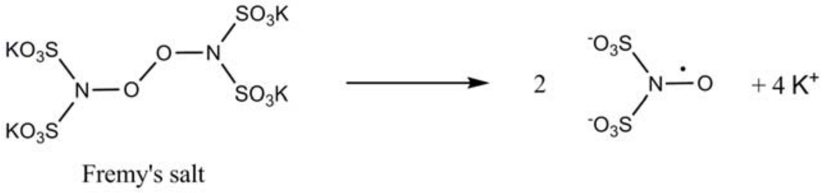

Scheme 3.2 Dissociation of Fremy’s salt dimer (orange) in aqueous solution into the paramagnetic nitrosodisulfonate ion (violet).

The solutions undergo fast decomposition, making the handling of this spin probe rather difficult. The rate of decomposition depends upon concentration, possible impurities, pH and temperature. The optimum pH for stability was found to be around 8 [169]. KOH solutions were explicitely used to adjust the pH in order to exclude the introduction of a new ion species (carbonate ions by pH adjusting with K_2CO_3) into the system.

Fremy’s salt concentrations of 2.5 mM were used for all EPR and ENDOR measurements. To reduce the inaccuracy due to weighing of small (milligram and sub-milligram) amounts of substance, stock solutions with a higher concentration were prepared and successively diluted. To this end, 10 mM Fremy’s salt stock solutions in water or deuterium oxide were prepared. To reduce decomposition, a stock solution of 2 M potassium hydroxide was added. Obtained solutions were diluted to 5 mM and stored at -18°C. This aqueous stock solutions were mixed with methanol in volume ratios 70:30, 50:50 and 30:70 (molar ratio x_M= 0.51, 0.31 and 0.16 respectively) as listed in Table 3.1. They were prepared under ambient conditions without the use of inert gases. Solutions with higher methanol ratios (x_M>0.5) were not prepared due to lower solubility of Fremy’s salt in these mixtures. Lower concentrations could not be tested because even at the lowest tested methanol ratio the signal intensity in echo detected spectra was already decreased. Lower methanol concentrations (x_M<0.16) do not form glassy solutions upon freezing within our experimental set-up and therefore mark the lower limit for the methanol content. In purely aqueous frozen solutions local crystallization will, first, change the solvation characteristics and, second, complicate data analysis and is therefore not desired. All experiments are analyzed under the assumption that the shock frozen solutions with methanol as cryoprotectant, represent the solvation characteristics at room temperature (or more precisely at the glass transition temperature). This is essential for data treatment.

Some properties of pure methanol-water mixtures are plotted in Figure 3.1. Due to the non-ideal behavior of alcohol-water mixtures empirical values were used for the viscosity η, the density ρ and the molar volume V_m. All shown properties are highly temperature dependent and are only shown for ambient conditions, under which the samples were also prepared (T~298 K). The temperature-dependent values for the dielectric constants were taken from experimental data [170]. Isotopic effects were not taken into account, meaning the data are strictly valid only for CH_3OH-H_2O mixtures. The studied compositions x_M are marked with the dotted lines.

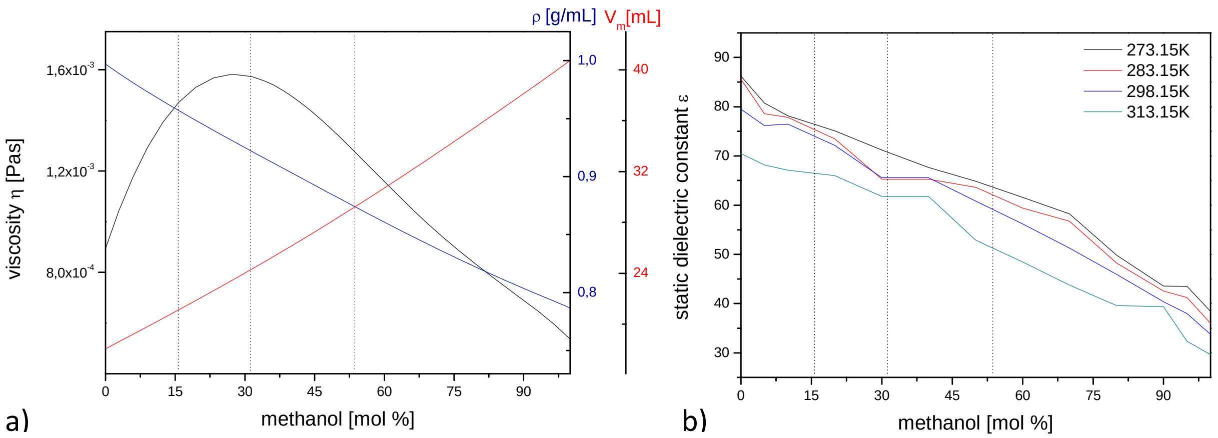

Figure 3.1 a) Absolute viscosity η, density ρ and molar Volume V_m for methanol-water mixtures as a function of the methanol content in mol %. All data are given for T=295.13 K. Values are calculated from an empirical power law series equation $y = \sum_{i=0}^{n} a_i x^i$ where y denotes η, ρ or V_m and x the alcohol mol percentage. Constants a_i for each quantity y were found by least square fittings to measured data at different temperatures (adapted from Ref. [3]). b) Dielectric constant of methanol-water mixtures as function of methanol content in mol% for different temperatures. At room temperature (T = 298.15 K blue line) pure water shows ε = 79.5 and pure methanol ε = 33.7. The dotted lines indicate the studied compositions.

Table 3.1 Investigated samples of 2.5 mM Fremy's salt in methanol-water mixtures. The properties of the solvent-mixtures are listed for pure binary solvent mixtures at T=298.15K. V_M,V_W: Volume ratio for methanol and water, x_M, w_M mole and weight percent methanol, ε: static dielectric constant, η: absolute viscosity.

Solvent	**$V_M : V_H$**	**x_M [mol%]**	**w_M [weight%]**	**ε**	**η [mPas]**
$\mathbf{CD}_3\mathbf{OD} : \mathbf{D}_2\mathrm{O}$	50 : 50	30.8	44.2	65.3	1.57
$CH_3OH : H_2O$	50 : 50	30.8	44.2	65.3	1.57
$CH_3O\mathbf{D} : \mathbf{D}_2\mathrm{O}$	50 : 50	30.8	42.3	65.3	1.57
$\mathbf{CD}_3OH : H_2O$	50 : 50	30.8	46.4	65.3	1.57
$C\mathbf{D}H_2OH : H_2O$	50 : 50	30.7	44.9	65.3	1.57
$CH_3O\mathbf{D} : \mathbf{D}_2\mathrm{O}$	30 : 70	15.0	23.9	76.5	1.47
$CH_3O\mathbf{D} : \mathbf{D}_2\mathrm{O}$	70 : 30	49.1	63.1	52.9	1.34

The main tool to achieve selectivity concerning the solvation of the small probe molecule FS in this investigation is the *selective isotope modification* of either *methyl* protons ($-CH_3$) of methanol or *exchangeable* protons from the alcohol-hydroxyl group and water.

In the sample mixture $C\mathbf{D}_3OH$-H_2O the *non-exchangeable methyl* protons are isotopically substituted. In the solvent mixture $CH_3O\mathbf{D}$-$\mathbf{D}_2O$ the *exchangeable protons* of the polar O-H groups of water and methanol that can undergo fast exchange (at room temperature) are exchanged by deuterons. This case is illustrated in Scheme 3.3. The advantage of this approach is the selective "switching off" of one chemical proton species (exchangeable or methyl protons) in one measurement. In a ^1H-ENDOR spectrum of the $CH_3O\mathbf{D}$-$\mathbf{D}_2O$ mixture, only methyl protons will contribute to the ENDOR signal and in a ^2H-ENDOR measurement of the same sample only exchangeable protons that are hyperfine-coupled to Fremy's salt will be monitored. This allows a simplified data interpretation.

Working at high magnetic field (W-Band, microwave frequency of 94.5 GHz) has two advantages: (*i*) the **g**- and **A**-tensors of the nitroxide EPR spectrum are fully resolved, thus allowing orientation-resolved EPR and ENDOR, and (*ii*) the Larmor frequency of ^1H is about 149 MHz and of ^2H at 23 MHz, hence they are well separated from each other.

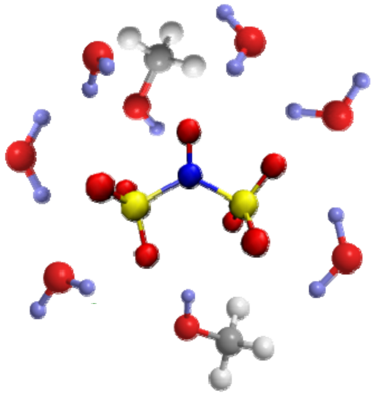

Scheme 3.3 Sketch of solvated a Fremy's salt anion $ON(SO_3)_2^{2-}$ in a $CH_3O\mathbf{D}$-$\mathbf{D}_2O$ mixture. Carbon atoms are shown in grey, oxygen atoms in red, hydrogen atoms (^1H) in white and deuteron (^2H) in purple. In a ^1H-ENDOR experiment only the *methyl protons* that are hyperfine-coupled to Fremy's salt contribute to the ENDOR signal. In a ^2H-ENDOR experiment hyperfine interactions between *exchangeable deuterons* and the nitroxide are monitored. It is not possible to differentiate between hydroxyl-OH and water-OH protons.

3.3 High-Field Pulsed Experiments

Standard Mims and Davies ENDOR-experiments (Section 2.9.4) were applied to study the solvation of Fremy's salt in methanol-water mixtures at 94.5 GHz. Mims ENDOR was recorded for both proton species (methyl and exchangeable protons) and both isotopes (^1H and ^2H). Davies ENDOR was recorded only for the ^1H isotope for both proton species, since the small deuterium couplings (~2 MHz) and weak signal intensities cannot be properly be detected by the Davies ENDOR sequence. Measurements at W-band were performed at 20K. First, field swept echo detected EPR spectra were recorded to determine the field position for ENDOR experiments. The characteristic turning points were assigned by visual judgment and typical positions chosen are shown as red circles in Figure 3.2. It is obvious from the figure that the high field position will have a worse signal-to-noise ratio. Even for long measurements (~16-20h) the z-position could not give comparable S/N ratios to other positions. For the other field positions an adequate S/N ratio is usually obtained by signal accumulation over two to five hours.

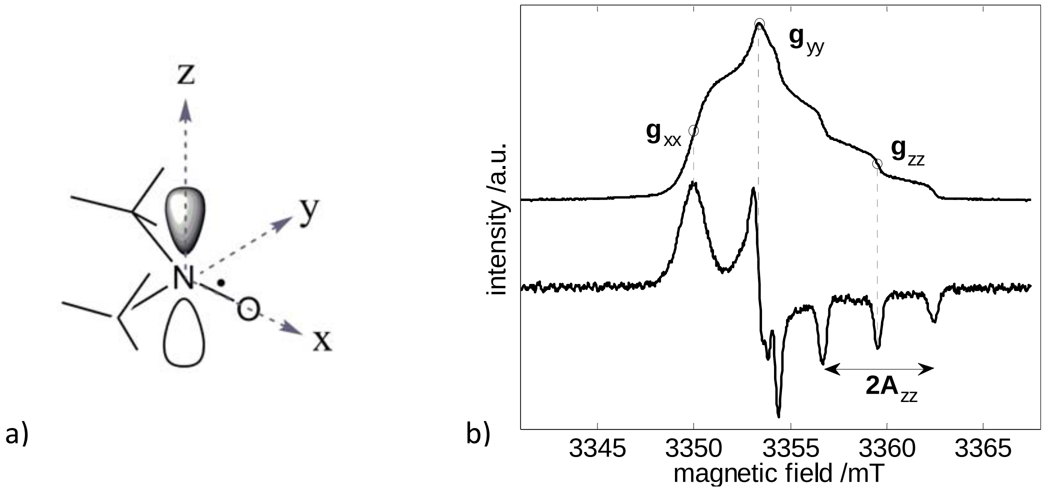

Figure 3.2 a) The nitroxide group and its molecular coordinate axis system with the x-axes along the NO bond and z-axes along the $2p_\pi$ orbital. The **g**-tensor principal axes system coincides with the molecular axes and the hyperfine tensor coordinate system [1] b) upper: Field-swept echo-detected EPR spectrum of 2.5 mM Fremy's salt in CH_3OD/D_2O with a volume ratio of *v/v*= 70:30, recorded at 94.18 GHz and 20 K. The pulse sequence was $\pi/2$-τ-π-τ-echo, with $t_{\pi/2}$= 48 ns, t_π= 96 ns and τ= 300 ns, lower: The pseudomodulated spectrum calculated with a modulation amplitude of 0.25 mT from the absorption spectrum. The dotted lines indicate the position of nitroxide principal axis components as shown in the left scheme. Circles indicate observer field positions B_{ENDOR} used for ENDOR measurements to obtain orientation selective hf spectra as described in Section 2.9.4.

3.3.1 Echo- Detected Measurements

The field-swept, echo-detected EPR spectra for methanol:water=1:1 mixtures (volume ratio) are shown in Figure 3.3. They exhibit the typical nitroxide powder pattern line shape expected for a dilute distribution of nitroxide radicals. The spectra were background-corrected using a home-written MATLAB program, by subtracting a first-order polynomial fit to the first and last 15% of the data points and normalized to their maxima. Differences between the spectra are better visualized in the pseudomodulated form of the absorption signal. Pseudomodulation simulates the effect of an applied field modulation on an ESE absorption signal (but relaxation processes may cause shape deviation of the pseudomodulated spectrum compared to the CW spectrum) [171]. A modulation amplitude of 0.35-0.4 mT was used to calculate the pseudomodulated spectra. In particular the A_{yy} hyperfine splitting is much better observable when compared to the respective ESE-detected spectra. The A_{yy} splitting is clearly visible in the sample mixture $CH_3O\mathbf{D}$-$\mathbf{D}_2O$ (Figure 3.3 c) and is indicated in all other spectra. Deuterium has a nuclear spin of I = 1 and hence quadrupole interactions have to be taken into account. However, as it follows from Figure 2.5, the quadrupole interaction acts in the same way on both m_s manifolds.

Therefore, if second order effects are not taken into account, the quadrupole interaction has no effect on the EPR spectrum (see Section 2.4.3).

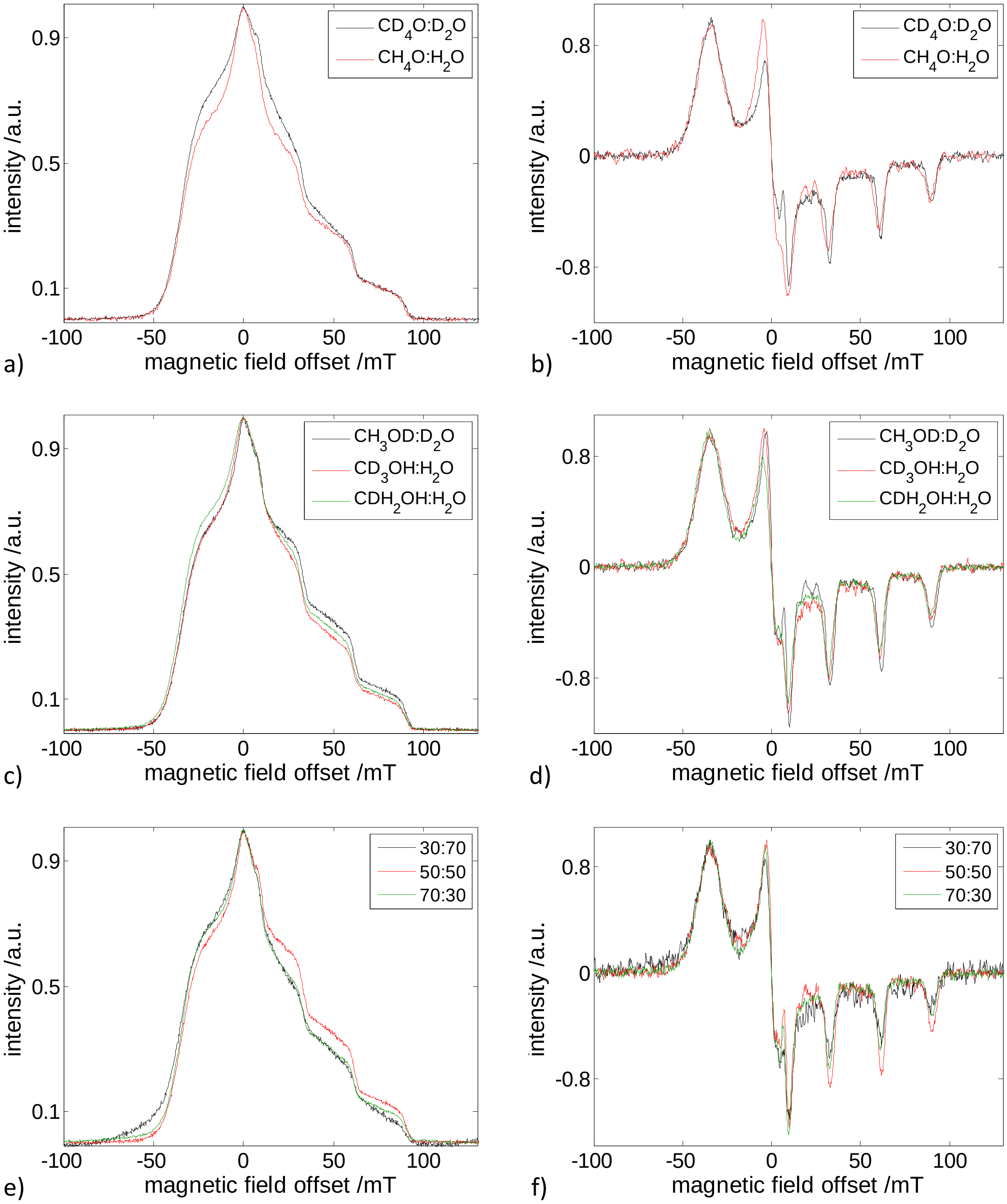

Figure 3.3 Amplitude-normalized echo-detected EPR spectra (a,c,e) of 2.5 mM Fremy's salt in water-methanol mixtures measured at 20 K and 94.5 GHz and their corresponding pseudomodulated spectra (b,d,f) calculated with a modulation amplitude of 0.35 mT. a)-d) Methanol/water mixtures of equal volume ratio *v*/*v*=50:50 and different isotope substitution. a,b) The completely deuterated sample $C\mathbf{D}_3O\mathbf{D}$-$\mathbf{D}_2O$ (black) vs. completely protonated sample CH_3OH-H_2O (red); c,d) black: $CH_3O\mathbf{D}$-$\mathbf{D}_2O$, red: $C\mathbf{D}_3OH$-H_2O, green: $C\mathbf{D}H_2OH$-H_2O. e,f) Fremy's salt samples in the solvent mixture $C\mathbf{D}_3OH$-H_2O. Solvent ratios were varied from low methanol content (black) to high methanol content (green). Experimental: τ=300 ns, $t_{\pi/2}$=48 ns, t_{π}= 96 ns.

The rigid-limit EPR spectra were simulated with the function *pepper* in EasySpin (see section 2.8). Best simulations were obtained by introducing an anisotropic line width (H-Strain) that can model small effects such as unresolved hyperfine splitting or $\mathbf{g}$- or $\mathbf{A}$ -strain. Typical parameters found from simulating the experimental EPR spectra are g=[2.00844, 2.00625, 2.00285] ± $2{\cdot}10^{-5}$, $\mathbf{A}$ =[0.41, 0.40, 2.86] mT ± 0.02 mT for the principal values of the $\mathbf{g}$- and $\mathbf{A}$ -tensor, respectively. A Voigtian-type line width is found with a FWHM of 0.3 mT (Gaussian part) and 0.09 mT (Lorentzian part). In solid state EPR spectra homogeneous line broadening (T_2 -broadening) is usually negligible. Thus, the slight mismatch between simulation with a purely Gaussian line and experiment might be due to nuclear relaxation effects. An orientation-dependent phenomenological broadening of 15-25 MHz is found along x, 8-17 MHz along y and 8-19 MHz along z, in which the magnitude follows the order x>z>y for all samples.

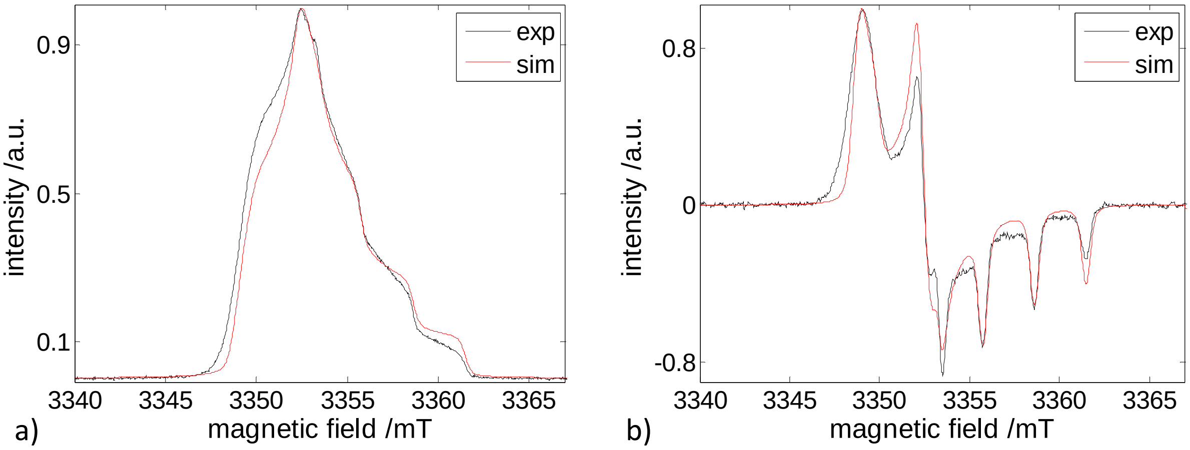

Figure 3.4 Experimental (a) and simulated (b) (pepper) powder EPR spectra in absorption and first-derivative (pseudomodulated) mode. The simulation was performed with a rhombic g-tensor, nearly axial $\mathbf{A}$-tensor and an additional orientation-dependent broadening ("H-Strain") as described in the text.

Due to this broadening the error for the x-component of the $\mathbf{A}$-tensor is much higher than for the other components. Even with this additional broadening the low field flank of the simulated spectra never reaches the experimental spectrum. Better results are obtained by simulation of two species with different g_{xx} value (with the other parameters identical). This could be indicative of the existence of Fremy's salt NO-groups which participate in hydrogen-bonded structures, as the g_{xx} value is known to be sensitive to the formation of hydrogen bonds. At this point I refrain from a more detailed analysis of this observation and show the simulated spectrum in Figure 3.4 (red) that were calculated with a single species.

Notably, the line width in completely deuterated solvent and in completely protonated solvent (Figure 3.3 a) differ only slightly from each other, indicating that the broadening due to unresolved (in particular ^{1}H) hyperfine couplings to solvent hydrogen atoms is negligible in low-temperature ESE-detected EPR spectra. No difference in the A_{zz} value was observed between the deuterated and nondeuterated sample mixture with a solvent ratio of *v/v*= 50:50 (ε = 65). Comparing the solvent mixtures with higher (70 vol.%, ε= 53) and lower (30 vol.%, ε= 77) amounts of methanol, no variation of A_{zz} with solvent polarity is observed either. The low field region of the ESE spectrum of the water rich solvent mixture (70 vol.% H_2O) is broadened and a slightly higher xx-value ($5 \cdot 10^{-5}$) is found. The best simulation for this sample is by introducing a second species with pronounced higher g_{xx}-value ($4 \cdot 10^{-4}$). No differences for the g_{xx}-values of the 50 vol% and 70 vol.% methanol are observed, which indicates that the hydrogen-bonding to NO is similar in the two latter.

3.3.2 ENDOR Measurements

In this Section, the obtained orientation-selective ENDOR spectra of Fremy's salt frozen solutions are presented. The following color code is used in all Figures and all spectra: black marks the x-, red the y- and green for the z- direction of the molecular reference frame (Figure 3.2 a). Figure 3.5 and Figure 3.6 display the Mims ENDOR spectra, while the recorded Davies ENDOR spectra are shown in Figure 3.7. Mims ENDOR spectra were recorded for volume mixtures of methanol/water=30:70, 50:50 and 70:30. Davies-ENDOR spectra were recorded for the 50:50 mixtures only.

- *Mims ENDOR*

In Figure 3.5 the orientation dependent Mims-ENDOR spectra for isotope substituted methanol/water mixtures with *equal volume ratio* are displayed. The left column (a,c,e) shows the deuterium spectra, the right column the proton spectra of the according solvent mixture. In the first row the completely deuterated $C\mathbf{D}_3O\mathbf{D}/\mathbf{D}_2O$ (a) and protonated CH_3OH/H_2O (b) solvent mixtures are shown. The second row contains the ^2H (c) and ^1H (d) spectra of the isotope substituted solvent mixture $CH_3O\mathbf{D}/\mathbf{D}_2O$ and the third row the ^2H (e) and ^1H (f) spectra of the solvent mixture $C\mathbf{D}_3OH/H_2O$. This means, that each chemical proton species is measured twice. For example methyl protons were monitored via the ^1H-ENDOR spectrum in the mixture $CH_3O\mathbf{D}/\mathbf{D}_2O$ (d) and via the ^2H- ENDOR spectrum in the mixture $C\mathbf{D}_3OH/H_2O$ (e). The same holds for the exchangeable protons in (c) and (f).

In all Mims ENDOR spectra an intense peak is observed in the center. Such matrix lines in ENDOR spectra are due to very weak hyperfine interactions of the unpaired electron with distant matrix nuclei and originate from simultaneous inversion of a large number of nuclear spins by the rf pulse [172]. The analysis of weakly coupled protons in the solvation shell is complicated as these resonances overlap with the matrix peak.

In Mims ENDOR, the intensity suffers from a periodic dependence of the interpulse spacing τ, given by $I_{ENDOR} \sim 1-\cos(2\pi A\tau)$ [25], where A is the hyperfine coupling constant and τ the pulse spacing between the last two $\pi/2$ pulses.

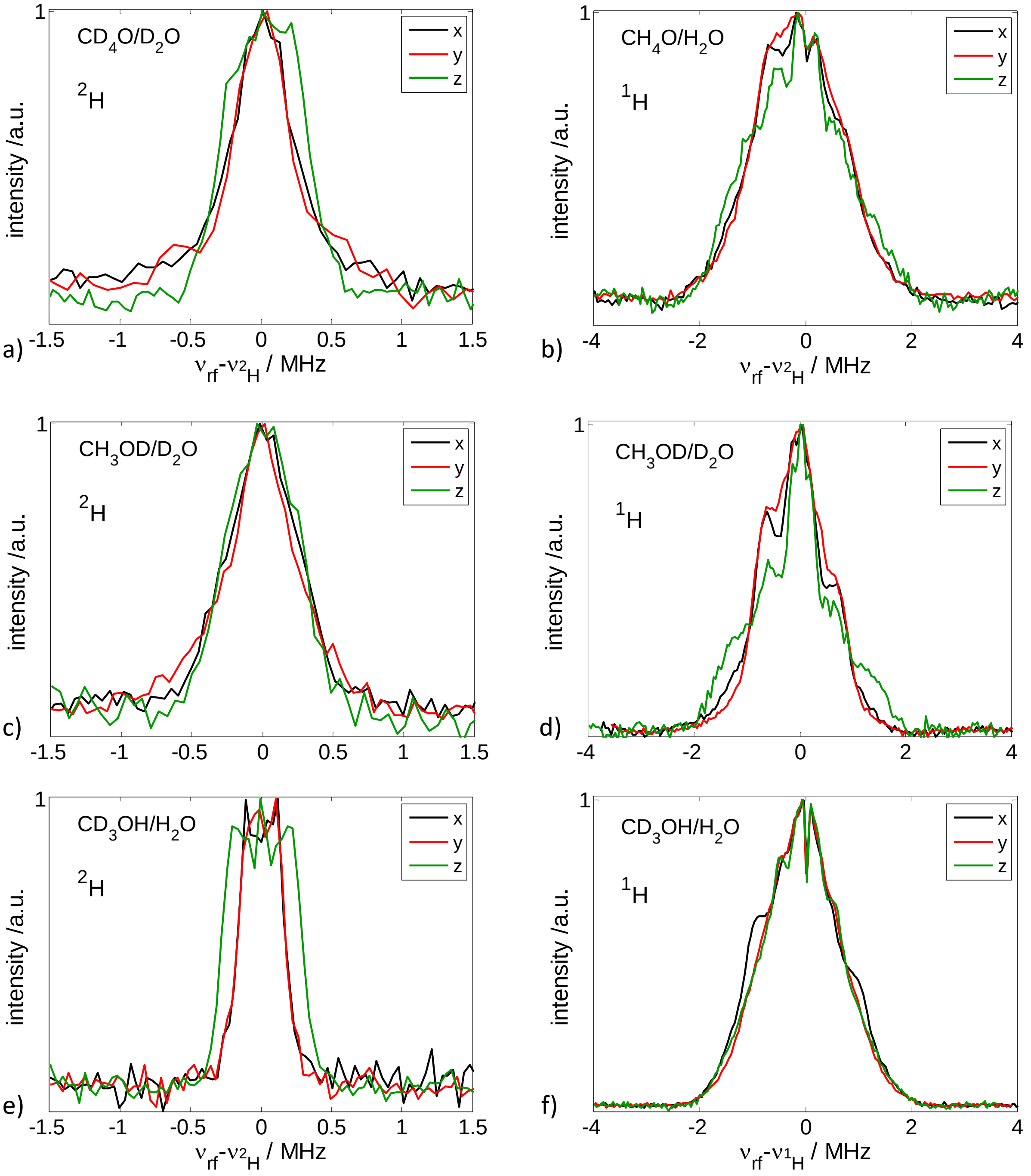

Figure 3.5 Orientation-selective Mims-ENDOR spectra of 2.5 mM Fremy's salt in frozen solution. Volume ratios of methanol/ water are always v/v=50:50. a) ^{2}H spectra of C$\mathbf{D}_3$O$\mathbf{D}$/$\mathbf{D}_2$O, b) ^{1}H spectra of CH_3OH/H_2O. c), d) ^{2}H and ^{1}H spectra of the solvent mixture CH_3O$\mathbf{D}$/$\mathbf{D}_2$O. e), f) ^{2}H and ^{1}H spectra of the solvent mixture C$\mathbf{D}_3$OH/H_2O. Spectra were recorded from the low-field turning point g_{xx} (black) to the high-field turning point g_{zz} (green) of the EPR spectrum. Experimental parameters: T: 20 K, MW $\pi/2$ pulse: 48 ns, τ for ^{1}H: 172 ns (b), 200 ns (d), τ for ^{2}H: 400 ns (a), 600 ns (c), RF π pulse: 20 μs for ^{1}H and 35 μs for ^{2}H.

An increased value for τ led to a symmetric narrowing of the spectra from both sides affecting mostly the width of the broadest coupling. This was pronounced in ^{2}H measurements since large τ-values have been used for their detection (600 ns). Attempts to measure ^{2}H with shorter τ values suffered from poor S/N ratio. Hence, analysis of ^{2}H spectra is only given in a qualitative way. Pronounced changes in the ENDOR spectra for the different observer field positions x, y and z are obtained for methyl protons (d,e).

At the molecular z-position a larger coupling is visible that is for ^{1}H at ~±2.1 MHz and for ^{2}H at ~±0.4 MHz. Comparison of the values of the hf couplings for methyl protons and methyl deuterons shows the expected scaling with the ratio of the magnetogyric ratios for the two isotopes.

Similar Mims ENDOR spectra showing identical magnitudes of hyperfine couplings and relative intensities for the different positions x, y and z like the shown in Figure 3.5 d for the solvent mixture CH_3OD/D_2O are also obtained for the solvent mixture with higher methanol (70 vol.%, ε = 53, Figure 3.6 a) and lower methanol (30 vol.%, ε = 77, Figure 3.6 b) content. The mixture with low methanol content gave only poor S/N ratio in the ENDOR experiments but shows also the same trend upon variation of the observer field position (Figure 3.6 b). Since the spectra obtained for other than 50:50 mixtures showed the same features and trends like the 50:50 mixtures they were not further analyzed.

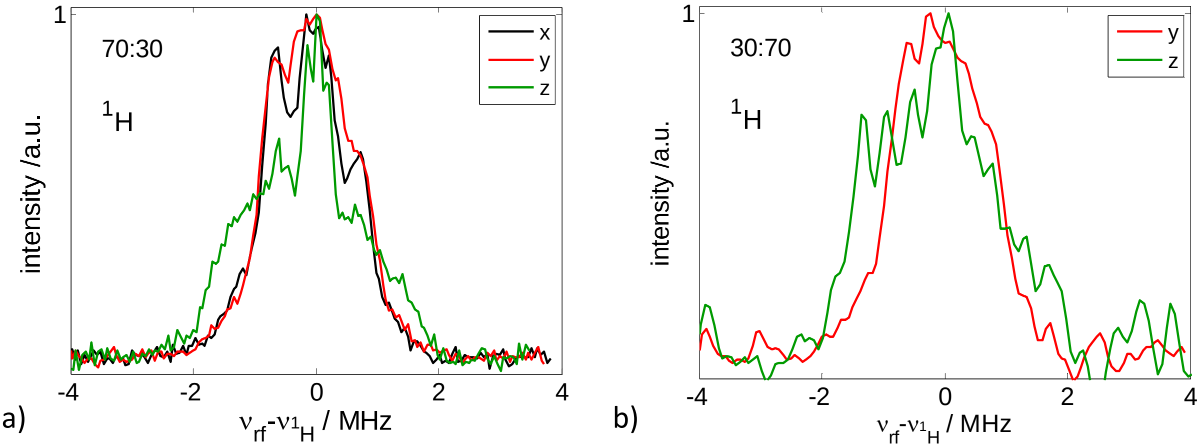

Figure 3.6 Orientation-selective ^{1}H Mims-ENDOR spectra of 2.5 mM Fremy's salt in frozen solution of $CH_3O\mathbf{D}/\mathbf{D}_2O$ with a volume mixture of a) *v*/*v*=70:30 (high methanol content x_M=0.49) and b) *v*/*v*=30:70 (low methanol content x_M=0.15). Spectra were recorded from the low-field turning point g_{xx} (black) to the high-field turning point g_{zz} (green) of the EPR spectrum. Experimental parameters: MW Frequency: 94.2 GHz, T: 20 K, MW $\pi/2$ pulse: 48 ns, τ: 172 ns, RF π pulse: 20 μs.

The largest hyperfine splitting observed in Mims-ENDOR spectra is ~4.2 MHz (at ±2.1 MHz) for ^{1}H and ~0.84 MHz (at ±0.42 MHz) for ^{2}H, both of which are still quite small (in particular when compared to the Davies ENDOR results presented later). No further splittings with larger hf couplings were observed in spectra recorded with wider rf sweep range.

- *Davies-ENDOR*

Davies ENDOR spectra were only recorded for the ^1H isotope and are shown in Figure 3.7 for the solvent mixtures with equal volume ratios *v/v*= 50:50 of methanol and water. Due to the weaker signal intensity (as compared to Mims ENDOR), it was impossible to record ^2H Davies ENDOR spectra within reasonable measurement time.

In Figure 3.7 a) the orientation-dependent ^1H-Davies ENDOR spectra for the solvent mixture $C\mathbf{D}_3OH/H_2O$ are shown, whereas Figure 3.7 b) displays the spectra for the mixture $CH_3O\mathbf{D}/\mathbf{D}_2O$. This means that exchangeable protons from the hydroxyl-group and water are monitored in (a) and the alkyl protons in (b).

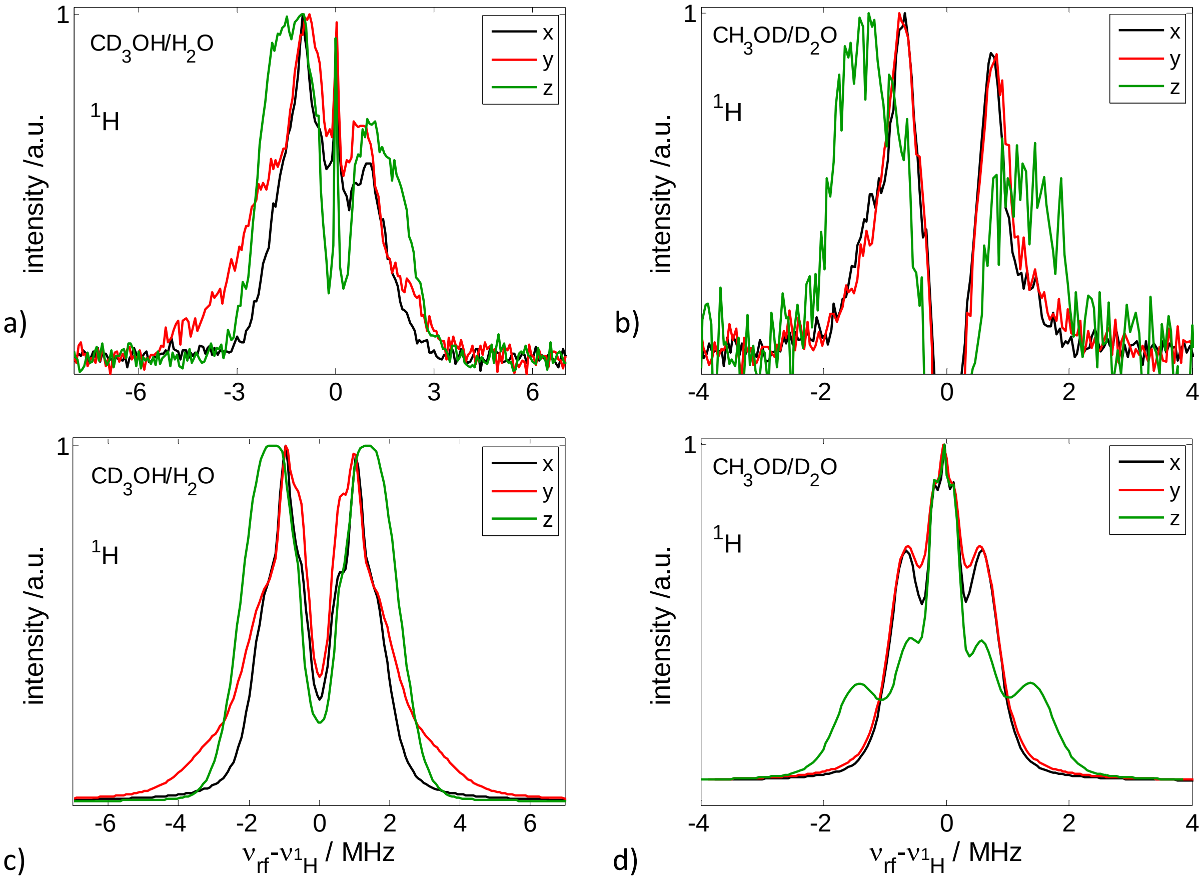

Figure 3.7 W-Band orientation-selective ^1H Davies-ENDOR spectra of 2.5 mM Fremy's salt in frozen solution of a) $C\mathbf{D}_3OH/H_2O$ and b) $CH_3O\mathbf{D}/\mathbf{D}_2O$. Both mixtures contain 50 vol.-% methanol. The spectra were recorded with the Davies ENDOR pulse sequence at field positions corresponding to the canonical values of the **g**-tensor g_{xx} (black), g_{yy} (red) and g_{zz} (green) as shown in Figure 3.2 a. Experimental parameters: T: 20 K, MW inversion pulse t_π= 200 ns, RF t_π= 20 μs, MW detection pulse $t_{\pi/2}$= 200 ns, τ= 548 ns. c) ^1H ENDOR simulation of exchangeable protons in the sample mixture $C\mathbf{D}_3OH/H_2O$, d) Simulation of methyl protons in the mixture $CH_3O\mathbf{D}/\mathbf{D}_2O$. The simulation in c) was performed without matrix protons, in d) they were included.

In Figure 3.7 a along the molecular x-axis (black spectrum) the coupling at ~±1.1 MHz (splitting= 2.2 MHz) is the most prominent feature in the spectrum. When changing the field position B_{ENDOR} to the molecular y-axis (red spectrum), this coupling is still observed but a second one at ~±2.5 MHz (splitting= 5 MHz), and a very broad flank that extends out to ~±6 MHz appear, too. When changing the field B_{ENDOR} to match the molecular z-orientation, the broad flank disappears again and the peaks at ~±2.5 MHz grow in intensity to now match the intensity of the peaks from the smallest splitting. In the ^{2}H Mims- ENDOR spectrum of the mixture $CH_3O\mathbf{D}/\mathbf{D}_2O$, that measures also exchangeable deuterons (Figure 3.5 c red line) these larger couplings found along the molecular y-position in Davies ENDOR spectra are also indicated, but the poor S/N ratio does not allow as precise an assignment as in the Davies- ENDOR case.

The situation is clearly different for the methyl protons. In this case (Figure 3.7 b), the proton hyperfine couplings along the molecular x- and y- directions are almost identical (a coupling of less than 2 MHz with peaks at ± 1 MHz), while a larger, relatively broad hf coupling grows in intensity when measuring along the molecular z-direction (splitting range of 2.5-4 MHz, the broad peaks are centered at ± 1.5 MHz). The spectra in Figure 3.7 b) suffer from a blind spot around the Larmor frequency, which makes it impossible to analyze small hf couplings. In fact, the ^{1}H Davies- ENDOR spectra (Figure 3.7 b) of the solvent mixture $CH_3O\mathbf{D}/\mathbf{D}_2O$ show the same features as the corresponding Mims- ENDOR spectra (Figure 3.5 d), but Davies- ENDOR spectra suffer from a "central" blind spot and Mims spectra from an "outer" blind spot, that scales down the largest hf coupling. This can be seen best at the molecular z-direction (green lines): In the Mims- ENDOR spectrum the outer flank reaches the baseline at ~±2.0 MHz, in the Davies at ~±2.4 MHz. This has direct consequences for the chosen simulation parameters, which is explained in the next Section.

- *ENDOR Simulation*

The chemically distinct methyl protons and exchangeable protons could be measured and hence also simulated individually. Since the ^{1}H Davies- ENDOR spectra for *exchangeable protons* $C\mathbf{D}_3OH/H_2O$ (Figure 3.7 a) show more distinct features than the respective Mims- ENDOR spectra (Figure 3.5 f) the former was chosen for the simulations. A set of couplings with independent line widths were defined and the **g**-tensor principal values were taken from the simulated EPR spectrum. For simulation of the ^{1}H ENDOR spectra (Figure 3.7 d) three proton couplings had to be assigned to fit the experimental results for the x- and z-positions. The matrix peak was neglected but can also be included with an isotropic hfc of 10^{-4} MHz. The pronounced feature in the experimental spectrum at the x-orientation is assigned to a hf coupling of $a_{iso}(1)$=1.13 MHz. The hf couplings $a_{iso}(2)$=2.04 MHz and $a_{iso}(3)$=3.04 MHz together describe the flank of the spectra. These couplings were found to be present in all three orientations with different weighting factors. Only the y- position could not be simulated successfully with these three hf couplings. As can be seen in the red spectrum in Figure 3.7 a, the very broad shoulder on the left wing requires an additional hf coupling. This was found to be a_{iso}(6)=6.20 MHz. This is by far the strongest coupling found in our measurements and simulations and is only present in this sample mixture and at the molecular y-position. The reason for not finding this coupling in the corresponding ^{1}H Mims ENDOR spectra is as follows: Assuming the maximum detectable hf coupling in Mims ENDOR to be A_{max}~1/(2τ) [25], with τ =172 ns one gets an approximate maximum detectable hf coupling of A_{max}~2.9 MHz for this experiment. Hence, this spectrum suffers from a blind spot at this value.

The blind spot in the Mims ENDOR spectra mostly affect the outer flank and the blind spot in the Davies ENDOR spectra affect the central region around the Larmor frequency. Therefore, the simulation of *methyl protons* $CH_3O\mathbf{D}/\mathbf{D}_2O$ was performed by combining both, spectral features from Davies- and Mims- ENDOR spectra that do not suffer from the blind spot behavior. This means that the small hf couplings (along the x- and y- molecular direction) were derived from the ^{1}H Mims ENDOR spectra (Figure 3.5 d black and red line) and the large hfc that becomes apparent at the molecular z-position from the corresponding ^{1}H Davies ENDOR spectrum (Figure 3.7 b green line). The parameters obtained from ENDOR simulation are summarized in Table 3.2.

Table 3.2 ENDOR simulation parameters for exchangeable –OH and methyl –CH_3 protons. If one value for the hyperfine coupling $\mathbf{A}$ is given, the simulation was performed with an isotropic hf coupling a_{iso}. If three values are given, the values represent the diagonal tensor elements A_{xx}, A_{yy} and A_{zz} of the hf tensor. Each proton (numbers 1-4) with the defined hf coupling $\mathbf{A}$ contributes the ENDOR spectrum at the position i (i=x,y,z) with the weighting factor f_i. Independent voigtian line widths were defined and ENDOR simulations were performed with the function 'salt' as implemented in the Easyspin package. The error of the hf coupling is ±0.2 MHz.

Exchangeable Protons -OH

No.	$\mathbf{A}$ /MHz	fx	fy	fz
1	1.13	0.25	0.24	0.04
2	2.04	0.27	0.13	0.07
3	3.04	0.48	0.45	0.89
4	6.02	-	0.17	-

Methyl Protons –CH_3

No.	$\mathbf{A}$ /MHz	fx	fy	fz
matrix	10^{-3}	0.06	0.03	0.05
1	0.33	0.25	0.25	0.28
2	1.22	0.56	0.64	0.34
3	-1.6,-1.6,3.2	0.13	0.08	0.33

For methyl protons, the small hf couplings were found to be nearly isotropic with a_{iso}(1)=0.33 MHz and a_{iso}(2)=1.22 MHz. The larger hf coupling was simulated with a purely anisotropic hfc $\mathbf{A}$ =$\mathbf{T}$=[-T, -T, 2T]=[-1.6, -1.6, 3.2] MHz ±0.2 MHz. From the component T=1.6 MHz a distance of r=3.5 Å ± 0.1 Å can be calculated within the point-dipole approximation.

In all ENDOR simulations it was found that convolution with a Gaussian and a Lorentzian function (Voigtian) with a larger Gaussian FWHM gives the best fits to the experimental spectra, indicating inhomogeneous broadening at all positions. Note that the asymmetry observed in the high-field ENDOR spectra may well stem from the cross- and/or nuclear-relaxation times being longer than the repetition times used in the experiments [173], which was not considered in the simulation.

3.3.3 HYSCORE Measurements

Hyperfine sublevel correlation (HYSCORE) experiments were recorded at X-Band (9.5 GHz, 20 K) at the maximum of the EPR spectrum for sample mixtures $CH_3O\mathbf{D}/\mathbf{D}_2O$ with a volume ratio of *v/v*= 50:50 and 70:30. Spectra were not analyzed quantitatively. HF couplings to ^1H and ^2H are very intense as expected. In the methanol rich solvent mixture (70:30) a signal at the potassium (^{39}K) Larmor frequency (a matrix line, see) is observed, while at equal volume ratio (50:50) no potassium signal appears (different τ values have been tested). The higher sensitivity of the HYSCORE experiment reveals this signal stemming from very weakly coupled potassium nuclei. No attempts have been made to detect the ^{39}K hf signal in an ENDOR measurement. These results suggest that in high methanol contents, the dissociated FS molecules may form ion pairs again.

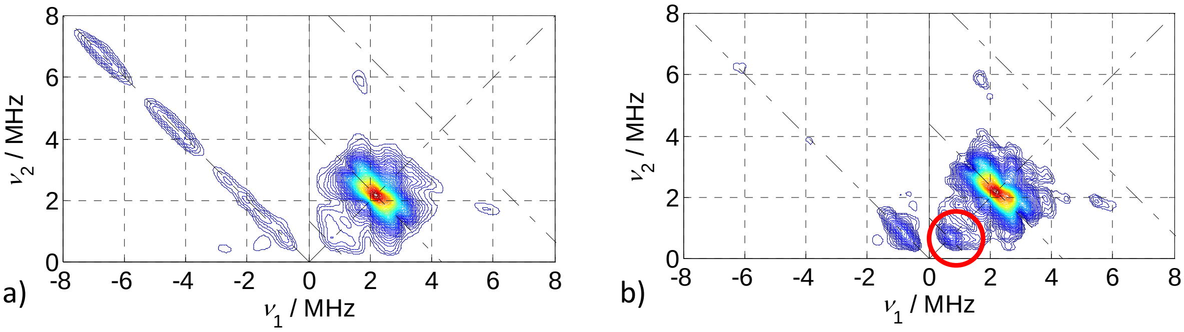

Figure 3.8 X-Band HYSCORE spectra of 2.5 mM Fremy's salt in $CH_3O\mathbf{D}/\mathbf{D}_2O$ mixtures of different volume ratios taken at the center of the EPR spectrum at 20 K. a) $CH_3O\mathbf{D}/\mathbf{D}_2O$ *v/v*=50:50, b) $CH_3O\mathbf{D}/\mathbf{D}_2O$ *v/v*=70:30. The dotted antidiagonal lines mark the Larmor frequency of ^{39}K, ^2H and $2x^2H$ at the measured field positions. Experimental parameters: τ= 448 ns, $\tau_{\pi/2}$ = tπ = 16 ns, a) B_0=331.54 mT, b) B_0=331.58 mT. The red circle marks the ^{39}K coupling (0.66 MHz).

3.4 Molecular Dynamics Simulation

The solvation of the nitrosodisulfonate anion by water and methanol was modeled computationally by means of molecular dynamics simulations using classical force fields. A trajectory of 10 ns duration was generated at a temperature of 300 K to extensively sample the available phase space for this binary solvent mixture. The low-temperature solvation configurations corresponding to the experimental situation were obtained by repeatedly annealing snapshots (200 in total) which were extracted from the 300 K-trajectory at regular intervals. More details about the simulation can be found in Section 2.8.

In the optimized geometry of Fremy’s salt dianion (Figure 3.10 a) a small deviation from a planar hybridization geometry at the nitrogen atom is found with a N-O bond length of 1.283Å. This is in excellent agreement with the 1.284 Å found by X-Ray diffraction [174].

For ionic solutes, the question of ion pairing in a given solvent is often a matter of concern. Thus, we have monitored the distances between the K^+- ions and the dianion in our simulations. In the initial configuration of the system, the dianionic salt was set up as a tight ion pair with the two potassium cations. Within 400 ps, both cations diffused away to a distance of 9 Å from the salt. Only four times during the whole trajectory of 10 ns, a potassium ion diffused back to the dianion. The lifetime of this ion pair never exceeded 100 ps. Thus, ion pairing is unlikely to be a significant issue in this system, especially when considering that our simulated concentration of 25 mM is about 10-fold higher than in experiment. Interestingly, this corresponds well with hyperfine sublevel correlation (HYSCORE) spectroscopy (Figure 3.8) in which hyperfine interaction between the radical and ^{39}K was only observed with larger volume ratios of methanol.

Three distinct types of protons can be analyzed with respect to their interactions with Fremy's salt: The water protons, the methanol hydroxyl (or alcohol) protons, and the hydrophobic protons of the methyl group. In principle, all sulfonate oxygens and the nitroxide oxygen in Fremy's salt can interact as hydrogen bond acceptors with the solvent. Table 3.3 lists the coordination numbers of the of the acceptor oxygens of the solvated anion obtained by integrating the corresponding radial distribution functions (RDF) $g_{OH}(r)$ up to the first minimum. Each of the electron rich sulfonate oxygens is fully solvated with two hydrogen bonds. In contrast to this, the nitroxide oxygen has a coordination number of only 0.75. This reflects the fact that this oxygen is sterically almost inaccessible, being flanked from both sides with sulfonate groups. This effect is also observable directly from the RDFs (data not shown).

Table 3.3 Calculated coordination numbers for the different oxygen species present in Fremy's salt.

	$\mathbf{H}_2O$	$\mathbf{H}O\text{-}CH_3$
Sulfonate-Oxygen	1.55	0.47
Nitroxide-Oxygen	0.62	0.13

The coordination of the nitroxide oxygen by water protons is almost five times larger than that by methanol, which approximately equals the statistical proton ratio in our simulation box (4.49). The slight preference for water solvation relative to the statistical ratio is probably due to the smaller size of the water molecules, in combination with the previously mentioned sterical hindrance by the sulfonate groups.

In order to gain further insight into the solvent structure, we have plotted the angular distribution functions of the different proton species relative to the NO bond in Figure 3.9. The angle θ is measured between the NO bond axis and the vector pointing from the NO bond center to the solvating proton. For the calculation of these angular distribution functions, solvent protons up to a certain radial cutoff value were considered; the plots in figure 5 show distribution functions for four different cutoff values.

Regarding the hydrophobic protons, there is a clear preference for θ= 90° at short distances (up to 3 Å), which corresponds to the area above the molecular plane. There is virtually no density in the direction of the NO-bond (θ= 0°) because the size of the methyl group results in a strong sterical hindrance. At 3.5 Å, the angular distribution has reached an almost uniform shape.

Regarding the water protons, we observe only little differences in the amplitudes of the distribution functions at small angles θ< 50° between cutoff values of 2.5..3.0 Å. This indicates that most of the hydrogen-bonding protons are located at distances shorter than 2.5 Å relative to the NO bond center. At a cutoff of 3.0 Å, a strong peak at θ= 60° appears, which can be attributed to the solvation of the sulfonate groups. Both these features are also found for the alcoholic hydrogen, except that the distribution function vanishes for very small angles θ< 15°. This illustrates again the sterical hindrance caused by the bulky sulfonates and possibly also the methyl group of methanol.

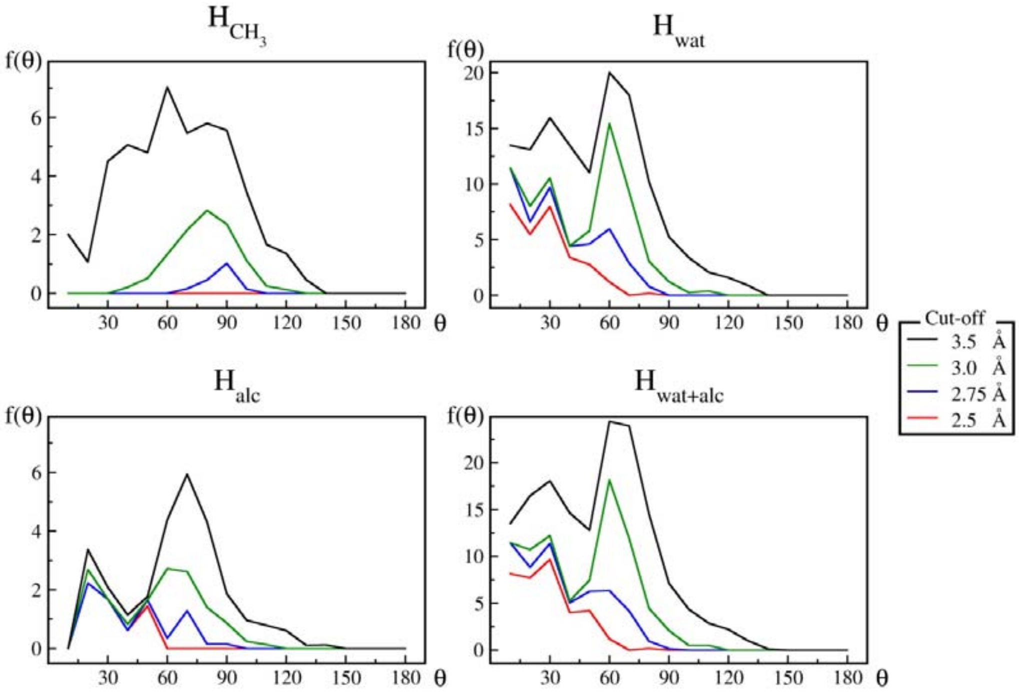

Figure 3.9 Angular distribution functions of the different proton species relative to the NO bond (water proton: H_{wat}, alcoholic proton: H_{alc}, methyl proton: H_{met}, exchangeable protons: H_{wat}+H_{alc}). The angle θ is measured between the NO bond axis and the vector pointing from the NO bond center to the solvating proton. In each plot, protons up to a four different radial cutoff value were considered.

It should be noted that up to 3.5 Å, an approach from θ= 180 is sterically impossible for all solvent protons.

3.5 Discussion

The solvation shell around Fremy’s salt dianions

When discussing the combined ENDOR and MD results one should always be aware that the ENDOR measurements depict a complete ensemble of ~10^{15} Fremy’s salt ions and their solvation shells in the solvent mixtures. Since it is highly unlikely that all FS molecules have the exact same solvation shell, the observable splitting shown in Figure 3.5 and Figure 3.7 and their respective simulations only represent a part of the ensemble. Hence, one main source of spectroscopic information is the interpretation of differences between the ENDOR and MD data of exchangeable and methyl protons.

When a solute ion such as Fremy’s salt is added to a methanol/water mixture, it is reasonable to assume distortion of the hydrogen-bonded network as a response to the existence of the solute ion. Water is a two H-bond donor and two H-bond acceptor, whereas methanol with its single hydroxyl H-atom is only a single H-bond donor and (theoretically) a two H-bond acceptor. By dissolving Fremy’s salt, the two sulfonate groups of Fremy’s salt will act mainly as hydrogen-bond acceptors, which force some molecules of water into close contact also with the N-O. This can be seen in the ^{1}H Davies- ENDOR spectra for the y-orientation (Figure 3.7 a, red spectrum). Thus, the biggest proton hf coupling with $a_{iso}(6)$=6.20 MHz can be assigned to hydrogen-bonded water at the sulfonate groups, which would approach the NO-group closest, when it is hydrogen-bonded to one of the adjacent sulfonate groups. The ENDOR measurements are in agreement with the MD simulation that found a coordination number of two for the sulfonate oxygen atoms and the closest approach (down to 2.2 Å) by water and methanol-OH protons to the NO-group at small angles (Figure 3.9). Interestingly, results from Mims and Davies ENDOR measurements along the x-position suggest that the N-O bond is not involved in (too many) hydrogen bonds, although EPR simulations indicate that a g-strain in the x-direction might be possible (Figure 3.4). Of course, statistically seen there will be some molecules that are hydrogen-bonded along N-O···H-OH, but by summation over the small amount of selected orientations this small number of H-bonded molecules is not enough to notably contribute to an ENDOR signal. This result also manifests itself in the MD simulations. The coordination number for the nitroxide group is much smaller than for the sulfonate groups, showing less hydrogen bonds along the molecular x-axis. When inspecting the low-field region of the ESE-detected EPR spectra of the different samples, we only observed a shift of the g_{xx}-value in the water rich solvent mixture with 70 vol. % water. Due to the smaller size of water compared to methanol it may approach the NO-group closer and the hydrogen-bond capability is much higher for water. The other two solvent compositions (50- and 70 vol.% MeOH) show no shifts, which indicates that the hydrogen bonding to the NO-group is similar for both.

The respective methyl proton splittings in the solvent mixtures show the same features for Mims (Figure 3.5 d) and Davies (Figure 3.7 b) ENDOR measurements. Here, two smaller hfc are found at each molecular orientation and are assigned to more distant methanol molecules for which and we cannot get distance orientation information. From the largest hfc, which arises along the molecular z-axis (parallel to the SOMO) and can be simulated purely anisotropically, a distance of 3.5 Å ± 0.1 Å can be extracted. Thus, methyl protons approach closest from "bottom" and "top" of the Fremy's salt molecule's (approximate) plane spanned by O-N-$(S)_2$.

Using a sum of the proton "densities" from an ensemble of snapshots from the MD simulations one can not only visualize but also understand the results of the MD simulations and the ENDOR experiments (Figure 3.5, Figure 3.7) and draw a molecular picture of the solvation around FS. Figure 3.10 b shows the chemically different types of protons around the probe molecule (hydrophobic methyl protons: green, exchangeable protons from water and the hydroxyl-group: cyan). The shortest distance for methyl protons is 2.8 Å along the SOMO of the nitrogen atom. The ENDOR experiments were performed at 20 K, where methyl group rotation is still active [175] and the three equivalent protons contribute to an averaged ^{1}H signal. Taking a CH bond length of 1.093 Å and a HCH angle of 109.3° [176], one can calculate that the distance from the center of the

NO group to the "averaged" proton is 1.03 Å longer than the distance to the closest proton (assuming that this closest proton is pointing towards the NO group). Since in pulse ENDOR experiments one measures an averaged proton-electron distance and setting the closest proton-electron distance to 2.8 Å, as found by MD simulation, one gets an averaged distance of 3.8 ± 0.1 Å for the experiments, which is - considering the broad ensemble of solvation situations - in good agreement with the 3.5 Å found in the ENDOR experiments.

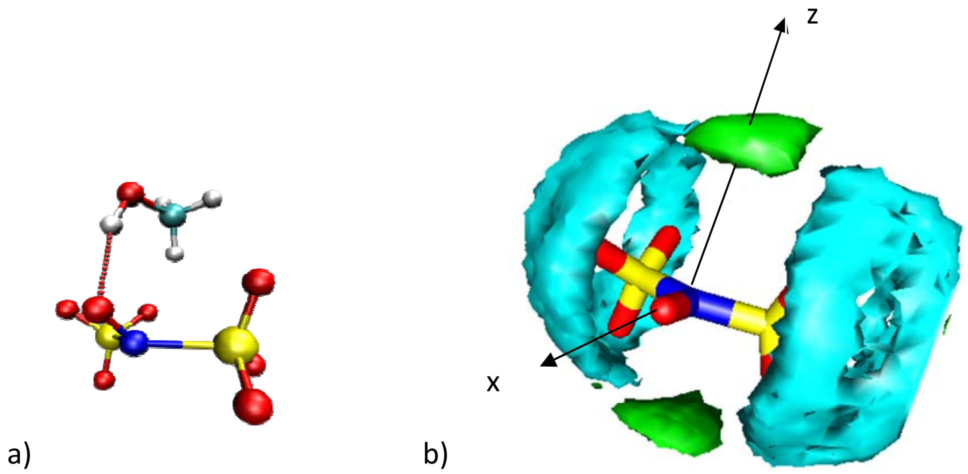

Figure 3.10 Solvated Fremy's salt. Nitrogen atoms are shown in blue, sulfur atoms in yellow and oxygen atoms in red. a) Simulation snapshot from the MD run showing a situation in which one methanol-OH-group is hydrogen-bonded to the NO-group. b) Isosurface of the spatial distribution function of the exchangeable protons (cyan), and hydrophobic methyl protons (green) in CH_3OH/H_2O (*v*/*v*=50:50). Along the z-axis of the molecular frame methyl protons are accumulated, whereas the charged sulfonate groups are strongly hydrogen-bonded. A cut off of 3 Å was used for this picture.

The preferential arrangement of the methyl groups above and below the NO-bond is due to two forces: First, in this way the strong H-bonded network around the two sulfonate groups (as seen in the MD simulations) is less disturbed. Methanol can act as one H-bond donor, and if the methanol-OH group is H-bonded to one of the highly hydrophilic sulfonate groups, having the methyl group at the sulfonate group (and hence reducing the number of H-bonds) would be energetically unfavorable. The second argument is of steric nature, the largest "free" space for the bulky methyl groups is then simply at these positions of the molecule due to the sulfonate groups. Thus, this specific solvation situation is found to be due to an interplay between electrostatic, hydrogen-bonding, and steric effects.

The microheterogenity of the binary solvent structure without solute molecules can be assumed to be highly similar in all our cases. As proposed by Zhao et al. [141] all our tested methanol molar ratios are in a composition region, in which methanol-water associates of one molecule methanol with two molecules of water have been observed by IR spectroscopy for the pure binary mixture [141]. When considering our experimental findings this indicates that also in the case with solute molecules, the same solvation characteristics are found for all volume ratios studied here. This, in turn, suggests that in a broad range of compositions, the solute molecules FS (or many of them, at least) "forces" the water and methanol molecules into a solvation shell that resembles the one found in our study and depicted in Figure 3.10 b.

Comparing EPR spectroscopy with other methods to study solvation

In literature many experimental techniques have been applied to study the problem of ion solvation in mixed solvents. Among them a well-established method is the use of solvatochromic dyes [85, 177-180]. Such dyes are usually big molecules with an extended π-electron system like pyrene. The longest-wavelength band of these compounds that is due to a charge-transfer transition within the solvated species (cybotactic region) is very sensitive towards a change in the immediate environment of the solute caused by a variation of the solvent. Measurement of absorption spectra (UV/VIS and near-IR) allow calculating the transition energy E_{12} which provides information about the composition of this (micro-)region. Such measurements are easy to perform and do not need high technical requirements. To assure pure solvent-solute interactions typically concentration regions for the dye are between 10^{-4}-10^{-5} M. At higher concentration the aromatic dyes may have also stacking tendencies. This concentration range is also accessible with EPR spectroscopy, but even higher concentration up to 10^{-3} M may be studied and potential EPR probes are much smaller compared to aromatic dyes. In fact all spectroscopic techniques (NMR, Raman, IR, UV/VIS) are sensitive to micro-environmental changes of a probe molecule, e.g H-bond formation upon addition of water and yield dynamic and structural aspects of the solvation sphere. ENDOR spectroscopy offers a big benefit to study preferential solvation compared to other spectroscopic techniques: The possibility to get spatial information around the probe molecule. Similar information can only be obtained by computer simulation [86, 88, 92, 94], where the exact pair correlation functions can be calculated for each nuclei of a solvent molecule. The only experimental methods that yield pair correlation functions are diffraction techniques [181]. These methods (e.g. neutron diffraction) are very powerful in terms of exact distance information between two nuclei but the obtained data is not always straight forward to interpret and require proper fitting and correct models to deduce structural information besides the drawback of the high technical requirements [181]. Thus, the combination of isotope substitution with high-field EPR/ ENDOR spectroscopy offers a versatile tool to study solvation of paramagnetic ions even with low g-anisotropy (like it is usual for organic radicals). With EPR we get exact information about the immediate surroundings, the first salvation shells of the ensemble of paramagnetic centers. Structural information about the bulk solvent regions in the system is not available with this method. Hydrogen bonds towards the nitroxide NO-group can be monitored upon solvent composition in the high-field EPR spectra since the value of g_{xx} and A_{zz} are affected by solvent polarity [102-104]. The spatial solvent distribution around the probe molecule along its molecular coordinates can be obtained by orientation-selective ENDOR spectroscopy.

3.6 Conclusion and Outlook

The molecular picture of the solvation around Fremy's salt in a 50:50 (*v/v*) mixture of methanol and water, which is derived from the MD simulations is in full agreement with the ENDOR results, as shown in Figure 3.10 b. Both exchangeable species (water and hydroxyl protons) are able to establish hydrogen bonds to the dianion, with an angular distribution that reflects the sterical hindrance of the nitroxide NO acceptor site by the sulfonate groups. Hence, exchangeable protons come in closest contact with the NO moiety along the molecular y-axis of the probe molecule. Thus, the preferential arrangement of methyl groups along the molecular z-direction of the nitroxide can be explained by the interplay of *electrostatic forces and hydrogen-bonding* (H-bonds around sulfonate groups) as well as *steric* (bulky methyl group) effects: If the methanol-OH group (instead of water) is hydrogen-bonded to the sulfonate groups, it is energetically favorable to *not* place the methyl group at the sulfonate group, as this would disturb the existing H-bond network and reduce the number of H-bonds. It is thus favorable to place the methyl groups on the "top" and the "bottom" of the (approximate) plane spanned by O-N-$(S)_2$. Also, the largest "free" space for the methyl groups is given at these positions of the molecule due to the bulky sulfonate groups.

The elucidation of the microscopic solvation of a small probe molecule in binary solvent mixtures represents the first step for understanding the interactions in more complex biochemical systems. In particular this includes the potential perturbation of H-bond network due to presence of a spin probe.

Further work on variable mixing time (VMT) ENDOR [63, 182] is of interest to get information about the sign of the hyperfine coupling, which is important for the unambiguous determination of the isotropic and anisotropic parts of the interaction. This approach of high-field ENDOR together with isotope substituted protons can easily be extended to other solvents and solute molecules and of course to other nuclei of interest.

4 Polyelectrolyte Solutions with Multivalent Salts

Polyelectrolytes (PEL) are water soluble macromolecules that carry ionic or ionizable monomeric units and can either be of natural (e.g. nucleic acids, DNA) or synthetic origin. Analogous to small electrolytes they can be divided into strong (complete dissociation) and weak (pH dependent dissociation) polyelectrolytes. Nonetheless, they cannot be understood as a simple superposition of electrolyte and polymer properties. The scaling approaches which were successful in elucidating the properties of non-ionic polymers have, so far, failed to provide full explanation of PELs behavior. While excluded volume effects are important interactions for neutral polymers, the long-range Coulomb interaction in PEL give rise to critical exponents [16] (see Section 4.1.1). First, the gain in entropy upon release of counterions leads to highly charged polymers, and electrostatic repulsion among the charged repeating units leads to an extended conformation of the polyelectrolyte. Second, PELs are usually dissolved in water, which are poor solvents for polymer backbone, which leads to favored polymer-polymer interaction (attractive hydrophobic interaction) and thus to a more collapsed structure [16].

It is known that the screening of intramolecular electrostatic repulsion by oppositely charged counterions can lead to dominance of hydrophobic attraction and thus to more collapsed, or pearls-necklage [183] conformations. In contrast to monovalent counterions, divalent ions may act as a inter- or intramolecular bridge.

In the first section a theoretical basis for the description of polymer conformations is given, followed by an introduction to the theory of simple, strong electrolytes starting from the Poisson-Boltzmann equation.

4.1 Polymers in Solution

The aim of this chapter is the review of the theoretical background used for interpretation of experimental data. In the first paragraph the principle chain models in polymer physics and important parameters that describe (neutral) polymers in solution are introduced while in the second paragraph the fundamental electrostatic interactions are reviewed. For a sophisticated treatment the reader is referred to basic text books in polymer physics [183-185]. Here, only a short overview is given.

4.1.1 Description of Polymer Shape in Solution

Flexible polymers in solution can adopt a number of different configurations. Thus, their size and shape can be understood only statistically. The quantities used characterize the size of chains are the mean square end-to-end distance $\langle R^2 \rangle$, the mean square radius of gyration $\langle R_g^2 \rangle$, and the contour length l_c (see Figure 4.1).

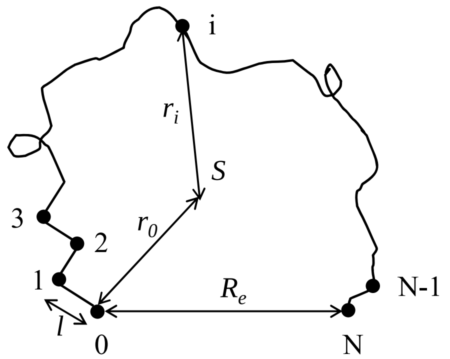

Figure 4.1 Scheme of a linear polymer chain with end-to-end distance R_e, center of mass S, spacing between two repeating units l and vector r_i connecting S with the i-th repeat unit.

The end-to-end distance $\langle R^2 \rangle$ is the mean distance between the two ends of the chain and its form is dependent on the model used to describe the average repeat unit distribution. Its advantage is the simplified number one obtains even for complicated polymer architectures like star shaped molecules.

The mean square radius of gyration $\langle R_g^2 \rangle$ is defined as the mean square distance of all segments r_i from the center of the mass of the chain S:

$$\langle R_g^2 \rangle = \frac{1}{N} \sum_{i=1}^{N} \langle r_i^2 \rangle \tag{4.1}$$

This is a quantity, which can be obtained experimentally by light scattering. Finally, the contour length l_c is the largest possible end-to-end distance as defined by the product of the number of bonds between the monomer units and the length that is projected onto the contour of the macromolecule.

- *Chain models*

For the description of the shape of macromolecules in solution different models ('chain models') have been developed. The simplest model is the *Freely Jointed Chain* (FJC) model - or Kuhn segment model - which is applicable on length scales above approximately 1 nm [184]. It is a simple chain model in which the bond vectors connecting successive segments are constrained to have a fixed length b, but the orientations of M bond vectors are distributed randomly, i.e. any angles between two segments is acceptable. Note, that the term 'segments' is not necessarily identical with the number N of chemical monomeric units. On short length scales of ~1 nm this model oversimplifies the bonding and steric constraints of real polymers since it incorporates only the *local* bonding rigidity over the

distance b. However on larger length scales ~5-10 nm, real flexible polymers in the ideal state exhibit a scaling behavior consistent with the freely jointed chain [184].
The mean square end-to-end distance for the FJC with the constant segment length l is:

$$\langle R^2 \rangle = M a_k^2 \tag{4.2}$$

With the statistical segment length a_k:

$$a_k = \frac{\langle R^2 \rangle}{l_c} \tag{4.3}$$

In solution, the mobility of the different segments makes it necessary to average over all conformations.

We can extend the FJC model and consider fixed valence (torsion) angles. In this case free rotation around the connection axes prevails and the end-to-end distance becomes larger due to fixed connection angles:

$$\langle R^2 \rangle = M l^2 \frac{1 + cos\theta}{1 - cos\theta}, \tag{4.4}$$

where θ is the valence angle and l is the monomer length. This model is called *Freely Rotating Chain* (FRC) model.

A further refinement of this model takes into account a hindered rotation around the connection axis as it is caused by steric effects of substitutents (side chain effects), which energetically favors certain rotation angles. An important quantity to describe the decay of correlation of bond vectors along the polymer chain is the persistence segment s_p:

$$s_p = -\frac{1}{\ln{(cos\theta)}}. \tag{4.5}$$

The *Worm Like Chain* (WLC or Kratky-Porod [18]) model is a special case of the FRC model assuming small bond angles, i.e. $\theta \ll 1$. This model is applicable to stiff polymers e.g. in liquid crystals, conjugated polymers and biological systems (DNA) where the macromolecules resemble rigid rods and not random coils. The WLC model will be of utmost importance for the description of PEL since the electrostatic repulsion in highly charged PEL increases the stiffness along the polymer backbone.

The persistence length l_p is the fundamental parameter in the WLC model that determines the stiffness of the chain. It is derived from the persistence segment in eq. (4.5) for small bond angles $\theta \ll 1$. Expansion of the cosine in a power series leads to:

$$s_p = -\frac{1}{\ln(cos\theta)} \approx \frac{2}{\theta^2}, \tag{4.6}$$

And the intrinsic persistence length l_p due to monomer structure and non-electrostatic interactions of the polymer is:

$$l_p = s_p l \approx l\frac{2}{\theta^2}. \tag{4.7}$$

It can be evaluated as the length scale at which the mean scalar product of the tangent vectors of the bond angles has decayed to $1/e$.

With the WLC model it is possible to describe the statistical mechanics of ideal polymers with a range of backbone flexibilities within the two limiting cases of the Gaussian coil and the rigid rod.

Going from ideal to real polymer chains one has to account for the intrinsic volume that each monomeric unit needs in space and by allowing interactions between the monomers if they come close to each other (short-range interaction). Such interactions lead to an increased coil size than that of an ideal chain and the effect is called *excluded volume effect*. In real polymers the nature of the excluded volume interference includes steric effects, van der Waals attraction between polymer segments and polymer-solvent and solvent-solvent interactions.

- *Solvent quality*

One of the most important concepts introduced by de Gennes [186] is the finding that the dependence of many physical quantities on the chain length N can be represented in form of an universal scaling law. The dependence for the average chain size is given by:

$$\langle R^2\rangle^{1/2}, \langle R_g^2\rangle^{1/2} \propto N^\nu, \tag{4.8}$$

with the critical indices

$$\begin{array}{ll} \nu = 1/3 & T < \Theta \\ \nu = 1/2 & T = \Theta \\ \nu = 0.588 & T > \Theta \end{array}$$

In Θ-solvents (or at the Θ-temperature) the chain shows ideal behavior where monomer attraction and hard-core repulsion cancel each other. Below the Θ-temperature (i.e. in poor solvents) the monomer-monomer attraction is significantly stronger than monomer-solvent interactions, which leads to a negative excluded volume and a more collapsed chain conformation (coil-to-globule transition). Finally, in good solvents monomer-monomer and monomer-solvent attraction are energetically almost similar and the excluded volume is positive but reduced as compared to the hard-core potential, which leads to a swollen chain conformation.

- *Concentration regimes*

The concentration regimes for polymers can be divided into three parts: dilute, semidilute and concentrated. In this work semidilute to dilute solutions were used in the experiments. In dilute solutions the concentration is low enough that the polymer coils are well separated from each other, which allows the characterization of a single polymer chain (see Figure 4.2 a). Each polymer occupies a region with a Flory- radius of $R_F \propto \langle R^2 \rangle^{1/2}$. The intermolecular interactions between the chains are weak and the solution can be described as nonideal gas of polymer coils. As the concentration is increased the coils come closer to each other and start to influence each other (see Figure 4.2 b).

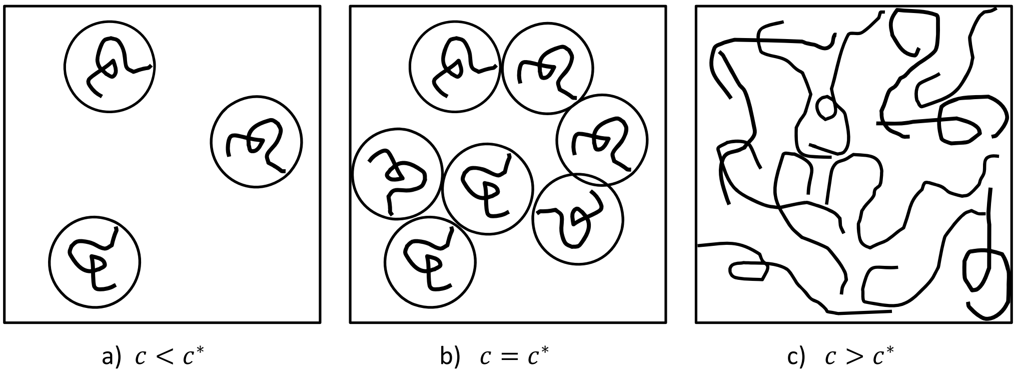
a) $c < c^*$ b) $c = c^*$ c) $c > c^*$

Figure 4.2 Schematic presentation of a dilute solution (a), a solution at overlap concentration (b) and semidilute solution (c).

The overlap concentration c^* is this concentration at which the polymer coils come into contact and is given by:

$$c^* = \frac{3M}{4\pi R_g^2 N_A}, \tag{4.9}$$

with M the molecular weight and N_A Avogadro's constant.

This classification is applicable to neutral polymers, but bears some problems for PELs, where due to long-range correlations the molecules interact even at very low concentrations [16]. Hence, PELs solutions are usually classified as semi-dilute even when there are no significant entanglements of the chains.

4.1.2 Polylelectrolytes in Solution

The electrostatic interaction of polyions in aqueous monovalent salt solutions can be described by classical mean-field theory of electrostatic interaction, the Poissson-Boltzmann (PB) equation which is discussed in the following section.

4.1.2.1 Poisson-Boltzmann Theory

The Poisson-Boltzmann (PB) equation can be derived from the Poisson equation that connects the electrostatic potential $\psi(r)$ with the charge density $\rho(r)$ according to:

$$\nabla^2\psi(r) = -\frac{1}{\varepsilon}\rho(r)\,, \tag{4.10}$$

with ε the dielectric constant of the solution. At any point within the potential$\psi(r)$ the electrostatic energy of an ion is determined by $eZ\psi(r)$, with e the electrical charge and Z the valence of the ion. The probability to find this ion within the potential is proportional to the Boltzmann factor $\exp\left(-eZ\psi(r)/k_BT\right)$. Hence, the charge density $\rho(r)$ in eq. (4.10) can be written as:

$$\begin{aligned} \rho(r) &= \rho_m(r) + eZc_0e^{-eZ\psi(r)/k_BT} - eZc_0e^{+eZ\psi(r)/k_BT} \\ &= \rho_m(r) - 2eZc_0 sinh\left(\frac{eZ\psi(r)}{k_BT}\right) \end{aligned} \tag{4.11}$$

Where ρ_m is the immobilized charge density of the macroion and c_0 the salt concentration for vanishing potential. Combining eq. (4.10) and (4.11) yields the classical non-linear Poisson-Boltzmann equation:

$$\nabla^2\psi(r) = \frac{2eZc_0}{\varepsilon} sinh\left(\frac{eZ\psi(r)}{k_BT}\right) - \frac{1}{\varepsilon}\rho_m(r) \tag{4.12}$$

The mean field approximation assumes point-like ions in thermodynamic equilibrium. Contributions from fluctuations as well as ion correlation effects are neglected. The PB equation (4.12) can only be solved exactly for a charged planar surface while for other geometries the equation can be solved within the Debye-Hückel approximation.

4.1.2.2 Debye-Hückel Approximation

In the Debye-Hückel (DH) regime the electrostatic interaction is smaller than the thermal energy. For this low potential $eZ\psi(r) < k_B T$, the charge density $\rho(r)$ in eq. (4.11) can be described by a Taylor expansion

$$\begin{aligned}\rho(r) &= \sum_i c_{0,i} e Z_i e^{-eZ_i\psi(r)/k_B T} + \rho_m(r) \\ &= \sum_{\substack{i \\ 0,m_+,m_-}} c_{0,i} e Z_i - \sum_i c_{0,i} e^2 Z_i^2 \frac{\psi(r)}{k_B T} + \rho_m(r)\end{aligned} \tag{4.13}$$

such that the PB equation (4.12) can be linearized to the Debye-Hückel equation:

$$\begin{aligned}\nabla^2\psi(r) &= \frac{e^2}{\varepsilon k_B T}\sum_i c_{0,i} Z_i^2 \psi(r) - \frac{1}{\varepsilon}\rho(r) \\ &= k^2\psi(r) - \frac{1}{\varepsilon}\rho(r)\end{aligned} \tag{4.14}$$

where the Debye screening length $k^{-1} = \lambda_D$ appears as a characteristical decay length of the potential and quantifies the range of an electrostatic potential of an ion in an ensemble of small ions (i.e. the distance at which the Coulomb interaction becomes screened by the surrounding ions). The Debye length is thereby defined by

$$\lambda_D = k^{-1} = \left(\frac{\varepsilon k_B T}{2e^2 I}\right)^{1/2} = (8\pi\lambda_B I)^{-1/2} \tag{4.15}$$

I is the ionic strength and λ_B the Bjerrum length, where $I = 1/2\sum_i c_{o,i} Z_i^2 = Z^2 c_0$ and $\lambda_B = e^2/(4\pi\varepsilon k_B T)$. The Bjerrum length is defined as the length at which the electrostatic interaction between elementary charges e equals the thermal energy $k_B T$. In water $\lambda_B \approx 0.7\ nm$ [184].

One has to solve the full non-linear PB equation (4.12) if the electrostatic potential becomes larger than $k_B T$. On the other hand it was shown, that the Debye-Hückel approximation is valid for a wide range of salt concentrations.

4.1.2.3 Counterion Condensation

In the presence of monovalent salt ions in solution, the situation of a macroion containing a charge Ze can be considered as follows: Let the number of ions that lie at a certain distance from the macroion be Z'. In this region the DH approximation is still valid. However, the remaining ions $(Z - Z')$ are condensed on the macroion having a local concentration that is higher than in the surrounding salt concentration. Hence, the effective charge of the macroion becomes screened to $Z'e$ [187].

An important parameter for counterion condensation is the dimensionless charge density (that is also known as Manning parameter ξ_M) which is defined as:

$$\xi_M = \frac{\lambda_B d_0}{e} = \frac{\lambda_B}{b}. \tag{4.16}$$

This parameter defines the ratio of electrostatic energy $eZ\psi$ to thermal energy k_BT. For a cylindrical geometry of a PEL with one charge per unit length $d_0 = e/b$ (b is the spacing per elementary charge along the chain), a certain amount of ions condense on the charged cylinder. This will reduce d_0 to $d_0 = \beta d_c$ with $0 \leq \beta \leq 1$, the fraction of free counterions and can be correlated to the Manning parameter [188]:

$$\begin{gathered} \xi_M < \frac{1}{Z_i} \Rightarrow \beta \to 1, d_c = d_0 \\ \xi_M \geq \frac{1}{Z_i} \Rightarrow \beta \to \frac{1}{\xi_M}, d_c = \beta d_0 = \frac{e}{\lambda_B} \end{gathered} \tag{4.17}$$

Thus, counterion condensation is observed for $\xi_M \geq 1/Z_i$ and the condensation threshold decreases with the valence of the counterion, i.e. multivalent counterions are always preferred to monovalent ions and may expel the latter from the condensed state. This effect is entropy driven since the condensation of a z-valent ion releases z monovalent ions.

As mentioned above, the electrostatic repulsion in PELs leads to an increased value of the persistence length l_p, that can be described by the Odijk, Skolnick and Fixman (OSF) theory [189-190]:

$$l_p = l_{p,0} + l_{p,e} \tag{4.18}$$

with $l_{p,0}$ the persistence length of a hypotethical neutral polymer (intrinsic persistence length) and $l_{p,e}$ the electrostatic contribution, as illustrated in Figure 4.3.

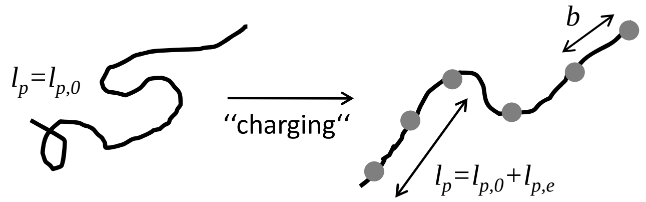

Figure 4.3 Scheme of the OSF model that describes the transition from a hypothetical neutral polymer to its analog macroion with equally spaced charges. The spacing distance between the charges is b.

In this picture the PEL chain is described by the WLC model near the rigid-rod limit but with significant bending at long length scales due to a screened exponential Coulomb potential. The electrostatic persistence length $l_{p,e}$ is given by:

$$\begin{aligned} l_{p,e} &= \frac{\lambda_D^2}{4\lambda_B} \propto \frac{1}{I}; \qquad \xi_M \geq \frac{1}{Z_i}\ (\lambda_B \geq b) \\ l_{p,e} &= \frac{\lambda_B \lambda_D^2}{4b^2} \propto \frac{1}{I}; \qquad \xi_M < \frac{1}{Z_i}\ (\lambda_B < b) \end{aligned} \tag{4.19}$$

For high salt concentration the intrinsic persistence length $l_{p,0}$ dominates, since $l_{p,e}$ decreases with increasing ionic strength. However, the linear dependence given in eq. (4.19) is verified only for PELs that already have an intrinsic stiffness in their polymer backbone. For flexible PELs most experiments [191-192] suggest a square-root relation of the ionic strength $l_{p,e} \propto I^{1/2}$.

At this point it should be mentioned that one has to be aware about the sensitive length scales of the EPR methods employed. In the case of DEER under the experimental conditions here, this length scale is up to ~5 nm. Hence, long-range interactions do not directly influence accessible parameters and the assumptions made for PEL conformations does *only* hold for the EPR length scale and can therefore be viewed as giving a local conformation rather than the averaged conformation of a whole macromolecule in solution as obtained by light scattering (where the hydrodynamic radius R_H is measured).

4.2 Studied Systems

In this work a statistically labeled strong PEL poly(diallyldimethylammonium chloride) (PDADMAC, Figure 4.4) was studied, that plays an indispensable part in modern technology of public water treatment [193]. The EPR measurements were carried out in five alcohol solvents: methanol, ethanol, n-propanol, ethylene glycol and glycerol and their respective mixtures with water. Note that the pulse EPR measurements in pure water were

impossible, as water does not vitrify but crystallizes upon freezing. The dielectric constant and density of the pure solvents are listed in
Table 4.1.

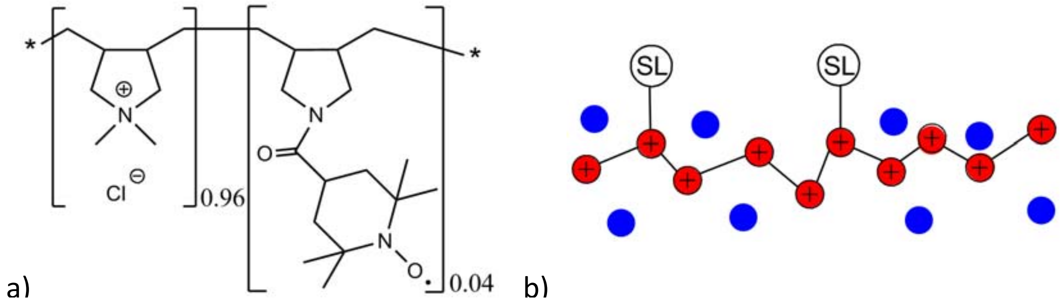

Figure 4.4 Spin labeled poly(diallyldimethylammonium chloride) (PDADMAC) a) chemical structure, b) scheme. The molecular weight of PDADMAC is M_w of 490000 g/mol and a M_n of 146000 g/mol. It is a statistically labeled copolymer with >99% labeling degree (4mol.-%).

Table 4.1 Investigated solvent systems and their properties. All data are given for 293 K and for the pure solvents. ε: dielectric constant and δ: density of the solvents. For DEER measurements their aqueous mixtures were used (25 Vol.-% organic solvent).

	formula	ε	δ **[gcm^{-3}]**
Methanol	CH_3OH	33.8	0.79
Ethanol	C_2H_5OH	24.3	0.79
n-Propanol	C_3H_7OH	20.3	0.80
Ethylene glycol (diol)	$(CH_2OH)_2$	37.0	1.10
Glycerol (triol)	$(CH_2OH)_3$	42.5	1.26
Water	H_2O	78.5	1.00

Besides the five pure organic solvents their aqueous mixtures in a volume ratio of 1:3 (organic solvent:water) were used. The solvents were chosen in order to compare effects on the PEL conformation by the homologues of the alcohols. This includes the effect of increasing hydrophobic alkyl parts from methanol, via ethanol, to n-propanol, as well as the effect of the number of hydroxyl groups (mono-, di and triols). Besides this chemical aspect these solvents show different viscosities. However, since DEER measurements were performed at 50 K viscosity effects are not explicitly studied.

The polymer fully dissolves in all these solvent mixtures. To study the effect of divalent salt, the ionic strength of sodium sulfate was varied between zero and 750 mM (0mM, 10mM, 100mM, 750mM). The PDADMAC concentration was kept constant to 40 mM for all investigated solutions in order to compare the different solvent effects and ionic strength effects. Due to entropic reasons it is expected that the divalent sulfate ions expel monovalent chloride ions from the condensed state and come into interaction with the oppositely charged PEL chains by electrostatic self-assembly. In a simple picture this can be anticipated by noting that divalent ions reach the critical Manning parameter ξ_M for counterion condensation already at lower values than monovalent ions: $\xi_M = \lambda_B/b$. The method applied to probe the local PEL conformation was double electron electron resonance (DEER, see section 2.9.3).

4.3 DEER Measurements: Influence of Solvent and Ionic Strength

The DEER results are shown in Figure 4.5. The analysis of the DEER data was performed as described in Section 7.3 by using the wormlike chain model. The fitted parameters are the mean distance r, width of the distribution $s(r)$, the persistence length l_p and the label-to-label distance L. These values are summarized in Table 4.2.

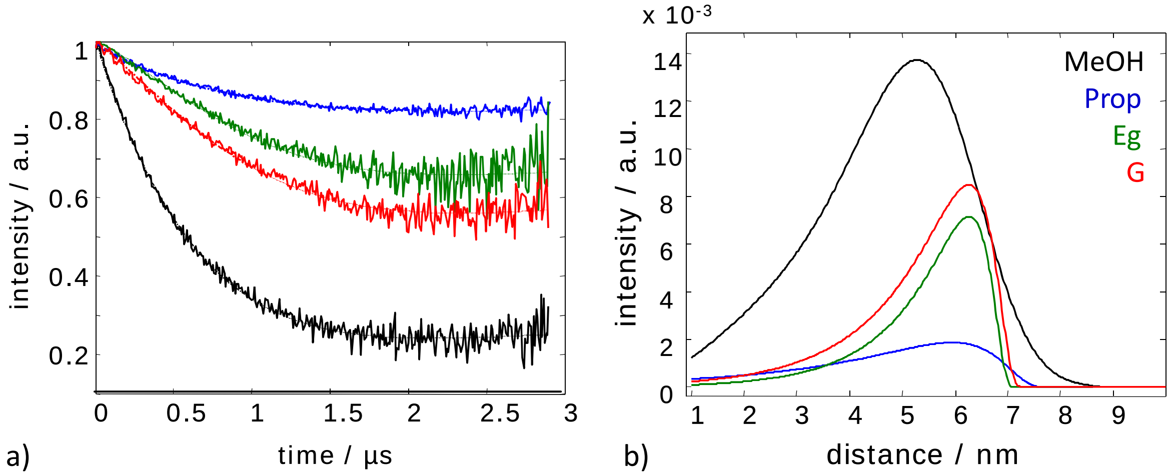

Figure 4.5 DEER measurements (50 K) of 40 mM SL-PDADMAC in organic solvent:water=1:3 (v/v) and ionic strength of sodium sulfate I=10 mM. a) Background corrected DEER data b) Distance distribution using the wormlike chain model. The color code in both pictures is the same: black: methanol, blue: *n*-propanol, green: ethylene gylco, red: glycerol.

This table contains only one value for each solvent mixture, although four different solutions with varying ionic strength of sodium sulfate with $I_{sulfat} = 0{,}10{,}100{,}750$ mM were measured. Remarkably, it was observed that the addition of sodium sulfate to organic solvent-water solutions of PDADMAC only led to experimental errors of ±0.1 nm in the mean distance r. However, changes in the distances and the distance distribution are much more pronounced going from one solvent mixture to another solvent mixture. Thus, the parameters listed in Table 4.2 are the mean values obtained by averaging the three sulfate-containing samples ($I_{sulfat} = 10, 100, 750$ mM). Although there was nearly no change (±0.1 nm) from 0 mM (pure organic solvent-water mixture) to 10 mM ionic strength, the salt-free samples were not included into the averaging.

Table 4.2 Results of the distance measurements of 40 mM PDADMAC in organic solvent:water mixtures (1:3) at 50 K as obtained by using the WLC model. L: label-to-label distance, l_p: persistence length, r: mean distance, $s(r)$: width of the distribution. All data were recorded with equal τ_1 and t-values. Ethanol-water data is set in brackets since it was not possible to record an equally long DEER time trace up to t=3.5 μs.

solvent	l_p [nm]	r [nm]	$s(r)$ [nm]	L [nm]
Methanol/water	2.8	4.7	1.3	7.7
(Ethanol/water	2.0	4.0	1.2	7.1)
n-Propanol/water	2.8	5.0	1.5	8.3
Ethylene glycol /water	3.7	5.0	1.3	7.7
Glycerol/water	3.6	5.3	1.3	7.9

The ethanol water mixtures showed relatively short T_2 relaxation times, which made it impossible to obtain DEER data of the same quality and the same length as in the other solvent mixtures. Therefore, the ethanol/water mixtures cannot be reliably used in a discussion of trends in the samples and is left out in the following.

The values for the persistence length l_p in the mono-alcohols methanol and *n*-propanol are equal ($l_p = 2.8$ nm). The l_p-values in the multi-alcohols ethylene glycol and glycerol, are similar as well, but are increased as compared to the mono-alcohol mixtures ($l_p = 3.6$ nm) The label-to-label distance L is nearly similar in methanol and ethylene glycol, while the value is increased for glycerol and finally propanol has the highest value.

Surprisingly, variation of the ionic strength by addition of sulfate seems to have very small influence on the persistence length and the label-to-label distance. This is directly indicative of only little change in local conformation of the polyelectrolyte within the lengthscale that is accessible for this experiment (up to ~5.8 nm for t=3.5 μs). Inspection of the ESE spectra did not indicate changes upon increase of the ionic strength, either. It is known that divalent ions expel monovalent ions from the condensed state on a PEL backbone with increasing the ionic strength I in water [194]. Contact ion pairs of sulfonate ions with PDADMAC were also confirmed in glycerol/water mixtures [124, 195]. Thus, these results might suggest a simple replacement of the Cl^--ion without significant local conformational changes of the polyelectrolyte backbone in the organic-water mixtures. Although there were slight changes upon sulfate addition, no clear trends were observed within the three sulfate concentrations that were used in this investigation.

However, since only 20% of the sulfonate ions were found in the condensed (contact-ion pair) state for different ratios of c(PEL):c(sulfonate)<0.25 [195] we might also argue that the we lack the accessible length scale of a possible local conformational change due to sulfate ions, i.e. the small number of multivalent sulfate ions per chain is not sufficient to modify the extended chain conformation. However, since the ionic strength was increased up to 750 mM – where all electrostatic interactions along the PEL should be screened- we should observe a decreased label-to label distances L, which was not the case.

All solvent mixtures are better solvents for the PDADMAC hydrocarbon chain than pure water and consist of a polar part (OH-groups) and an unpolar part (hydrocarbon chain). Their trends in permittivity (Table 4.1) do not resemble the trend in the label-to-label distance L, which indicates that they should not be considered as dielectric continuum, but rather that individual molecular features need to be taken into account. The alkyl chains may solvate the hydrophobic groups of the polymer chains any may thus screen hydrophobic interactions as it was also supposed in [195]. The hydrophobic screening of the monomer-monomer interaction close to the polymer backbone impedes a counterion-mediated collapse of the PEL, as it is predicted for PEL in water [Khok02] and should work best for the longest alkyl chain alcohol that is in the present case n-propanol. Indeed in n-propanol/water the longest label-to-label distance L was found (L=8.3 nm), followed by glycerol (L=7.9 nm), methanol (L=7.7 nm) and ethylene glycol(L=7.6 nm). Interestingly, the L-values for MeOH and ethylene glycol are nearly identical, but slightly higher for methanol, that even supports this molecular picture of a hydrophobic selt assembly in a cylindrical volume around the PEL chain, where water might be pocket-like embedded towards the ammonium groups, building a H-bonding network with the alcohol-hydroxy groups. For the charged ions it is energetically more favorable to stay in the solvation sphere outside this cylinder in the water-enriched phase. This leads to a different solvent composition around the polymer chain as compared to the bulk. In particular the effect of nearby organic molecules to the PEL should lead to another hydrodynamic radius and intrinsic viscosity of the polymer.

These data suggest a less serve impact on conformational changes due to salt than usually predicted for PEL [194] and stress the importance of the delicate balance of hydrophobic *and* electrostatic interactions, in particular in the presence of organic solvents, which are preferentially solvating the PEL backbone.

For elucidating this aspect a detailed analysis on conformational changes in different solvents rather than salt addition should be investigated, a trend that is currently also observed in literature.

5 Characterization of Structure and Dynamics of Miniemulsions

This chapter starts with the motivation of performing EPR experiments on miniemulsions followed by the introduction into micellar and colloidal solutions (Section 5.2) and the presentation of the basic components of a miniemulsion (Section 5.3). In Section 5.3.3 the model miniemulsion and the standard preparation is described. The EPR measurements for characterization of miniemulsions and the interpretation of the experimental results are given in Section 5.4 to 5.8. In Section 5.9 the implications of the EPR results for the structural and dynamic aspects of miniemulsions are discussed.

The EPR parameters analyzed in this study were the rotational correlation time τ_{corr} for the spin probe motion, which is related to the microviscosity of the probe environment, the nitrogen hyperfine coupling a_{iso} that is related to the dielectric constant of the medium (polarity) and finally, the EPR line shape. In the analysis, slow-motional CW EPR spectral simulations were used as the main tool, providing rotational diffusion rates for the individual spin probe components.

5.1 Motivation

In previous studies, it was shown that the addition of a lanthanide β-diketonate complex of the type M(tmhd)$_3$ (M=trivalent lanthanide ion, tmhd=anionic ligand, for more details see Figure 5.9) to a miniemulsion that was polymerized, leads to lamellar-like structures on a nanometer lengthscale [196]. X-Ray scattering of the freeze-dried polymer particles reveals a peak that could be correlated to a lamellar repeat period of ~0.4-0.5 nm and the structural features were visualized with a transmission electron microscope (TEM) (see Figure 5.14, Figure 5.21)[197]. First experiments have shown that the repeating distance depend on the chain length of the surfactant that was used to prepare the miniemulsion [198]. The aim of this work was the better understanding of this structure formation, to obtain insights when this structuring takes place and to characterize the structured region with the help of spin-labeled fatty acids (SLFA). These SLFA are also amphiphiles and hence, are known to mix with the used surfactant. Thus, they may report from the ordered region by means of EPR spectroscopy. The spectral parameters of EPR spin probes are significantly affected by the environment's viscosity, polarity, pH and molecular ordering. Analysis of CW EPR spectra gives insights into the dynamics of the spin probe (diffusion, tumbling), the frequency of exchange processes or molecular collisions. EPR spectroscopy is a very useful method for characterization of colloidal systems; in particular here it offers the possibility to study miniemulsions before and after polymerization.

5.2 Introduction

A miniemulsion is a rather complex system, containing a variety of components, therefore, each component and its effect on the structure formation in the miniemulsions is briefly presented. The scope of this introduction is the discussion of the relevant parameters necessary for the interpretation of the obtained results.

5.2.1 Surfactants and Surfactant Aggregates

Surfactants are amphiphile molecules with a hydrophobic (e.g. alkyl-, flourocarbon, or silioxane chain) and a polar part, which may be ionic (anionic, cationic or amphiphile) or non-ionic. They are water soluble if their alkyl chain is not too long (usually not more than 20 C-atoms) and lower the surface tension between two phases (liquid-liquid or liquid-vapor) due to monolayer formation at the interface. At concentrations above the *critical micelle concentration* (cmc) and temperatures above the Krafft temperature T_K, they form aggregates with the alkyl chains associating such that they point inwards the micelle and the head groups are exposed to water. Such micelles contain 20-100 surfactant molecules (typical diameter 5-10 nm) that are in equilibrium with free surfactants in bulk [199]. The value of the cmc is dependent on the solvent, surfactant type and temperature. The general phase diagram of an ionic surfactant is given in Figure 5.1.

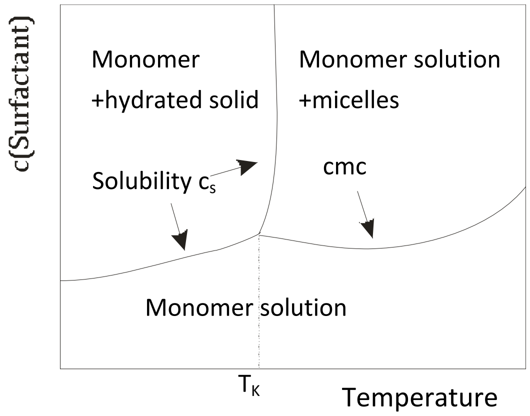

Figure 5.1 Schematic phase diagram of an ionic surfactant. The two curves in the diagram represent the critical concentrations of the surfactant: the cmc is the critical micelle concentration above which the surfactant forms micelles while the solubility c_s is the concentration above which the surfactant forms a hydrated solid. The Krafft point T_K is the critical point in the phase diagram, above which the solubility of the surfactant rises sharply. At this temperature the solubility and the cmc become equal. The cmc often shows a minimum at a certain temperature (for SDS this is above T_K).

For ionic single alkyl chain surfactants the cmc is primarily determined by the size of the hydrophobic part, and a higher number of carbon-atoms n_c will lead to a decrease in the value of the cmc according to following equation [200]:

$$\log \mathrm{cmc} = A - Bn_C \tag{5.1}$$

A and B are constants specific to the homologous series under constant conditions (T,p). The values of A and B have been determined for a variety of surfactants [200]. For non-ionic surfactant, among which poly(oxyethylene) PEO is the most commonly used, an empirical relationship between the EO units and the cmc exists, too [200]. The cmc for ionic surfactants is ~1 mM while that of the non-ionic one with an identical alkyl chain is ~0.1 mM. The solubilization for non-ionic surfactants relies solely on hydrogen-bonding to the EO and thus, their cmc and aggregation number strongly depends on the temperature and they show an inverse temperature-solubility relationship. At concentrations below the cmc surfactants are homogeneously distributed in the solvent. High above the cmc the average *aggregation number* begins to increase significantly, which alters the shape of a spherical micelle and they can self-assemble into lamellae, hexagonally packed, coil-like micelles or cubic phases [199]. Their self-organization depends on their chemical structure and the balance between hydrophilic and hydrophobic interactions, solvent and temperature. In Figure 5.2 the most important surfactant aggregates are shown [201].

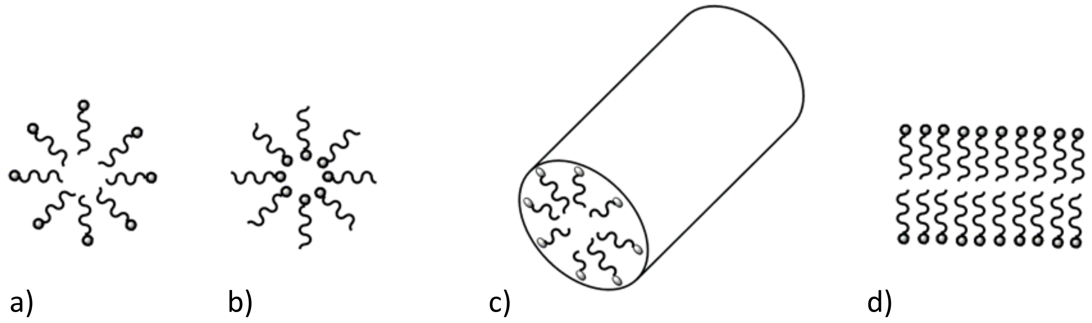

Figure 5.2 Possible surfactant aggregates. Spherical micelles (a) are formed for a surfactant parameter of N_S≈0.33 (e.g. SDS). Inverted micelles (b) are usually found in non-polar solvents. Rod-shaped (or cylindrical) micelles (c) are formed for increasing surfactant parameter N_S≈0.5. The ends of the cylinders are not flat as shown but capped by hemispheres of surfactant. At high surfactant concentrations cylinders pack into hexagonal phases (e.g. SDS at high salt concentrations). Bilayers (d) are formed for N_S>0.5. A prominent example are lipids (e.g. phosphatidyl choline), that have two alkyl chains. Their headgroup is much too small and their alkyl chains too bulky to form a micelle. At high lipid concentrations lamellar phases are built that arise from stacks of parallel bilayers.

The packing can be estimated by the surfactant parameter [201]:

$$N_S = \frac{V_c}{L_c a_h} \tag{5.2}$$

V_c is the volume of the hydrophobic part, L_c is the length of the hydrocarbon chain and a_h is the effective area per headgroup. The volume V_c is can be easily estimated from the density of pure hydrocarbons, with n_c carbon-atoms:

$$V_c \approx (0.027 \cdot n_c + 0.029)\mathrm{nm}^3 \tag{5.3}$$

The length can be obtained from the carbon-carbon bond length (0.127 nm) in an all-trans configuration

$$N_c \approx (0.127 \cdot n_c + 0.15)\mathrm{nm} \tag{5.4}$$

where the number 0.15 is the van der Waals radius of the terminal methyl group minus 0.127 nm. The area per headgroup is more problematic in estimation and usually needs experimental proof, since it is very sensitive to the surfactant and electrolyte concentrations. The surfactant number varies from 0 to 1, which is related to the curvature of the aggregate. Spherical micelles (that have a large a_h, e.g. sodium dodecyl sulfate) are formed for N_s~0.33, rod like micelles for N_s~0.5 and bilayers for $N_s = 0.5 \ldots 1$.

In aqueous environment, the headgroups of the surfactants in the micelle are more or less dissociated into their individual ions and the such formed charged interface largely determines micellar stability and interfacial processes like adsorption and adhesion of colloidal particles [136]. The distribution of the counterions in solution (and with this the electric potential profile from the surface) was subject of many theories [136]. The simplest charge double layer imaginable is the *molecular condenser,* where all counterions (point-charges) are located at a distance δ from a charged (flat) surface (e.g. a clay surface). This double layer is determined by the radius of the ions (point-charges) and is characterized by a linearly decreasing potential. If one accounts for the thermal motion of the ions counteracting the attraction of the surface, the Boltzman equation gives the proper description of the system. The Boltzmann equation gives rise to an exponential potential with the characteristic Debye length k^{-1} (see eq.(4.15)), which is the distance over which the electrical potential ψ reduces from ψ_0 to ψ_0/e, and which is usually referred to as the thickness of the electrical double layer. This diffuse double layer model (also known as Guoy-Chapman model) works well for systems with low electrolyte concentration (<10^{-2} M) and low surface potential (< few tens of mV). At higher ionic strength and surface potential the outer part of the double layer may still obey this model, but the inner part close to the surface tends toward the molecular condenser. Therefore, these two pictures are integrated into the Guoy-Chapman-Stern model which is illustrated in Figure 5.3. For the inner Stern-Layer, a finite volume to the counter- and co-ions is added, which may even be adsorbed specifically.[1] In the absence of specifically adsorbed ions there is a charge-free layer (Stern-Layer), adjacent to the surface that extends to a distance δ, where δ is the distance of closest approach of a *hydrated* ion to the surface. For specific adsorption, the

---

[1] Ions in solution of the same sign as the charged surface are referred to as co-ions. Specifically interactions are partly non-electrical in nature so that co-ions can overcome the repelling electric potential at the surface.

surface charge σ_0 is partly compensated by the charge of *dehydrated* ions that are located at a distance m, and partly by the diffusely distributed charge σ_δ:

$$\sigma_0 = -(\sigma_m + \sigma_\delta) \tag{5.5}$$

As in the molecular condenser the potential $\psi(x)$ drops linearly in the region 0< x< m:

$$\psi_0 - \psi_m = -\frac{\sigma_0}{\varepsilon_m \varepsilon_0} m \tag{5.6}$$

The same holds for the region $m < x < \delta$.
For the diffuse part of the double layer $x \geq \delta$, $\psi(x)$ drops exponentially:

$$\psi(x) = \psi(\delta) \exp\left[-\kappa(x - \delta)\right] \tag{5.7}$$

Under most conditions ψ_δ is much smaller than ψ_0 and the potential decays for the largest part within the Stern-Layer. For the stability of colloids ψ_δ plays a more important role [202]. Thus, $\psi(x)$ can be derived over the entire double layer if σ_0 and σ_d are known. For smooth, solid surfaces this is an easy task, as σ_0 can be obtained by titration and σ_d may be approximated [202]. It is obvious that for micellar and colloidal systems, where an interface region rather than a clear boundary and a curved rather than a flat interface is present, the electrical potential will not exactly follow these ideal equations. In such systems a *porous* electrical double layer exists, in which the charge may extend into the solid phase up to a certain depth (e.g. biological membranes or polymer-like surfaces). Also, these 'solids' have an open, more gel-like structure that is penetrable for water, counter- and co-ions.

As a consequence of the nature of amphiphilic molecules, the formed micelle represents what might be considered as a 'second liquid phase' in solution. The solubilization of organic oily materials (that are merely insoluble in water) is highly increased in presence of aqueous surfactants as illustrated in Figure 5.4.

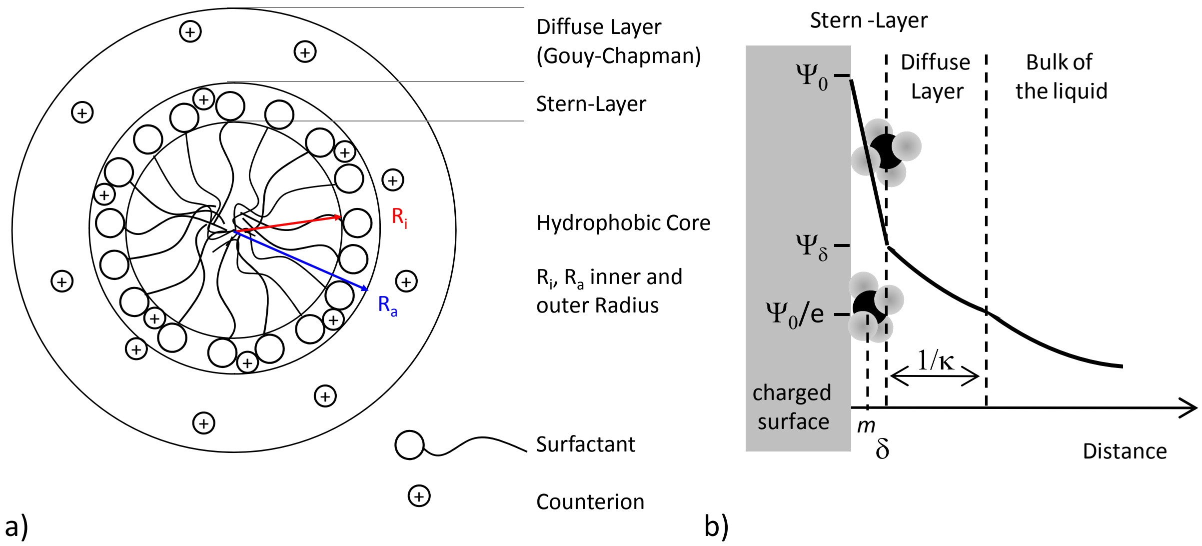

Figure 5.3 a) The picture of the idealized micelle formed by anionic surfactant molecules in water. The hydrophobic alkyl chains build the inner core with the radius R_i and the charged headgroups are located at the surface of a sphere. The simplified model of the electric double layer contains adsorbed counterions in the immobile Stern layer and a diffuse Guoy-Chapman-Layer with counter- and coions (Gouy-Chapman-Stern model) that fulfill charge neutrality. b) Guoy-Chapman-Stern electrical double layer at a charged surface with specific ion adsorption in the Stern-Layer $0<x<\delta$.

The loci of the solubilized additive molecule will mainly depend on its chemical structure, thus, a hydrocarbon will be found in the core (a), while slightly more polar material will be oriented towards the headgroups, in a transition region between the hydrophobic and core and the surface head groups (b). In special cases for ionic surfactants the additive may become directly associated with the electrical double layer (c). Each type of interaction will increase the micelle’s diameter.

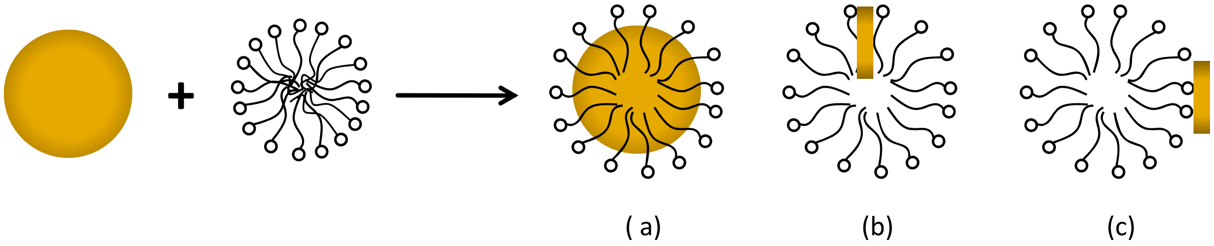

Figure 5.4 The presence of micellar aggregates in aquesous solutions enhances solubilization of organic materials (e.g. monomers) that leads to swollen micelles. a) Unpolar molecules are found in the micellar core. b) Polar molecules will be found in a region between the core and the surface. c) Ionic micelles can interact with their charged headgroups with an additive.

With this additive, the phase diagram of pure surfactant/water mixtures becomes that of a ternary mixture showing a varity of phases that are highly temperature depended.

5.2.2 Miniemulsions

Miniemulsions are dispersions of relatively stable oil droplets with a size range of 50-500 nm [203]. They are formed by homogenization, through which the droplets of a coarse emulsion are broken into much smaller and more numerous droplets by the application of intensive shear forces and energy. The sheared system contains water, oil, surfactant and an osmotic pressure agent that is insoluble in the continuous phase (a so called hydrophobe, e.g. hexadecane) [203]. The process is illustrated in Figure 5.5. The energy input is achieved by an ultrasound probe that is inserted into the liquid operating at a frequency of 20 kHz. At the beginning of the homogenization, the droplet size distribution is broad, however this polydispersity decreases with time and reaches a stable state [204]. The oil may be a monomer, thus polymerization in miniemulsions results in latex particles that have the same size as the initial dispersed monomer droplets. The nucleation loci are the monomer droplets that contain the oil-soluble initiator and the hydrophobe and hence, this process differs substantially from emulsion polymerization. There, a water soluble initiator is used and the polymerization kinetics are determined by diffusion of the monomer from the monomer droplets to the micelles [205].

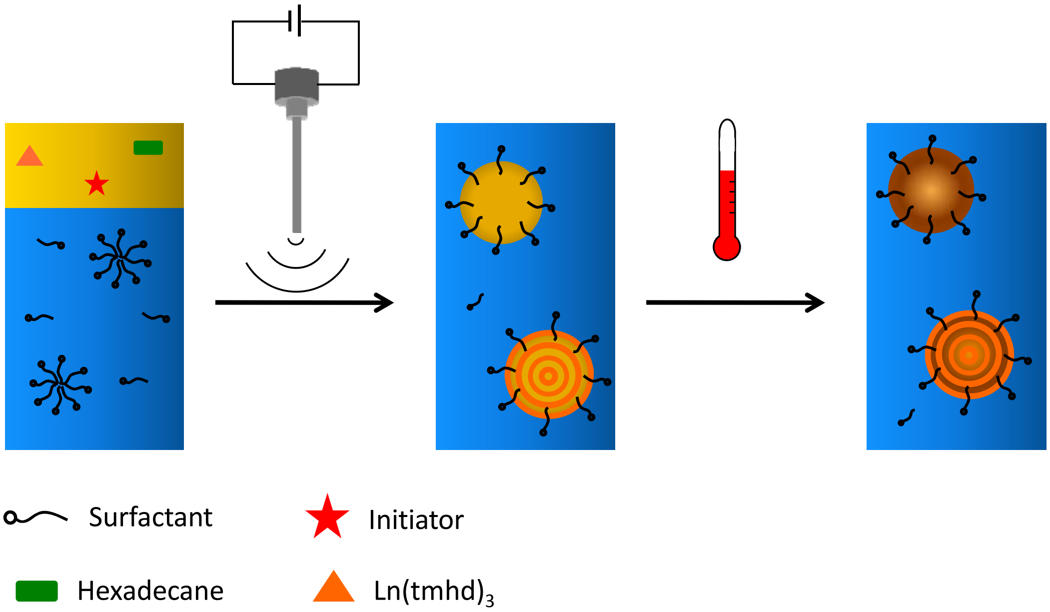

Figure 5.5 The miniemulsion process: The water phase (blue) contains the surfactant, the monomer phase (yellow) the initiator and hexadecane to prevent Ostwald ripening. Additionally, an oil soluble substances may be added like a lanthanide β-diketonate complex. The phases are mixed and treated for 3 minutes with ultrasound by inserting the ultrasonic probe directly into the mixture in an ice bath. This forms small droplets that can be radically polymerized without changing their distribution.

The role of the hydrophobe is to prevent Ostwald ripening, which is driven by the differences in the Laplace pressure between droplets having different radii: the dispersed phase is transferred from the smaller to the larger droplets which results in the gradual disappearance of small droplets. The hydrophobic agent serves to build up an osmotic pressure that counteracts the inherent Laplace pressure of the droplet, for this it is important to choose an agent which can hardly diffuse from droplet to droplet. Hexadecane was found to stabilize miniemulsions very effectively [206]. A theoretical treatment with derived kinetic expressions for this diffusion process can be found in [207-208].

Directly after miniemulsification the dispersions are only critically stabilized in terms of collisions, and the droplets can increase in size by collision, which break up the interface and leads to fusion into a bigger droplet (upper part of Figure 5.6).

The handling of this problem may be solved by addition of appropriate surfactants, which provide the necessary colloidal stability against coalescence.

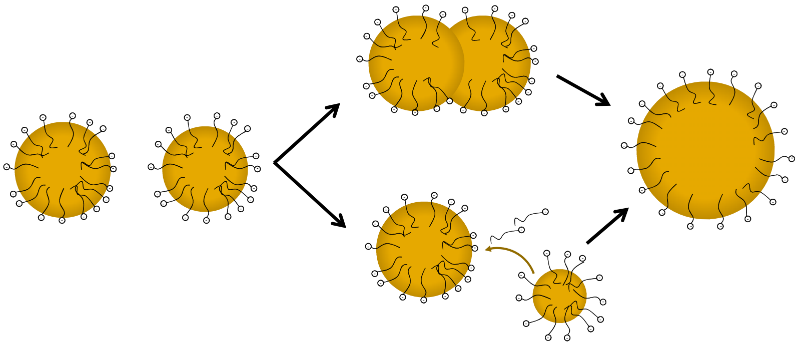

Figure 5.6 Mechanisms that account for instability of miniemulsions. In the upper part destabilization occurs by collision (bimolecular process) and fusion of two droplets resulting in coalescence to one larger droplet. Ostwald ripening (lower part) describes the process where smaller droplets decrease in size due to diffusive mass transport to bigger droplets.

Thus, the surfactant provides stabilization against coalescence and the hydrophobe against Ostwald ripening and an appropriate formulation of the miniemulsion recipe is necessary to obtain particles upon polymerization that resemble the initially formed droplets.

5.3 The Components of a Miniemulsion

5.3.1 Surfactants and Spin Probes

In these studies, different anionic surfactants with alkyl chain lengths of C_{12} and C_{18} and with the anionic head groups sulfate and carboxylate were used and are shown in Figure 5.7. These were the sodium salts of: dodecyl sulfate (SDS), octadecyl sulfate (SOS), laurate (SL) and stearate (ST).

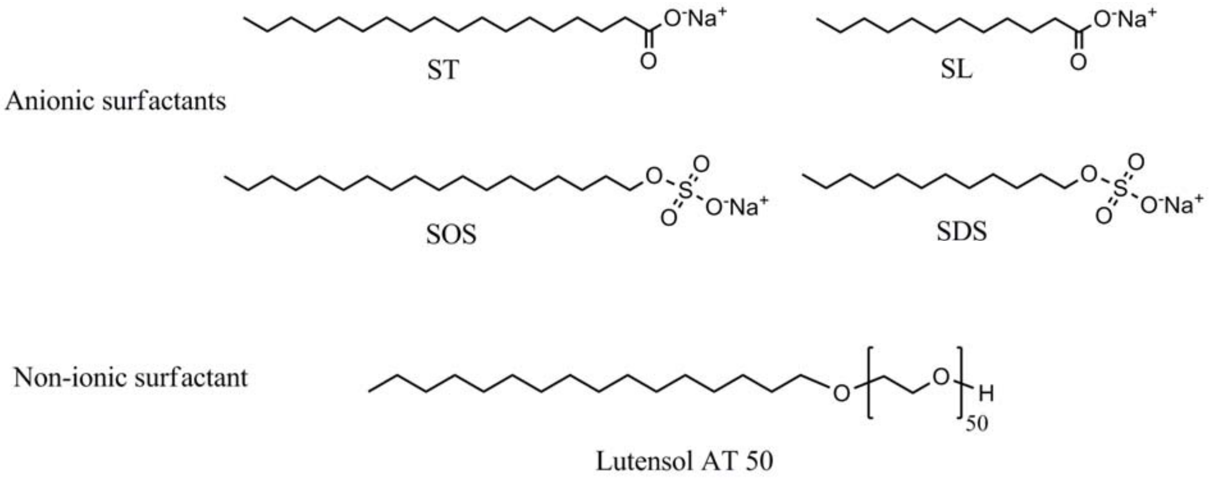

Figure 5.7 The anionic surfactants used in this work were sodium stearate (ST) $C_{17}H_{35}COONa$, sodium laurate (SL) $C_{11}H_{23}COONa$, sodium octadecyl sulfate (SOS) $C_{18}H_{37}OSO_3Na$ and sodium dodecyl sulfate (SDS) $C_{12}H_{25}OSO_3Na$. These surfactants differ in their alkyl chain lengths (C12 or C18) and their headgroups (sulfate or carboxylate). The non-ionic surfactant Lutensol AT 50 is a poly(ethyleneoxide) monoalkyl ether where the hydrophilic part consists of 50 ethylene oxide (EO) units and the hydrophobic alkyl part is a mixture of hexadecyl $R=C_{16}H_{13}$ and octadecyl $R=C_{18}H_{37}$ chains ($C_{16}/C_{18}EO_{50}$). Lutensol has shown to effectively stabilize polymerdispersions.

Miniemulsions prepared with a single anionic surfactant had the tendency to gradually coagulateduring the time needed to perform the EPR experiments. Thus, Lutensol AT 50$^{®}$, a poly(ethyleneoxide) monoalkyl ether was added as a second, non-ionic amphiphile. Such water soluble polymers are expressed by the general formula C_xEO_n where x is the number of carbon atoms and EO the number of ethylene oxide units. Lutensol AT 50$^{®}$ contains 50 ethylene oxide units and, compared to this, only a small hydrophobic alkyl rest consisting of a mixture of 16 and 18 carbon atoms ($C_{16,18}E_{50}$). Hence, it is a very effective emulsifier for hydrophobic substances such as fatty acids or monomers and it is commonly used to stabilize (mini-)emulsions or to disperse suspended solids in water [203, 209].

The surfactants were dissolved in water together with a spin probe x-DOXYL stearic acid (Figure 5.8) with the nitroxide group in position x=5 and 16 along the stearic acid chain. The probes x-DSA are very sparingly soluble in water and complete solubilization was obtained after addition to the monomer solution.

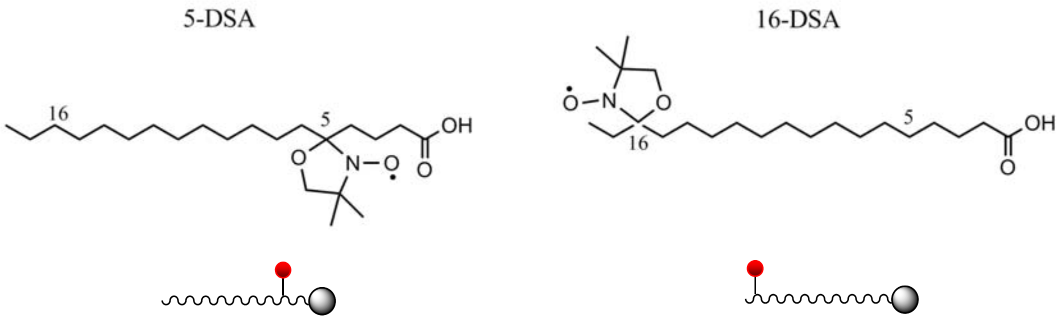

Figure 5.8 The fatty acid spin probes used in this work were x-DOXYL stearic acid (4,4-dimethyl-oxazolidine-*N*-oxyl octadecanoic acid) with x= 5 (5-DSA) and x=16 (16-DSA). In 16-DSA the spin label is located at the end of the alkyl chain, whereas in 5-DSA it is located near to the head group.

The spin labels at the different positions report about different regions within a micelle or a lamellar layer. Assuming a micelle or a bilayer in aqueous solution made of an ionic surfactant, the acid is anchored to the hydrophilic region near the Stern Layer and the C5-position will sense a more hydrophilic environment than the C16-position, which is located more towards the hydrophobic interior.

The cmc of the used surfactants and DSA are listed in Table 5.1 (literature values). The value of the cmc usually depends on the method that was used and the purity of the surfactant (see cited references). For 5-DSA very different cmc values were found. Note that the cmc for 5-DSA was obtained from buffer solution, and it is known that with increasing buffer concentration or ionic strength the value of the cmc for ionic surfactant is decreased [210]. This may also influence the cmc of non-charged fatty acids.

Table 5.1 The critical micelle concentration of the used surfactants in water at 25°C as taken from literature. The values for 5-DSA were obtained from phosphate buffer solutions.

	C-atoms headgroup	**cmc /mM**	**T /°C**	**Ref.**
Sodium laurate (SL)	C11 -COO$^-$	2.7	30	[211]
Sodium stearate (ST)	C17 -COO$^-$	1.8	30	[211]
Sodium dodecyl sulfate (SDS)	C12 -OSO$_3^-$	8.1-8.7	25-30	[211-214]
Sodium octadecyl sulfate (SOS)	C18 -OSO$_3^-$	-	-	-
5-DSA	C17 -COOH	0.035	37	[215]
		~1.5	n.a.	[216]

5.3.2 Lanthanide *β*-diketonates [M(tmhd)$_3$]

Lanthanide *β*-diketonates are complexes of *β*-diketones (1,3-diketones) with lanthanide ions, which are the most popular and most investigated lanthanide coordination compounds. The simplest 1,3-diketone is acetylacetone Hacac (Figure 5.9 with R=H). It bears two carbonyl groups separated by a methylene group and capped by a methyl group on each side. All other *β*-diketones can formally be derived from Hacac by substitution of the rest R. The tmhd (2,2,6,6-tetramethyl-3,5-heptanedionate) ligand that was used in this work contains bulky *tert.*-butyl groups (Figure 5.9 with R=CH_3) and its lanthanide complexes are more stable as compared to acac complexes [217]. In the conjugated base of a *β*-diketone, the *β*-diketonate ion, the negative charge is delocalized:

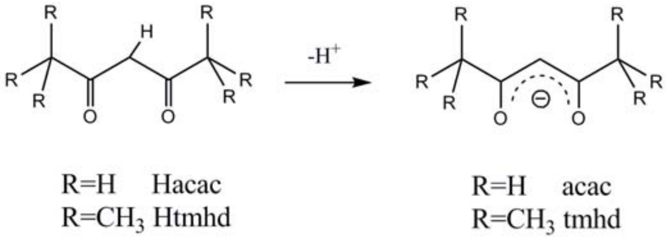

Figure 5.9 Deprotonation of a *β*-diketone removes the acidic proton from the α-carbon atom. The negative charge of the *β*-diketonate ligand is delocalized. The general structure for a *β*-diketone is acetylacetone Hacac with a methyl group (R=H) on both carbonyl functions. Substitution of the methyl groups by *tert*-butyl groups yield the ligand Htmhd that was used in this work. The abbreviation Htmd stands for 2,2,6,6-tetramethyl-3,5-heptanedione and tmhd for the conjugated base, which is the ligand that was used in this work.

Three *β*-diketonate ligands are necessary to form neutral complexes with trivalent rare earth ions represented by the formula [M(*β*-diketonate)$_3$]. In such *tris*-complexes the two oxygen atoms of each *β*-diketonate form a six-membered chelate ring (Figure 5.10 a) with the lanthanide ion leading to a trigonal prismatic coordination polyhedron around the ion (Figure 5.10 b). Since the coordination sphere of the metal ion is unsaturated in these six-coordinate complexes, adducts with Lewis-bases (e.g. water and other O- and N-donors present in a solution) are formed easily. Depending on the adduct-ligand, complexes of the formula [M(tmhd)$_3$·x(adduct)] were isolated in the past [218-220]. Saturation of the coordination sphere is also obtained in *tetrakis*-complexes with four *β*-diketonate [M(tmhd)$_4$]$^-$ where a coordination number of eight is obtained. Usually, lanthanide *β*-diketonates are eight-coordinate complexes [221] but sixfold coordinated tris-complexes of very bulky *β*-diketones are also stable. They are stable toward moisture and air and soluble in common organic solvents and monomers.

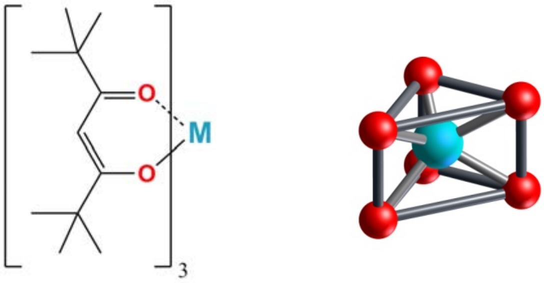

a) b)

Figure 5.10 a) Chemical structure of the lanthanide(III)-*tris*(2,2,6,6-tetramethyl-3,5-heptanedionate) compound [M(tmhd)$_3$]. The metal ion M is colored in cyan and oxygen atoms in red. In *tris*-β-diketonates, the metal ion is coordinated by six oxygen atoms from three ligands. b) The six oxygen atoms constitute a trigonal prismatic coordination polyhedron, the average M-O distance is 2.3-2.4 Å [218]. This holds for many trivalent lanthanide ions in the unsolvated state. Some ions, however, show the tendency to saturate the coordination sphere by dimerization [M$_2$(tmhd)$_6$] or adduct formation [M(tmhd)$_3$·x(adduct)] and thus may reach coordination number up to nine [221].

Originally, these complexes were used as NMR shift agents [222], but have now been established as volatile precursors for chemical vapor deposition (CVD). They owe their popularity to their excellent luminescent properties. An extensive review that covers all aspects on lanthanide β-diketonates (synthesis, structure, properties, applications) has been written by Binnemans [221].

For this work the complexes of Ln(tmhd)$_3$ are considered to be an important building part of the nanostructures formed in polymer particles that were prepared in presence of this complex with different surfactants. As central metal ions we used the diamagnetic (EPR-inactive ground state *J*=0) Eu^{3+}- and the paramagnetic Gd^{3+}-ion. Their electronic properties are summarized in Table 5.2. We used gadolinium(III) to study the distance between the nitroxide and the metal ion via the relaxation enhancement of the nitroxide by Gd(III).

Table 5.2 Electronic configuration of the trivalent lanthanide ions Ln^{3+} used in this work. Eu^{3+} is diamagnetic while Gd^{3+} is paramagnetic [36].

Symbol	**Atomic number**	**Electronic Ln^{3+}**	**Configuration**			**Ground state Ln^{3+}**
			S	***L***	***J***	
Eu^{3+}	63	[Xe]4f^6	3	3	0	$^7F_0$
Gd^{3+}	64	[Xe]4f^7	7/2	0	7/2	$^8S_{7/2}$

The trivalent gadolinium ion is in ^{8}S ground state having 7 electrons ($S = 7/2$) in the half-filled 4f shell. With its *spherical* electron distribution it is an exception from other f-block ions that typically represent a complicated situation for EPR due to their high contributions from orbital angular momentum ($L > 0$), but for Gd(III) the standard spin Hamiltonian (that includes the zero-field-splitting term) is applicable. The CW EPR solution spectrum of Gd^{3+} complexes (with water or organic ligands) is very broad, which requires a high concentration of the complex to observe the signal (typically ~5-80 mM [223]). The peak-to-peak line width depends on the ligands, solvent, temperature and especially on the field strength and is in the range of 200-700 G [224]. The line shape is determined by the coupling of the ZFS tensor with a random motion (for the basic theory for ^{8}S-ion's electron spin relaxation see [225] and a recent refinement [226]) and usually only the main transition $m_s = \pm 1/2$ is observed at the resonance field corresponding to the isotropic g-value of approximately g_{iso}~1.99. Depending on the interaction of the nitroxide's electron spin with a metal ion, two cases can be distinguished: either the spins do not interact, then the metal ion signal appears at g_{metal} and the nitroxide triplet at $g_{nitroxide}$ in the EPR spectrum and both are undistorted. If there is an interaction between the nitroxide and the metal ion the resulting spectra depend on the strength of the interaction and the electron relaxation rate of the metal ion. Signals from interacting nitroxides are much broader than from non-interacting nitroxides and the broadening can be due to either spin exchange or dipolar interaction [227]. In frozen solution the nitroxide spin-metal interaction is static, in solution it can be either static or dynamic. In solutions of low viscosity electron spin-electron spin dipolar interactions are averaged out by fast tumbling of the molecules and the exchange interaction between the metal and the nitroxide becomes important as the main broadening mechanism. In such a case the rate constant of dynamic exchange can be obtained from the line broadening of room temperature CW EPR spectra and the distance of closest approach between the two colliding centers can be calculated [33]. Spectral broadening in CW EPR spectra due to dipolar interaction between the metal ion and the nitroxide can also be used to obtain distance information according to the Leigh method [228]. A basic feature of this theory is that the relaxed nitroxide spin spectra are broadened to an extent that they do no longer significantly contribute to the observed spectral amplitude [229]. The key assumption for this method is that the interaction is dipolar and not exchange, which is valid if the metal is in an immobilized position relative to the nitroxide, and the interaction takes place between one nitroxide and one metal in a rigid lattice (e.g. frozen solution). If the nitroxide is *not* rigidly immobilized the obtained distance from the quenching of the EPR signal, which is proportional to $T_{1,metal} \cdot r^{-6}$ can only be seen as an upper limit. These are methods to obtain the distance between the metal and the nitroxide in liquid solution. In frozen solution the relaxation enhancement of the nitroxide in presence of the metal can be used determine the distance between the two centers [230].

5.3.3 The Model Miniemulsion: Basic Recipe

The basic recipe for constitution of the investigated miniemulsions is displayed in Table 5.3. The used composition is frequently used in miniemulsion polymerization [198, 231]. It contains water as dispersion medium, the monomer methyl methacrylate (MMA) as dispersed phase, an anionic surfactant, the EPR spin probe x-DOXYL stearic acid (x=5,16; DOXYL=4,4-dimethyl-3-oxazidine-*N*-oxyl), the non-ionic surfactant Lutensol AT 50 (a polyethylene glycol ether $RO(CH_2CH_2O)_{50}H$) and hexadecane. Hexadecane was added to prevent Ostwald ripening [203]. Additionally, an oil soluble initiator and/or a rare earth β-diketonate of the type [$M(tmhd)_3$] were added in some cases (M: a trivalent lanthanide ion, tmhd: the conjugate base of 2,2,6,6-tetramethyl-3,5-heptanedione see Figure 5.10). From these components a miniemulsion is prepared as described in Chapter 7.1 and divided into two parts. The first, which I call 'miniemulsion' in this chapter, is the sample, which was immediately obtained from this procedure. The second part was polymerized and is called 'plolymerdispersion'.

Table 5.3 The ingredients for the miniemulsion. The typical recipe contains water as dispersion medium, the monomer as dispersed phase (MMA: methyl methacrylate), the hydrophobe hexadecane $C_{16}H_{34}$, an anionic surfactant, the spin probe x-DOXYL-stearic acid (DSA) and a nonionic surfactant $C_{16}/C_{18}EO_{50}$ (Lutensol AT 50, a poly(ethyleneoxid)ether). Variably a lanthanide complex $M(tmhd)_3$ ($M=Eu^{3+},Gd^{3+}$) and an oil soluble initiator (V59 or V70) were added to selected miniemulsions to monitor structural and dynamic changes upon complexation and polymerization. In this recipe the amount of spin probe is 5 mol.-% with respect to the surfactant and the molar ratio n(complex):n(MMA)=1:50. Other spin probes ratios were 2.5 and 0.5 mol.-%.

	Molar mass [g mol^{-1}]	**Mass [g]**	**n [mmol]**	**c [mM]**
Water	18.0	2.7	150	
MMA	100.1	0.3	3	985.7
Surfactant (Stearate)	306.5	0.035	0.114	37.6
DSA	384.6	$2.3\cdot10^{-3}$	$6.1\cdot10^{-3}$	2.1
Hexadecane	226.4	0.016	0.071	23.2
Lutensol AT 50	~2460	0.052	0.021	~7.2
$M(tmhd)_3$	701.8	0.042	0.060	19.7
Initiator (V70)	308.4	0.024	0.078	25.6

5.4 DSA Spin Probes in Micellar Solutions

- *DSA spin probes in aqueous solutions*

The dynamics of different spin probes in micelles is well understood (see Review [232]) and chemically different spin probes have been used to characterize ionic [233-234], nonionic [235] and mixed micelles [236-237]. Hence, this section has the aim to recapitulate the basic principles of EPR spectroscopy on micelles and, what is much more important, to obtain reference values for the EPR parameters of the used DSA spin probes in micellar systems formed by different surfactants. The main parameters are the rotational correlation time τ_{corr} and isotropic hyperfine coupling a_{iso} (the isotropic g-value g_{iso} in these samples was found to be not as sensitive as the a_{iso} value at X-Band frequencies).
For a given concentration of 16-DSA the dependence of the spectra on surfactant concentration was measured. The obtained spectra for 16-DSA in aqueous 5 mM and 25 mM SDS solution are shown in Figure 5.11 (all measured concentrations of SDS are not shown in this plot but included in Table 5.4).

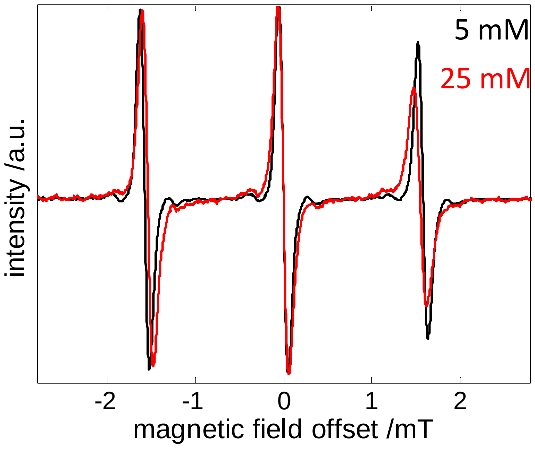

Figure 5.11 X-Band CW EPR spectra of 0.16 mM 16-DSA in water at different concentrations of sodium dodecyl sulfate (SDS). The black spectrum contains 5 mM SDS, which is below the cmc of pure SDS. The red spectrum contains 25 mM SDS, which is above the cmc of pure SDS. This spectrum shows insertion of the DSA into SDS micelles by a decreased rotational correlation time by a factor two and decreased isotropic hyperfine coupling.

The spectrum shown in black contains 5 mM aqueous SDS, a value still below the cmc of SDS (which is 8.1-8.7 mM at 25°C [213-214]). The nitroxide three-line spectrum is characteristic for fast rotation and stems from individual, non-aggregated spin probe in aqueous solution. The shoulders discernable on all three lines are due to hyperfine coupling with ^{13}C in natural abundance and these satellites are spaced by 0.6 mT, each having an intensity of 0.04 relative to the main lines. When the SDS concentration is increased above the cmc (up to 25 mM, red spectrum), the isotropic hyperfine coupling a_{iso} is shifted towards smaller values (from 1.58 mT for 5 mM, below the cmc to 1.54 mT at 25 mM, above the cmc) and the rotational correlation time τ_{corr} is decreased. The spin label is located in a more unpolar region and is hindered in rotation. This is a clear indication that DSA is solubilized into SDS micelles. Table 5.4 lists the EPR parameters for a series of measurements with increasing SDS concentration up to 100 mM (spectra not shown). The spectral parameters were obtained by using isotropic, fast motion CW EPR simulations combined with least-square fitting (see Chapter 2.8). The hf values obtained by simulation correspond very well with those obtained by graphical evaluation, where the zero crossing points between the low -and high field lines (divided by two) were used (see Figure 2.11 b) and are plotted in Figure 5.12 against the SDS concentration.

Table 5.4 Isotropic hyperfine coupling a_{iso} and rotational correlation time τ_{corr} for 0.16 mM 16-DSA in sodium dodecyl sulfate (SDS) solutions, measured at X-Band (9.4 GHz). The EPR parameters were obtained by spectral simulation in the motional narrowing regime using a Voigtian linewidth (0.1 mT Gaussian, 0.04 mT Lorentzian component) and g=[2.0088, 2.0061, 2.0030]. The error for a_{iso} is ±0.05 G, for τ_{corr} ±20 ps. For the simulation an axial hyperfine tensor A was used and a_{iso}=trace(A) was calculated.

Solvent	**[SDS] /mM**	**T /°C**	**a_{iso} /mT**	**τ_{corr} /ps**
Water	5	30	1.580	90
	25	28	1.547	160
	50	25	1.545	180
	100	25	1.542	185

From Table 5.4 on can see that above the cmc of the surfactant, the value for a_{iso} is decreased as compared to a_{iso} for the free nitroxide in solution, which is further accompanied with a slower rotation (the trend is observable). As the surfactant concentration is increased, it is well known that the aggregation number of surfactant molecules is increased, too [232, 238]. This leads to packing of more surfactant molecules and the spin probes sense a more viscous environment, and is thus more restricted in motion as can be seen by the increase in the rotational correlation time in the spectrum. When increasing the SDS concentration further up to 100 mM there is only a slight further decrease of the value of a_{iso}. Similar results were obtained with sodium laurate (data not shown), that contains also 12 C-atoms. Generally, the solubility of the DSA was increased in micellar systems compared to that in water, which already indicates the co-mizellation of DSA (see Discussion, Section 5.9).

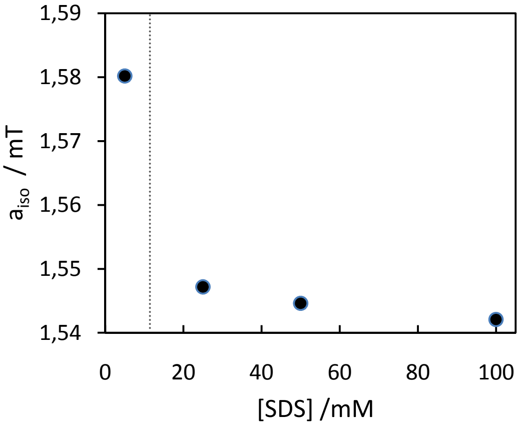

Figure 5.12 Isotropic hyperfine coupling a_{iso} for 0.16 mM 16-DSA in aqueous sodium dodecyl sulfate solutions, obtained from X-band measurements at 25°C. The value for the cmc of SDS (8.3 mM) is indicated with a dotted line.

CW EPR measurements with sodium stearate were unsuccessful, since the low solubility of stearate in water prevents the observation of the cmc and only the isotropic 'water' spectrum of free DSA was obtained. No attempts have been made with sodium octadecylsulfate (SOS). The observation of no micelle formation might be due to the high Krafft point for higher alkyl chain surfactants. For example, the Krafft point for SDS (C12) is T_K(SDS)=16°C [239] whereas that of SOS (C18) is T_K(SOS)=56°C [240]. For the carboxylate surfactants a similar temperature regime for sodium laurate and stearate was found (T_K(laurate)=25°C and T_K(stearate)=65°C [241]). Below the Krafft point no micelles are formed. Thus, only the monomer solution of sodium stearate was obtained at ambient conditions, for which at low DSA concentrations the CW EPR spectrum has nearly the same shape as in pure water.

These first studies in water involved only 16-DSA as spin probe and the values for the hf coupling constant a_{iso} correlate well with reported values in literature for the same system [242]. For 5-DSA no analogue measurements were performed, the values reported in literature are a_{iso}=1.56-1.59 mT [235, 238] (obtained from pure 5-DSA in water).

It should be stressed that the micelle still is a dynamic entity, with exchange of surfactant and DSA molecules with the bulk and other micelles and the lifetime of a surfactant molecule in the micelle is normally 10^{-7}-10^{-6} s. The half-life of the micelle is 10^{-3}-1s [238]. Further, the whole micelle moves freely in space. Thus, the fast, segmental motion of the nitroxide in the micelle is overlaid with a slow motion, which has different contributions: The rotation of the micelle and the diffusion of the probe over the curved surface of the micelle (lateral diffusion) [243-244]. The rotational dynamic of the whole micelle τ_{mic} is determined by its outward size, including the Stern-Layer in the pure solvent water and the rotational correlation time of the DSA moiety τ_{rel} is governed by the size and viscosity of the hydrocarbon core (see Figure 5.3) and the location of the nitroxide within the micelle. The values for the rotational correlation times τ_{corr} listed in Table 5.4 are only the observed 'effective' rotational correlation times of the probe but the spectrum is a superposition of the above mentioned dynamic processes. Under the assumption that the nitroxide probe is fixed in its position in the micelle (no lateral diffusion) the nitroxide and the micelle reorientation can be treated as independent [244]:

$$\frac{1}{\tau_{eff}} = \frac{1}{\tau_{rel}} + \frac{1}{\tau_{mic}} \tag{5.8}$$

τ_{mic} can be estimated by the Stokes-Einstein eq. (2.51) with η the viscosity of pure water (η= 1.1016 mPas [36]) at T=295K and an estimated radius of a SDS micelle R_{mic}=2.56 nm (calculated value from Ref. [245] for an SDS micelle) to $\tau_{mic}\approx 20$ ns. This is only a rough estimation under the assumption of an ideal spherical rotating body but it shows that τ_{mic} is slower than the reorientation of the nitroxide moiety τ_{rel} that is in the range of 0.1 ns (Table 5.4), so that eq.(2.22) can be approximated as $\tau_{eff}^{-1}\approx\tau_{rel}^{-1}$. However, lateral diffusion may have a stronger impact on the spectrum, especially at higher temperatures, where the aggregation number of an ionic micelle is known to decrease [246]. This leads to a less confined surfactant packing combined with the shorter lifetimes of micelle formation kinetics and overall increased mobility due to decreasing viscosity. Further, due to the R^3-dependence in eq. (2.51) it is obvious that the measured effective τ_{corr} and also τ_{mic} will increase with the number n of C-atoms of the used surfactant.

This shows that CW EPR spectroscopy is almost insensitive to collective properties arising from intermicellar interaction but reflects single-particle properties, therefore it is possible to separate those contributions in the analysis of the experimental data.

The results from reference measurements on aqueous micellar aggregates using fatty acid spin probes:

- Below the cmc of the pure surfactant, the spin probe shows characteristics of non-aggregated monomers in dilute aqueous solution, which manifests itself in constant values of hyperfine coupling a_{iso} and rotational correlation time τ_{corr}, independent of the used surfactant (at a given temperature).
- At the cmc of the pure surfactant, DSA is co-micelliced and does not form micelles on its own. Such micellization would be indicated by spin-spin interactions that are not observed in the spectra for the used surfactants (SDS, sodium laurate) in the tested concentration range.

- At higher surfactant concentrations (and with this higher aggregation numbers that will alter the size and the shape of a micelle) the probe 16-DSA is effectively located at the same position (no shift toward the core or the interface).
- The rotation of the whole micelle can be neglected for analysis of the EPR spectra at this temperature.

This shows that CW EPR experiments, the simplest EPR experiments, can be used to obtain cmc values of surfactants: by increasing the surfactant concentration in small steps while keeping the spin label concentration constant. A simple plot of the isotropic hyperfine coupling constant a_{iso} vs. the temperature shows a clear kink at the cmc. For obtaining a_{iso} it is not necessary to perform spectral simulation, it can be read out from the spectra as the separation of the zero-crossing points of the low and high-field line divided by two (see Figure 2.11 b). For examples see Review [232], and how to correlate this data further to the viscosity within the micelle Ref. [247]. This method for cmc determination is not restricted to DSA, but hydrophobic or at least non-ionic spin probes should be preferred, as ionic probes may interact strongly with the headgroups of the tested surfactant. This would lead to other ionization degrees and changes in the area per headgroup by the replacement of water (the molecular order of the interface would change). In the systems under investigation here one should keep in mind that the system contains an additive that may change the value of the cmc compared to the pure surfactant.

- *DSA spin probes in non-aqueous solutions*

The last section has treated the behavior in aqueous micellar systems, but miniemulsions contain a second, oily phase, and the observed nanostructures are formed within a monomer droplet. Hence, reference measurements of DSA in MMA are important to obtain information about the solubility of the spin probe and reference values for its EPR parameters in MMA. Intuitively, one would envisage that DSA will preferably be solubilized in this less polar monomer phase, as it is only slightly soluble in water. In the next sections, though, some of the spectra presented show strong exchange broadening and it was not clear if this could be assigned to insoluble DSA (due to poor solubility in MMA or too high chosen concentrations). Due to lack of miscibility of water and MMA, the reference measurements were performed in pure MMA. Since none of the used anionic surfactants could be dissolved in MMA (dielectric constant of ε=6 [36]), only the CW EPR spectra of the pure spin probes 5- and 16-DSA in MMA were recorded. They are shown in Figure 5.13 (a) for a concentration of 4.4 mM, which is *above* those used in the measurements with miniemulsions.

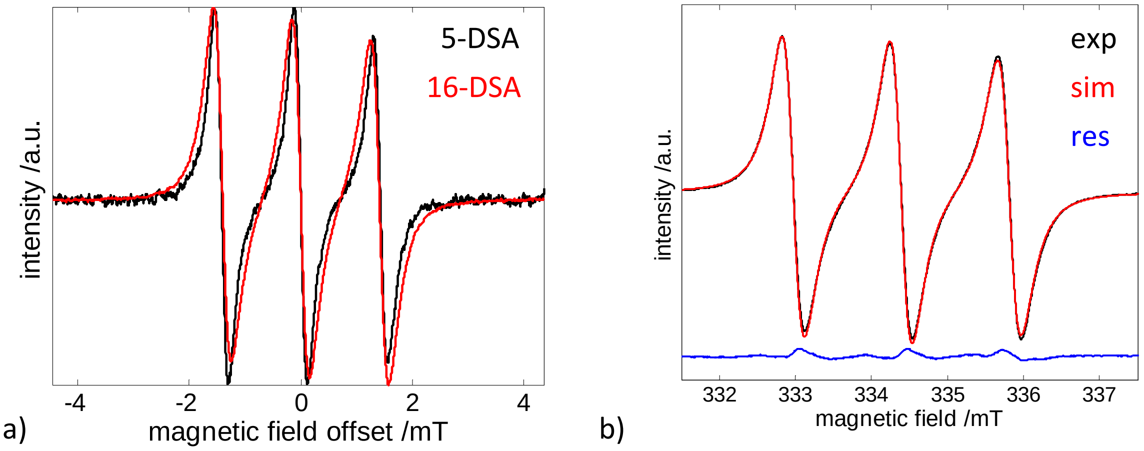

Figure 5.13 a) X-Band CW EPR spectra of the pure spin labels 5-DSA (black) and 16-DSA (red) in methyl methacrylate (MMA) at 25°C. The concentration of both fatty acids is 4.4 mM. 5-DSA gave an inherently worse signal as compared to 16-DSA. The line shapes are indicative of spin-spin interactions among the probes. b) Spectral simulation in the slow motion regime (easyspin function chili) (red) of the 16-DSA CW EPR spectrum (black) with an exchange frequency of 3.4 MHz as found by least-square fitting. Simulation parameters: τ_{corr}= 20 ps, a_{iso}= 1.436 mT, g_{iso}= 2.0058, lorentzian linewidth= 0.25 mT.

At a given concentration the signal to noise (S/N) ratio of 5-DSA is lower than that of 16-DSA in all experiments. Since in a freshly delivered charge the S/N ratio of two samples 5- and 16-DSA was nearly identical this is indicative of simple chemical decomposition in one batch of 5-DSA, which needs to be taken into account during data analysis. This batch of 5-DSA, which was further used in this work, has shown to have an effective spin concentration of 79 %. Hence, the differences for the recorded spectra in Figure 5.13 (a) are mainly due to concentration effects. Nonetheless, the broad line shapes in the CW EPR spectra are clear indications for spin-spin interactions even in the lower concentrated 5-DSA sample (black spectrum). Since the system is still in the fast tumbling regime, the broadening can be assigned to be due to Heisenberg spin exchange and not dipolar interactions, which could be further substantiated and quantified in spectral simulations. Spin exchange interaction between two paramagnetic molecules depends on the radical concentration (see chapter 2.5.1), and higher concentrations increase the probability of a molecular collision. Further, the ratio T/η is important (with η denoting the shear viscosity of the solvent). High temperatures and low viscosities enhance spin exchange. In particular for nitroxides, the viscosity limit where spin exchange dominates the line width was found [32]:

$$\frac{T}{\eta} > 1.5 \cdot 10^4 \frac{°C}{Poise} \tag{5.9}$$

which is $1.5 \cdot 10^5$ °CPa^{-1}s^{-1} in the conventional viscosity unit. For pure MMA at 25°C and $\eta = 0.584 \cdot 10^{-3}$ Pa^{-1}s^{-1} [248], the ratio is T/η $= 4.3 \cdot 10^4$ °CPa^{-1}s^{-1} and is not above but at the borderline of the limiting value. Overall, the exchange frequency is an excellent measure of the local spin probe concentration.

The spectrum for 16-DSA was simulated using slow-motion theory with an exchange frequency of 1.4 MHz and is shown in Figure 5.13 (b). A Voigtian line shape, i.e. a Gaussian - Lorentzian convolution, with 0.085 mT for the Gaussian and 0.33 mT for the Lorentzian part was found. The apparent hf coupling, that was read off the spectrum can be given as a_{iso}= 1.41(9) ±0.008 mT, and is smaller than that found by simulation a_{iso}= 1.43(6) ±0.005 mT. The latter is listed with the other simulation parameters in Table 5.5. From the lower viscosity of MMA (0.6 mPas compared to 1.0 mPas for water at 25°C [36]) a smaller value for τ_{corr} was expected (eq. Stokes). In MMA the value τ_{corr}=20 ps was found, and indeed smaller than for the aqueous samples in SDS (τ_{corr}=90 ps in 5 mM SDS, Table 5.4). It is obvious that DSA is solubilized by MMA since the solubility limit would become noticeable in the EPR spectrum as one broad line (exchange narrowing), as was observed for high DSA concentrations [249]. Furthermore, other studied concentrations in MMA above 4.5 mM DSA show the same lineshapes but with higher exchange frequency: the exchange frequency for 7 mM 16-DSA rose up to 4.3 MHz, and increased further with increasing temperature (data not shown), which is a clear indication for exchange interaction. Hence, for the studied DSA concentrations in the miniemulsion, which were around 2 mM (see basic recipe Table 5.3), we can be sure that the DSA probe is solubilized in the MMA droplets and does not form an insoluble precipitate. From these data one cannot directly tell unambiguously how DSA is solubilized, e.g. if it is homogeneously distributed or forms aggregates. To achieve this, smaller concentrations have to be measured since exchange interactions are a significant effect in the concentration regime of mM and above [27].

Table 5.5 Isotropic hyperfine coupling a_{iso}, rotational correlation time τ_{corr} and exchange frequency ω_{Ex} for 16-DSA in MMA[a] and in 5 mM stearic acid solution[b] (in MMA) at X-Band frequency (9.4 GHz). The EPR parameters were obtained by spectral simulation and least-square fitting in the slow motion regime with isotropic rotational diffusion tensor and a Lorentzian line width of 0.23 mT and g=[2.0086, 2.0057, 2.0030]. The error for a_{iso} is ±0.005 mT, for τ_{corr} ±20 ps and for ω_{Ex} ±0.3 MHz.

Solvent	**[16-DSA] /mM**	**T /°C**	**a_{iso} /mT**	**τ_{corr} /ps**	**ω_{Ex} /MHz**
MMA	4[a]	25	1.428	50	1.4
	0.1[b]	25	1.444	60	0.7

In order to obtain an undistorted a_{iso} value and to mimic the surfactant environment present in miniemulsions, samples of low [DSA] in MMA/ stearic acid solutions were prepared. The spin label concentration was kept constant at 0.1 mM (1/30 part of the above reported concentration in pure MMA) and different stearic acid concentrations were used (5, 50, 100 mM). The spectra (data not shown) were very similar to the ones in pure MMA (Figure 5.13 a). The S/N ratio was worse as compared to higher [DSA], but the line shape again was reproduced best by simulation with a small value of exchange broadening ω_{Ex} (~0.7 MHz). This value is smaller than ω_{Ex} for pure DSA in MMA, but exchange broadening is still present even at this low concentration. The a_{iso} values only differ in the second decimal as compared to those of 3mM DSA in MMA, which can be neglected.

Form these CW EPR experiments in water and MMA one can see that the a_{iso} (and also g_{iso}) value of DSA is very sensitive to the environment. Therefore, the values can be used to characterize the location of a spin probe in a micelle. A higher value indicates an effective position towards the (more polar) interface, a lower value can be assigned to a location towards the (more hydrophobic/apolar) core. The same holds true for more complicated systems like colloidal emulsions or dispersions, where a third phase is present. For a system composed of water, MMA and DSA one can now immediately predict the spectra for a partitioning of DSA between the water and MMA phase by combination of the spectral parameters of DSA in the two pure phases (Table 5.4, Table 5.5). In the Appendix a simple program is given built on the program package *EasySpin* for MATLAB [48].

5.5 Miniemulsions Containing Sulfate Surfactants

This chapter summarizes the performed X-Band CW EPR measurements and results for sulfate-containing surfactants, SDS and SOS (C12 and C18). Polymer particles, prepared via miniemulsion with sulfate surfactant in presence of Ln(tmhd)$_3$, are known to form multilamellar (onion-like) nanostructures [196, 231]. A TEM picture of such a particle is shown in Figure 5.14. The spin probes 5-DSA (head label) and 16-DSA (chain end label) were used and each sample was prepared twice, once without a lanthanide-β-diketonate complex and once with the complex Eu(tmhd)$_3$. In the following figures spectra without complex are colored in black, and spectra with complex in red.

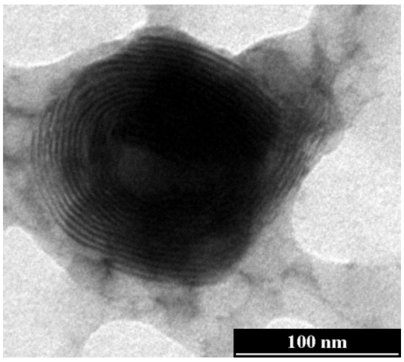

Figure 5.14 TEM picture of an onion structured nanoparticle, prepared via miniemulsion polymerization of MMA with SDS in presence of Eu(tmhd)$_3$ (made by C. Hauser).

5.5.1 Miniemulsions Prepared with 16-DSA

Figure 5.15 compares the CW EPR spectra of SDS (a) with SOS (b) for the spin probe 16-DSA.

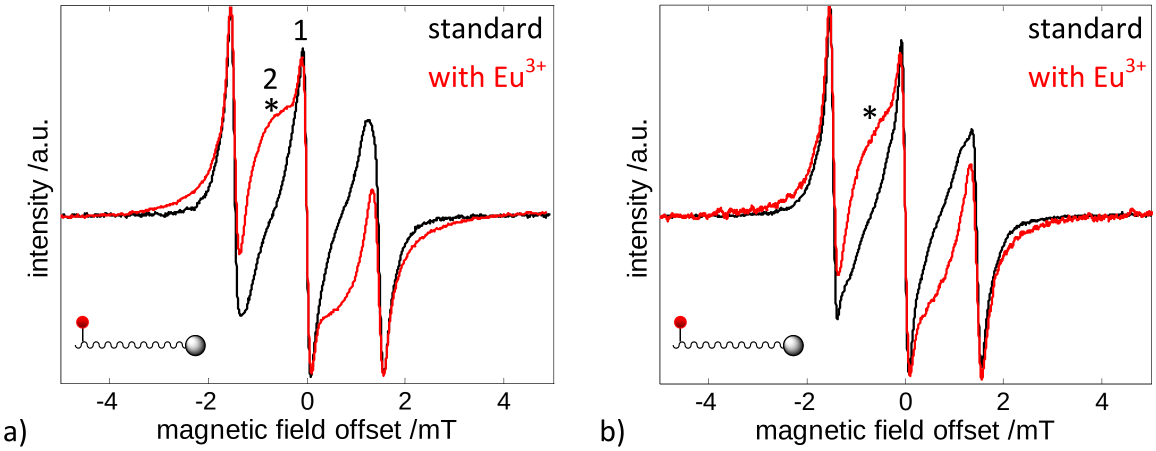

Figure 5.15 16-DSA CW EPR spectra of miniemulsions prepared with a) sodium dodecyl sulfate (SDS) and b) sodium octadecyl sulfate (SOS). The spectra in black are miniemulsions prepared without lanthanide-β-diketonate whereas the red ones contain Eu(tmhd)$_3$. Measurements were performed at 25°C at X-Band frequencies (9.5 GHz). The concentration of 16-DSA was 5 mol.-% with respect to the according surfactant (Table 5.3). The numbers mark the two components of the EPR spectrum. Species 1 is attributed to fast rotating DSA molecules at the MMA/water interface, species 2 is located in the MMA droplet (see text). Spectra are normalized to their maxima.

The CW EPR spectrum of 16-DSA in a miniemulsion prepared with SDS (black spectrum in Figure 5.15 a) shows remarkably line broadening. The presence of two DSA species is indicated at the minimum of the low field line and the maximum of the high-field line as an asymmetric distortion of the extrema. With addition of Eu(tmhd)$_3$ complex to the miniemulsion, these two species are clearly separated in the spectrum (red), as indicated by the numbers '1' and '2'. The signal marked with '1' is formed from faster rotating 16-DSA molecules that exhibit a usual nitroxide three line spectrum with relatively narrow line widths. It is overlaid with a second spectrum of a broadened component '2' (marked by an asterisk). The origin of this experimental finding of a bimodal EPR spectrum is the existence of two spin probe species with different mobilities. These species do not exchange with each other on the EPR time scale. The line broadening is due to Heisenberg spin exchange, again as found from spectral simulation. Attempts were made to simulate the spectrum of the miniemulsion without complex (black) with only one single component with an exchange frequency ω_{Ex}, which accounts for collisions between two nitroxide moieties. The simulation could be acceptable with respect to line broadening. But the relative heights of the three lines and the remarkable distortion of the two extrema could not be reproduced. A much better simulation result (Figure 5.16 a) was obtained with introduction of a second species. Each spectrum was computed separately and subsequently they were added. The fraction (i.e. weighted contribution) of each species was allowed to vary to reproduce the experimental spectrum. One spin probe was defined as faster rotating species (blue) and a second one that is slower and has a defined exchange broadening (green). This procedure could reproduce the observed line shape very well and the sum spectrum of the two species is plotted in Figure 5.16 b. The best simulation was obtained with 90 % of the broad species 2 with an exchange frequency ω_{Ex}=9 ± 1 MHz, an isotropic hf coupling a_{iso}= 1.43 ± 0.008 mT (calculated from hf tensor elements **A**=[0.5,0.5,3.3] mT) and a rotational correlation time of τ_{corr}=560 ± 250 ps. Due to the broad lines the error of the latter with ±250 ps is relatively high. The faster species 1, which is faster than the broadened component, is characterized by a_{iso}= 1.46 ± 0.01 mT (calculated from **A**=[0.51,0.51,3.37] mT), and a rotational correlation time of τ_{corr}=170 ± 70 ps (fast motion regime). In the previous chapter it was shown that even diluted, fast rotating DSA molecules in MMA show exchange broadening. Therefore, it was assumed that this fast species intrinsically has roughly 1/4 of the exchange broadening (ω_{Ex}=0.37 MHz) that was obtained from pure DSA in MMA solution (ω_{Ex} (MMA)=1.4 MHz, Chapter 4.4).

The hf coupling of 16-DSA in MMA was a_{iso}=1.43 mT, and in water/SDS micelles a_{iso}=1.54-1.58 mT (see Chapter 4.4). Thus, the faster species 1 can be attributed to DSA molecules on the surface of MMA droplets, in the MMA-water interface. The value a_{iso}= 1.46 mT for this DSA fraction is slightly higher than for those found in pure MMA, and too low to be attributed to DSA molecules that may be free in aqueous solution (but of course there is an equilibrium exchange between inerfacial bound DSA and non-bound, aqueous DSA). The different environments for the DSA labels cannot be seen clearly in the simulated spectra of each component (Figure 5.16 a), since g_{iso} was only slightly higher for the monomer phase (green spectrum). From this analysis we may assume that there are no free, unswollen surfactant micelles with DSA molecules, since such a fraction would be visible in the spectrum due to their small line width and large hf value. Note that the amount of the fast fraction is only 10 ± 4 %. Due to the sharp lines such a fast fraction is visible in the spectrum even if its relative amount is low.

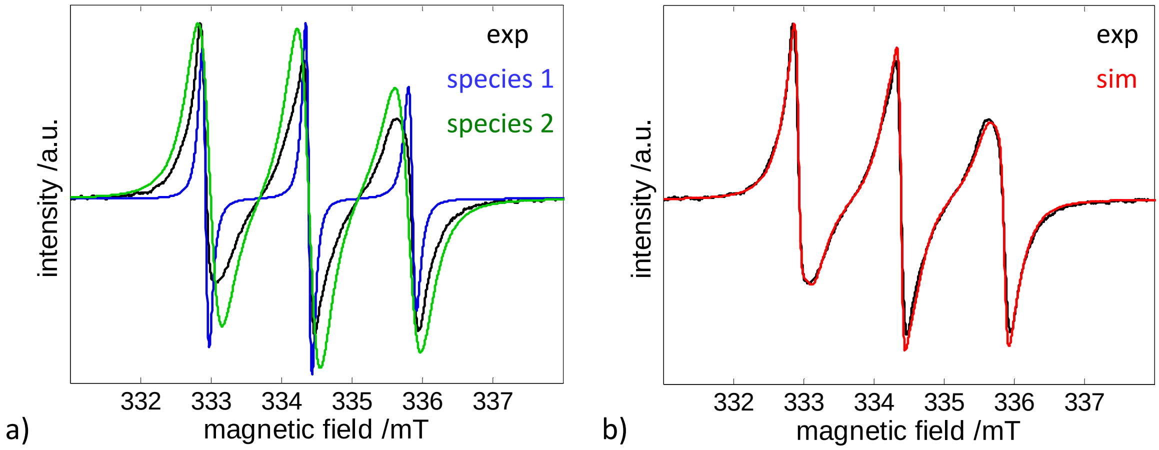

Figure 5.16 a) Fast motion simulation of the two components that contribute to the observed EPR spectrum (black) of the miniemulsion *without* complex in SDS from Figure 5.15 a (16-DSA). The broadened species 2 (green) was simulated with an exchange frequency ω_{Ex}=9 MHz. b) The sum spectrum (red) of the two components, where the broadened species 2 contributes to 90 %.

By visual comparison of the spectra without vs. with complex in Figure 5.15 a (black vs. red spectrum) one can see the much broader line width of species “2”, which is most pronounced at the central line but also clearly visible at the outer flanks of the low- and high-field line. This behavior may either arise from an increase in the fraction of the broadened species 2 or from an increased exchange broadening. By inspection of the pure spectrum of the broadened species 2 (green spectrum in Figure 5.16 a, which is 100 % of this species 2), it is obvious that even 100 % of this broad component cannot lead to the observed spectrum in Figure 5.15 a. Indeed, spectral simulations show a strong increase in the exchange frequency ω_{Ex} of this species up to 44 ±2 MHz for the sample with complex.

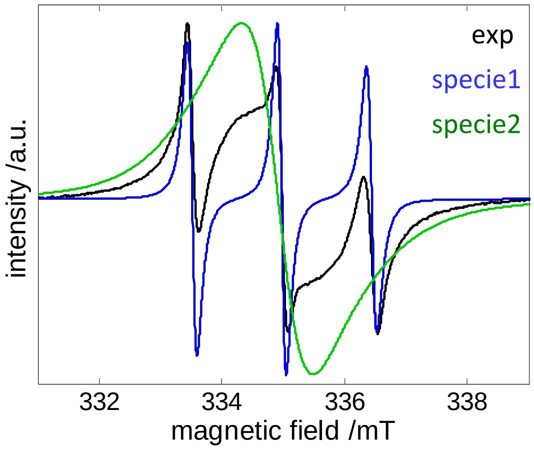

Figure 5.17 Simulation of the two components of the miniemulsion *with* complex from Figure 5.15 a (SDS, 16-DSA, Eu(tmhd)$_3$), with a Heisenberg exchange frequency ω_{Ex}=44 MHz for the broad component (specie 2, green).

This is such a high frequency, that the pure spectrum of species 2 is already in the exchange narrowed region (fast exchange) and only shows one broad peak (green spectrum in Figure 5.17). This means that the effective local concentration of electron spins has become very high in this sample only for this component. For such a broad component the value of observed rotational correlation time may be wrong. For the sake of completeness, the values for τ_{corr} and the hf tensor **A** for the simulation of the broad component are given in Table 5.6 but have a rather large margin of error. As a good approximation the fast component of this spectrum has the same simulation parameters as in the simulation without complex, hence, the fast component does not change its motional characteristics upon complex addition.

Table 5.6 The two spin system as defined for spectral simulation with the easyspin function 'chili' (slow motion) to fit the experimental spectra of 16-DSA in SDS miniemulsion with and without the complex Eu(tmhd)$_3$ from Figure 5.15 (at 25°C). The g-value was g_{iso}= 2.0057 for both components. The rotational correlation time was calculated from the isotropic rotational diffusion tensor D by τ_{corr}=1/6D (eq. (2.51)) Numbers in brackets have an error of more than 25%. The remarkable change upon complex addition is the Heisenberg exchange frequency. The simulated EPR spectra of both components are illustrated in Figure 5.17 (90% slow component).

Component	**EPR parameter**	**Without Complex**	**With Complex**
Broad Species 2	A /mT	0.5,0.5,3.3	(0.5,0.5,3.3)
	lw /mT	0.2	0.3
	τ_{corr} /ns	0.56	(0.66)
	ω_{Ex}/MHz	**9**	**44**
Fast Species 1	A /mT	0.51,0.51,3.37	0.51,0.51,3.37
	lw /mT	0.2	0.2
	τ_{corr} /ns	0.21	0.21
	ω_{Ex}/MHz	0.37	0.37

16-DSA is non-symmetric and it is assumed that the rotational diffusion about the long axis (the C18 alkyl chain) is slower compared to that about the x-or y-axis (see Figure 2.14). The introduction of anisotropic motion did not improve the simulation results, though, as the broad lines allow simulations within a range of correlation times and orientations of the diffusion tensor leading to an identical quality of the sum spectrum of both components.

To clarify the question whether the appearance of this strongly exchange-broadened component is an intrinsic property of the sample or due to a concentration effect of too much spin probe or precipitated DSA (although we know from Section 5.4 that in this concentration regime DSA is solubilized), the concentration was reduced by a factor 2 (corresponding to 2.5 mol % with respect to the surfactant). To check that the spin probes leading to the broadened signal are actually located in the miniemulsion and do not participate in clusters of undissociated carboxylic acid DSA molecules. Hence, this sample was prepared in 0.1 m NaOH, in which 16-DSA is soluble and completely dissociated (COO^-). The EPR spectrum of this sample fully reproduces the previous spectra obtained for 5 mol.% DSA. The broad feature was still observable besides the faster rotating species. The relative amounts of the two components were slightly different but still within the experimental error. We can conclude from the spectra that neither insoluble DSA nor a change of the effective location of both DSA components due to incomplete dissociation are existent in the samples. The spectra for this sample (including its temperature-dependence up to 55°C) are shown in the Appendix.

Going from C12 (SDS) to the C18 (SOS) surfactant (comparing Figure 5.15 (a) with b), one can notice two things. First, the observed line shapes for both miniemulsions (without complex in black and with complex in red) are very close to those found in the C12 surfactant. Again, two species are observable in the miniemulsion without complex, and the exchange frequency of the broadened component (species 2) increases upon complex addition. Second, the exchange broadening of this component seems to be less severe as compared to the case in C12 surfactant for both types of miniemulsions (with and without complex). The flanks of the nitroxide spectrum with complex are not as broad, and the central line is not as high as for the similar C12 surfactant. The exchange frequency for C18 sulfate surfactant is ω_{Ex}=33 ±3 MHz and is ~10 MHz less than for C12 surfactant (obtained from simulations). The relative fractions of each component are similar to those in C12 surfactant miniemulsions (10 ± 5% “fast” species 1, 90 ± 5% “slow” species 2).

To summarize the results found for *16-DSA* in miniemulsions that were prepared with sulfate surfactants: Two dynamic (and spatially) different DSA species are present in miniemulsions in presence and absence of $Eu(tmhd)_3$ that do not site-exchange on the EPR time scale, otherwise an averaged signal would be observed. Upon complex addition we see extreme changes in the EPR spectrum that can be attributed to an increase of the Heisenberg spin exchange frequency ω_{Ex} of one component. ω_{Ex} of the broadened component (species 2), which is also present in the complex-free miniemulsion, increases by a factor of ~5 for C12 surfactant and ~4 for C18 surfactant. Hence, with increasing chain length of the surfactant, the exchange frequency drops down. The fraction of both components in both surfactant systems is virtually identical. Species 1 with sharp lines (faster rotation) has slightly higher isotropic hf coupling values, which indicates a location more exposed to water, but not fully solvated by water. Species 2 (broad EPR spectrum) has an isotropic hf coupling value that is typical for DSA in pure MMA and hence can be assumed to be located within the monomer droplet. One should be aware, though, that this value of a_{iso} could also be (partially) due to the increased exchange frequency [29].

We can assign this exchange-narrowed component in the presence of Eu(tmhd)$_3$ to 16-DSA, distributed within layered structures (as observed after polymerization in TEM), where the flexible alkyl chains can interact very strongly with each other even for low DSA concentrations. The spectra were measured at 25°C, and in liquid solution such high exchange interaction was not assumed. This can only be explained with a quite high rigidity of these structures in the head group region, that lead to a very confined region in the interior for the alkyl chain ends of 16-DSA. With increasing surfactant chain length from C12 to C18 the exchange interaction becomes less pronounced, which could be explained by a widened thickness of the bilayers as illustrated in Figure 5.18 that leads to less interaction possibilities between the spin probe parts on the chain ends.

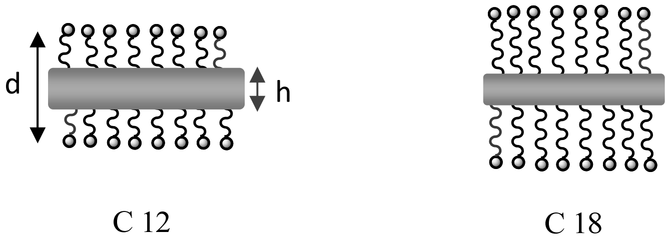

Figure 5.18 The interacting volume for 16- DSA incorporated in a C12 bilayer is higher than in a C18 bilayer. The interacting volume represents the effective volume for spin exchange and is determined by the bilayers width d (e.g. the surfactant chain length) and the flexibility of the doxyl- label hydrocarbon chain. In this picture the chains are fully extended, which will never be the case but illustrates the maximum height of the interacting volume. In a C12 bilayer, the flexible 16-DSA chain end can bend back and, hence, the nitroxide has more degrees of freedom which will also increase the possibility for spin exchange.

In a C12 bilayer the thickness between the head groups d is smaller than in the C18 bilayer. For simplicity we assume *fully extended* alkyl chains. 16- DSA possesses a C18 alkyl chain and engages a higher volume in the center of a C12 bilayer as compared to a C18 bilayer. This is shown as a grey box in Figure 5.18, where the height h of the volume is given by the label position of two (extended) DSA molecules from opposite monolayers. Due to alkyl chain flexibility spin exchange may happen within this volume. But alkyl chains are never fully extended in bilayers and 16-DSA can adopt several conformations (a decrease of h) that increase the spin concentration in the center of the bilayers. Due to the effectively higher interacting volume we find a higher exchange frequency for 16-DSA in C12 bilayers than in C18 bilayers.

The samples *without* and *with* Eu(tmhd)$_3$ (Figure 5.15 a) were prepared with same DSA concentrations and under the same conditions. In the complex-free miniemulsion we have noticed the presence of a similar exchange broadened component to that within the layer-structures in presence of Eu(tmhd)$_3$. In pure water and pure MMA we observe only one DSA species. It is not clear if more fluid counterparts of such structures exist even in complex-free miniemulsions. This cannot be excluded from these measurements.

5.5.2 Miniemulsions Prepared with 5-DSA

In Figure 5.19 the CW EPR spectra of 5-DSA in miniemulsion prepared with sodium dodecyl sulfate SDS are shown for the complex-free miniemulsion (black) and with complex Eu(tmhd)$_3$ (red).

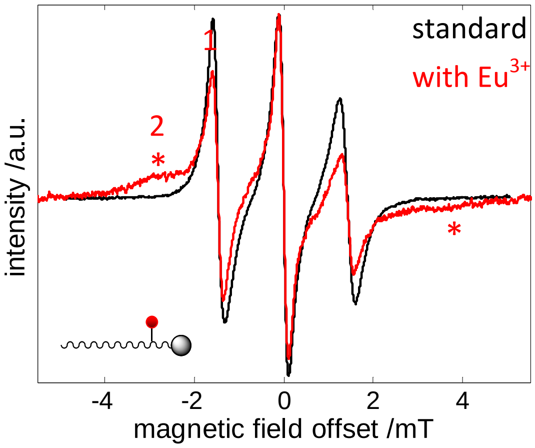

Figure 5.19 5-DSA CW EPR spectra of miniemulsions prepared with sodium dodecyl sulfate (SDS) in the presence (red) and absence (black) of Eu(tmhd)$_3$. Measurements were performed at 25°C at X-Band frequencies (9.5 GHz). The concentration of 5-DSA was 5 mol.-% with respect to SDS (Table 5.3). The composition of both miniemulsions is the same as in Figure 5.15 a, where 16-DSA was used. The asterisks mark the slow component of the spectrum. Spectra are normalized by their maximum.

The spectrum in black was prepared without complex. It seems to exhibit a typical nitroxide three line pattern but spectral simulations again reveal that the best reproduction of the experimental spectra is achieved by defining two species. The two components do not differ much from each other, hence, their spectral features are not resolved. The values for the hf tensor elements were adapted from the former simulation and are listed in Table 5.7. The parameters obtained for the fast component are similar to those of the fast component in 16-DSA, but the spin label now is attached at the 5th position, which leads to a remarkable decrease in spin label mobility.

For the 5-DSA spectrum in miniemulsion *with* complex (red spectrum), a decreased nitroxide intensity is observed. Such a decreased intensity upon complex addition was also observed for 16-DSA miniemulsions, but the effect for 5-DSA is much more pronounced. Furthermore, the spectrum now reveals two components of significantly different rotational mobility; a faster rotating one (marked with number 1) with three relatively sharp lines and one very slowly rotating component (number 2). The distance between the left maximum and right minimum is ~6.0 mT. It is a powder like spectrum and this splitting is characteristic for a nitroxide in a nearly frozen state (see Table 2.2). In this sample a fraction of 5-DSA exists, in which the nitroxide moiety is strongly immobilized. This is not seen in the corresponding spectrum of the miniemulsion without the complex (shown in black). The simulated EPR spectrum of each component is shown in Figure 5.20 a) and the sum spectrum of both in (b). The same sum spectrum could be obtained by two different methods: either the broad component 2 was defined with very slow rotation τ_{corr}=10 ± 5 ns combined with exchange broadening ω_{Ex}= 5 ±1 MHz in the slow motion limit ('chili'), or the simulation of this component was performed in the in the rigid limit with additional H-Strain[2] (τ_{corr} >10^{-6}s). Since this miniemulsion is a liquid, measured at 25°C together with the fact that the latter results in a slightly larger rms deviation from the experimental spectrum, the first set of simulations can be identified as describing the system properly. The parameters obtained for the best simulation of both components are listed in Table 5.7. The listed value for τ_{corr} of the broad component is 12 ns, which is in the slow motion regime; this was the value with the best fit to the experimental spectrum, although a much broader range of correlation times could be used (10 ± 5 ns). This is immediately obvious from the experimental spectrum (shown in red in Figure 5.19): The flanks of the broad component extend over a range of more than 1 mT (between -2 to -3 mT field offset). This is too high to be attributed to the intrinsic line width of this component. It seems more to be due to a distribution of correlation times between ~10-20 ns (distribution between slow motion to rigid DSA spectra). The presence of one defined correlation time would be visible as a much sharper peak. The implementation of anisotropic motion (assumption of axially symmetric rotational diffusion tensor) did not improve the outcome, unless Euler angles were defined (that describe the orientation of the rotational diffusion tensor in the molecular frame). For simulations with Euler angles the outer flank could also be reproduced as a distribution over motional orientations, while keeping the diffusion rate constant. This method seems also applicable since DSA is expected to show anisotropic motion. However, the resulting spectra were similar in their shape to the isotropic ones, and the listed values in Table 5.7 were adapted from the isotropic simulation.

It can be seen that the fast component only slightly slows down upon complex addition. The mobility of this fast 5-DSA component (τ_{corr}=0.55 ns) is slightly decreased compared to the fast component in 16-DSA from the previous section (τ_{corr}=0.21 ns, Table 5.6), but of the same order of magnitude. 16-DSA is expected to have higher degrees of motional freedom than 5-DSA due to the flexibility near the alkyl chain end. The slow component, on the other hand, is significantly slowed down upon complex addition in the case of 5-DSA but less so for 16-DSA. If one assumes that the surfactant headgroups bind to the complex and form an interface layer (as indicated by other experiments) the 5-DSA slowdown can be viewed as a straightforward consequence, as the 5-position must be affected much more severely by complexation than the 16-position.

---

[2] H-Strain is a line broadening model that accounts for unresolved hyperfine splitting in EPR simulations [49].

Table 5.7 The two species system as defined for spectral simulations of the experimental spectra of 5-DSA in SDS miniemulsion with and without the complex Eu(tmhd)$_3$ from Figure 5.19 (at 25°C). Slow motion theory was used. The g-value for both components was g_{iso}= 2.0057. The rotational correlation time was calculated from the rotational diffusion tensor D by τ_{corr}=1/6D with isotropic D eq.(2.50). The remarkable change upon complex addition is the decrease in rotational correlation time of the slow component. The simulated EPR spectra with these parameters are illustrated in Figure 5.20 a (with 80% slow component).

Component	**EPR parameter**	**Without Complex**	**With Complex**
Slow	A /G	5.0,5.0,33.0	5.0,5.0,33.0
Species 2	lw /mT	0.18	0.3
	τ_{corr} /ns	**0.55**	**12**
	ω_{Ex}/MHz	4	4
Fast	A /G	5.1,5.1,33.7	5.1,5.1,33.7
Species 1	lw /mT	0.18	0.18
	τ_{corr} /ns	0.33	0.55
	ω_{Ex}/MHz	0.37	0.37

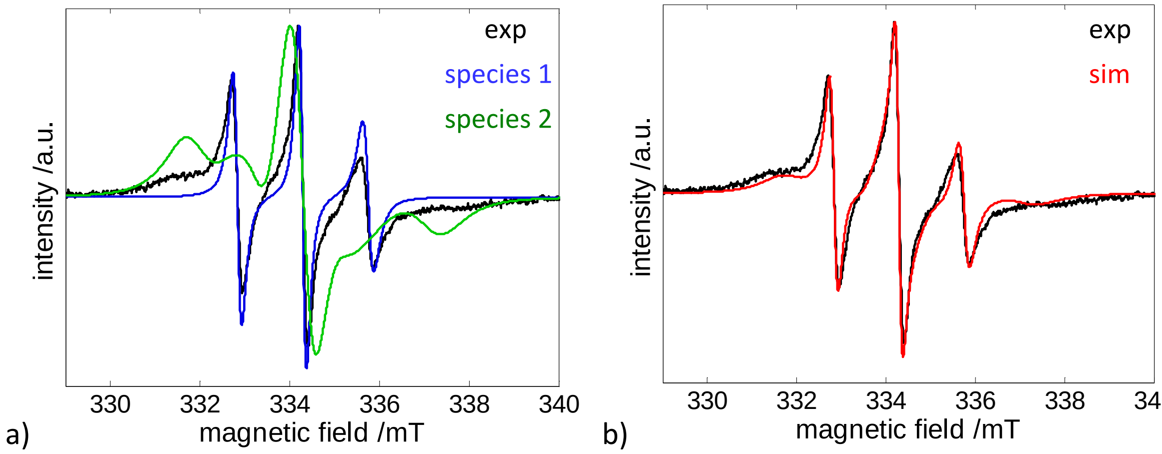

Figure 5.20 a) Simulation (slow motion regime) of the two components that contribute to the observed EPR spectrum (black) of the miniemulsion *with* complex in SDS from Figure 5.19 (5-DSA). The slow species (green) was simulated with an exchange frequency ω_{Ex}=4 MHz and a rotational correlation time τ_{corr}= 12 ns and the fast component (blue) with τ_{corr}= 0.6 ns. b) The sum spectrum (red) of the two components, where the slow component contributes to 80 %.

Hence (see Table 5.7) the factor, that most strongly influences the spectrum of 5-DSA (and in particular the *slow* DSA-component) upon lanthanide complex addition is the rotational correlation time τ_{corr}, while for 16-DSA it was the Heisenberg exchange frequency ω_{Ex}. Comparing the rotational correlation times for slow component of those two DSA types shows for 5-DSA: τ_{corr}= 12 ns (Table 5.7) and for 16-DSA: τ_{corr}~ 0.5-0.7 ns (Table 5.6). Thus, by changing the spin label position from the head to the tail the motional reorientation of the nitroxide is increased more than 17-fold. The fraction of this component found by simulation in 16-DSA (with 90 %) is higher than that for 5-DSA (80 %).

The data obtained for 5-DSA in SDS in complex-free and complex-containing miniemulsion confirm the picture of a very rigid structure in presence of the complex for the structured region. This rigidity has dramatic effects for the 5th position of DSA that exhibits a nearly rigid limit EPR spectrum and indicates an ordered head-group region of the surfactant.

5.6 Miniemulsions Containing Carboxylate Surfactants

In Chapter 4.5 the CW EPR spectra of miniemulsions prepared with sulfate surfactant were discussed. This chapter summarizes the performed EPR measurements on miniemulsions, which were prepared with sodium stearate as surfactant (C18 alkyl chain). PMMA particles, prepared via radical miniemulsion polymerization with this surfactant in presence of Ln(tmhd)$_3$, are known to from lamellar nanostructures [231]. A TEM picture of a PMMA particle that contains these nanostructures is shown in Figure 5.21. The spin probes 5- and 16-DSA were used. Again, the same miniemulsion was prepared twice, once without and once with the complex Eu(tmhd)$_3$. The surfactant sodium laurate (C12) is not shown explicitely in this chapter but is compared to sodium stearate in the discussion (Section 5.9).

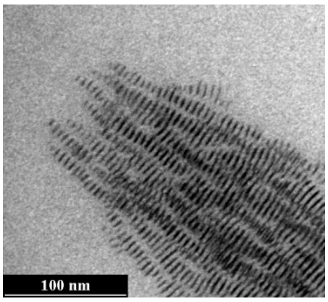

Figure 5.21 TEM picture of lamellar tructures of PMMA particles, polymerized via miniemulsion with sodium stearate in presence of Eu(tmhd)$_3$ (C. Hauser).

5.6.1 Comparison of 5- and 16-DSA

Figure 5.22 displays the CW EPR spectra of 16-DSA (a) and 5-DSA (b) in miniemulsions that were prepared with sodium stearate.

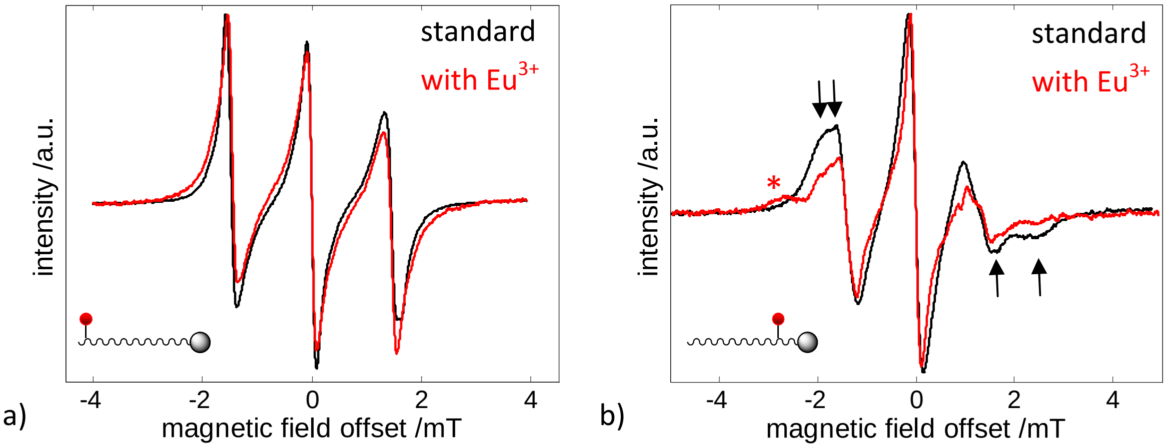

Figure 5.22 CW EPR spectra of miniemulsions prepared with sodium stearate in the presence (red) and absence (black) of Eu(tmhd)$_3$ with a) 16-DSA, b) 5-DSA. Measurements were performed at 25°C at X-Band frequencies (9.5 GHz). The concentration of DSA in both cases was 5 mol.-% with respect to stearate (Table 5.3). Spectra are normalized by their maximum.

The visual inspection of the 16-DSA spectra (a) in *absence* (black) of Eu(tmhd)$_3$ leads to the assumption that the local environment for 16-DSA in sodium stearate is similar to 16-DSA in SDS or SOS complex-free miniemulsions (Figure 5.15 a and b, respectively): Two components contribute to the observed spectrum. In particular, this can be seen by careful inspection of the line widths and relative heights, and was again confirmed by simulation. Thus, a sharp line (faster component) is overlaid with an exchange broadened one (slower component). The comparison of the spectrum of the miniemulsion with complex (red) shows a slight increase in the line width of the broad component, which can be attributed to an increase of the exchange interaction. However, the difference to the spectrum without complex is very small. Nearly the same spectra were obtained for miniemulsions with sodium laurate (C12, COO^-) and 16-DSA. Simulation parameters are close to those reported in Table 5.6 for 16-DSA in SDS (only the left column without complex) and are not presented.

The EPR spectrum *with* complex, however, differs obviously from the previously shown spectra in SDS or SOS. Here, there is only a slight increase in the exchange frequency of the slower component that causes increased line widths, which can be seen at the outer flanks in the red spectrum. The increased ω_{Ex} (~9 MHz± 5%) is also responsible for the decrease of the low-field line minimum and high-field line maximum.

The EPR spectrum of 5-DSA in a stearate containing miniemulsion is shown in Figure 5.22 b. In the absence of lanthanide-β-diketonate complex (black) more or less well defined extrema are found in the spectrum. These spectral features are characteristic for highly anisotropic motion [44] of the DSA molecule and the observed shape arises from axial symmetry of the nitroxide group motional characteristics: The rotation about the x- and y axes is much slower as compared to the motion along the z-axis that is co-linear with the long axis of the alkyl chain of the fatty acid (see Figure 2.14). Although the spectrum is highly anisotropic, the line width is relatively sharp, which indicates fast motion. This situation may arise due to a strong anchoring of the carboxylate head group at an interface or an ordered structure of surfactant molecules like a lamellar phase, where chains are more or less regularly packed, which would lead to anisotropic motion.

In the presence of the lanthanide complex Eu(tmhd)$_3$, the obtained EPR spectrum (red in Figure 5.22 b) is still anisotropic in nature, but a further feature that is marked with an asterisk can be seen. This is a small fraction of immobilized DSA, similar to that found in the 5-DSA/SDS miniemulsion (Figure 5.19). Further, the signal intensity has decreased compared to the complex-free miniemulsion by a factor of 4.5. This was also observed for 5-DSA spectra in SDS with Eu(tmhd)$_3$ and it seems, that it is a special property of 5-DSA in addition with the lanthanide complex. Indeed the intensity is also reduced for 16-DSA but not as much as for 5-DSA. This effect is discussed in Section 5.6.2. Thus, the similarities of the EPR spectra from *one* spin probe in *different* surfactant systems are highly visible. Remarkably, the line width of the central line is decreased in presence of the complex.

For simulation of 5-DSA spectra, different models were assumed. The previously used *two-species* model with *isotropic reorientation* well reproduces the 5- and 16-DSA CW EPR spectra in SDS and SOS and also 16-DSA in sodium stearate. This model assumes two DSA species, which differ in their mobility, which in return reflect their environment. This is also what we assume from the system, where one component is located at the monomer/water interface and one within the structured region in the bilayers and thus give rise to different mobilities of the spin probes. But it is clearly not applicable to 5-DSA in stearate-based miniemulsion: The apparent splittings present at the extrema of the low- and high-field line (indicated with arrows Figure 5.22 b) cannot be achieved by changing *only* τ_{corr} of the components, since the splitting at the low field line is very small compared to the difference between the two minima at the high-field line, and the line widths within the used rotational model (that has to assume a slow motion to account for the relative heights of the lines) is always much too broad. In this case the introduction of anisotropic motion improves the results and two different anisotropic diffusion tensors that differ in their magnitude were defined. Both components are in the slow-motion regime (τ_{corr}~1-10 ns). In this regime, the heights and position of the outer peaks are very sensitive towards small changes in the motion. The components can be characterized by diffusion rates with a lower limit of ~30 MHz for the slower and ~80 MHz ±20 MHz for the faster component, which corresponds to averaged values for τ_{corr} of ~5 and 2 ns respectively. The simulation was not satisfactory with respect to relative heights of the lines. The implementation of Euler angles were defined for motional reorientation, with β=30° for both components which improved the results. A single-species model was tested and did not deliver satisfactory results.

However, quite good results were obtained by applying the MOMD model (*microscopic order macroscopic disorder*), that was originally introduced for explaining EPR spectra of protein-containing lipid dispersions [250]. Such spectra showed very similar line shapes to the one found in the discussed miniemulsions. The model can be generally used for samples where regions with high microscopic order exist, like for example the multilamellar fragments in the present miniemulsion, and where these (highly ordered) fragments are distributed randomly over the whole sample (e.g. a dispersion). Thus, the spectrum is a superposition of all bilayers orientations. The MOMD model is a single-species model where slow motion-spectra over the possible ‘director’ orientations are summed. Here, the director axis is the normal to each bilayer’s fragment surface Figure 2.14. The molecules in the ordered bilayers experience an ordering potential, which restrict the amplitude of rotational motion and the larger the ordering potential, the smaller will be the range of orientations sampled by the motion [250].

5.6.2 Comparison of Eu(tmhd)$_3$ and Gd(tmhd)$_3$

In this Section, CW EPR spectra of 5-and 16-DSA in miniemulsions with either Eu^{3+} or Gd^{3+} as metal ion in the β-diketonate complex are compared. The change of the metal ion was only done in sodium stearate containing miniemulsions and the spectra for 5-DSA are shown in Figure 5.23, and for 16-DSA in Figure 5.24. The figures show the integral normalized spectra of DSA in absence of complex (black), with Eu(tmhd)$_3$ (red) and Gd(tmhd)$_3$ (blue). In all measurements, the composition was held fixed and the DSA content was 5 mol.-% with respect to sodium stearate, thus all spectra contain the same concentration of DSA and are normalized to the complex-free spectrum.

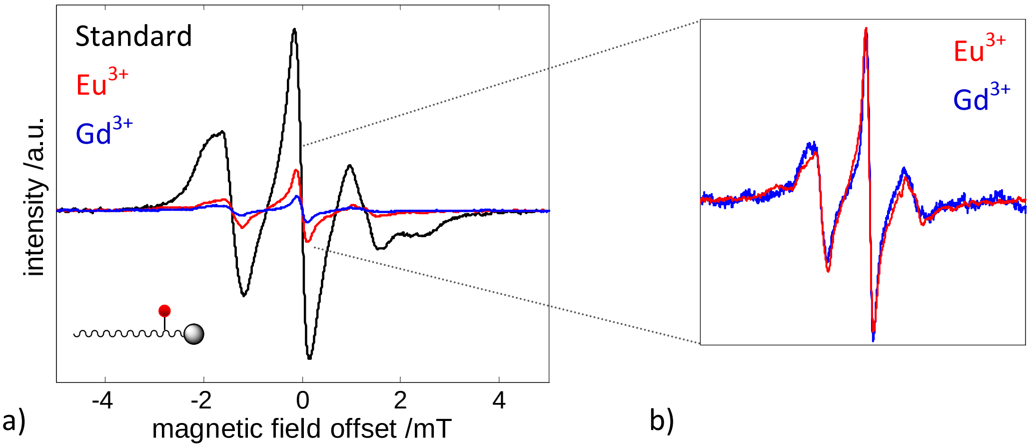

Figure 5.23 a) Integral normalized CW EPR spectra of 5 mol% **5-DSA** in sodium stearate miniemulsion without complex (black), with diamagnetic Eu(tmhd)$_3$ (red) and paramagnetic Gd(tmhd)$_3$ (blue). The spectra without complex and in presence of Eu^{3+} were measured at 25°C, the spectrum with Gd^{3+} at 0°C. b) For comparison of the DSA-spectra with Eu^{3+} and Gd^{3+} these spectra are normalized by their maximum. Spectra in presence of a lanthanide complex show reduced signal amplitudes.

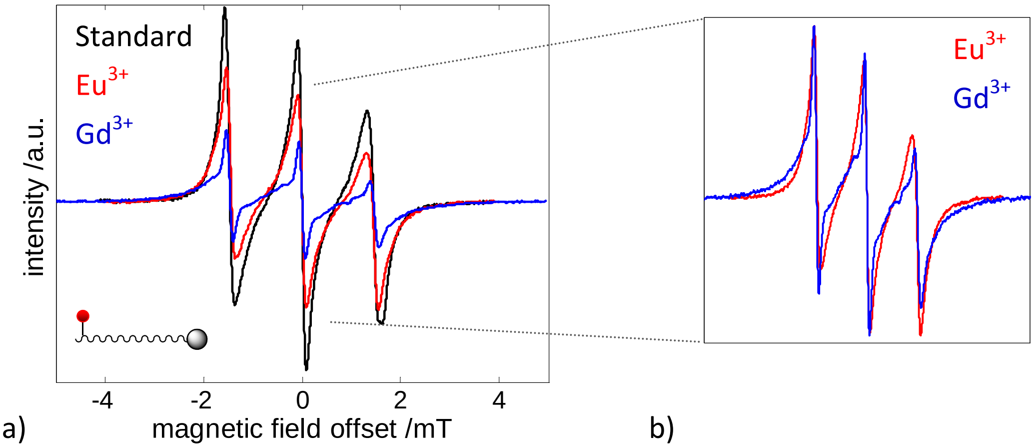

Figure 5.24 a) Integral normalized CW EPR spectra of 5 mol% **16-DSA** in sodium stearate miniemulsion without complex (black), with diamagnetic Eu(tmhd)$_3$ (red) and paramagnetic Gd(tmhd)$_3$ (blue). All spectra were measured at 25°C. b) For comparison of the DSA-spectra with Eu^{3+} and Gd^{3+} these spectra are normalized by their maximum.

The CW EPR spectrum of Gd^{3+} complexes is very broad (20.0-70.0 mT [224]) in aqueous solution at room temperature and was not observed in the present samples. In presence of a second spin (the paramagnetic metal ion) the effect of the metal on the nitroxide EPR signal is a function of the strength of the interaction and the electron spin relaxation rate of the metal. The rapid electron spin relaxation of the Gd^{3+}-ion decouples the two spins, and in this limit the nitroxide signal appears as a normal triplet in fluid solution (for other metals with *slow* T1 the interaction between the two spins may also be decoupled, but may lead to complex spectra due to splitting of the EPR lines [227]). As mentioned above, the CW EPR signal intensity upon addition of $Eu(tmhd)_3$ (red) is reduced as compared to complex-free (black) miniemulsions and the relative loss is higher for 5-DSA (Figure 5.23 a) than for 16-DSA (Figure 5.24 a). The change of the metal ion in the lanthanide complex from diamagnetic Eu^{3+} to paramagnetic Gd^{3+} results in a further decrease in the signal intensity. For 5-DSA, the signal is reduced in presence of Eu^{3+} by a factor of 4.5, with Gd^{3+} it is even reduced 12.5-fold as compared to the complex-free miniemulsion (thus, the relative signal reduction due to the change of the ion is 2.8). For 16-DSA the signal is quenched by a factor of 1.5 for Eu^{3+} and 2.8 for Gd^{3+} (factor 1.8 for metal ion change). Although the intensity changes are substantial, the relative heights and shape of the nitroxide lines in presence of Eu^{3+} and Gd^{3+} are very similar and no shifts in a_{iso} are observed (indeed, a_{iso} is slightly higher in presence of Gd^{3+} but the smaller value in presence of Eu^{3+} can be assigned to the larger exchange broadening present for this component). This means that the environment for the DSA label is nearly identical for both complex-containing miniemulsions. In general, the loss of an EPR signal can be due to chemical processes or magnetic interactions. Magnetic metal spin-nitroxide spin interaction (that can be either dipolar or Heisenberg spin exchange interactions) can explain the nitroxide signal reduction in presence of Gd^{3+} as compared to Eu^{3+}: the paramagnetic metal with a short electron relaxation time broadens the nitroxide spectrum due to enhanced relaxation effects of the nitroxide (both, T_1 and T_2 of the nitroxide are enhanced) [33]. An ‘obvious’ broadening of the nitroxide signal is not observed for 5-DSA (Figure 5.23 b) but for 16-DSA (Figure 5.24 b). Actually, for 5-DSA the spectra with Eu^{3+} and Gd^{3+} are nearly identical, and the line width of the central line is even slightly smaller in presence of Gd^{3+}. In the 16-DSA CW EPR spectrum, a clear broadening in the outer wings is observed that is characteristic for dipolar interaction. The fast component (sharp lines) shows a reduced line width as compared to the spectrum with Eu^{3+}. In the present case it is not clear if the signal loss is due to dipolar interactions between the metal ion spin and the nitroxide spin or exchange interactions. For the 5th position no obvious broadening is seen, which indicates a high relaxation enhancement of the nitroxide. The residual, strongly reduced signal is the residual signal from spin probes that are not affected by interaction with Gd^{3+}. As proposed by Leigh [228] broadening of the nitroxide spectrum is not observed if the two interacting spins can be treated in a rigid lattice in the Redfield limit, so that the dipolar interaction between the two spins is dependent on the orientation of the interspin vector with respect to the magnetic field B_0, the distance r between the two spins and the relaxation time T_{1e} of the metal. Then, the relaxed spins are broadened to such an extent, that they do not longer contribute to the observed spectral amplitude. The dipolar broadening coefficient is given by:

$$C = \frac{g\mu_B\mu^2\tau_c}{\hbar r^6} \qquad (5.10)$$

With the nitroxide g-value g, the Bohr magneton μ_B, the magnetic moment μ of the metal and τ_c, the correlation time of the process modulating the dipolar interaction is assumed to be equal to T_{1e}, the electron relaxation rate of the metal ion. Thus, from comparison of the spectral amplitude in absence and presence of the paramagnet, it is possible to calculate the distance between the nitroxide and the metal if a proper calibration plot is available and the T_1 value of the metal is known [251].

The mechanism that leads to spectral broadening may also be Heisenberg exchange that results from direct collisions of the metal with the nitroxide. The collision frequencies of the nitroxide with the paramagnetic compound are dependent on the nitroxide position in the bilayer and the collision between the unlike spins effectively shortens the spin-lattice relaxation time T_1 of the nitroxide [252]. The mechanism that is present for enhanced relaxation is not available from the simple CW EPR measurement. However, for the investigated miniemulsion the obtained signal reduction, especially for the 5th position of DSA, confirms the proposed model [231] of surfactant binding to the complex. The Gd^{3+} induced broadening decreases progressively as the label is moved from the head to the center of the bilayer. The measurements indicate a mean location of the Gd^{3+}-complex (and hence, also for the Eu^{3+}-complex) in the head group region of the bilayer and a hindered immersion depth of the complex into the hydrophobic core region. Diffusion of the complex into the bilayers region cannot be excluded since the ligands are highly hydrophobic, but this would lead to relaxation enhancement for the 16th position in a similar way like the 5th position, which is not observed. Since the observed line width for the 5th position (Figure 5.23 b) is even smaller in presence of Gd^{3+}, we may conclude that this residual spectral feature may arise only from remaining DSA molecules on the MMA/water interface and those within the structured region can be regarded as being completely suppressed due to a very short distance to the Gd^{3+}-ion.

5.6.3 Comparison of Miniemulsion and Polymerdispersion

This Section treats the CW EPR spectra obtained after polymerization of miniemulsions that were prepared with sodium stearate and contained a lanthanide β-diketonate complex. The general problem that arose during these measurements was the loss of signal intensity due to the radical polymerization technique that chemically consumes a large part of the radicals. This leads to very poor S/N ratios of the obtained nitroxide spectra. The CW EPR spectra for 5- and 16-DSA before and after polymerization are shown in Figure 5.25 the spectra for the miniemulsion were already discussed in the previous chapter, and thus only the spectra for the polymerdispersion are described. Upon polymerization a slow-motion EPR spectrum is obtained for 5-DSA that shows only one spectral component with a rotational correlation time of ~20 ns. In contrast, the 16-DSA spectrum shows a faster correlation time with ~2 ns. The hyperfine coupling a_{iso} is 1.42 mT and is slightly decreased as compared to the miniemulsion (a_{iso}=1.43 mT). For both DSA types the line width is increased after polymerization, and for 5-DSA more than for 16-DSA.

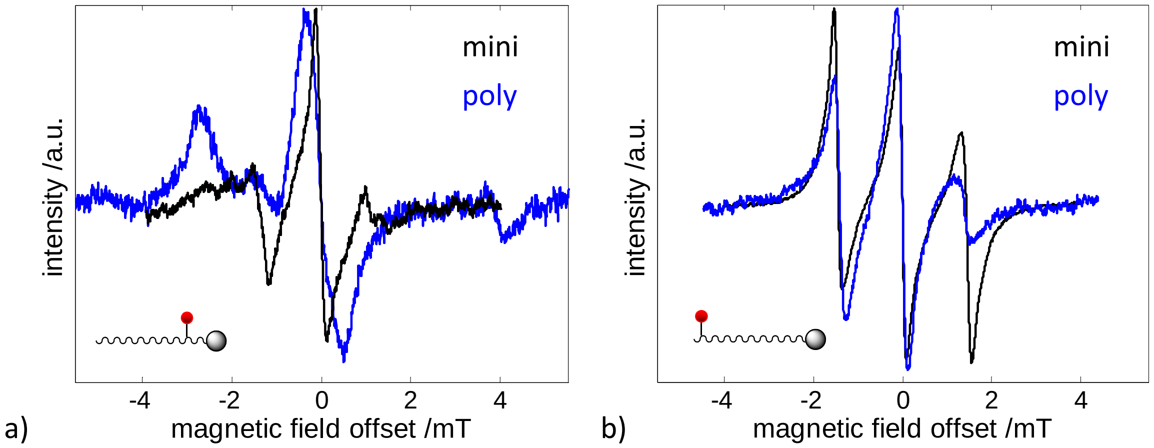

Figure 5.25 CW EPR spectra of a) 5-DSA and b) 16-DSA in miniemulsion prepared with sodium stearate as surfactant and in presence of Eu(tmhd)$_3$. Black spectra are miniemulsions, corresponding polymerdispersion are colored in blue. Radically polymerization was performed at 30°C with an oil soluble initiator within two hours.

5.7 Temperature Dependence of Miniemulsions that contain Lanthanide *β*-diketonate Complexes

In the previous chapters the difference between 5-DSA and 16-DSA spectra in miniemulsions with added Eu(tmhd)$_3$ was characterized. It was shown that while 5-DSA spectra show a highly immobilized fraction, 16-DSA exhibit an exchange broadened fraction of DSA that can be attributed to DSA molecules in a structured, probably layered region. To obtain better insights into the dynamic nature of the two DSA components and the behavior of miniemulsions upon temperature increase itself, temperature-dependent CW EPR measurements have been performed. In this Section, the EPR spectra for miniemulsions in presenceheut of Eu(tmhd)$_3$ for 5-DSA in SDS (C12) and 16-DSA in SOS (C18) are shown. Spectra for miniemulsions without complex and other surfactants are listed in the Appendix. The motivation for these measurements was the fact that the radical polymerization is usually carried out at 50-60°C. Thus, the studied temperatures were in the range of 5°C to 65°C. The question we address is: Has the temperature an influence on the structure formation and/or on the stability of the miniemulsion?

5.7.1 Temperature Dependence of 5-DSA Spectra

The temperature dependence of the low field line of 5-DSA in a SDS miniemulsion is displayed in Figure 5.26. The complete CW EPR spectra are given in Appendix.

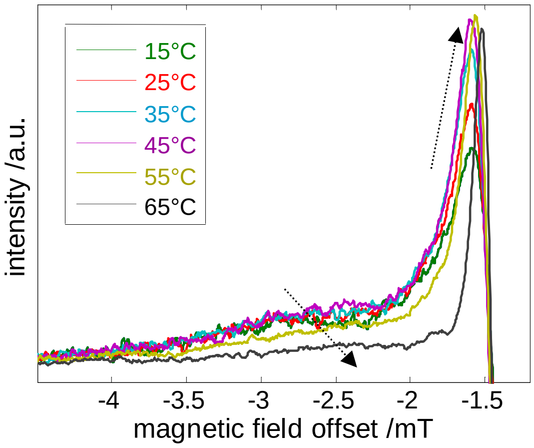

Figure 5.26 Temperature dependence of CW EPR spectra of a 5-DSA/SDS miniemulsion with Eu(tmhd)$_3$ and 5 mol.-% DSA with respect to SDS. Only the maximum of the low-field line is illustrated. With increasing temperature the maximum of the slow component (left peak) shift towards the maximum of the fast component (right peak). Each spectrum was measured with exactly the same parameters, so they are directly comparable. At 65°C the miniemulsion shows phase separation.

When increasing the temperature from 15°C to 45°C the spectral feature of the broad component (between -2 mT and -3.5 mT field offset) remains nearly constant. The peak maximum is shifted from ~-2.8 mT at 15°C to ~-2.5 mT at 45°C, indicating an increased mobility of this component, which is expected due to increased thermal energy. Accordingly, the motional reorientation of the faster (sharp) component (between -1.5 mT and -2.5 mT field offset) gets also faster. Between 55°C and 65°C some broad component is still visible but its intensity relative to the fast component has decreased sizeably. This means, that the relative amount of the immobilized component is reduced at this temperature. Despite the fact that the margin of error from spectral simulation is very high due to the broad lines and the weak signal intensity, a trend towards a higher fraction of fast rotating species was obtained from ~20% (15°C) to ~25% (65°C). This is a small yet noticeable rise. In the anisotropic rotational model, the axial diffusion rate determines the shape of the spectra and the temperature dependence could be reproduced very well by increasing this rate. The fast component was simulated with an isotropic diffusion tensor. The extracted axial diffusion rates $D_{\perp}$ for both components are plotted versus the temperature in Figure 5.27 a. For the isotropic hf coupling a_{iso} (extracted from the experimental spectra) an analogous plot is obtained, which includes the data from the miniemulsion without complex (Figure 5.27 b).

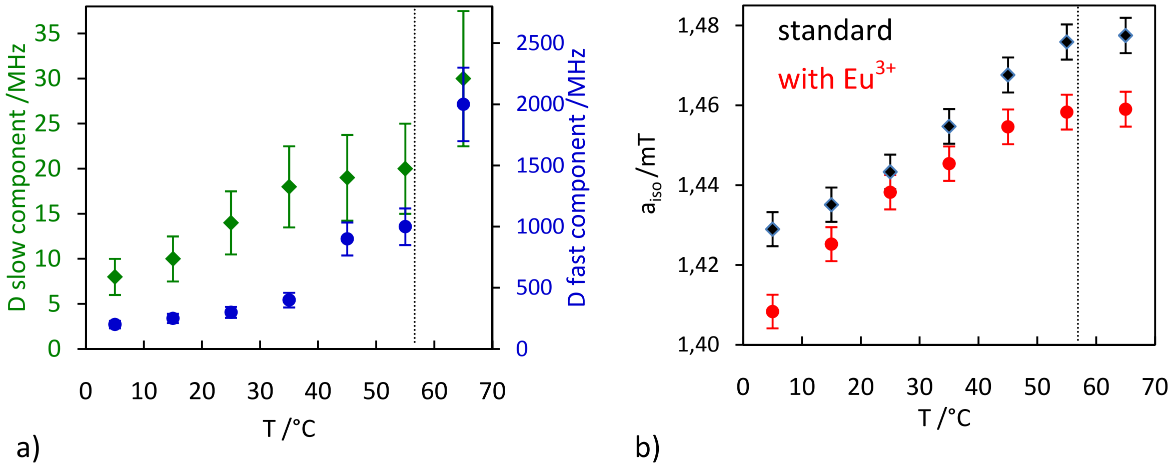

Figure 5.27 Temperature dependence of CW EPR spectra of a 5-DSA/SDS miniemulsion with Eu(tmhd)$_3$ (from Figure 5.26) a) the rotational diffusion tensor $D_{\perp}$ of the immobilized and fast component extracted from slow motion simulation of two components. b) The apparent isotropic hf coupling a_{iso} for miniemulsions without (black) and with complex (red) obtained from experimental spectra.

The inspection of the rotational diffusion rates reveals a difference of two orders of magnitude between the two components. With increasing temperature the rates of both components increase nearly linearly up to 35°C. Between 55°C and 65°C an abrupt increase is visible. At 65°C, macroscopic phase separation was observable. In contrast, the isotropic hf values, as obtained from the experimental spectrum (Figure 5.27 b) increase nearly linear in the range between T=15-55°C and no severe change is found. The a_{iso} values for the miniemulsion *with* complex are always smaller than the ones without complex which indicates a less polar environment for DSA in presence of complex. From 55°C to 65°C apparently no change in the a_{iso} value is found. This holds for both miniemulsions (with and without complex). A small departure from linearity may be assumed in both plots for the lowest temperature under investigation in the region between 5-15°C. From temperature dependent measurements of the anisotropic spectra it is possible to determine the activation energy E_A in an Arrhenius plot according to

$$ln\ D_{\perp} = \ln A - \frac{E_A}{RT} \qquad (5.11)$$

where ln $D_{\perp}$ is plotted vs. 1/T. A is the pre-exponential factor, *R* the universal gas constant (8.3145 J mol^{-1} K^{-1}), *T* the temperature and $D_{\perp}$ the axial rotational diffusion rate. In this plot $D_{\perp}$was used (not the overall rotational reorientation time), as it was found that this component is more sensitive towards temperature than the axial tensor element $D_{\parallel}$. In simulations it was possible to fit experimental spectra with defining $D_{\parallel}$ as nearly constant and just increasing the slower perpendicular diffusion rate $D_{\perp}$. Thus, the choice of this element provides more precise values. The Arrhenius plot reveals allows the calculation of the activation energy for this type of dynamic process from the slope $-E_A/R$ of the straight line.

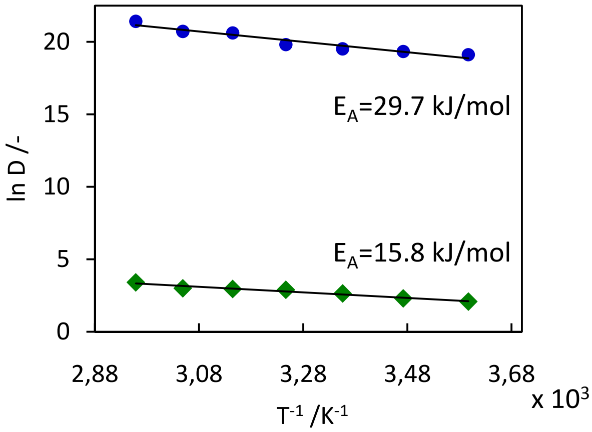

Figure 5.28 Arrhenius plot of axial rotational diffusion tensor $D_{\perp}$of 5-DSA in SDS miniemulsion in presence of Eu(tmhd)$_3$(from Figure 5.26). Blue and green represent the fast/narrow and slow/broad components, respectively. The values were obtained from simulation within a two-specie model in the slow motion regime. The fit includes all data points.

In the Arrhenius plot in Figure 5.28 all data points within the measured temperature regime (5-65°C) were used for linear fit. This yield the activation energy of + 29.7 kJ/mol for the fast component and + 15.8 kJ/mol for the broad component. Linear fits in which the last temperature point (65°C) was neglected give 26.1 kJ/mol and 14.8 kJ/mol, respectively. The higher value for the fast component implies that this component is more sensitive to temperature than the broadened component.

A decrease in an outer peak separation can arise from an increase in the rotational diffusion rates, from an decrease in the lamellar ordering or from a combination of both. In 2.7.4 it was figured out that for anisotropic DSA spectra the order parameter S can be obtained from the spectral splitting of the CW EPR spectra (see Figure 2.15).

It is important to note, that the discussion of the order parameter S obtained from eq. (2.42), depends on the model that is applied to explain anisotropic EPR spectra. For the miniemulsion with SDS/5-DSA it was argued in section 5.5.2, that the spectrum constists of an immobilized and a more mobile component and the diffusion rates of both components were plotted against the temperature. The order parameter can be used to get information about the local ordering of the spin probe within the structured region. Furthermore, the splittings are directly accessible from the spectra and the assignment is easy to perform, whereas spectral simulation are necessary for determing the diffusional rates. This method is only applicable to 5-DSA spectra since we did not observe spectral splitting for 16-DSA, the chain flexibility at the 16-position has randomized all order. The dependence of the order parameter for 5-DSA as a function of temperature is plotted in Figure 5.29 (a) for SDS (+ Eu^{3+}) and b) for sodium stearate without complex in black and with Eu^{3+}-complex in red. Further, the apparent hyperfine splitting $2A_{\parallel}$, that were obtained from the experimental spectra and were used to calculate the order parameter are included in the plot (green). This shows, that the shape of the oder parameter curve is mainly influence by the outer splitting $2A_{\parallel}$ and only minor by $2A_{\perp}$.

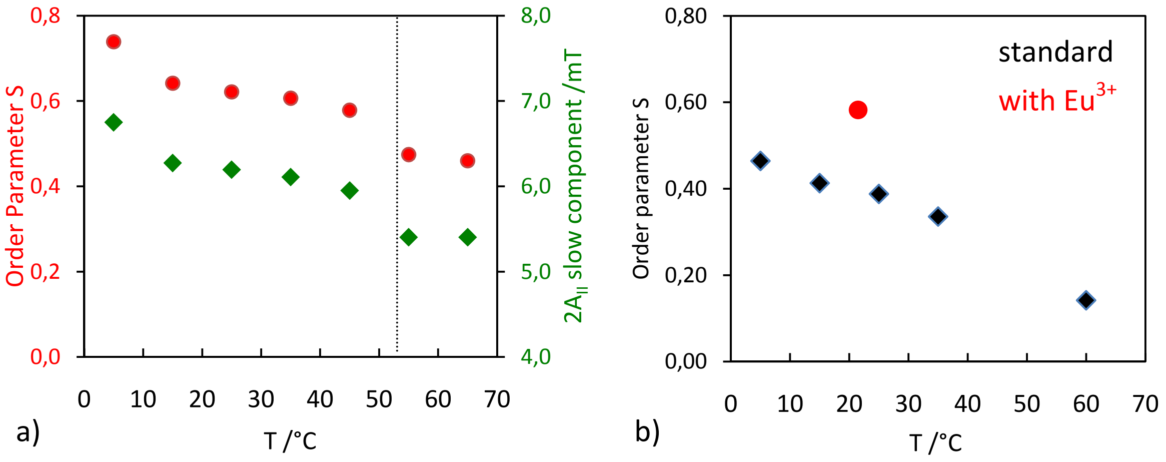

Figure 5.29 Temperature dependence of anisotropic 5-DSA spectra in miniemulsions. The order parameter was obtained using eq. (2.42), with the principal values for the hf tensor A=[0.5,0.5,3.27] mT were used. The values for $2A_{\parallel}$ and $2A_{\perp}$were read out from the spectra. a) Order parameter S and the $2A_{\parallel}$ value of the slow component for SDS-based miniemulsion in presence of $Eu(tmhd)_3$. b) Order parameter S for complex-free (black) and $Eu(tmhd)_3$-containing (red) miniemulsions with sodium stearate.

For the miniemulsion with $Eu(tmhd)_3$ in SDS in Figure 5.29 (a) one can see a decrease in the order parameter with increasing temperature. Particularly, there is a sharper decrease between 45-55°C. We have evaluated the T-dependence of the 5-DSA spectra with two methods: directly from the experimental spectra ($2A_{\parallel}$ vs. T or S vs. T) and by simulation (diffusion rates $D_{\perp}$vs. T). Both methods indicate a temperature range between 45-55°C where the motional characteristics of the spin probe are altered in a jump-like manner. The temperature dependence of S in complex-free miniemulsion of *sodium stearate* is shown in Figure 5.29 (b) (black), that can be further compared with the order parameter in presence of Eu(III)-complex (red) (spectra are given in the Appendix. With increasing T, the value of S drops down from 0.48 at 5°C and at 60°C reaches a value of 0.14. The order parameter is higher in complex-containing (S=0.71) than in complex-free miniemulsion and nearly equal for SDS or stearate miniemulsion.

5.7.2 Temperature Dependence of 16-DSA Spectra

The temperature dependent CW EPR spectra of 16-DSA in sodium octadecyl sulfate (C18) are shown in Figure 5.30. Only the center line is shown, the full spectra are given in the Appendix.

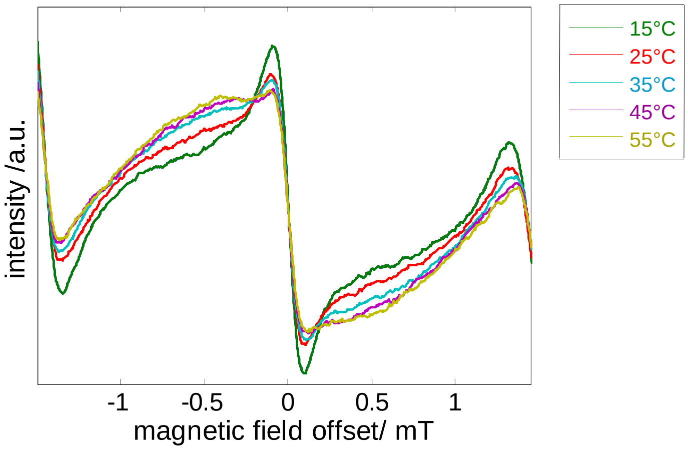

Figure 5.30 Temperature dependence of CW EPR spectra of a 16-DSA miniemulsion with Eu(tmhd)$_3$ prepared with sodium octadecyl sulfate (SOS). The DSA concentration is 5 mol.-% with respect to SOS. The spectra were recorded with identical parameters and are not further normalized. Only the center line is shown, the complete EPR spectra are given in the Appendix.

With increasing temperature the height of the center line is reduced and a second peak is growing on both sides of the line. In the former chapter this was explained by an increased exchange frequency ω_{Ex} of the broad component and the spectrum of this component consists of one single line. Upon temperature increase, the viscosity of the solvent is reduced, which enhances the spin exchange rate according to eq. (2.27). The difference to the above-reported T-dependence of 5-DSA in SDS (Section 5.7.1) is the lack of an increased fraction of the fast component that was apparent in SDS at T>45°C (see Figure 5.29). The miniemulsion presented here (16-DSA/SOS) up to 55°C only shows an increase in the exchange frequency while the relative fraction of both components remains constant.

It is of interest if this observation can be traced back to the used spin probes (5-DSA/16-DSA) or to the used surfactant (SDS/SOS). It is not obvious per se, since increasing temperature will change the dissociation equilibrium between COOH ↔ $COO^- + H^+$, which may affect the head group region of DSA more than the tail end region. Thus, we have performed T-dependent EPR measurements for 16-DSA/SDS up to 55°C (CW EPR spectra are given in the Appendix. Up to 45°C the spectra behave like the shown ones, but already at 55°C the fraction of the fast component has immensely increased. This process was not reversible and was also found in complex-free miniemulsions (16-DSA/SDS see Appendix). The increase of the fast fraction in the CW EPR spectra is accompanied by an increase in the effective isotropic hyperfine value, which possibly mirrors that of some of the DSA spin probes are more exposed to water. This might be due to enhanced release of surfactant molecules from the MMA/water interface into water or due to a larger interface region with a more 'open' structure for water molecules. The latter is assumed to be reversible upon cooling. Hence the higher a_{iso} value is indicative for an instability mechanism of the miniemulsion, as the release of surfactant molecules into the water phase would imply coagulation of monomer droplets due to increased collisions rates at higher temperatures. The fusion of two monomer droplet to a larger droplet leads to a decrease of the surface-to-volume ratio of the droplet. Hence, less surfactant molecules are needed at the interface for effective stabilization of the oil in water emulsion. We can conclude that for each surfactant a defined temperature or temperature region exists, where dynamic changes take place that alter the previously established phase behavior of the miniemulsion. Note that this happens before the macroscopic phase separation is observed. For SOS we found a stable miniemulsion up to 55°C, for SDS only up to 45°C (the temperature is between 45° and 55°C and was not determined exactly). This point can be determined very precisely by monitoring line shape changes in CW EPR spectra (that reflect dynamic changes of EPR spin probes). The critical temperature for initiation of this process is dependent on the viscosity of the used monomer, the type of surfactant (ionic or non-ionic) and the ratio water-monomer-surfactant.

One can furthermore analyze the temperature-dependence of the broad component in the CW EPR spectra. The increase in the exchange frequency can be explained with the previous assignment that the broadened component denotes the fraction of DSA that is distributed within the layers. The increase in the exchange frequency is correlated with the lateral diffusion of DSA molecules (diffusion perpendicular to the bilayer normal). This two-dimensional process can be assumed to occur via an exchange of position of two neighboring molecules A and B (Figure 5.31 b) [27].

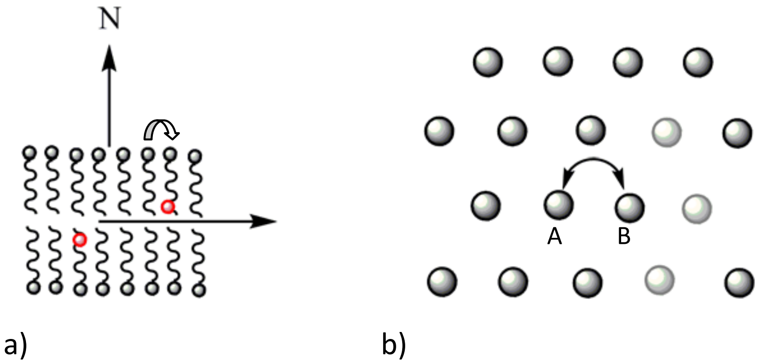

Figure 5.31 Schematic structure of a spin labeled bilayer in the side view (a) and in top view (b), where the surfactant molecules are approximated as hexagonal packed cylinders. Lateral diffusion within a layer occurs perpendicular to the bilayers normal N. b) Molecule A acquires three new neighbors (grey) as a result of the position exchange with B ('diffusion jump').

After the position change each surfactant has three new neighbors (grey spheres for molecule A). Thus, the probability to get into contact with other DSA molecules increases with lateral diffusion, and with this also the exchange frequency between DSA molecules. Hence, the value of the exchange frequency is due to the combined effects: in the static case (which is only theoretical possible) the exchange frequency is represented by the interaction volume present for the flexible 16th position in the layer (see Figure 5.18) and with allowing lateral diffusion the position jump increases the absolute value.

Spectral simulation reveals the value of the exchange frequency at each temperature and the T/η-dependence of ω_{Ex} is shown in Figure 5.32. The viscosity values for MMA were linearly interpolated from two points given in the literature [253].

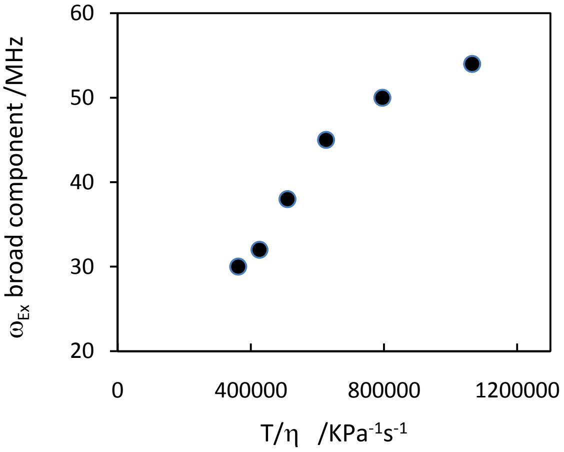

Figure 5.32 Exchange frequency of the broad component in 16-DSA CW EPR spectra of a miniemulsion with SOS in presence of Eu(tmhd)$_3$. The values were obtained by simulation in the slow motion regime (function 'chili') with two components.

The increase is nearly linear with T/η as it is characteristic for fast exchange [27] (for weak exchange the trend should be opposite in character and the exchange rate is supposed to increase with viscosity (see eq.(2.26)). The deviation from linearity for higher T/η values are too small to be interpreted, and could be well within the margin of error of e.g. interpolation of η from only two data points. For fast exchange we can calculate the rate exchange constant according to eq. (2.27) at 25°C to $K_e \sim 1.8 \cdot 10^{10}$ Lmol^{-1}s^{-1}, which is a typical magnitude for a diffusion controlled process as we assume it here.

These temperature dependent CW EPR measurements for miniemulsions in presence of Eu^{3+}-complex yield valuable insights into dynamic processes in miniemulsions.

5.8 Pulse EPR Measurements

Electron spin echo experiments on frozen solutions of miniemulsions have been performed at 50 K. The spin probes 5- and 16-DSA are compared for miniemulsions that were prepared with sodium stearate in presence of either Eu(tmhd)$_3$ or Gd(tmhd)$_3$.

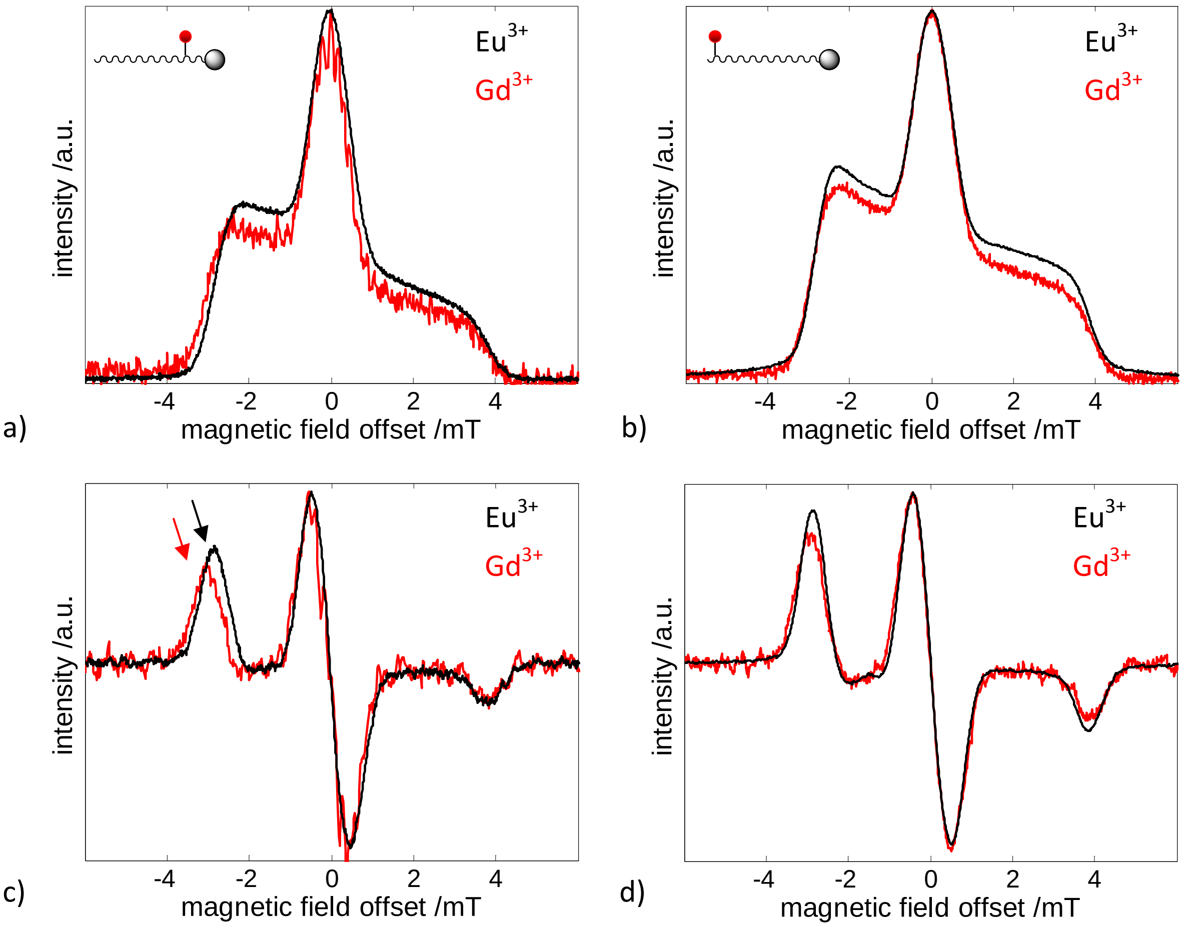

Figure 5.33 Echo detected (a,b) and pseudomodulated (c,d) EPR spectra of DSA in miniemulsions prepared with sodium stearate in presence of either Eu(tmhd)$_3$ (black) or Gd(tmhd)$_3$ (red). Measurements were perfomed at X-band (9.3 GHz) in frozen solution at 50 K. Experimental parameters: $t_{\pi/2}$=16 ns, τ=200 ns. The pseudomodulated spectra were calculated from the ESE spectra with a modulation amplitude of 0.3 mT.

The comparison of the ESE spectra of 16-DSA (Figure 5.3.3 a) in presence of Eu(tmhd)$_3$ or Gd(tmhd)$_3$ shows two remarkable points. First, the overall intensity of the nitroxide signal and SNR is decreased for Gd^{3+}-containing samples (for comparison: the spectrum with Eu^{3+} was recorded with 30 scans, Gd^{3+} with 83 scans) and second, the hyperfine splitting $2A_{zz}$ seems to be larger. The increase of $2A_{zz}$ is more obvious in the pseudomodulated spectrum (c), where the two peaks are marked with arrows. The A_{zz} values are listed in Table 5.8. The apparent additional splittings in the ESE-spectrum of 5-DSA in presence of Gd^{3+} stem from proton hyperfine couplings of some decomposed initiator, that was confirmed by a reference measurement of an incompletely polymerized miniemulsion in presence of Eu^{3+}. The shift in A_{zz} for 5-DSA (16-DSA) in Gd^{3+}-containing miniemulsion is 0.1 mT (0.06 mT) higher as compared to Eu^{3+} -containing samples.

Table 5.8 Hyperfine splitting $A_{zz}$and relaxation times T$_1$ and T$_2$ for 5- and 16-DSA in miniemulsions containing Ln(tmhd)$_3$ obtained from electron spin echo spectra, inversion recovery and two pulse ESEEM in frozen solution (T=50K, Ln=Eu^{3+}, Gd^{3+} , tmhd= 2,2,6,6-teramethylheptane- 3,5 dione). The error is ±0.07 G.

	Metal Ion	**A_{zz} /mT**	**T_1 /μs**	**T_2 /ns**
5-DSA	Eu^{3+}	3.34(6)	795	1000
	Gd^{3+}	3.44(5)	-	310
16-DSA	Eu^{3+}	3.36(8)	420	690
	Gd^{3+}	3.42(7)	340	300

The dependence of A_{zz} on the central ion of the lanthanide complex indicates that the magnetic environment is altered at the 5th position but not at the 16th position. The interpretation of the change in the hyperfine splitting should be done with some caution since we cannot completely rule out effects from the present carbon-based radicals.

Pulsed relaxation measurements have been performed at 50 K (experimental details are given in Chapter 7). An enhancement in the nitroxide T_1 and T_2 relaxation times in the presence of Gd^{3+} were observed, the 5th position is more affected than the 16th position. At this temperature it was not possible to obtain an inversion recovery signal for 5-DSA in presence of Gd^{3+}. The longer relaxation times for 5-DSA indicate a higher degree of order for this position than for the 16th position.

5.9 Discussion

- *The location of the spin probe DSA in micellar solutions and miniemulsions*

From the isotropic hyperfine coupling a_{iso} that is accessible via CW EPR spectroscopy, one can obtain information about the location of the probe in micelles [238] and colloidal systems such as miniemulsions. Numerous reference values for 5-and 16-DSA in aqueous environment are given in the literature, since these probes are frequently used inbiological systems [39, 216, 254-255], but EPR parameters in other solvents are rare and depend on the system under investigation [256]. Hence, it turned out that reference measurements in the respective phases of the miniemulsion are very helpful for the assignment of the location of the spin probe in a miniemulsion. The hf coupling value for 4 mM 16-DSA in MMA (a_{iso}=1.44 mT) is much lower than in water/SDS solutions (a_{iso}=1.54-1.58 mT), which is also expected due to the lower permittivity of MMA (see Chapter 0). The EPR spectra of 16-DSA and 5-DSA in MMA showed line broadening due to Heisenberg spin exchange, even in low concentration DSA-samples (in 0.1 mM DSA and unlabeled stearic acid). The value of a_{iso} in SDS/water were depended on the surfactant concentration. In higher concentration solutions lower a_{iso} values were found, which is due to the higher aggregation numbers of surfactants in which the alkyl chains act as a better solvent for the unpolar DSA. This was also confirmed by light scattering, where aggregation numbers were calculated from the diameter of the micelles [257]. Such it is possible to distinguish between free DSA molecules in solution *below* and *above* the cmc. As pointed out in Section 0, the spin probe is solubilized by the surfactant micelles [258] as the cmc of the surfactant is reached and higher aggregation numbers (far above the cmc of the pure surfactant) lead to more densely packed micelles; the hindered rotation of the nitroxide group can be seen in the CW EPR spectra as changes in the relative heights of the lines and the increased line widths [243]. In this picture it is assumed that the DSA probe remains at a fixed position in the micelle with no motion across the curved surface of the micelle (lateral diffusion) possible. The rotation of the whole micelle is much slower than the segmental motion of the nitroxide moiety and the separation of internal nitroxide motion and overall motion is possible according to the hydrodynamic Stokes-Einstein model [259]. We found no evidence for unsolubilized DSA precipitate in these reference spectra obtained in MMA (up to 6 mM DSA) and micellar SDS solutions (up to 100 mM, see Chapter 0). Previous studies have shown that the location of a nitroxide spin probe in micellar systems is dependent on the interactions that the probe

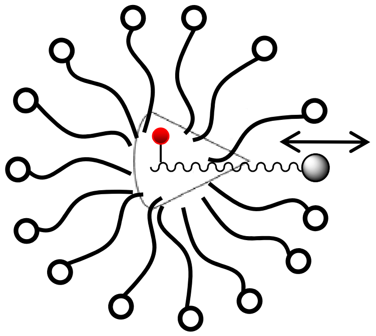
Figure 5.34 Location of DSA in a micelle.

experiences with the micelle [233, 260]: ionic nitroxides prefer an adsorbed state near the micelle/water interface, non-polar ones favor the hydrocarbon core and surfactant-like nitroxides are 'comicellised' [258]. The anchoring of the carboxylate group at the interface is dependent on the dissociation degree, which is a function of pH and temperature. At pH values > 9, DSA is assumed to be fully deprotonated (–COO^-), whereas at acidic conditions, the neutral acid form (-COOH) is present (and DSA is less soluble in aqueous solutions). The charged headgroup is more strongly anchored in the Stern-Layer than the neutral form, which can be shifted towards the core or even outside of the Stern-Layer in the diffuse region (this possible shift is indicated by an arrow in Figure 5.34). If a strong anchoring is present, the nitroxide group at the 5th position has less conformational degrees of freedom compared to the 16th position, and the reduced mobility, which is usually anisotropic in nature due to the extended shape of the DSA molecule, can be observed in CW EPR spectra. The anchoring behavior of the head group and its exact position in micellar systems was studied in detail elsewhere [232, 242, 260-261] In the here performed reference measurements, only one DSA component was present in the CW EPR spectrum, which indicates a fast exchange between molecules in micelles and free surfactant in water or MMA. This was expected for a homogeneous phase.

The studied model miniemulsion contains surfactant far above the cmc (~ 20 mM see Table 5.3) and an additional third phase, MMA. The application of shear stress results in small MMA droplets and the surfactant is assumed to be located at the MMA/water interface. The surfactant thus has a stabilizing effect on the small droplets that have a high surface-to-volume ratio and are thermodynamically instable. In complex-free miniemulsions the spin probe 16-DSA was found in two different environments that differ in their polarity and mobility as observed by CW EPR spectroscopy (see section 5.5.1). The two components were separated by computer simulation. The slightly faster component has a higher isotropic hf coupling (a_{iso}=1.46 mT). The second component shows exchange broadening (4 MHz) and a lower a_{iso} value (a_{iso}=1.44 mT). It is known, that exchange broadening becomes visible in CW EPR spectra as an apparent decrease in the hf coupling a_{iso} [27]. Thus, the value may be slightly underestimated [262]. From the a_{iso}-values it seems reasonable to assign the faster component to DSA molecules at the MMA/water interface that are in exchange with free DSA molecules in the water phase. The diffusive region of the interface can explain the higher a_{iso} value than found for DSA in pure MMA. A higher a_{iso}-value for this component may also be due to the mean location of the carboxylate group in the diffuse Layer, slightly farther away from the Stern Layer (where the charged surfactant head groups are located), where the nitroxide group may be more exposed to water. From the EPR measurements it is not possible to distinguish between these two cases, both are possible and both imply the same picture of a more or less disordered interface region without a clear boundary. The second, less mobile component exhibits a lower a_{iso}-value that is comparable to the a_{iso}-value of 16-DSA in MMA and a line shape characteristic for Heisenberg spin exchange interaction. This suggests a location of the probe within the MMA droplets. The two components do not exchange on the EPR time scale (otherwise the lines would emerge into one single nitroxide spectrum). At a first sight it seems not reasonable why a DSA spin probe in the MMA phase is not in fast exchange with DSA at the MMA/water interphase. Note that the meaning of 'exchange' is not the spin-spin exchange interaction between two DSA molecules but the spatial change of the position of the probe to the other sides of interaction present in the sample. One might assign the two components to different dynamic processes that are present in miniemulsion. This is the segmental motion of the nitroxide moiety and the rotation of the monomer droplet. From an estimation according to the Stokes eq.(2.51) with a droplet-diameter of 180 nm and the viscosity of water the correlation time for the monomer reorientation is ~7 ms which is too slow to be detectable by EPR spectroscopy. The size distribution of the droplets that is frequently discussed for miniemulsion polymerization [263], has less impact on the CW EPR spectra as long as the DSA molecules are distributed statistically over all droplets. A small size distribution <1.04 [263] cannot influence the CW EPR spectra since the droplets are large enough that the movement of the droplet can be neglected and only the much faster internal processes are visible. Thus, the two DSA components are due to a heterogeneous distribution of DSA molecules that was also obtained from simulation where a higher amount (80%) of the broadened component was found (for the case of complex-free and complex-containing miniemulsion). As mentioned, the partitioning between water and the hydrophobic phase can be related to the polarity of the molecule. In solution DSA can either exist in neutral (COOH) or ionized form (COO^-) and each form shows significantly different water solubility (and with this different affinity to be located at the MMA/water interface). Stearic acid (C18) has a rather high partition coefficient[3] log P=8.23 (for comparison dodecaonoic acid: log P=4.6 [36]), thus the non-polar DSA preferentially resides in the MMA phase where additional hexadecane is also present. This in turn would go along with most DSA molecules not being dissociated, since otherwise a higher amount of the interface active form ($-COO^-$) would have been observed. If nonetheless charged DSA were present in the sample, it would preferentially be located at the MMA/water interface.

Further, we might assume that no free (unswollen) surfactant micelles are present, since the sharp lines and higher a_{iso}-value (~1.54 mT) of DSA solubilized by aqueous micelles would be directly visible in the EPR spectrum (see section 0). Such a fraction was not observed from which we can conclude that all surfactant is distributed within the monomer

---

[3] The partition coefficient *P* is a measure for the distribution of a substance between a non-polar phase (usually n-octanol) and water and is defined as the ratio of the equilibrium concentration of the solute in the non-polar phase to that in the water phase [36]. Usually this ratio is given in the logarithmic scale, thus, a small value stands for a high partition in water and a large value for high partition in the non-polar phase.

droplets or which may be the case if all micelles are swollen with monomer (and are only in exchange with free surfactant molecules from the water phase). This is not a direct discrepancy with theory, which claims free (unswollen) surfactant micelles in the water phase. It seems probable that only a few percent of the DSA are located in the water phase and the exchange with DSA at the interface happens probably very fast. The second possibility is simple the case that no micelles exist, since the cmc hasn't been reached, which seem improbable in the studied concentration range.

Since the used DSA concentrations of 5 mol.-% with respect to surfactant are rather high (~2mM overall concentration), other concentrations were also tested in presence of Eu^{3+}-complex: 2.5 mol% (see Appendix Figure 3) and 0.5 mol%, which is about one tenth of the previous concentration. The exchange broadening was indeed decreased according to the reduced concentration upon diluting, and the fraction of the exchange-broadened component was smaller than for the higher DSA concentration. The latter observation, though, could be traced back to the fact that the line width was also much sharper, giving a significantly reduced margin of error in the simulations. The general problem due to broad lines in determination of the a_{iso}, τ_{corr} values and also relative fractions was discussed in Section 5.5. The study of these lower DSA concentrations proves that it is not precipitated DSA that causes this broadening effect in 16-DSA CW EPR spectra. This broadening is an intrinsic property of the sample and was found for all 16-DSA miniemulsions, regardless of the used surfactant and the presence or absence of complex. Upon complex addition, the DSA component at the MMA/water interface does not change its motional characteristics, but the broader component becomes more broadened (Figure 5.15 for SDS and Figure 5.22 for stearate).

We can estimate the concentration of *unswollen* micelles from the used surfactant concentration according to [264]:

$$[micelle] = \frac{[surfactant] - cmc}{N_{agg}} \tag{5.12}$$

Where cmc is the critical micelle concentration and N_{agg} the aggregation number of surfactant molecules at the cmc. For SDS the aggregation number at the cmc (8.3 mM) is ~60 [265]. We used ~40 mM surfactant concentration and can calculate a micelle concentration *before* MMA addition of ~0.5 mM. Assuming Poisson statistics, we obtain the following distribution for 2.1 mM DSA: 13% of the micelles contain 2 DSA molecules, three, four, and five DSA molecules are each found in 20% of the micelles, and 11% contain 6 DSA molecules. Only 6% of the micelles contain one DSA molecule. Hence, at our used DSA concentration we probe each particle (micelle) with on average more than one DSA molecule. Typical radical concentrations are roughly 1:100 with respect to the surfactant concentration [243, 264]: Increasing the DSA concentration was advantageous for several reasons. On the one hand the addition of monomer and the applied shear stress results in a much higher concentration of monomer droplets so that to probe each of these particles we need the “reserve” in DSA molecules. On the other hand we wanted to observe CW EPR spectra after radical polymerization that destroyed our spin label.

However, the high nitroxide concentration complicates data analysis of the CW EPR spectra due to the presence of electron spin-electron spin interactions, which might be dipolar or exchange interactions. The interactions were not separated into their individual contributions, which is possible but requires high effort [31] and was not the scope of this study. Besides spin-pin interactions the observed line shapes and line widths were determined by several other factors: (a) the (anisotropic) rotational motion (correlation time)) of a spin probe, (b) the ordering of the spin probes in the aggregates (c) unresolved proton hyperfine splitting. The contributions of all these effects to the line shape were not analyzed in detail. Since the investigated system is highly complicated we applied a simple two-species model for computer simulation (a MatLab program is given in the Appendix). This model is reasonable for the present system. The two components were analyzed with respect to their spectral weights, rotational correlation times and Heisenberg exchange frequencies. The fraction that could be attributed to the MMA/water interface was always between 10-20%.

The exchange broadened component of x-DSA spectra that is due to partitioning of DSA between the MMA and the MMA/water interphase. In presence of Eu^{3+}-β-diketonate complex characteristic spectral features are observed: 16-DSA showed increased exchange interaction and 5-DSA displays a highly immobilized component. The exchange frequency for the 16-DSA component shows typically different values in carboxylate (~ 15 MHz) and sulfate (>33 MHz) containing miniemulsions. The immobilized 5-DSA component showed a typical rotational correlation time of ~ 10 ns.

For 16-DSA, the fast component shows identical motional characteristics and constant a_{iso}-values in all miniemulsions, regardless of the used surfactant and if complex was added or not. These are DSA molecules at the MMA/water interface where this behavior is supposed. For 5-DSA the ‘fast’ component is - compared to the 16-DSA counterpart - always much slower (but still faster than the immobilized component) due to its location near the interface and (if applicable) also the complex. In the following spectra of x-DSA in the different surfactant types are compared to each other.

- *Comparison of x-DSA CW EPR spectra in different surfactant miniemulsions*

The difference of the *16-DSA* spectra in miniemulsions with different surfactant chain lengths (C12 and C18) and anionic head groups (stearate, sulfate) is shown in Figure 5.35. The spectrum in sodium laurate has not been shown previously, spectra in SDS and SOS were given in Section 5.5.1 and this of sodium stearate in Section 5.6.1.

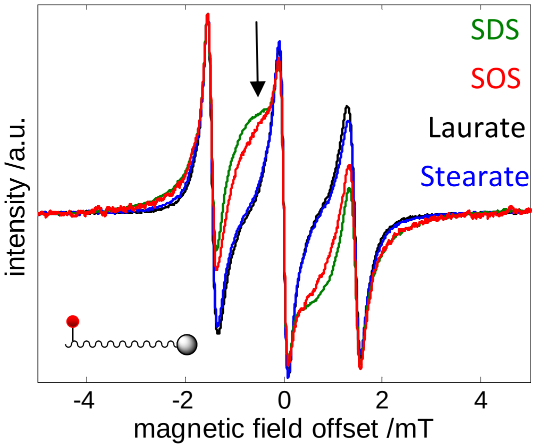

Figure 5.35 CW EPR spectra of **16-DSA** miniemulsions with Eu(tmhd)$_3$, measured at X-Band (9.4 GHz) at 25°C. The DSA concentration was 5 mol.-% with respect to the used surfactant. Spectra are normalized by their maximum. Sodium dodecylsulfate (C12, OSO_3^-) is plotted in green, sodium octadecyl sulfate (C18, OSO_3^-) in red, sodium laurate (C12, COO^-) in black and sodium stearate (C18, COO^-) in blue. The exchange broadened component is marked with an arrow.

The exchange interaction for the broad component that is marked with an arrow is the central feature in 16-DSA CW EPR spectra and increases in the order:

sodium stearate ≈ sodium laurate << SOS < SDS

The highest value of 44 MHz was found for SDS. The chain length has fewer effects on the broadening than a change in the head group. For sodium stearate and laurate the differences in the EPR spectra are marginal. However, by changing the head group from carboxylate to sulfate, spin exchange (mainly at the broad central line) and dipolar interactions (broadening in the outer wings of the low- and high-field line) between nitroxide radicals are increased. The increase of exchange interaction from C18 surfactant SOS to C12 surfactant SDS can be explained due to the higher interacting volume between 16th positions in a C12 bilayer (see Figure 5.18). However, for bilayers made of either sodium laurate (C12) or stearate (C18) no difference in exchange interaction for 16-DSA was found. The overall higher exchange frequency in bilayers made of sulfate surfactant might be due to higher translational diffusion of DSA in those layers (see Figure 5.31). Since the layer thickness for the pair SDS + sodium laurate (both C12) and SOS + sodium stearate (both C18) should be approximately the same, the differences in the exchange frequency between one pair can be correlated with a different coordination of the carboxylate and the sulfate head groups, respectively, with the metal ion. Thus, carboxylates is assumed to be bound more strongly to the lanthanide so that it retards lateral diffusion, which would explain a lower exchange frequency in carboxylate surfactant and the fact that for both carboxylate surfactants (sodium laurate vs. stearate) nearly identical spectra were found. Vice versa, sulfate head groups should be bound more loosely to the metal, leading to

increased lateral diffusion and increased exchange interactions.
The exact coordination geometry of the head group to the metal ion lies beyond the scope of this work for which UV-VIS spectroscopy will give complementary information.

The CW EPR spectra of *5-DSA* in miniemulsion with two different surfactant types is shown in Figure 5.36.

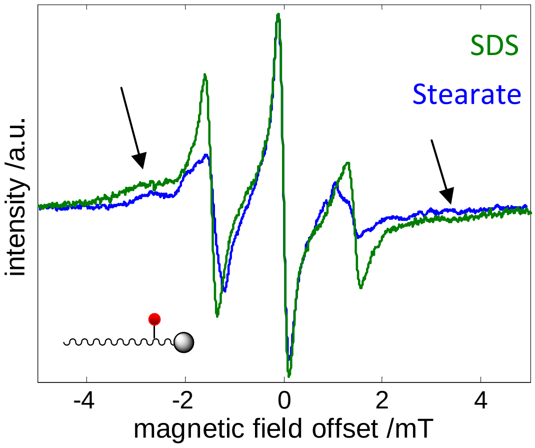

Figure 5.36 CW EPR spectra of **5-DSA** miniemulsions with Eu(tmhd)$_3$, measured at X-Band (9.4 GHz) at 25°C. Spectra are normalized by their maximum. Sodium dodecylsulfate (C12, OSO_3^-) is plotted in green, sodium stearate (C18, COO^-) in blue. The 'immobilized' DSA component is marked with arrows.

5-DSA spectra show a strongly immobilized fraction of DSA for both surfactant classes, regardless of the chain length and head group present. In miniemulsion with stearate, this immobile component shows slightly sharper spectral feature than for SDS. Moreover the 'faster' fraction in SDS is faster compared to that in stearate at least by a factor of 2.5-3. Note that the line width of the central line is still very narrow and indicative of fast rotation, although the separation of the outer splitting already indicates rather slow rotation. This is a typical sign of anisotropic motion of DSA molecules potentially due to the decreased mobility triggered by the head group coordination to the metal ion. The sharper feature of the 'slow' component present in stearate might indicate a more homogeneous binding of the surfactant to the metal ion than in SDS, where a broader distribution is present that smears out these slow-motion spectral features. This might indicate different coordination sites for sulfate head groups to the metal.

- *Order parameter for 5-DSA CW EPR spectra*

In Section 2.7.4 the order parameter S for anisotropic EPR spectra was introduced and the method was applied to 5-DSA EPR spectra in miniemulsions with and without complex. The order parameter S was originally introduced for lipid bilayers/membranes [40, 42, 44], where elongated spin labels like DSA undergo rapid anisotropic motion about the long axis of the alkyl chain, superimposed on which is a wobbling motion that arises from (trans-gauche) isomerizations. This leads to a confined, cone-shaped region for the nitroxide moiety due to the bilayer environment (see Figure 2.14). In a miniemulsion with 5-DSA and sodium stearate the order parameter S could be obtained for spectra in absence of a complex (S=0.39) and in presence of Eu^{3+}(S=0.71) (Figure 5.29). For the same spin probe in SDS, the order parameter in presence of $Eu^{3+}$was determined as S=0.64. A more ordered (more rigid) bilayer imposes greater restrictions on the rotational mobility of the nitroxide, resulting in an increase in the order parameter (an increase in the order parameter can be described as a decrease in the spin probe mobility, hence, as a decrease in the bilayer fluidity). Thus, a sodium stearate miniemulsion already in absence of the complex shows a slight order at the 5th position of DSA, which becomes enhanced in the presence of Eu^{3+}-complex. 5-DSA experiences less order in the structures that are built by SDS and Eu^{3+}-complex than in those built from stearate (this was already discussed due to the broader signal of the slow component in SDS). Despite the fact that DSA has a carboxylate head group and one could assume that the EPR results are only reliable when used in combination with stearate-based miniemulsions (which also has a carboxylate head group) and not in combination with SDS, one can reliably use the information obtained here to draw conclusions about the order in the layered structures. Since the head-group behavior of DSA should be identical and only dependent on whether lanthanide complex was employed or not, both types of DSA molecules (5-DSA and 16-DSA) are effective reporters for the structuring and fluidity of the layers: the mobility of DSA in more rigidly ordered layers (carboxylate-based surfactants) is reduced while in less rigid structures (sulfate-based surfactants) it is increased.

In the layered structures made from sulfate-based surfactants, the presence of DSA certainly induces distortions in the onion-like structure due to the carboxylate-complex coordination but since the amount of DSA is low, the distortions can be seen as being important only on the local scale. The impact on changing the structure mainly depends on the binding capabilities of the head group to the metal-ion. Hence, the charged sulfate headgroup of SDS that is supposed to have higher Lewis-basicity, is preferred by the metal-ion as compared to the undissociated -COOH group of DSA. Keeping this in mind, we can interpret the order parameter or fluidity of the structures from the DSA point of view in SDS as being more fluid. This is immediately obvious from the CW EPR spectra: For 16-DSA (Figure 5.35) in sulfate surfactant higher exchange interaction is present than in carboxylate surfactant. For 5-DSA (Figure 5.36) in sulfate surfactant a higher mobility is observed than in carboxylate surfactant. Possibly the coordination constant between sulfate and complex is lower than between carboxylate and complex. This should be checked by comparing experiments with spin-labeled SDS.

The comparison of 5-DSA spectra in complex-free and complex-containing miniemulsions lead further to the assumption that the self assembly of the surfactant molecules into layered structures takes already place in “standard” miniemulsions (complex-free). In the ternary phase diagram (water/MMA/surfactant) the used composition with the low surfactant concentration (see basic miniemulsion recipe, Table 5.3) is near the water edge, where basically no surfactant aggregates should be found. Since phase diagrams are highly pressure and temperature dependent, it seems possible that the energy input due to ultrasonification leads to a transition into a phase with surfactant aggregates.

- *Effect of temperature on the model miniemulsion*

Monomer droplet stability during storage or particle nucleation is a basic requirement to obtain a latex with narrow particle size distribution upon polymerization. Since the radical polymerization is performed at higher temperatures (T~60°C) it was of particular interest to investigate the influence of temperature on the structured regions.

In Chapter 5.7 the temperature dependence of CW EPR spectra of 5- and 16-DSA in miniemulsions was presented. With both spin labels it was possible to monitor a defined temperature range of enhanced mobility before macroscopic phase separation occurs. For the given miniemulsion composition (see Table 5.3) the temperature was dependent on the used surfactant: for SDS the temperature is between 45-55°C and for SOS above 55°C. The values of the isotropic hyperfine coupling increased with temperature indicating a more disordered interface with deeper water penetration into the droplet or an increased release of DSA molecules into the water phase. Indeed this might be possible since the dissociation degree of DSA increases at higher temperatures. Below the characteristic temperature, the fraction of the fast component was found to increase only very slightly with temperature, thus, the structured regions are very stable in this temperature regime. Above this temperature the fraction of the fast DSA component was increased, which indicates a breaking of the structures. It seems possible that at this temperature the formation of larger monomer droplets takes place since this would release surfactant and DSA into the water phase as a result of a decreased surface-to-volume ratio.

- *Signal decrease in presence of diamagnetic and paramagnetic lanthanide complex*

The signal decrease of the nitroxide signal due to enhanced relaxation in presence of paramagnetic Gd^{3+}-ions was discussed in section 5.6.2. However, the proposed mechanism cannot explain the signal decrease in presence of diamagnetic Eu(III) that is observed in the CW spectra in Figure 5.23 and Figure 5.24. Since diamagnetic Eu^{3+} has no magnetic interactions with the nitroxide radical the decreased signal has to be due to the chemical loss of radicals. Theoretically, the free radical could be decomposed in a recombination or redox reaction. The recombination of two doxyl-moieties is sterically hindered and thus highly unfavorable. The metal ion Eu^{3+} is already in the oxidized form (the paramagnetic Eu^{2+} ion is the reduced form), so that we can exclude a redox reaction between the metal and the nitroxide, too. Dependent on the pH of the solution, two nitroxides are known to undergo a disproportionation reaction into a nitrone (C=NRO) and a hydroxylamine (C-NOH), which is an effective radical-destroying reaction at low pH values. The miniemulsions were kept at a pH of 6.5-7 in all measurements, an interval were nitroxides are usually stable. The presence of complex did not significantly alter the pH value. Of course, there is still MMA in the solution and the nitroxide may start a polymerization reaction. However, this should also happen in the complex-free miniemulsion, which was not the case. Thus, the signal loss can only be traced back to the presence of the lanthanide-complex. Again, this effect is more pronounced for 5- than for 16-DSA, thus it may be due to a direct interaction between the metal-complex and the nitroxide in the head group region. Indeed this is other evidence for interactions between the charged headgroups and the metal ion.

Ln^{3+} ions are hard Lewis acids, therefore the *tris* β-diketonate complexes preferentially form complexes with oxygen-donor (or nitrogen-donor) Lewis bases. It was found that various adducts occur with Lewis-basic *oxygen* and *nitrogen* donors, e.g. dimethylsulfoxide and bipyridine [221]. Interestingly, one compound $[M(tmhd)_3 \cdot x(adduct)]$ containing x molecules of adduct may form different coordination polyhedra that can be considered as isomers. The lanthanide ions are large and can adopt different geometrical shapes for a given coordination number. Thus, the different coordination polyhedra can be attributed to packing effects [221].

The nitroxide N-O moiety is a Lewis-base (π-basic) and can coordinate to a metal ion (Lewis-acid) via the nitroxide-oxygen N-O····M [266]. If the metal ion is paramagnetic, the coordination results in a strong metal-nitroxide spin-spin interaction that can be ferromagnetic (parallel alignment of the spins) or antiferromagnetic (antiparallel alignment) in nature, depending on the orthogonality and overlap between the magnetic metal orbitals and the radical SOMO π^* orbital. Such complexes of paramagnetic metals with nitroxides have become very popular in the recent years due to their easily adjustable magnetic properties and extension in one, two or three directions (such materials are called molecular based magnets) [266] and it was found that nitroxide-metal complexes that are coordinated via the oxygen atom are coupled essentially *antiferromagnetically*. However, this can still not explain the signal loss of the nitroxide in presence of the Eu^{3+}-ion with a diamagnetic ground state: the coordination of one nitroxide group would preserve the S=1/2 state. If we assume the coordination of two nitroxide groups to one metal center, that are coupled antiferromagnetically to an S=0 state, the EPR signal could vanish due to superexchange of the nitroxide spins (superexchange is defined as a spin coupling between two metal ions via a diamagnetic ligand M-L-M [267], thus, a coupled radical pair via a diamagnetic metal would be the 'inverse' case). This might be possible by polarization of the diamagnetic electron pairs of the metal without direct interaction of the two radical centers, as shown in Figure 5.37.

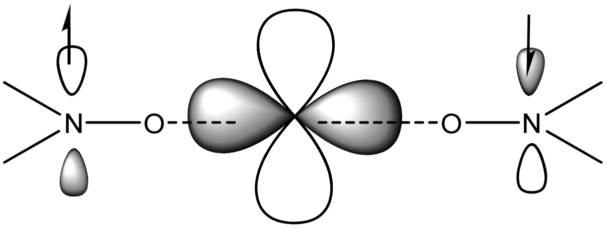

Figure 5.37 Symmetry relation between the dx^2-y^2 and pπ orbitals of a nitroxide and possible scheme of an antiferromagnetic exchange coupling of two nitroxide radicals, mediated through the metal orbital. The pπ orbital is not necessarily located at the nitrogen rather than extendend between the N- and the O-atom. It might be possible that such a complex is formed for a short time that acts further as catalyst for the disproportionation reaction.

Indeed this seems to be unlikely, since two DSA molecules have to adapt a T-shape, bent conformation that results in a steric hindrance for the NO-coordination to the metal. Further, due to the bulkiness of this T-shaped molecule, this is not imaginable for a $Ln(L)_3$ complex without a ligand exchange. It might be more probable for a $Ln(L)_2$ complex, that has free coordination sites (in solution the LnL_3 complex is in equilibrium with LnL_2^+ and LnL_4^-), but with a ratio of 94% on the educt site LnL_3 [268] the signal loss cannot be explained properly.

Staying in a picture of highly coordinated lanthanide ions one could also speculate that the lanthanide ions may as well act as catalytic centers for disproportionation of some of the nitroxide radicals. Either by binding the NO-oxygen directly (as shown in Figure 5.37), which is not very likely, or simply due to stronger immobilization (as compared to complex-free solution) of two DSA molecules with their carboxylate headgroups on the same or on neighboring lanthanide complexes. Such, due to local confinement, one could imagine that in particular for 5-DSA, hydronium ions may come in close contact with two NO-groups. This can be achieved by penetration of the (acidic) protons into the layered structures. In such a case, it was shown in thermoresponsive hydrogels that even at moderate pH values, a combination of strong local confinement of two or more spin probes and the presence of acidic protons can lead to accelerated nitroxide disproportionation [269]. Since in 16-DSA the nitroxide moiety is buried much deeper in the layered hydrophobic structures, disproportionation in this case becomes are less likely than for 5-DSA.

- *The extraction of distance information between paramagnetic metal and nitroxide*

The Leigh effect [228], which is the proposed mechanism to account for the observed signal amplitude loss in the CW EPR spectra in presence of paramagnetic Gd^{3+}-complex (see section 5.6.2) is strictly valid only for interacting spins in a rigid lattice, since otherwise the dipolar interaction is averaged out. Further, it only accounts for the interaction between two unlike spins (and not for nitroxide-nitroxide interaction). Thus, the used concentration of DSA should be reduced in order to extract reliable distance information (especially exchange interactions should be eliminated). For the application of the Leigh method, the electron relaxation rate T_1^{-1} of the metal ion has to be known and the rigid lattice condition can be fulfilled by measurements at lower temperature (e.g.-20°C).

For short distances between Gd^{3+} and the nitroxide, exchange effects between the two spins must be considered as a possible contribution to the broadening. Such interactions are assumed to be dependent on the concentration of Gd^{3+} and the steric hindrance of the ligands. The bulkier the ligands, the less effective the orbital overlap between the nitroxide p- and the metal orbital becomes. Furthermore, the electron bearing orbital in Gd^{3+} are the 4f orbitals, that are shielded by higher lying 5d and 6s orbitals. Thus, Heisenberg spin exchange interactions might not be the dominant spin interaction with a nitroxide, especially not at low temperatures. This would make the Leigh method an easy experiment to extract distance information in a quantitative way. This was not done in detail here but from the amplitude-normalized spectra of 5-DSA (Figure 5.23) and 16-DSA (Figure 5.24) in presence of Gd^{3+}-complex it is immediately noticed that the signal amplitude is more severely reduced for 5-DSA than for 16-DSA (note, that in these figures the DSA spectra are normalized to the double integral of the complex-free DSA counterpart, for application of the Leigh method the Gd^{3+}-spectrum needs to be normalized to the double integral of the Eu^{3+}-spectrum). This proves a closer location of the 5th position to the metal than the 16th position. Pulsed relaxation measurements (Section 5.8) confirm this trend (as seen in the smaller values in longitudinal and transversal relaxation times in the presence of Gd^{3+}).

5.10 Conclusion and Outlook

CW and pulse EPR measurements were performed on miniemulsions and polymer-dispersion that were prepared with different surfactant types in presence and absence of a lanthanide-β-diketonate complex M(tmhd)$_3$ (M=Eu^{3+}, Gd^{3+}). It had previously been established that surfactants with sulfate head groups ($-OSO_3^-$) form onion-like multilamellar and those with carboxylate head groups ($-COO^-$) form lamellar structures. In both cases, the layer thickness could be adjusted via the surfactant chain length [231]. In the present study, the layer thickness was varied between 12 and 18 carbon atoms. The spin probes 5- and 16-DSA (generally 5 mol.-% with respect to the surfactant) were used to report about different region within the layers and CW EPR spectra were analyzed with respect to the observed spectral features of the used type of DSA. For 16-DSA, the Heisenberg spin exchange frequency ω_{Ex} was the key variable, while for 5-DSA the rotational correlation times τ_{corr} under different conditions gave significant dynamic information. The CW EPR spectra were composed of two DSA types that differ in their mobility and the chemical and

magnetic environment. The slower and broader component with lower isotropic hyperfine coupling values a_{iso} could be assigned to DSA in the structured, layered regions. We found characteristic exchange frequencies for DSA incorporated into layers that were formed by carboxylate (ω_{Ex}~ 15 MHz) and sulfate (ω_{Ex}> 33 MHz). In layers of carboxylate surfactants, the exchange frequency was independent on the surfactant chain length; in layers of sulfate surfactant ω_{Ex} decreased with increasing chain length. Layers made of carboxylate surfactant are less fluid than sulfate-surfactant based layers.
These changes in τ_{corr} and ω_{Ex} in the different surfactant based bilayers are indicative for different binding strengths or binding geometries of the surfactant head groups to the metal ion. Layers made of sulfate surfactant are more fluid and obey a lower order than carboxylate based surfactant layers which indicates a lower coordination constant between sulfate and the metal ion which in turn enhances lateral diffusion (see Figure 5.31) within the layers.

The EPR measurements show that the self assembly of the surfactant into layered structures in a miniemulsion is already established without addition of the complex, which might be due to energetically favored phases. The addition of lanthanide β-diketonate complex Eu(tmhd)$_3$ or Gd(tmhd)$_3$ to a miniemulsion results in a remarkably higher ordering of the bilayer structures, as proofed by the calculated order parameters for 5-DSA spectra ($S \approx 0.4$ complex free, $S \approx 0.7$ with complex, see Section 5.7.1).
In presence of Gd^{3+}-complex the signal amplitudes of the nitroxide spectra were decreased without broadening of the signal, which points to the Leigh-effect [228] as a potential method to extract distance information between the nitroxide and the metal.

Temperature dependent measurements suppose a polymerization temperature below 45-55°C (dependent on the used surfactant, see Section 5.7) in order to obtain a maximum in structured regions. We found a characteristic temperature for each type of surfactant above which instability mechanisms (coagulation) of the miniemulsion occur. The beginning of coagulation can be easily observed by signal decrease in CW EPR spectra already before it is visible macroscopically.

For further investigation it is advisable to use DSA to surfactant ratios of 1:100 since the present spin-spin interactions complicate data analysis. Further it should be clarified how and if at all the carboxylate head group in DSA changes the onion-like structures present in layers made by interactions between sulfate surfactant and complex. CW EPR experiments on spin-labeled SDS could give this information.

6 Summary

In this work, three nitroxide based ionic systems of increasing complexity were used to investigate structure and dynamics of their respective aqueous solutions by means of EPR and ENDOR spectroscopy at X- and W-band (9.5 and 94.5 GHz, respectively). The results obtained in this thesis are summarized below for each system.

- *The solvation of Fremy's salt (Chapter 3)*

The solvation of Fremy's salt, the paramagnetic nitrosodisulfonate anion $ON(SO_3^-)_2$, in binary solvent mixtures was investigated by means of pulse (Mims- and Davies-type) electron nuclear double resonance (ENDOR) spectroscopy and molecular dynamics simulations. ^1H and ^2H pulse ENDOR measurements were performed on small Fremy's salt radicals in isotope-substituted solvent mixtures of methanol and water in frozen solution. We were able to obtain well-resolved, orientation-selective high-field/high-frequency pulse ENDOR spectra of methyl protons from the alcohol moiety and exchangeable protons from the alcohol-hydroxyl group and water. In the studied solvent systems (volume ratio v/v= 30:70, 50:50, 70:30) the solvation of 2.5 mM Fremy's salt by methyl protons was found to be almost identical. From the analysis of the dependence of pulse ENDOR spectra on the observer field position and spectral simulations we obtained the principal components of the hyperfine coupling (hfc) tensor for each class of protons. The combination of Mims- and Davies-type pulse ENDOR measurements was necessary to obtain blind spot free information on hfc that span a broad range of 0.25 - 6 MHz. Using the point-dipole approximation, the dipolar hfc component yields a prominent electron-nuclear distance of 3.5 Å between Fremy's salt and methyl protons, which was found along the molecular z-axis (perpendicular to the approximate plane spanned by $ON(S)_2$) of the probe molecule. Exchangeable protons were found to be distributed nearly isotropically, forming a hydrogen-bonded network around the sulfonate groups. The distribution of exchangeable and methyl protons found in MD simulations is in very good agreement with the pulse ENDOR results and we find that solvation is dominated by an interplay of H-bond (electrostatic) inter-

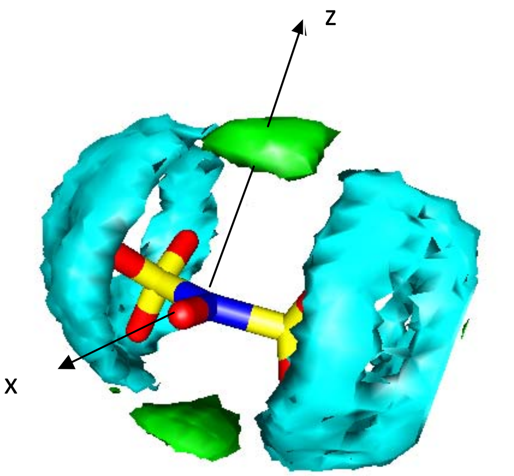

Figure 6.1 The solvation of Fremy's salt in CH_3OH/H_2O (*v*/*v*=50:50). Along the z-axis of the molecular frame methyl protons (green) are accumulated, whereas the charged sulfonate groups are strongly hydrogen-bonded and surrounded by exchangeable- protons (cyan).

actions and steric considerations. The elucidation of the microscopic solvation of a small probe molecule in binary solvent mixtures represents the first step for understanding the interactions in more complex biochemical systems. In particular this includes the potential perturbation of H-bond networks due to presence of a spin probe or other polar molecules.

- *Polyelectrolyte solutions with divalent salts (Chapter 4)*

The conformation of spin labeled poly(diallyldimethylammonium chloride) (PDADMAC) solutions in aqueous alcohol mixtures in dependence of added divalent sodium sulfate was investigated with double electron-electron resonance (DEER) spectroscopy. The solvent:-to-water ratio was 1:3 in all solutions (*v/v*) and the used solvents were methanol, ethanol, n-propanpl, ethylene glycol and glycerol. The ionic strength was varied from 0 mM to 750 mM. The mean distance r, the distribution $s(r)$ and the label-to-label distance L between the spin labels were extracted from DEER data using the wormlike chain (WLC) model.

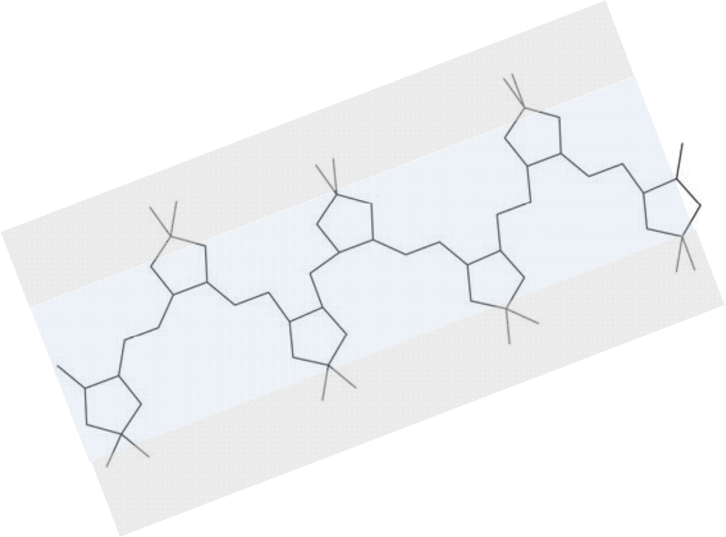

Figure 6.2 PDADMAC chain with hydrophobic (grey) and hydrophilic (blue) solvent domains in a binary aqueous solvent mixture.

For the mixture *n*-propanol/water the longest label-to-label distance (L=8.3 nm) was found, the smallest value L=7.7 nm was found in the short chain alcohol methanol/water mixture. The difference between the two alcohols resemble their impact on the hydrophobic solvation of the polymer backbone, where *n*-propanol is better suited than methanol and may thus screen hydrophobic interactions among the monomer-monomer units of the polymer as supposed in [194-195].

The obtained data suggest a less serve impact on conformational changes due to salt than usually predicted in polyelectrolyte theory and stress the importance of a delicate balance of hydrophobic and electrostatic interactions, in particular in the presence of organic solvents, that preferentially solvate the polymer backbone (grey in Figure 6.2).

- *Structure and dynamics of miniemulsions (Chapter 5)*

The structure and dynamics of miniemulsions and polymerdispersions prepared with anionic C12 and C18 surfactants (sodium laurate, sodium stearate, sodium dodecyl sulfate, sodium octadecyl sulfate) with MMA as oil phase in presence and absence of a lanthanide β-diketonate complex M(tmhd)$_3$ (M=Eu(III), Gd(III)) was characterized using CW and pulse EPR spectroscopy. From CW EPR spectra the EPR parameters were extracted using spectral simulations. The CW EPR spectra were composed of two DSA types that differ in their mobility and their chemical and magnetic environment. The slower and broader component with lower isotropic hyperfine coupling values a_{iso} was assigned to DSA molecules in the structured, layered regions; the faster component was assigned to DSA at the MMA/water interface. We found characteristic exchange frequencies ω_{Ex} for DSA incorporated into layers in the order:

$$\text{sodium stearate} \approx \text{sodium laurate} \ll \text{SOS} < \text{SDS}$$

For carboxylate based surfactants the typical value is $\omega_{Ex}\sim$ 15 MHz and for sulfate based $\omega_{Ex}>$ 33 MHz.

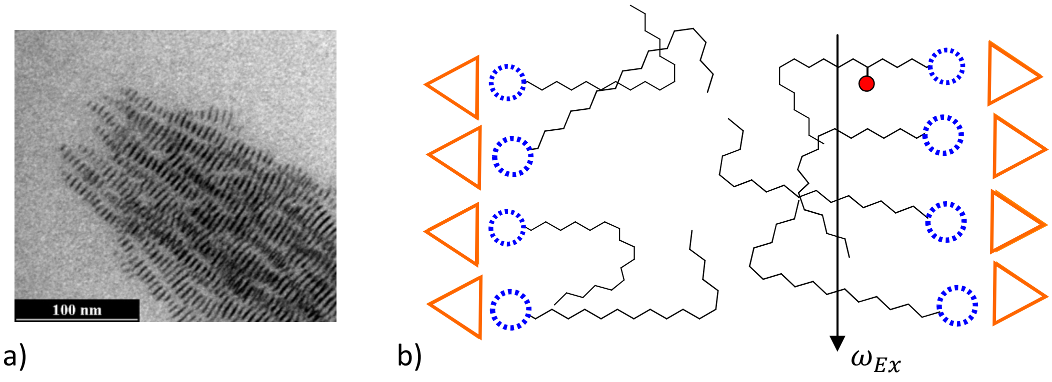
a) b)

Figure 6.3 Structured region of a polymer particle prepared via miniemulsion polymerization. A) TEM picture (without contrastation) b) scheme of the surfactant bilayers where the headgroup is coordinated to the free binding site of the lanthanide complex. The value of the exchange frequency is correlated with the ease of lateral diffusion, which is a function of the binding strength of the head group to the metal ion. The black regions of the TEM picture (a) correspond to the orange triangles in (b).

In layers of carboxylate surfactants, the exchange frequency was independent on the surfactant chain length; in layers of sulfate surfactant ω_{Ex} decreased with increasing chain length (Section 5.5).

Furthermore we found a higher mobility for 5-DSA in sulfate based (τ_{corr}~12 ns, Section 5.5.2) than in carboxylate (τ_{corr}~2-5 ns, Section 5.6.1) based surfactant bilayers.

These changes in τ_{corr} and ω_{Ex} in the different surfactant based bilayers are indicative for different binding strengths or binding geometries of the surfactant head groups to the metal ion. Layers made of carboxylate surfactant are less fluid and obey a higher order than sulfate surfactant based layers which indicates a higher coordination constant between carboxylate and the metal ion which in turn restricts lateral diffusion (diffusion perpendicular to the bilayers normal as indicated with an arrow in Figure 6.3 b) within the layers.

The EPR measurements show that the self assembly of the surfactant into layered structures in a miniemulsion is already established without addition of the complex. The addition of lanthanide β-diketonate complex Eu(tmhd)$_3$ or Gd(tmhd)$_3$ to a miniemulsion results in a remarkably higher ordering of the bilayer structures, as proofed by the calculated order parameters for 5-DSA spectra ($S \approx 0.4$ complex free, $S \approx 0.7$ with complex, see Section 5.7.1).

In presence of Gd^{3+}-complex the signal amplitudes of the nitroxide spectra were decreased without broadening of the signal (Section 5.6.2), which points to the Leigh-effect [228] as a potential method to extract distance information between the nitroxide and the metal.

For temperatures >45°C (see Section 5.7) the structures break down. Thus, temperature dependent CW EPR measurements suppose a polymerization temperature below 45-55°C (dependent on the used surfactant) in order to obtain a maximum in structured regions. We found a characteristic temperature for each type of surfactant above which instability mechanisms (coagulation) of the miniemulsion occur. The beginning of coagulation can be easily observed as a signal decrease in the CW EPR spectra already before it is visible macroscopically.

7 Experimental Part

7.1 Materials and Sample Preparation

- *Fremy's salt*

Fremy's salt, FS, ($K_2[ON(SO_3)_2]$ potassium nitrosodisulfonate, ICN Biomedicals Inc.) was used without purification. D_2O (99.9%), Methanol-d1 (CAS 1455-13-6, CH_3OD, 99.5%), Methanol-d3 (CAS 1849-29-2, CD_3OH, 99.8%) and Methanol-d4 (CAS 811-98-3, CD_4O, 99%) were obtained from Aldrich. All solutions were prepared at ambient conditions without the use of inert gas. KOH solutions were used to adjust the pH in order to exclude the introduction of a new ion species (carbonate ions) into the system. In all samples we used a KOH concentration of c_{KOH}= 9.8 $\cdot 10^{-4}$ M and FS concentrations of 2.5 mM.

Stock solutions of 10 mM FS in MilliQ water (Millipore) and D_2O were prepared and a solution of 2 M KOH solution was added. The obtained solutions were diluted to 5 mM FS concentration and stored at -18°C. From the aqueous solutions the alcohol/water mixtures were prepared by adding the according volume of methanol.

- *PDADMAC*

Cationic poly(dimethyldiallylammonium chloride) was a gift from Dr. J. Storsberg (Fraunhofer Institute for Applied Polymer Research, Golm). It was prepared by radicalic polymerization of diallydimethylammoniumchloride and diallylamine (96:4 molar ratio) in aqueous solution. In a second step the amine was esterificated with 4-Carboxy-Tempo (CAS 37149-18-1) to yield the statistically labeled polycation. Purification from unreacted monomer and nitroxide was achieved by dialysis against water. The white, hygroscopic polymer was obtained by freeze drying. Its molecular weight was determined by gel permeations chromatography to M_w of 490000 g/mol and a M_n of 146000 g/mol.

Stock solutions of PDADMAC (100 mM) in MilliQ water, ethanol, ethylene glycol and glycerol were prepared and stored at -18°C. These stock solutions were further diluted to yield the wished end concentration of polymer. Sodium sulfate containing solutions were prepared by adding the salt as fine powder.

- *Miniemulsions*

5- and 16-DSA were obtained from Aldrich and used as received. Hexadecane, sodium dodecyl sulfate, sodium lauryl sulfate, sodium octadecy sulfate, sodium stearate and the lanthanide complexes $Eu(tmhd)_3$ and $Gd(tmhd)_3$ were obtained from Aldrich and used as received. Methyl methacrylate (Aldrich) was purified from stabilisator by column chromatography (silica gel) and stored at -18°C. The non-ionic surfactant Lutensol AT 50 (a polyethylene glycol ether RO(CH_2CH_2O)$_{50}$H) was purchased from BASF. The water soluble initiator V59 (WAKO) was used as obtained.

All samples were prepared under ambient conditions, only the ultrasonification was performed in an ice bath. The surfactant and spin probe were dissolved in water. The complex, initiator and hexadecane were dissolved in the monomer. After homogenization of both solutions for one hour they were mixed, stirred again for one hour and than ultrasonified for 3 minutes in an ice bath (BRANSON digital sonifier model 450 D with 1/8 inch tip). The samples were divided in two fractions. The first fraction was used as obtained from this procedure (‘miniemulsion’). The second part was polymerized (‘polymer-dispersion’). Problems in the sample preparation arose with C18 surfactants since these are only little water soluble and did not dissolve within one hour. However, upon addition of the monomer solution, no unsolubilized surfactant was visible. Some samples had the tendency to coagulate with time. In the worst case this happened 30 minutes after sample preparation, but only for sodium stearate as surfactant. The most stable miniemulsions were achieved with C12 surfactants and didn’t coagulate within 3 weeks. Notably, miniemulsions with added complex showed fewer tendencies to coagulate than their complex-free counterparts. Again, the C12 systems were more stable than the C18 systems. To avoid any ageing effects in the EPR measurements, parts of each sample were filled in the 3 mm EPR tubes and shock frozen immediately after preparation. These samples were stored under liquid nitrogen and were used for pulse measurements. Room temperature CW EPR measurements were all performed within 5 hours after sample preparation.

7.2 EPR Measurements

- *X-band measurements*

The CW EPR spectra were measured on a Miniscope 200 spectrometer (Magnettech GmbH) with a TE102 rectangular resonator. Temperature was controlled with a TC HO2 temperature controller (Magnettech). Samples were loaded into 50µl capillaries (1.5 mm diameter, ringcap H®, Hirschmann Larborgeräte).

The typical microwave power of 10 µW was applied during these measurements and did not lead to saturation broadening. The modulation amplitude was set to 0.02 mT with a width of the central line of the nitroxide spectrum around 1 mT.

The sweep width was 1 mT. Depending on the S/N ratio ten to 99 scans were averaged, with 4096 data points and a scan time of 60 s each.

X-band ESE and DEER measurements were performed on a Bruker ELEXSYS E580 spectrometer using a Bruker Flexline split-ring resonator (ER 4118X MS3). The resonator was overcoupled to Q≈100. The temperature was set to 50 K by cooling with liquid helium using an Oxford cryostat and cooling system or a closed cycle cryostat (ARS Inc.). 80 μl sample were loaded with a syringe into homemade quartz tubes of 3 mm outer diameter (Wilmad Corp. USA). Samples were shock frozen in nitrogen cooled iso-pentane and inserted into the probe head.

EPR spectra were measured with field-swept echo detected EPR using a Hahn echo sequence $\pi/2$- τ - π- τ -$echo$ and a 20 mT field sweep. The interpulse delay time τ was 200 ns and the pulse lengths were 16 ns for $\pi/2$ and 32 ns for π pulses. The integration gate length was 200 ns.

The transversal relaxation data (T_2) was acquired with a Hahn echo sequence $\pi/2$-τ-π-τ-$echo$ and applying a $[(+x)-(-x)]$ phase cycle to the $\pi/2$ pulse. An initial interpulse delay τ of 200 ns was incremented by 8 ns. The integrated echo intensity was measured as a function of this increment with an integration gate of 32 ns length centered at the echo maximum. The pulse lengths were 16 ns for the $\pi/2$ pulse and 32 ns for the π pulse.

The longitudinal relaxation data (T_1) were acquired with an inversion recovery pulse sequence π- T- $\pi/2$- τ- π- τ-$echo$ with a $[(+x)-(-x)]$ phase cycle applied to the $\pi/2$ pulse. The delay time T with an initial value of 2000 ns was incremented in steps of 5800 ns and the interpulse delay τ= 400 ns was kept constant. The pulse lengths were 52 ns for the $\pi/2$ pulse and 104 ns for the π pulse for the detection subsequence and 24 ns for the inversion π pulse.
The integration gate length of 104 ns matched the longest pulse in the detection subsequence to maximize the signal-to-noise ratio. The inversion pulse was tuned by maximizing the negative echo at a delay time T=1000 ns.

The field position for relaxation measurements corresponded to the maximum of the nitroxide spectrum and was determined by the ESE experiment.

DEER experiments were performed with a $\pi/2(\nu_{obs})$-τ_1-(ν_{obs})-t'- $\pi(\nu_{pump})$-($\tau_1+\tau_2-$ t')-$\pi(\nu_{obs})$-t_2-$echo$ pulse sequence with a $[(+x)-(-x)]$ phase cycle applied to the $\pi/2$ pulse. The time t` was incremented in steps of 8 ns. The time $\tau_1$=200 ns was kept constant. The $\tau_2$was varying between 0.8 ms and 2.5 ms depending on the T2 relaxation properties of the sample and distance that needed to be measured. The dipolar evolution time is defined as t= t`-τ_1. The data analysis was performed for t>0 ns. The pump frequency $\nu_{pump}$was set to the center of the resonator dip that is also coincident with the maximum of the nitroxide

EPR spectrum, whereas the observer frequency ν_{obs} was approximately 65 MHz higher and coincided with the low field local maximum of the EPR spectrum. The observer pulse lengths were 32 ns for both $\pi/2$ and π pulses. The π pump pulse length was 12 ns. The width of the integrator gate was 32 ns. Proton modulation was averaged by adding traces at eight different $\tau_1$values, starting at τ_1= 200 ns and incrementing it by 8 ns. The repetition time between every pulse experiment was 2 ms and the measurement time was typically around 8 to 12 hours.

- *W-band measurements*

W-band measurements were performed on a BRUKER Elexsys E680 spectrometer using a Bruker EN 660-1021 H TeraFlex ENDOR-resonator. The resonator was not overcoupled. All measurements were performed at 20 K with liquid helium cooling by an Oxford CF935 cryostat with an Oxford ITC4 temperature controller. Samples were loaded with a Hamilton syringe into 0.7 mm inner diameter home-made CFQ-quartz capillaries to a height of about 3 mm and inserted into the resonator at 50 K and then cooled down to 20 K.

The field-swept, electron spin echo (ESE) detected EPR spectra were recorded by integrating over the echoes created with the pulse sequence $\pi/2$-τ-π- τ-*echo*, with the pulse lengths $t_{\pi/2}$= 48 ns, t_{π}= 96 ns and an interpulse delay of τ= 300 ns. From echo detected spectra, the characteristic points for ENDOR measurements were assigned as shown in Figure 3.2(b). ^{1}H and ^{2}H ENDOR spectra were recorded using the Mims three-pulse scheme ($\pi/2$- τ- $\pi/2$-T- $\pi/2$) [61], with the radiofrequency (RF) pulse applied during time *T*. A $\pi/2$ pulse length of 48 ns was used. Since Mims-type ENDOR spectra are hampered by blind spots depending on the pulse interval τ, measurements for different values of τ were performed. For ^{1}H measurements typical values for τ were 172 or 200 ns, for ^{2}H 400 to 600 ns. The rf pulse length varied for ^{1}H and ^{2}H nuclei and was optimized for the studied nucleus. A typical value for ^{1}H was 20 μs. The rf frequency was swept from 20 to 24 MHz for detection of deuteron hf couplings and from 139 to 147 MHz for proton hf couplings. The Davies ENDOR sequence [62] π-T- $\pi/2$- τ-π-*echo* was used to record ^{1}H spectra. The inversion π pulse was 200 ns. A radio frequency pulse length of 20 μs was applied during the time T. In the detection sequence ($\pi/2$-τ-π τ-*echo*), a pulse length of $t_{\pi/2}$=200 ns and t_{π}=400 ns were used with an interpulse delay of τ=548 ns. The signal was accumulated over two to five hours for the x- and y-position and at least 14 hours for the z-position.

7.3 Data Analysis

- *CW data*

The shown CW spectra were background corrected using a home written MATLAB program, by subtracting the first order polynomial fitted on the first and last 15 % of the spectral data points. The values for the isotropic hf splitting and exchange frequency were obtained from CW data by using a home written MatLab fitting routine that is able to account for anisotropic motion and broadening due to spin-spin interactions (exchange and dipolar) as described in Section 2.5.

- *Relaxation*

The T_2 data was fitted by the second order exponential decay curve given in eq. (7.1) with A, T_{2A}, B, T_{2B} and C being the fitting parameters.

$$I(t) = A \exp\left(-\frac{\tau_1}{T_{2A}}\right) + B \exp\left(-\frac{\tau_2}{T_{2B}}\right) + C \qquad (7.1)$$

The τ_2 parameter is computed from the parameters of the fit as the time where the biexponential function has decayed to $1/e$ of its initial value. As the expression $I(t)$ for a biexponential decay cannot be solved analytically for the $1/e$ time, τ_2 was determined by numerically minimizing $|I(t) - 1/e|$ with a home-written Matlab program. The transversal relaxation parameters relate to twice the interpulse delay τ so that the determined relaxation times or relaxation parameters should be multiplied with two.

Longitudinal relaxation data were fitted by the biexponential decay function given by:

$$I(t) = I_0\left(1 - 2\left[A \exp\left(-\frac{\tau_1}{T_{2A}}\right) + B \exp\left(-\frac{\tau_2}{T_{2B}}\right)\right]\right) \qquad (7.2)$$

with I_0, A, T_{1A}, B and $T_{\ 1B}$ the fitting parameters. The relaxation parameter τ_1 is defined as the time where a fraction of $1 - 1/e$ of the echo signal has recovered and is computed from the parameters of the fit as the time where the biexponential function has decayed to $1/e$ of its initial value. For the $1/e$ time, τ_1 was determined by numerically minimizing $|I(T) - 1/e|$ with a home-written MATLAB program also used for τ_2 determination.

- *X- Band DEER*

Commonly, the DEER data are analyzed under the assumption that the isotropic exchange coupling is negligible versus the anisotropic dipolar coupling. The DEER measurements were analyzed using the “DeerAnalysis2008” program (Gunnar Jeschke). Basically, it divides out the homogeneous part of the signal and FT the modulation, which gives the Pake pattern in Figure 2.8 b. After loading the experimental data into the program and performing a phase correction, the starting (‘cero time’) and the final point (‘cut off’) of the data analysis are defined. The latter is chosen in such a way that no modulation coming from interpulse crossing is analyzed. Furthermore the starting point for the background fit has to be defined (‘background’). All these points can be defined manually or automatically. Since all data should be evaluated using the same parameters for cero time and background both were set manually. The starting point for data analysis is at 105 ns and the start for the background fit at 1500 ns. The background subtraction step is very important, since the obtained distance distribution is sensitive to the starting point of the background decay subtraction and to the type of the function assumed for the background, herein a three-dimensional homogeneous spin-distribution is assumed (exponential decay function). After the background subtraction, which originates from intermolecular interactions, the data contains only intramolecular contributions and is fitted by a distance distribution. The transformation of the dipolar evolution function to a distance distribution is an ill-posed problem, meaning that similar dipolar evolution functions may produce highly different distance distributions [270] and is thus highly sensitive to the initial parameters. Therefore only good S/N DEER spectra are used for further evaluation. In the present work the wormlike chain model is applied (note that for biradicals the Tikhonov regularization is commonly applied). This fitting model is included in the software package and considers the distance distribution in the range between 1.5 nm to 10 nm. The extraction of the valuable parameters L, lp, r and $s(r)$ (lable-to-label distance, persistence length, mean distance and width of the distribution, respectively) is explained in ref. [271] for semiflexible polymers. Figure 7.1 summarizes the procedure of dipolar spectra analysis. From the fit of the WLC model the persistence length is obtained. From the singularities of the Pake pattern the dipolar coupling frequency ω_{dip} can be read off to calculate the spin-spin distance r_{12} according to:

$$r_{12} = \sqrt[3]{\frac{52.16\,MHz}{\omega_{dip}}} \tag{7.3}$$

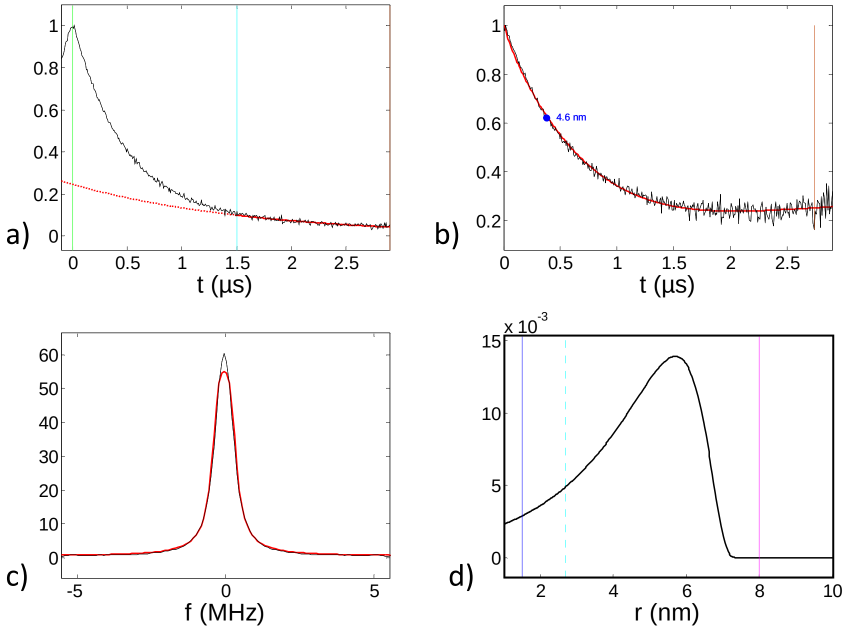

Figure 7.1 DEER spectrum analysis procedure. a) original data, green cursor for cero time, cyan line for background correction time, orange line for cut off, b) background corrected dipolar spectrum in time domain, c) Fourier transform of background corrected data (frequency domain), d) distance distribution.

8 References

1. T. I. Smirnova; A. I. Smirnov, High-Field ESR Spectroscopy in Membrane and Protein Biophysics. In *Biological Magnetic Resonance*, Hemminga, M. A.; Berliner, L. J., Eds. Springer: New York, 2007; Vol. 27, pp 165.

2. A. Perera; F. Sokolic; L. Zoranic; *Microstructure of neat alcohols*; *Phys. Rev. E* **2007,** *75*, 060502.

3. S. Z. Mikhail; W. R. Kimel; *Densities and Viscosities of Methanol-Water Mixtures*; *J. Chem. Eng. Data* **1966,** *6*, 533.

4. P. Atkins; J. de Paula, *Physical Chemistry* 8 ed.; W. H. Freeman: 2006.

5. Y. Marcus, *Solvent Mixtures Properties and Selective Solvation* Marcel Dekker: Basel, 2002.

6. R. G. Barraza; H. E. Rios; *Counterion association to cationic polyelectrolytes in methanol/water mixtures*; *Polym. Int.* **1995,** *38*, 387.

7. M. Deserno; A. Arnold; C. Holm; *Attraction and Ionic Correlations between Charged Stiff Polyelectrolytes*; *Macromolecules* **2002,** *36*, 249.

8. M. Deserno; *Mesoscopic Membrane Physics: Concepts, Simulations, and Selected Applications*; *Macromol. Rapid Commun.* **2009,** *30*, 752.

9. A. Ben-Naim, Hydrophobic - Hydrophilic Forces in Protein Folding. In *Structure and Reactivity in Aqueous Solution*, American Chemical Society: Washington, DC, 1994; pp 371.

10. G. Jeschke; *Determination of the Nanostructure of Polymer Materials by Electron Paramagnetic Resonance Spectroscopy*; *Macromol. Rapid Commun.* **2002,** *23*, 227.

11. C. Altenbach; S. L. Flitsch; H. G. Khorana; W. L. Hubbell; *Structural studies on transmembrane proteins. 2. Spin labeling of bacteriorhodopsin mutants at unique cysteines*; *Biochem.* **1989,** *28*, 7806.

12. B. Sukhorukov Gleb, From Polyelectrolyte Capsules to Drug Carriers. In *Carrier-Based Drug Delivery*, American Chemical Society: Washington, DC, 2004; pp 249.

13. T. M. Herrington; B. R. Midmore; J. C. Watts, Flocculation of Kaolin Suspensions by Polyelectrolytes. In *Colloid-Polymer Interactions*, American Chemical Society: Washington, DC, 1993; pp 161.

14. S. Beyer; W. C. Mak; D. Trau; *Reverse-Phase LbLEncapsulation of Highly Water Soluble Materials by Layer-by-Layer Polyelectrolyte Self-Assembly*; *Langmuir* **2007,** *23*, 8827.

15. B. Sun; S. A. Mutch; R. M. Lorenz; D. T. Chiu; *Layered Polyelectrolyte−Silica Coating for Nanocapsules*; *Langmuir* **2005,** *21*, 10763.

16. H. Dautzenberg, *Polyelectrolytes: Formation, Characterization and Application* Hanser München, 1994.

17. M. Pannier; S. Veit; A. Godt; G. Jeschke; H. W. Spiess; *Dead-Time Free Measurement of Dipole-Dipole Interactions between Electron Spins*; *J. Magn. Reson.* **2000,** *142*, 331.

18. O. Kratky; G. Porod; *Röntgenuntersuchung gelöster Fadenmoleküle*; *Rec. Trav. Chim. Pays-Bas.* **1949,** *68*, 1106.

19. A. Schweiger; G. Jeschke, *Principles of Pulse Electron Paramagnetic Resonance* Oxford University Press: 2001.

20. C. Rudowicz; S. Misra; *Spin-Hamiltonian formalisms in electron magnetic resonance (EMR) and related spectroscopies*; *Appl. Spectrosc. Rev.* **2001,** *36*, 11.

21. P. Zeeman; *On the influence of Magnetism on the Nature of the Light emitted by a Substance*; *Astrophys. J.* **1897,** *5*, 332.

22. J. C. del Toro Iniesta; *On the discovery of the zeeman effect on the sun and in the laboratory*; *Vistas Astron.* **1996,** *40*, 241.

23. W. Gerlach; O. Stern; *Das magnetische Moment des Silberatoms*; *Z. f. Physik A* **1922,** *9*, 353.

24. N. I. o. S. a. Technology The NIST Reference on Constants, Units and Uncertainty; latest (2006) values of the constants. http://physics.nist.gov/cuu/Constants/index.html.

25. A. Schweiger; G. Jeschke, *Principles of Pulse Electron Paramagnetic Resonance* Oxford University Press: New York, 2001.

26. *Electron Paramagnetic Resonance, A Practitioner's Toolkit* Wiley: New Jersey, 2009.

27. Y. N. Molin; K. M. Salikhov; K. I. Zamaraev, *Spin Exchange* Springer-Verlag: Berlin, 1980; Vol. 8.

28. P. W. Andersson; *New Approach to the Theory of Superexchange Interactions*; *Phys. Rev.* **1959,** *115*, 2.

29. B. L. Bales; M. Peric; *EPR Line Shifts and Line Shape Changes Due to Spin Exchange of Nitroxide Free Radicals in Liquids*; *J. Phys. Chem. B* **1997,** *101*, 8707.

30. B. L. Bales; M. Peric; *EPR Line Shifts and Line Shape Changes Due to Spin Exchange of Nitroxide Free Radicals in Liquids 2. Extension to High Spin Exchange Frequencies and Inhomogeneously Broadened Spectra*; *J. Phys. Chem. A* **2002,** *106*, 4846.

31. B. L. Bales; M. Meyer; S. Smith; M. Peric; *EPR Line Shifts and Line Shape Changes due to Spin Exchange of Nitroxide Free Radicals in Liquids: 6. Separating Line Broadening due to Spin Exchange and Dipolar Interactions*; *J. Phys. Chem. A* **2009,** *113*, 4930.

32. B. Berner; D. Kivelson; *The electron spin resonance line width method for measuring diffusion. A critique*; *J. Phys. Chem.* **1979,** *83*, 1406.

33. S. S. Eaton, *Distance Measurements in Biological Systems by EPR* Springer: New York, 2001; Vol. 19.

34. G. Likhtenshtein; J. Yamauchi; S. i. Nakatsuji; A. I. Smirnov; R. Tamura, *Nitroxides: Applications in Chemistry, Biomedicine, and Materials Science* Wiley VCH: Weinheim, 2008.

35. N. Kocherginsky; H. M. Swartz, *Nitroxide Spin Labels, Reactions in Biology and Chemistry* CRC Press: Florida, 1995.

36. *CRC Handbook of Chemistry and Physics* 89 ed.; Taylor & Francis: 2008-2009.

37. A. Nilsen; R. Braslau; *Nitroxide decomposition: Implications toward nitroxide design for applications in living free-radical polymerization*; *J. Polym. Sci., A* **2006,** *44*, 697.

38. S. Stoll, Spectral Simulations in Solid-State Electron Paramagnetic Resonance. PhD thesis ETH Zürich, 2004.

39. H. Schindler; J. Seelig; *EPR spectra of spin labels in lipid bilayers*; *J. Chem. Phys.* **1973,** *59*, 1841.

40. W. L. Hubbell; H. M. McConnell; *Molecular motion in spin-labeled phospholipids and membranes*; *J. Am. Chem. Soc.* **1971,** *93*, 314.

41. M. S. Broido; E. Meirovitch; *Doxyl nitroxide probes and the intrinsic flexibility gradient. A slow-motional line shape analysis study*; *J. Phys. Chem.* **1983,** *87*, 1635.

42. W. L. Hubbell; H. M. McConnell; *Orientation and Motion of Amphiphilic Spin Labels in Membranes*; *Proc. Natl. Acad. Sci. USA* **1969,** *64*, 20.

43. J. Seelig; *Spin label studies of oriented smectic liquid crystals (a model system for bilayer membranes)*; *J. Am. Chem. Soc.* **1970,** *92*, 3881.

44. B. J. Gaffney; H. M. McConnell; *The Paramagnetic Resonance Spectra of Spin Labels in Phospholipid Membranes*; *J. Magn. Reson.* **1974,** *16*, 1.

45. P. Jost; L. J. Libertini; V. C. Hebert; O. H. Griffith; *Lipid spin labels in lecithin multilayers. A study of motion along fatty acid chains*; *J. Mol. Biol.* **1971,** *59*, 77.

46. S. P. Van; G. B. Birrell; O. H. Griffith; *Rapid Anisotropic Motion of Spin Labels. Models for Motion Averaging of the ESR Parameters*; *J. Magn. Reson.* **1974,** *15*, 444.
47. H. M. McConnell; B. G. McFarland; *Physics and chemistry of spin labels*; *Q. Rev. Biophys.* **1970,** *3*, 91.
48. S. Stoll The *EasySpin* sofware package is available free of charge. http://easyspin.org/.
49. S. Stoll; A. Schweiger; *EasySpin, a comprehensive software package for spectral simulation and analysis in EPR*; *J. Magn. Reson.* **2006,** *178*, 42.
50. S. Stoll; R. D. Britt; *General and efficient simulation of pulse EPR spectra*; *Phys. Chem. Chem. Phys* **2009,** *11*, 6614
51. S. Stoll; A. Schweiger, EasySpin: Simulating CW ESR Spectra. In *Biological Magnetic Resonance*, Hemminga, M. A.; Berliner, L. J., Eds. Springer: New York, 2007; Vol. 27, pp 299.
52. G. Breit; I. I. Rabi; *Measurement of Nuclear Spin*; *Phys. Rev.* **1931,** *38*, 2082.
53. B. H. Robinson; C. Mailer; A. W. Reese; *Linewidth Analysis of Spin Labels in Liquids: II. Experimental*; *J. Magn. Reson.* **1999,** *138*, 210.
54. D. J. Schneider; J. H. Freed, Calculating Slow Motional Magnetic Resonance Spectra: A User's Guide. In *Biological Magentic Resonance*, Berliner, L. J.; Reuben, J., Eds. Plenum Press: New York, London, 1989; Vol. 8, pp 1.
55. C. P. Slichter, *Principles of Magnetic Resonance* 3 ed.; Springer: Berlin, 1990; Vol. 1.
56. M. Lindgren; G. R. Eaton; S. A. Eaton; B. H. Jonsson; P. Hammarström; M. Svensson; U. Carlsson; *Electron spin echo decay as a probe of aminoxyl environment in spin-labeled mutants of human carbonic anhydrase*; *J. Chem. Soc., Perkin Trans. 2* **1997**, 2549.
57. A. D. Milov; A. G. Maryasov; Y. D. Tsvetkov; *Pulsed Electron Double Resonance (PELDOR) and its Application in Free Radical Research*; *Appl. Magn. Reson.* **1998,** *15*, 107.
58. A. D. Milov; A. B. Ponomarev; Y. D. Tsvetkov; *Electron-electron double resonance in electron spin echo: Model biradical systems and the sensitized photolysis of decalin*; *Chem. Phys. Lett.* **1984,** *110*, 67.
59. B. E. Bode; D. Margraf; J. Plackmeyer; G. Durner; T. F. Prisner; O. Schiemann; *Counting the Monomers in Nanometer-Sized Oligomers by Pulsed Electron−Electron Double Resonance*; *J. Am. Chem. Soc.* **2007,** *129*, 6736.
60. G. Jeschke; G. Panek; A. Godt; A. Bender; H. Paulsen; *Data analysis procedures for pulse ELDOR measurements of broad distance distributions*; *Appl. Magn. Reson.* **2004,** *26*, 223.
61. W. B. Mims; *Pulsed Endor Experiments*; *Proc. R. Soc. (London), Ser. A* **1965,** *283*, 452.
62. E. R. Davies; *A New Pulse Endor Technique*; *Phys. Lett. A* **1974,** *47*, 1.
63. M. T. Bennebroek; J. Schmidt; *Pulsed ENDOR Spectroscopy at Large Thermal Spin Polarizations and the Absolute Sign of the Hyperfine Interaction*; *J. Magn. Reson.* **1997,** *128*, 199.
64. M. W. Makinen; *Electron nuclear double resonance determined structures of enzyme reaction intermediates: structural evidence for substrate destabilization*; *Spectrochim. Acta, Part A* **1998,** *54*, 2269.
65. G. H. Rist; J. S. Hyde; *Ligand ENDOR of Metal Complexes in Powders*; *J. Chem. Phys.* **1970,** *52*, 4633.
66. W. B. Mims; K. Nassau; J. D. McGee; *Spectral Diffusion in Electron Resonance Lines*; **1961,** *123*, 2059.
67. P. Höfer, Entwicklung von Puls-ENDOR-Verfahren und ihre Anwendung auf Polyazetylen Universität Stuttgart, 1988.
68. B. Epel; D. Arieli; D. Baute; D. Goldfarb; *Improving W-band pulsed ENDOR sensitivity-random acquisition and pulsed special TRIPLE*; *J. Magn. Reson.* **2003,** *164*, 78.

69. C. Reichardt, *Solvents and Solvent Effects in Organic Chemistry* 2 ed.; VCH: Weinheim, 1988.

70. S. Bagotsky, *Fundamentals of Electrochemistry* 2 ed.; Wiley-Interscience: New Jersey, 2006.

71. P. M. E. Mancini; A. Terenzani; C. Adam; L. R. Vottero; *Solvent effects on aromatic nucleophilic substitution reactions. Part 9. Special kinetic synergistic behavior in binary solvent mixtures*; *J. Phys. Org. Chem.* **1999,** *12*, 430.

72. E. Humeres; R. J. Nunes; V. G. Machado; M. D. G. Gasques; C. Machado; *Ion-Dipole SN2 Reaction in Acetone−Water Mixtures. Electrostatic and Specific Solute−Solvent Interactions*; *J. Org. Chem.* **2001,** *66*, 1163.

73. P. Chatterjee; S. Bagchi; *Study of Preferential Solvation in Mixed Binary Solvents by Ultraviolet-Visible Spectroscopy*; *J. Chem. Soc. Faraday Trans.* **1990,** *86*, 1785.

74. M. Holz; *D_2O–H_2O isotope effect on nuclear magnetic relaxation of alkali halide nuclei and preferential solvation in mixed solvents*; *J. Chem. Soc., Faraday Trans. 1* **1978,** *74*, 644.

75. R. A. Ransdell; C. C. Wamser; *Solvent and substituent effects on the redox properties of free-base tetraphenylporphyrins in DMSO and aqueous DMSO*; *J. Phys. Chem.* **1992,** *96*, 10572.

76. R. M. Tarkka; I.-H. Um; H.-Q. Xie; A.-P. Chatrouse; F. Terrier; S. Hoz; E. Buncel; *Effect of solvent composition on the acidity of phenols in dimethyl sulfoxide-water mixtures*; *J. Phys. Org. Chem.* **1998,** *11*, 847.

77. B. Chaufer; J. Lesec; C. Quivoron; *Preferential Solvation Study of Polyvinylpyrrolidone in Organic or Aqueous Mixed Solvents by GPC*; *J. Liq. Chromatogr. Related Technol.* **1979,** *2*, 633

78. M. Holz; *Preferential solvation of Na^+ in aqueous mixtures of simple amides. Application of the D_2O–H_2O isotope effect to $^{23}Na^+$ nuclear magnetic relaxation*; *J. Chem. Soc., Faraday Trans. 1,* **1982,** *78*, 1899.

79. A. Ben-Naim; *Preferential solvation in two-component systems*; *J. Phys. Chem.* **1989,** *93*, 3809.

80. T. Kimura; R. Nagaishi; Y. Kato; Z. Yoshida; *Luminescence study on preferential solvation of Europium(III) in water/non-aqueous solvent mixtures*; *J. Alloys Compd.* **2001,** *323-324*, 164.

81. W. A. Alves; C. A. Téllez Soto; E. Hollauer; R. B. Faria; *Vibrational studies on the selective solvation of Na^+ and ClO_3^- ions in dimethylformamide-formamide mixture*; *Spectrochim. Acta, Part A* **2005,** *62*, 755.

82. G. Hefter; *Ion solvation in aqueous–organic mixtures*; *Pure Appl. Chem.* **2005,** *77*, 605.

83. A. Wahab; S. Mahiuddin; *Solvation Phenomena of Potassium Thiocyanate in Methanol–Water Mixtures*; *J. Sol. Chem.* **2005,** *34*, 537.

84. E. Ivanov; V. Korolev; O. Antonova; V. Abrosimov; *Enthalpies of solution of urea in water-methanol mixtures at 298.15 K*; *Russ. J. Phys. Chem. A* **2006,** *80*, 193.

85. C. Reichardt; *Solvatochromic Dyes as Solvent Polarity Indicators*; *Chem. Rev.* **1994,** *94*, 2319.

86. E. Hawlicka; D. Swiatla-Wojcik; *Molecular dynamics studies on the structure of methanol-water solutions of NaCl*; *Chem. Phys.* **1995,** *195*, 221.

87. Y. P. Puhovski; B. M. Rode; *Molecular dynamics simulations of Na+ and Cl- ions solvation in aqueous mixtures of formamide*; *Chem. Phys.* **1997,** *222*, 43.

88. E. Hawlicka; D. Swiatla-Wojcik; *Molecular dynamics studies of NaCl solutions in methanol-water mixtures.: An effect of NaCl on hydrogen bonded network*; *Chem. Phys.* **1998,** *232*, 361.

89. A. Yoshimori; T. J. F. Day; G. N. Patey; *Theory of ion solvation dynamics in mixed dipolar solvents*; *J. Chem. Phys.* **1998,** *109*, 3222.

90. A. Tongraar; B. M. Rode; *A Born−Oppenheimer Ab Initio Quantum Mechanical/Molecular Mechanical Molecular Dynamics Simulation on Preferential Solvation of Na+ in Aqueous Ammonia Solution*; *J. Phys. Chem. A* **2000,** *105*, 506.

91. A. Tongraar; K. Sagarik; B. M. Rode; *Effects of Many-Body Interactions on the Preferential Solvation of Mg2+ in Aqueous Ammonia Solution: A Born−Oppenheimer ab Initio QM/MM Dynamics Study*; *J. Phys. Chem. B* **2001,** *105*, 10559.

92. E. Hawlicka; D. Swiatla-Wojcik; *MD Simulation Studies of Selective Solvation in Methanol−Water Mixtures: An Effect of the Charge Density of a Solute*; *J. Phys. Chem. A* **2002,** *106*, 1336.

93. E. Hawlicka; D. Swiatla-Wojcik; *Aggregation of ions in methanol - water solutions of sodium halides*; *J. Chem. Phys.* **2003,** *119*, 2206.

94. A. Tongraar; B. M. Rode; *Ab initio QM/MM molecular dynamics simulation of preferential K+ solvation in aqueous ammonia solution*; *Phys. Chem. Chem. Phys.* **2004,** *6*, 411.

95. D. Attanasio; *Structural information from ENDOR spectroscopy: the frozen solution proton spectra of some vanadyl(2+) complexes*; *J. Phys. Chem.* **1986,** *90*, 4952.

96. D. Mustafi; M. W. Makinen; *ENDOR-Determined Solvation Structure of VO2+ in Frozen Solutions*; *Inorg. Chem.* **1988,** *27*, 3360.

97. H. van Willigen; *Proton endor on VO(acac)$_2$ in frozen solution*; *Chem. Phys. Lett.* **1979,** *65*, 490.

98. H. van Willigen; *Proton ENDOR on $VO(H_2O)_5^{2+}$ in solid solution*; *J. Magn. Reson.* **1980,** *39*, 37.

99. T. A. Henderson; G. C. Hurst; R. W. Kreilick; *Angle-selected ENDOR spectroscopy. 2. Determination of proton coordinates from a polycrystalline sample of bis(2,4-pentanedionato)copper(II)*; *J. Am. Chem. Soc.* **1985,** *107*, 7299.

100. M. B. Yim; M. W. Makinen; *ENDOR Study of Gd3+ Conplexes in Frozen Solutions*; *J. Magn. Reson.* **1986,** *70*, 89.

101. G. Feher; *Observation of Nuclear Magnetic Resonances via the Electron Spin Resonance Line*; *Phys. Rev.* **1956,** *103*, 834.

102. H.-J. Steinhoff; A. Savitsky; C. Wegener; M. Pfeiffer; M. Plato; K. Möbius; *High-field EPR studies of the structure and conformational changes of site-directed spin labeled bacteriorhodopsin*; *BBA - Bioenergetics* **2000,** *1457*, 253.

103. M. Plato; H.-J. Steinhoff; C. Wegener; J. T. Törring; A. Savitsky; K. Möbius; *Molecular orbital study of polarity and hydrogen bonding effects on the g and hyperfine tensors of site directed NO spin labelled bacteriorhodopsin*; *Mol. Phys.* **2002,** *100*, 3711.

104. H.-J. Steinhoff; *Inter- and intra-molecular distances determined by EPR spectroscopy and site-directed spin labeling reveal protein-protein and protein-oligonucleotide interaction*; *Biolog. Chem.* **2005,** *385*, 913.

105. J. A. Weil; J. R. Bolton; J. E. Wertz, *Electron Paramagnetic Resonance* Wiley: New York, 1994.

106. G. E. Pake; J. Townsend; S. I. Weissman; *Hyperfine Structure in the Paramagnetic Resonance of the Ion $(SO_3)_2NO^{2-}$*; *Phys. Rev.* **1952,** *85*, 682.

107. J. Townsend; S. I. Weissman; G. E. Pake; *Hyperfine Structure in the Paramagnetic Resonance of the Ion $(SO_3)_2NO^{2-}$*; *Phys. Rev.* **1953,** *89*, 606.

108. J. P. Lloyd; G. E. Pake; *Spin Relaxation in Free Radical Solutions Exhibiting Hyperfine Structure*; *Phys. Rev.* **1954,** *94*, 579.

109. M. T. Jones; *Electron Spin Exchange in Aqueous Solutions of $K_2(SO_3)_2NO$*; *J. Chem. Phys.* **1963,** *38*, 2892.
110. M. T. Jones; R. Ahmed; R. Kastrup; V. Rapini; *Electron spin resonance studies of ion pair formation in solutions of Fremy's salt*; *J. Phys. Chem.* **1979,** *83*, 1327.
111. S. I. Weissman; D. Banfill; *Anisotropy in the Paramagentic Resonance Spectrum of Peroxylamine Disulfonate Ion*; *J. Am. Chem. Soc.* **1953,** *75*, 2534.
112. B. D. Perlson; D. B. Russell; *Nitrosodisulfonates and hydroxylamine-N,N-disulfonates. III. Magnetic properties of the triclinic modification of potassium nitrosodisulfonate*; *Inorg. Chem.* **1975,** *14*, 2907.
113. T. E. Gangwer; *Solid-state study of the potassium nitrosodisulfonate radical*; *J. Phys. Chem.* **1974,** *78*, 375.
114. P. J. Hamrick; H. Shields; T. Gangwer; *Structure of $(KSO_3)_2NO$ in X-Irradiated Single Crystals of $(KSO_3)_2NOH$*; *J. Chem. Phys.* **1972,** *57*, 5029.
115. R. W. Holmberg; B. J. Wilson; *ESR study of free radicals in irradiated single crystals of potassium hydroxylamine disulfonate*; *J. Chem. Phys.* **1974,** *61*, 921.
116. M. T. Jones; S. A. Trugman; V. Rapini; R. Hameed; *An electron spin resonance study of Fremy's salt in a dilute polycrystalline environment*; *J. Phys. Chem.* **1977,** *81*, 664.
117. B. L. Bales; *EPR of frozen aqueous solutions of Fremy's salt: Resolution enhancement of polycrystalline spectra*; *Chem. Phys. Lett.* **1971,** *10*, 361.
118. B. L. Bales; E. Wajnberg; O. R. Nascimento; *Temperature-Dependent Hyperfine Coupling Constant of the Dianion Radical of Fremy's Salt, a Convenient Internal Thermometer for EPR Spectroscopy*; *J. Magn. Reson., Ser. A* **1996,** *118*, 227.
119. T. P. Holler; P. B. Hopkins; *Ovothiols as free-radical scavengers and the mechanism of ovothiol-promoted NAD(P)H-O2 oxidoreductase activity*; *Biochemistry* **1990,** *29*, 1953.
120. Z.-L. Liu; Z.-X. Han; P. Chen; Y.-C. Liu; *Stopped-flow ESR study on the reactivity of vitamin E, vitamin C and its lipophilic derivatives towards Fremy's salt in micellar systems*; *Chem. Phys. Lipids* **1990,** *56*, 73.
121. H. Sanuki; R. Komatsu-Watanabe; T. Ideguchi; S. Sakamoto; K. Ichimori; K. Kanaori; K. Tajima; *Stopped-flow-optical and -ESR Study on Oxidative Reaction of Quercetin by Nitrosodisulfonate Radical as a Model of Reactive Oxygen Species*; *Chem. Lett.* **2007,** *36*, 1388.
122. J. Zielonka; H. Zhao; Y. Xu; B. Kalyanaraman; *Mechanistic similarities between oxidation of hydroethidine by Fremy's salt and superoxide: Stopped-flow optical and EPR studies*; *Free Radical Biol. Med.* **2005,** *39*, 853.
123. D. Hinderberger; H. W. Spiess; G. Jeschke; *Radial counterion distributions in polyelectrolyte solutions determined by EPR spectroscopy*; *Europhys. Lett.* **2005,** *70*, 102.
124. D. Hinderberger; H. W. Spiess; G. Jeschke; *Dynamics, Site Binding, and Distribution of Counterions in Polyelectrolyte Solutions Studied by Electron Paramagnetic Resonance Spectroscopy*; *J. Phys. Chem. B* **2004,** *108*, 3698.
125. D. Hinderberger; O. Schmelz; M. Rehahn; M. Jeschke; *Electrostatic Site Attachment of Divalent Counterions to Rodlike Ruthenium(II) Coordination Polymers Characterized by EPR Spectroscopy*; *Angew. Chem.* **2004,** *116*, 4716.
126. M. J. Prandolini; V. P. Denysenkov; M. Gafurov; B. Endeward; T. F. Prisner; *High-Field Dynamic Nuclear Polarization in Aqueous Solutions*; *J. Am. Chem. Soc.* **2009,** *131*, 6090.
127. N. M. Atherton; M. Brustolon; *ENDOR of Fremy's salt*; *Mol. Phys.* **1976,** *32*, 23
128. B. Giethlen; J. M. Schaus; *Oxidation of indolines with Fremy's salt: A mechanistic proposal*; *Tetrahedron Lett.* **1997,** *38*, 8483.

129. Z. Yang; E. S. Gould; *Electron transfer. 154. Reaction of the nitrosodisulfonate anion radical with one- and multi-electron inorganic reductants*; *Res. Chem. Intermed.* **2003,** *29*, 181.

130. G. A. Kraus; N. Selvakumar; *A novel Fremy's salt-mediated oxidation and rearrangement of anilines into amino ortho-diketones. Applications to the synthesis of pyrrolobenzodiazepines*; *Tetrahedron Lett.* **1999,** *40*, 2039.

131. Z. Yang; E. S. Gould; *Reactions of the nitrosodisulfonate anion radical with s2 reducing centers*; *J. Chem. Soc., Dalton Trans.* **2002**, 3840.

132. P. N. Balasubramanian; E. S. Gould; *Electron transfer. 61. Reactions of the nitrosodisulfonate anion radical with inorganic reductants*; *Inorg. Chem.* **1983,** *22*, 1100.

133. S. P. Nayak; B. T. Gowda; *Kinetics and mechanisms of oxidation of thiosemicarbazide, its metal complex and hydrazones by N-chlorobenzamide in water methanol medium*; *J. Phys. Org. Chem.* **1992,** *5*, 755.

134. K.-C. Lee; S.-E. Lee; B.-K. Song; *Dispersion Polymerization of Acrylamide in Methanol/Water Media*; *Macromol. Res.* **2002,** *10*, 140.

135. M. G. Han; S. P. Armes; *Preparation and characterization of polypyrrole-silica colloidal nanocomposites in water-methanol mixtures*; *J. Colloid Interface Sci.* **2003,** *262*, 418.

136. P. Kumar; K. L. Mittal, *Handbook of microemulsion science and technology* Marcel Dekker: New York, 1999.

137. A. Rizzi, Retention and Selectivity. In *Handbook of HPLC*, Katz, E.; Eksteen, R.; Schoenmakers, P.; Miller, N., Eds. Dekker: New York, 1998; Vol. 78.

138. E. Bosch; P. Bou; H. Allemann; M. Roses; *Retention of Ionizable Compounds on HPLC. pH Scale in Methanol−Water and the pK and pH Values of Buffers*; *Anal. Chem.* **1996,** *68*, 3651.

139. E. D. Katz; C. H. Lochmuller; R. P. W. Scott; *Methanol-water association and its effect on solute retention in liquid chromatography*; *Anal. Chem.* **1989,** *61*, 349.

140. M. Kiselev; S. Noskov; Y. Puhovski; T. Kerdcharoen; S. Hannongbua; *The study of hydrophobic hydration in supercritical water-methanol mixtures*; *J. Mol. Graphics Modell* **2001,** *19*, 412.

141. Z. Zhao; E. R. Malinowski; *Detection and Identification of a Methanol−Water Complex by Factor Analysis of Infrared Spectra*; *Anal. Chem.* **1998,** *71*, 602.

142. D. Adachi; Y. Katsumoto; H. Sato; Y. Ozaki; *Near-Infrared Spectroscopic Study of Interaction Between Methyl Group and Water in Water-Methanol Mixtures*; *Appl. Spectrosc.* **2002,** *56*, 357.

143. N. Micali; S. Trusso; C. Vasi; D. Blaudez; F. Mallamace; *Dynamical properties of water-methanol solutions studied by depolarized Rayleigh scattering*; *Phys. Rev. E* **1996,** *54*, 1720.

144. J. H. Guo; Y. Luo; A. Augustsson; S. Kashtanov; J. E. Rubensson; D. K. Shuh; H. Ågren; J. Nordgren; *Molecular Structure of Alcohol-Water Mixtures*; *Phys. Rev. Lett.* **2003,** *91*, 157401.

145. S. Dixit; J. Crain; W. C. K. Poon; J. L. Finney; A. K. Soper; *Molecular segregation observed in a concentrated alcohol-water solution*; *Nature* **2002,** *416*, 829.

146. S. Dixit; A. K. Soper; J. L. Finney; J. Crain; *Water structure and solute association in dilute aqueous methanol*; *Europhys. Lett.* **2002,** *59*, 377.

147. S. Y. Noskov; M. G. Kiselev; A. M. Kolker; B. M. Rode; *Structure of methanol-methanol associates in dilute methanol-water mixtures from molecular dynamics simulation*; *J. Mol. Liq.* **2001,** *91*, 157.

148. A. Laaksonen; P. G. Kusalik; I. M. Svishchev; *Three-Dimensional Structure in Water−Methanol Mixtures*; *J. Phys. Chem. A* **1997,** *101*, 5910.

149. H. S. Frank; W.-Y. Wen; *Ion-Solvent Iinteractions Structural Aspects of Ion-Solvent Interactions in Aqueous Solutions: A Suggested Picture of Water Structure*; *Discuss. Faraday Soc.* **1957,** *24*, 133.

150. H. S. Frank; A. S. Quist; *Pauling's Model and the Thermodynamic Properties of Water*; *J. Chem. Phys.* **1961,** *34*, 604.

151. H. Eyring; T. Ree; N. Hirai; *Significant Structures in the Liquid State. I*; *Proc. Natl. Acad. Sci. USA* **1958,** *44*, 683.

152. D. Eisenberg; W. Kauzmann, *The Structure and Properties of Water* Oxford University Press: Oxford, 2005.

153. A. Ben-Naim, *Molecular theory of solutions* Oxford University Press: Oxford, NY, 2006.

154. S. Sarkar; R. N. Joarder; *Molecular clusters and correlations in liquid methanol at room temperature*; *J. Chem. Phys.* **1993,** *99*, 2032.

155. T. Yamaguchi; K. Hidaka; A. K. Soper; *The structure of liquid methanol revisited: a neutron diffraction experiment at -80 °C and +25 °C*; *Mol. Phys.* **1999,** *96*, 1159.

156. S. W. Benson; *Some Observations on the Structures of Liquid Alcohols and Their Heats of Vaporization*; *J. Am. Chem. Soc.* **1996,** *118*, 10645.

157. M. A. Wendt; T. C. Farrar; *An indirect method for the measurement of deuterium quadrupole coupling constants in liquids*; *Mol. Phys.* **1998,** *95*, 1077.

158. L. Saiz; J. A. Padro; E. Guardia; *Structure and Dynamics of Liquid Ethanol*; *J. Phys. Chem. B* **1997,** *101*, 78.

159. W. L. Jorgensen; *Quantum and statistical mechanical studies of liquids. 7. Structure and properties of liquid methanol*; **1980,** *102*, 543.

160. F. Weinhold; *Quantum cluster equilibrium theory of liquids: General theory and computer implementation*; *J. Chem. Phys.* **1998,** *109*, 367.

161. S. W. Cochran; J. C. Holste; K. N. Marsh; B. E. Gammon; K. R. Hall; *Enthalpies of water + methanol mixtures between 180 K and 320 K*; **1993,** *88*, 171.

162. H. Yilmaz; S. Güler; *Excess properties of methanol-water binary system at various temperatures*; **1998,** *20*, 1853.

163. H. S. Frank; M. W. Evans; *Free Volume and Entropy in Condensed Systems III. Entropy in Binary Liquid Mixtures; Partial Molal Entropy in Dilute Solutions; Structure and Thermodynamics in Aqueous Electrolytes*; *J. Chem. Phys.* **1945,** *13*, 507.

164. J. S. Hoye; G. Stell; *Dielectric constant of dipolar fluid mixtures*; *J. Chem. Phys.* **1979,** *70*, 2894.

165. J. H. Guo; Y. Luo; A. Augustsson; S. Kashtanov; J. E. Rubensson; D. Shuh; V. Zhuang; P. Ross; H. Ågren; J. Nordgren; *The molecular structure of alcohol-water mixtures determined by soft-X-ray absorption and emission spectroscopy*; *J. Electron. Spectrosc. Relat. Phenom.* **2004,** *137-140*, 425.

166. R. A. Kuharski; P. J. Rossky; *A quantum mechanical study of structure in liquid H_2O and D_2O*; *J. Chem. Phys.* **1985,** *82*, 5164.

167. B. Tomberli; P. A. Egelstaff; C. J. Benmore; J. Neuefeind; *Isotopic effects in the structure of liquid methanol: II. Experimental data in Fourier space*; *J. Phys. Cond. Matter* **2001,** *13*, 11421.

168. W. Moser; R. A. Howie; *Nitrosodisulphonates. Part I. Fremy's salt (potassium nitrosodisulphonate)*; *J. Chem. Soc. A* **1986**, 3039.

169. B. J. Wilson; D. M. Ritter; *Decomposition of Nitrosyl Disulfonate Ion in Mildly Alkaline Solution*; *Inorg. Chem.* **1963,** *2*, 974.

170. Static Dielectric Constants of Pure Liquids and Binary Liquid Mixtures. In *Landolt-Börnstein - Group IV Physical Chemistry Numerical Data and Functional Relationships in Science and Technology* Landolt-Börnstein, Ed. Springer: Berlin Heidelberg, Vol. 17.
171. J. S. Hyde; A. Jesmanowicz; J. J. Ratke; W. E. Antholine; *Pseudomodulation: A computer-based strategy for resolution enhancement*; *J. Magn. Reson.* **1992,** *96*, 1.
172. A. V. Astashkin; A. Kawamori; *Matrix Line in Pulsed Electron-Nuclear Double Resonance Spectra*; *J. Magn. Reson.* **1998,** *135*, 406.
173. B. Epel; A. Pöppl; P. Manikandan; S. Vega; D. Goldfarb; *The Effect of Spin Relaxation on ENDOR Spectra Recorded at High Magnetic Fields and Low Temperatures*; *J. Magn. Reson.* **2001,** *148*, 388.
174. R. A. Howie; L. S. D. Glasser; W. Moser; *Nitrosodisulphonates. Part II. Crystal structure of the orange-brown triclinic modification of Fremy's salt (potassium nitrosodisulphonate)*; *J. Chem. Soc. A* **1986**, 3043.
175. V. J. McBrierty; *N.m.r. of solid polymers: a review Polymer* **1974,** *15*, 503.
176. E. V. Ivash; D. M. Dennison; *The Methyl Alcohol Molecule and Its Microwave Spectrum*; *J. Chem. Phys.* **1953,** *21*, 1804.
177. T. Bevilaqua; D. C. da Silva; V. G. Machado; *Preferential solvation of Brooker's merocyanine in binary solvent mixtures composed of formamides and hydroxylic solvents*; *Spectrochim. Part A* **2004,** *60*, 951.
178. P. Chatterjee; S. Bagchi; *Preferential Solvation in Mixed Binary Solvents by Ultraviolet-Visible Spectroscopy: N-Ethyl-4-cyanopyridinium Iodide in Alcohol-Acetone Mixtures*; *J. Chem. Soc. Faraday Trans.* **1991,** *87*, 587.
179. S. Trivedi; A. Sarkar; S. Pandey; *Solvatochromic absorbance probe behavior within 1-butyl-3-methylimidazolium hexafluorophosphate + propylene carbonate: Preferential solvation or solvent-solvent interaction?*; *Chem. Eng. J.* **2009,** *147*, 36.
180. Y. G. Wu; M. Tabata; T. Takamuku; *Preferential Solvation in Aqueous–Organic Mixed Solvents Using Solvatochromic Indicators*; *J. Sol. Chem.* **2002,** *31*, 381.
181. A. K. Soper; K. Weckström; *Ion solvation and water structure in potassium halide aqueous solutions*; *Biophys. J.* **2006,** *124*, 180.
182. B. Epel; P. Manikandan; P. Kroneck; D. Goldfarb; *High-field ENDOR and the sign of the hyperfine coupling*; *Appl. Magn. Reson.* **2001,** *21*, 287.
183. M. Rubinstein; R. H. Colby, *Polymer Physics* Oxford University Press: Oxford, 2003.
184. G. H. Fredrickson, *International Series of Monographs on Physics 134* Oxford University Press: Oxford, 2006.
185. P. Flory; J. G. Jackson; C. J. Wood, *Statistical mechanics of chain molecules* Hanser: München, 1989.
186. P. G. de Gennes, *Scaling Concepts in Polymer Physics* Cornell University Press: Ithaca, NY, 1979.
187. G. S. Manning; *Limiting Laws and Counterion Condensation in Polyelectrolyte Solutions I. Colligative Properties*; *J. Chem. Phys.* **1969,** *51*, 924.
188. B. H. Zimm; M. Le Bret; *Counter-ion condensation and system dimensionality.* ; *J. Biomol. Struct. Dyn.* **1983,** *1*, 461.
189. T. Odijk; *Polyelectrolytes near the rod limit*; *J. Polym. Sci., Polym. Phys Edn* **1977,** *15*, 477.
190. J. Skolnick; M. Fixman; *Electrostatic Persistence Length of a Wormlike Polyelectrolyte*; **1977,** *10*, 944.
191. S. Ghosh; X. Li; C. E. Reed; W. F. Reed; *Apparent persistence lengths and diffusion behavior of high molecular weight hyaluronate*; *Biopolymers* **1990,** *30*, 1101.

192. L. W. Fisher; A. R. Sochor; J. S. Tan; *Chain Characteristics of Poly(2-acrylamido-2-methylpropanesulfonate) Polymers. 1. Light-Scattering and Intrinsic-Viscosity Studies*; *Macromolecules* **1977,** *10*, 949.
193. C. Wandrey; W. Jaeger; W. Starke; J. Wotzke; *New cationic polyelectrolyte as an aid in water management*; *Wasserwirt. Wassertechnik* **1984,** *34*, 185.
194. A. Kundagrami; M. Muthukumar; *Theory of competitive counterion adsorption on flexible polyelectrolytes: divalent salts*; *J. Chem. Phys.* **2008,** *128*, 244901.
195. D. Hinderberger, Polyelectrolytes and Their Counterions Studied by EPR Spectroscopy Mainz, 2004.
196. L. P. Ramírez; M. Antonietti; K. Landfester; *Formation of Novel Layered Nanostructures from Lanthanide-Complexes by Secondary Interactions with Ligating Monomers in Miniemulsion Droplets*; *Macromol. Chem. Phys.* **2006,** *207*, 160.
197. C. Hauser, Dissertation Universität Mainz, Mainz, 2009.
198. C. Hauser, Personal Communication. 2009.
199. P. M. Kruglyakov *Hydrophile - Lipophile Balance of Surfactants and Solid Particles, Physicochemical aspects and applications* Elsevier Science: Amsterdam, 2000; Vol. 9.
200. D. Myers, *Surfaces, Interfaces and Colloids* 2 ed.; Wiley-VCH: New York, 1999.
201. H.-J. Butt; K. Graf; M. Kappl, *Physics and Chemistry of Interfaces* Wiley-VCH: Weinheim, 2003.
202. W. Norde, *Colloids and Interfaces in Life Science* Marcel Dekker: New York, 2003.
203. K. Landfester; *Polyreactions in Miniemulsions*; *Macromol. Rapid Commun.* **2001,** *22*, 896.
204. K. Landfester; N. Bechthold; F. Tiarks; M. Antonietti; *Formulation and Stability Mechanisms of Polymerizable Miniemulsions*; *Macromolecules* **1999,** *32*, 5222.
205. C. D. Anderson; E. S. Daniels, *Emulsion Polymerisation and Latex Applications* Rapra Technology: 2003; Vol. 14.
206. K. Landfester; *Synthesis of Colloidal Particles in Miniemulsions*; *Annu. Rev. Mater. Res.* **2006,** *36*, 231.
207. L. Ratke; P. W. Voorhees, *Growth and Coarsening- Ripening in Material Processing* Springer: Berlin, 2002.
208. P. Walstra, Emulsion Stability. In *Encyclopedia of EmulsionTechnology*, Bacher, P., Ed. Marcel Dekker: New York, 1996; Vol. 4.
209. K. Landfester; M. Willert; M. Antonietti; *Preparation of Polymer Particles in Nonaqueous Direct and Inverse Miniemulsions*; *Macromolecules* **2000,** *33*, 2370.
210. C.-E. Lin; K.-S. Lin; *Determination of critical micelle concentration and interactions between cephalosporins and charged surfactants*; *J. Chromatogr. A* **2000,** *868*, 313.
211. M. S. Akhter; S. M. Alawi; *The effect of organic additives on critical micelle concentration of non-aqueous micellar solutions*; *Colloids Surf. A Physicochem. Eng. Asp.* **2000,** *175*, 311.
212. F. Gadelle; W. J. Koros; R. S. Schechter; *Solubilization Isotherms of Aromatic Solutes in Surfactant Aggregates*; *J. Colloid Interf. Sci.* **1995,** *170*, 57.
213. S. Javadian; H. Gharibi; B. Sohrabi; H. Bijanzadeh; M. A. Safarpour; R. Behjatmanesh-Ardakani; *Determination of the physico-chemical parameters and aggregation number of surfactant in micelles in binary alcohol-water mixtures*; *J. Mol. Liquids* **2008,** *137*, 74.
214. C.-E. Lin; M.-J. Chen; H.-C. Huang; H.-W. Chen; *Capillary electrophoresis study on the micellization and critical micelle concentration of sodium dodecyl sulfate: Influence of solubilized solutes*; *J. Chromatogr. A* **2001,** *924*, 83.

215. S. J. Rehfeld; D. J. Eatough; W. Z. Plachy; *The binding isotherms for the interaction of 5-doxyl stearic acid with bovine and human albumin*; *J. Lipid Res.* **1978,** *19*, 841.
216. M. Ge Shenkara; B. Rananavare; J. H. Freed; *ESR studies of stearic acid binding to bovine serum albumin*; *BBA* **1990,** *1036*, 228.
217. R. E. Sievers; J. E. Sadlowski; *Volatile Metal Complexes*; *Science* **1978,** *201*, 217.
218. I. Baxter; S. R. Drake; M. B. Hursthouse; K. M. Abdul Malik; J. McAleese; D. J. Otway; J. C. Plakatouras; *Effect of Polyether Ligands on Stabilities and Mass Transport Properties of a Series of Gadolinium(II) β-Diketonate Complexes*; *Inorg. Chem.* **1955,** *34*, 1384.
219. J. A. Cunningham; R. E. Sievers; *Structures of europium complexes and implications in lanthanide nuclear magnetic resonance shift reagent chemistry*; *Inorg. Chem.* **1979,** *19*, 595.
220. J. A. Darr; D. Michael; P. Mingos; D. E. Hibbs; M. B. Hursthouse; K. M. Abdul Malik; *A volatile erbium(III)/β-diketonate compound symmetrically bridged by tetraglyme*; *Polyhedron* **1996,** *15*, 3225.
221. K. Binnemans, Rare-earth Beta-Diketonates. In *Handbook on the Physics and Chemistry of Rare Earths*, Gschneidner, K. A., Jr.; Bünzli, J.-C. G.; Pecharsky, V. K., Eds. Elsevier: Amsterdam, 2005; Vol. 35, pp 107.
222. C. C. Hinckley; *Paramagnetic shifts in solutions of cholesterol and the dipyridine adduct of trisdipivalomethanatoeuropium(III). A shift reagent*; *J. Am. Chem. Soc.* **1969,** *91*, 5160.
223. J. Reuben; *Electron spin relaxation in aqueous solutions of gadolinium(III). Aquo, cacodylate, and bovine serum albumin complexes*; *J. Phys. Chem.* **1971,** *75*, 3164.
224. R. B. Clarkson; A. I. Smirnov; T. I. Smirnova; H. Kang; R. L. Belford; K. Earle; J. H. Freed; *Multi-frequency EPR determination of zero field splitting of high spin species in liquids: Gd(III) chelates in water*; *Mol. Phys.* **1998,** *95*, 1325.
225. A. Hudson; J. W. E. Lewis; *Electron spin relaxation of 8S ions in solution*; *Trans. Faraday Soc.* **1970,** *66*, 1297.
226. S. Rast; A. Borel; L. Helm; E. Belorizky; P. H. Fries; A. E. Merbach; *EPR Spectroscopy of MRI-Related Gd(III) Complexes: Simultaneous Analysis of Multiple Frequency and Temperature Spectra, Including Static and Transient Crystal Field Effects*; *J. Am. Chem. Soc.* **2001,** *123*, 2637.
227. S. S. Eaton; G. R. Eaton; *Interaction of spin labels with transition metals: Part 2*; *Coord. Chem. Rev.* **1988,** *83*, 29.
228. J. J. S. Leigh; *ESR Rigid-Lattice Line Shape in a System of Two Interacting Spins*; *J. Chem. Phys.* **1970,** *52*, 2608.
229. R. A. Dwek; H. R. Levy; G. K. Radda; P. J. Seeley; *Spin label and lanthanide binding sites on glyceraldehyde-3-phosphate dehydrogenase*; *BBA* **1975,** *377*, 26.
230. A. V. Kulikov; G. I. Likhtenstein; *The use of spin relaxation phenomena in the investigation of the structure of model and biological systems by the method of spin labels*; *Adv. Mol. Relax. Interact. Proc.* **1977,** *10*, 47.
231. C. Hauser, Dissertation Universität Mainz, Mainz, 2010.
232. A. M. Wasserman; *Spin Probes in Micelles*; **1994,** *63*, 373.
233. M. F. Ottaviani; P. Baglioni; G. Martini; *Micellar solutions of sulfate surfactants studied by electron spin resonance of nitroxide radicals. 1. Use of neutral and positively charged spin probes*; *J. Phys. Chem.* **1983,** *87*, 3146.
234. M. F. Ottaviani; N. D. Ghatlia; N. J. Turro; *Nitroxide-labeled ruthenium(II)-polypyridyl complexes as EPR probes to study organized systems. 1. Micellar solutions and micellization of sodium alkyl sulfates*; *J. Phys. Chem.* **1992,** *96*, 6075.

235. H. Caldararu; A. Caragheorgheopol; M. Vasilescu; I. Dragutan; H. Lemmetyinen; *Structure of the Polar Core in Reverse Micelles of Nonionic Poly(oxyethylene) Surfactants, As Studied by Spin Probe and Fluorescence Probe Techniques*; *J. Phys. Chem.* **1994,** *98*, 5320.
236. J.-M. di Meglio; P. Baglioni; *Sodium Dodecyl Sulfate-Poly(ethylene oxide) Association by Spin Labeling*; *J. Phys. Chem.* **1994,** *98*, 5478.
237. M. Cao; M. Hai; *Investigation on the Interaction between Sodium Dodecyl Sulfate and Polyethylene Glycol by Electron Spin Resonance, Ultraviolet Spectrum, and Viscosity*; *J. Chem. Eng. Data* **2006,** *51*, 1576.
238. A. M. Wasserman; V. A. Kasaikin; V. P. Timofeev; *EPR spin probe and spin label studies of some low molecular and polymer micelles*; **1998,** *54*, 2295.
239. J. S. Zhang; S. Lee; J. W. Lee; *Solubility of Sodium Dodecyl Sulfate near Propane and Carbon Dioxide Hydrate-Forming Conditions*; *J. Chem. Eng. Data* **2007,** *52*, 2480.
240. J. Weil; N. Parris; W. Noble; F. Smith; A. Stirton; *Tallow alkanolamides: Preparation and effect on surfactant solutions*; *J. Am. Oil Chem. Soc.* **1971,** *48*, 674.
241. M. N. G. de Mul; H. T. Davis; D. F. Evans; A. V. Bhave; J. R. Wagner; *Solution Phase Behavior and Solid Phase Structure of Long-Chain Sodium Soap Mixtures*; *Langmuir* **2000,** *16*, 8276.
242. P. Baglioni; E. Rivara-Minten; L. Dei; E. Ferroni; *ESR study of sodium dodecyl sulfate and dodecyltrimethylammonium bromide micellar solutions: effect of urea*; *J. Phys. Chem.* **1990,** *94*, 8218.
243. G. Wikander; L. B. A. Johansson; *Micelle size determined by electron spin resonance and fluorescence spectroscopy*; *Langmuir* **1989,** *5*, 728.
244. N. Lebedeva; R. Ranganathan; B. L. Bales; *Location of Spectroscopic Probes in Self-Aggregating Assemblies. II. The Location of Pyrene and Other Probes in Sodium Dodecyl Sulfate Micelles*; *J. Phys. Chem. B* **2007,** *111*, 5781.
245. K. R. Gopidas; A. R. Leheny; G. Caminati; N. J. Turro; D. A. Tomalia; *Photophysical investigation of similarities between starburst dendrimers and anionic micelles*; *J. Am. Chem. Soc.* **1991,** *113*, 7335.
246. M. Benrraou; B. L. Bales; R. Zana; *Effect of the Nature of the Counterion on the Properties of Anionic Surfactants. 1. Cmc, Ionization Degree at the Cmc and Aggregation Number of Micelles of Sodium, Cesium, Tetramethylammonium, Tetraethylammonium, Tetrapropylammonium, and Tetrabutylammonium Dodecyl Sulfates*; **2003,** *107*, 13432.
247. M. A. Bahri; M. Hoebeke; A. Grammenos; L. Delanaye; N. Vandewalle; A. Seret; *Investigation of SDS, DTAB and CTAB micelle microviscosities by electron spin resonance*; *Coloid Surf. A* **2006,** *290*, 206.
248. Viscosity of methyl methacrylate. In *Data extract from Landolt-Börnstein IV/25: Viscosity of Pure Organic Liquids and*
Binary Liquid Mixtures, Landolt-Börnstein, Ed. Springer: Berlin Heidelberg.
249. M. Junk, Personal Communication, 8.8 mM 5-DSA was prepared in 0.1 M KOH. The resulting X-Band CW EPR spectrum showed one broad peak. 2009.
250. E. Meirovitch; A. Nayeem; J. H. Freed; *Analysis of protein-lipid interactions based on model simulations of electron spin resonance spectra*; **1984,** *88*, 3454.
251. J. Voss; L. Salwiński; H. R. Kaback; W. L. Hubbell; *A method for distance determination in proteins using a designed metal ion binding site and site-directed spin labeling: evaluation with T4 lysozyme*; *PNAS* **1995,** *92*, 12295.
252. W. K. Subczynski; J. S. Hyde; *Concentration of oxygen in lipid bilayers using a spin-label method.*; *Biophys. J.* **1983,** *41*, 283.
253. N. V. Sastry; J. George; *Int. J. Thermophys.* **2003,** *24*, 1089.

254. N. A. Nusair; G. A. Lorigan; *Investigating the structural and dynamic properties of n-doxylstearic acid in magnetically-aligned phospholipid bilayers by X-band EPR spectroscopy*; *Chem. Phys. Lipids* **2005,** *133*, 151.
255. J. Seelig; *Flexibility of hydrocarbon chains in lipid bilayers*; *J. Am. Chem. Soc.* **1971,** *93*, 5017.
256. M. S. Broido; I. Belsky; E. Meirovitch; *Comparative study of the ESR behavior of doxyl-labeled and (minimum steric perturbation) azethoxyl-labeled fatty acids in several liquid crystalline mesophases*; *J. Phys. Chem.* **1982,** *86*, 4197.
257. C. Thévenot; B. Grassl; G. Bastiat; W. Binana; *Aggregation number and critical micellar concentration of surfactant determined by time-dependent static light scattering (TDSLS) and conductivity*; *Colloids & Surf. A* **2005,** *252*, 105.
258. J. Oakes; *Magnetic resonance studies in aqueous systems. Part 1. Solubilization of spin probes by micellar solution*; *J. Chem. Soc., Faraday Trans. 2* **1972,** *68*, 1464.
259. N. V. Lebedeva; A. Shahine; B. L. Bales; *Aggregation Number-Based Degrees of Counterion Dissociation in Sodium n-Alkyl Sulfate Micelles*; *J. phys. Chem. B* **2005,** *109*, 19806.
260. P. Baglioni; E. Ferroni; G. Martini; M. F. Ottaviani; *Micellar solutions of sulfate surfactants studied by ESR of nitroxide radicals. 2. Use of C8, C12, and C16 derivatives of piperidinyl-1-oxy*; *J. Phys. Chem.* **1984,** *88*, 5107.
261. P. Baglioni; R. Bongiovanni; E. Rivara-Minten; L. Kevan; *Electron spin-echo modulation of x-doxylstearic acid in nonionic surfactants*; *J. Phys. Chem.* **1989,** *93*, 5574.
262. B. L. Bales; F. L. Harris; M. Peric; M. Peric; *Electron Paramagnetic Resonance Line Shifts and Line Shape Changes Due to Spin Exchange of Nitroxide Free Radicals in Liquids. 7. Singly Charged Surfactant Nitroxide*; *J. Phys. Chem. A* **2009,** *113*, 9295.
263. K. Landfester; F. J. Schork; V. A. Kusuma; *Particle size distribution in mini-emulsion polymerization*; *C. R. Chimie* **2003,** *6*, 1337.
264. B. L. Bales; C. Stenland; *Statistical distributions and collision rates of additive molecules in compartmentalized liquids studied by EPR spectroscopy. 1. Sodium dodecyl sulfate micelles, 5-doxylstearic acid ester, and cobalt(II)*; *J. Phys. Chem.* **1993,** *97*, 3418.
265. B. L. Bales; L. Messina; A. Vidal; M. Peric; O. R. Nascimento; *Precision Relative Aggregation Number Determinations of SDS Micelles Using a Spin Probe. A Model of Micelle Surface Hydration*; *J. Phys. Chem. B* **1998,** *102*, 10347.
266. S. Kaizaki; *Coordination effects of nitroxide radicals in transition metal and lanthanide complexes*; *Coord. Chem. Rev.* **2006,** *250*, 1804.
267. P. W. Anderson; *New Approach to the Theory of Superexchange Interactions*; *Phys. Rev.* **1959,** *115*, 2.
268. H. Samelson; C. Brecher; A. Lempicki; *Spectroscopy and coordination chemistry of europium chelate solutions: Concentration and solvent effects*; *J. Mol. Spectrosc.* **1966,** *19*, 349.
269. M. J. N. Junk; U. Jonas; D. Hinderberger; *EPR Spectroscopy Reveals Nanoinhomogeneities in the Structure and Reactivity of Thermoresponsive Hydrogels*; *Small* **2008,** *4*, 1485.
270. G. Jeschke, DEERAnalysis manual 2008. 2008.
271. J. Wilhelm; E. Frey; *Radial Distribution Function of Semiflexible Polymers*; **1996,** *77*, 2581.

9 Appendix

9.1 MatLab based program for simulation of a nitroxide spin label partitioning between two phases

For the latest *EasySpin* version see [48].

```
% Program for simulation of CW EPR spectra for a spin label partitioning
% between an aqueous and lipid phase
clear all; close all;

f_w=0.2; % arbitrary set fraction of DSA in water

% define spin system
% DSA in water
g_w = [2.0057 2.0037 2.0021];           % g tensor elements [gxx gyy gzz]
A_w = mt2mhz([5.6  5.6  35.1]/10, g_w); % A tensor elements [Axx Ayy Azz]  /G
lw_w =[0.12, 0];                        % Gaussian line width(FWHM) /mT
tcorr_w=1.5E-10;                        % isotropic rotational correl. time /s

% DSA in MMA
g_m = [2.0064 2.0039 2.0021];
A_m = mt2mhz([5.0  5.0  33.25]/10, g_m);% axial A tensor /G
lw_m = [0.0, 0.2];                      % Lorentzian line width(FWHM) /mT
Diff_m=[1e9, 2e9];                      % rotational diffusion rates [Dxy Dzz]
/Hz
Diffpa_m=[0 0 0]*pi/180;                % Euler angles[α β γ] /degree
Ex_m=4.7e6;                             % Heisenberg exchange frequency /Hz

% experimental settings
exp=struct('Range',[330 339],'mwFreq',9.377,'nPoints',4096,'Harmonic',1);

%simulate
% DSA in water using isotropic, fast motion EPR simulation (garlic)
Sys_w=struct('S',1/2,'g',g_w,'Nucs','14N','A',A_w,'lw',lw_w,'tcorr',tcorr_w);
[bs,sim_w]= garlic(Sys_w,exp);
sim_w=sim_w/sum(cumsum(sim_w)); % normalize to double integral

% DSA in MMA using slow motion EPR simulation (chili)
Sys_m=struct('S',1/2,'g',g_m,'Nucs','14N','A',A_m,'lw',lw_m,'Diff',Diff_m,'Dif
fpa',Diffpa_m,'Exchange',Ex_m);
[bs,sim_m]= chili(Sys_m,exp);
sim_m=sim_m/sum(cumsum(sim_m)); % normalize to double integral

% combine both simulations
sim=f_w*sim_w+(1-f_w)*sim_m;

% plot
figure(1), clf;
plot(bs,sim_w/max(sim_w),'k--', bs,sim_m/max(sim_m),'b--',
bs,sim/max(sim),'r', 'Linewidth',2);
legend('pure water','pure MMA','partitioning between water and MMA phase');
title('DSA partitioning between water and MMA');
xlabel('magnetic field / mT');
ylabel('intensity / a.u.');
axis tight;
```

9.2 Temperature dependent CW EPR measurements of miniemulsions

Temperature dependent X-Band (9.37 GHz) CW EPR-spectra of x-DSA in miniemulsions prepared in absence and presence of the lanthanide β-diketonate complex Eu(tmhd)$_3$. The water to MMA + hexadecane ratio was kept constant, if lanthanide complex was added, the ratio MMA to complex was also fixed, thus only the types of DSA (5-DSA and 16-DSA) and surfactant (SDS, SOS, ST, SL) were varied. The composition of the miniemulsion is listed in Table 5.3, molar ratios of DSA are given with respect to the surfactant. In all plots the color code for a certain temperature remains constant. Spectra within one series of measurements were measured with the same modulation amplitude, microwave attenuation, receiver gain and number of scans. Therefore the spectra do not have to be normalized and are just given baseline corrected. If not other noted, the microwave attenuation was 200 mG (0.02 mT).

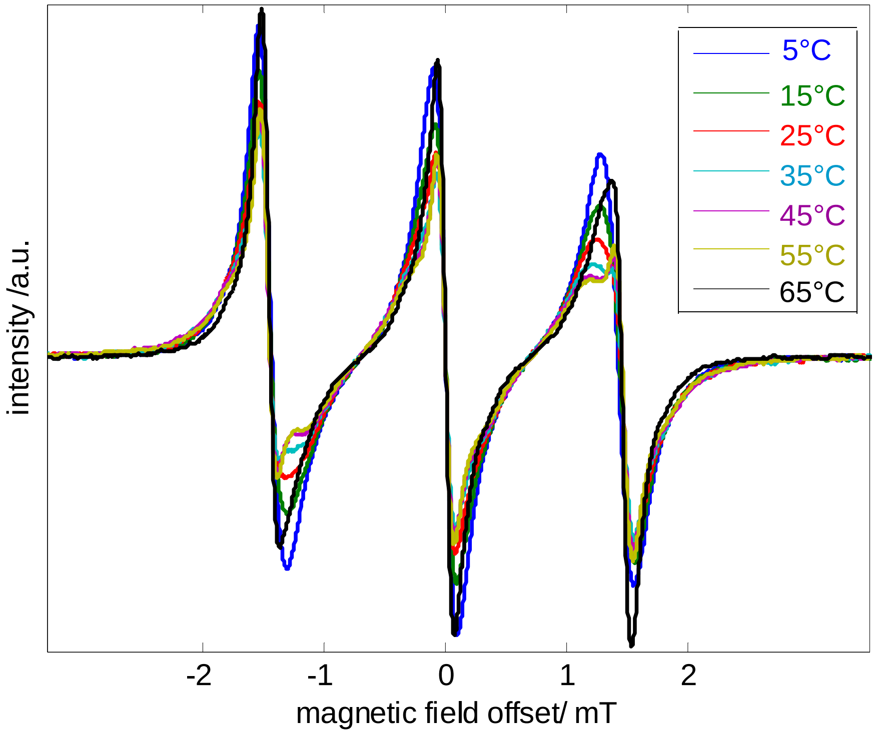

9.1

Figure 9.1 Miniemulsion with 5 mol.-% **16-DSA** in sodium dodecyl sulfate (**SDS**). Experimental: 20 scans, 22 dB microwave attenuation.

Note that in the plot below the minimum of the center line at 55°C is cutted; this was necessary in order to achieve this series of measurements with the same parameters.

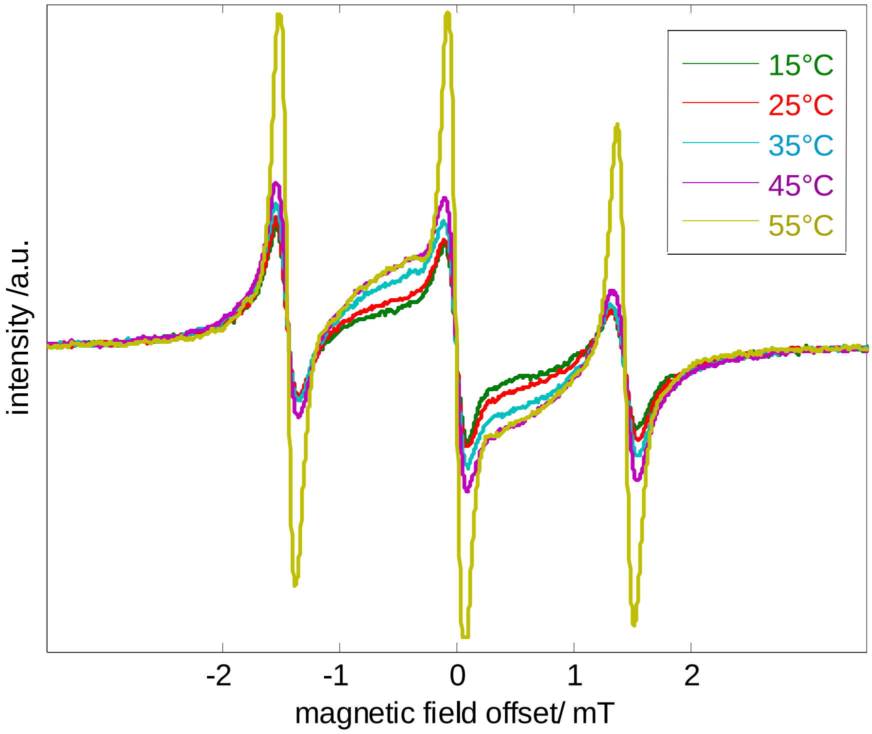

Figure 9.2 Miniemulsion with 2.5 mol.-% **16-DSA** in sodium dodecyl sulfate (**SDS**) in presence of **Eu(tmhd)$_3$**, prepared in 0.1 M NaOH. Experimental: 20 scans, 300 mG modulation amplitude, 18 dB microwave attenuation.

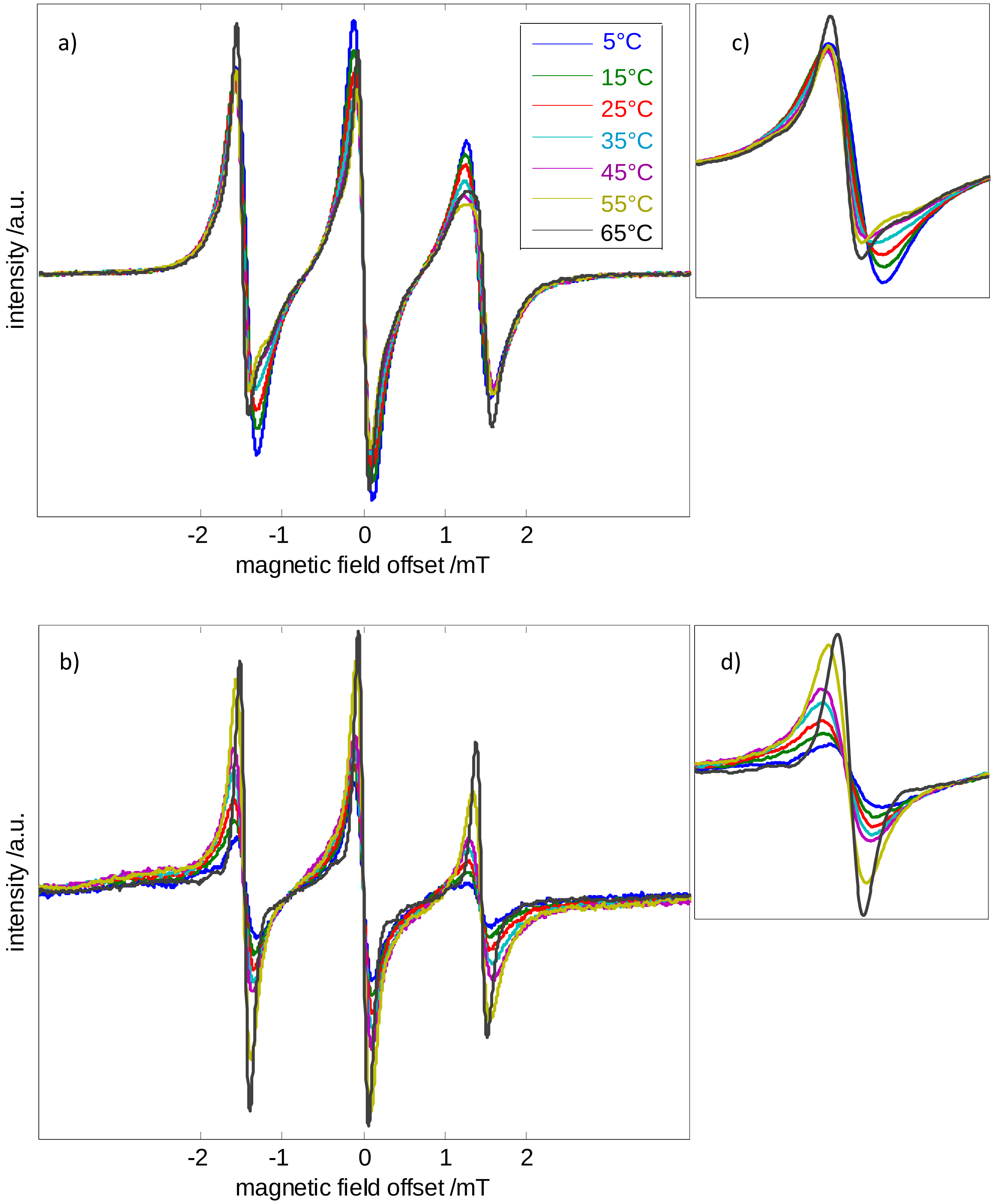

Figure 9.3 Miniemulsion with 5 mol.-% **5-DSA** in sodium dodecyl sulfate (**SDS**). a) complex-free, b) **Eu(tmhd)$_3$**, c,d,) zoom of the low-field line (m_I=1).
Experimental: 20 scans, 22 dB microwave attenuation.

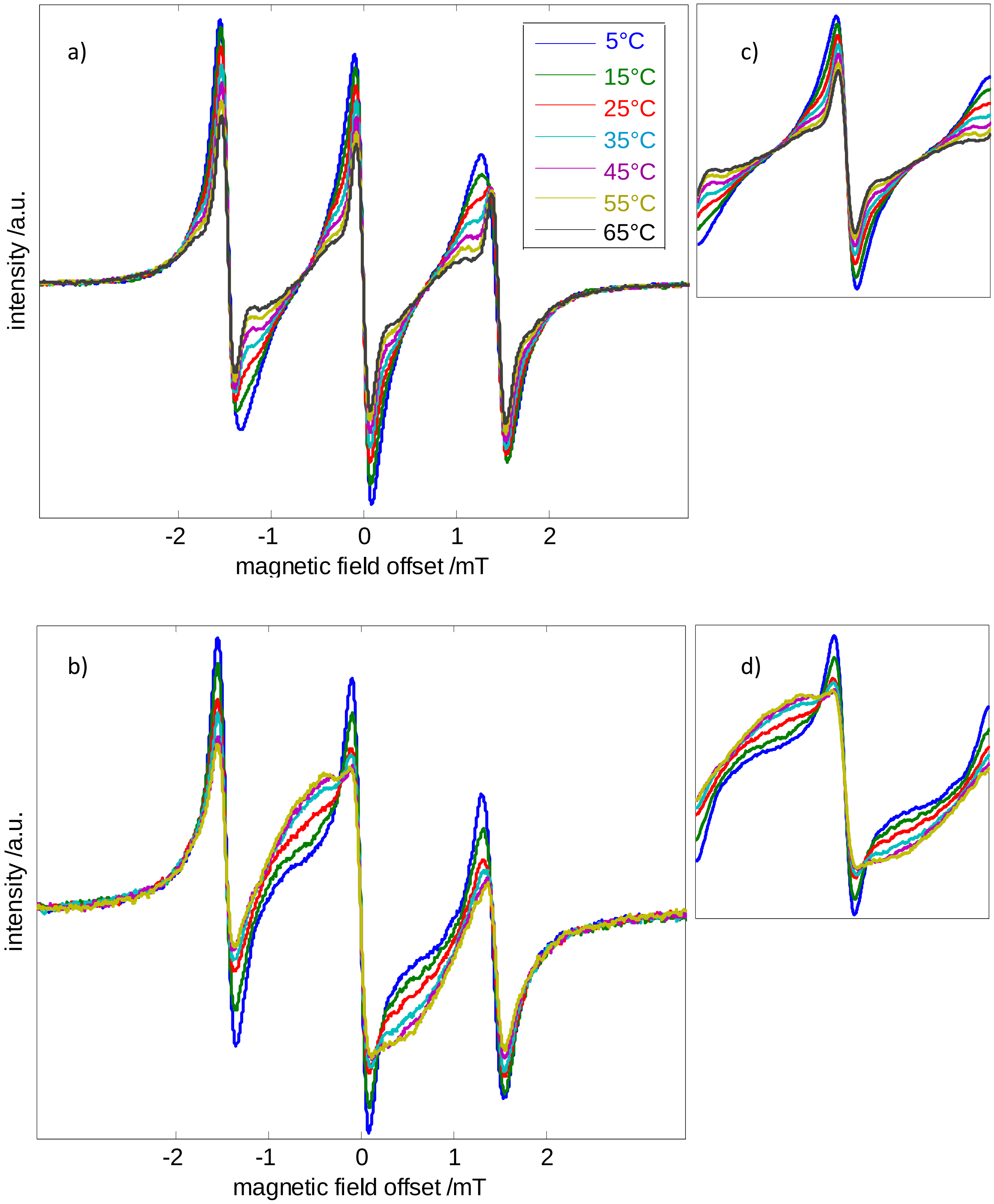

Figure 9.4 Miniemulsion with 5 mol.-% **16-DSA** in sodium octadecyl sulfate (**SOS**). a) complex-free, b) **Eu(tmhd)$_3$**, c,d,) zoom of the central line (m_I=0). In b) the spectrum at 65°C was not recorded. Experimental: 20 scans, 20 dB microwave attenuation.

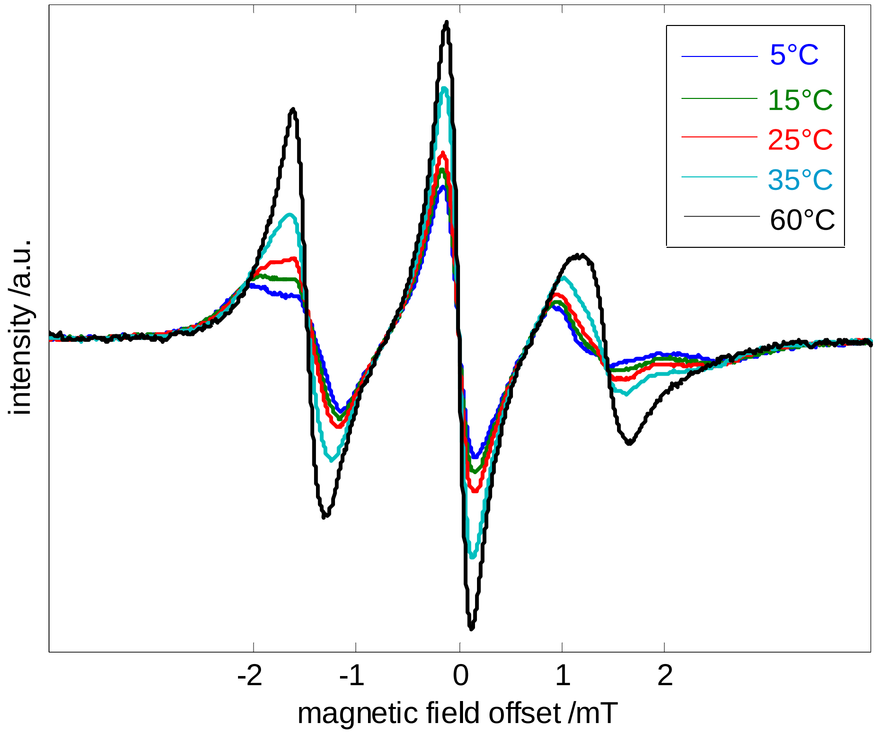

Figure 9.5 Miniemulsion of 5 mol.-% **5-DSA** in **sodium stearate**, complex-free. Exsperimental: 20 scans, 20 dB microwave attenuation.